Amyloid Oligomer Formation and Interferences

Inaugural dissertation

zur
Erlangung der Würde eines Doktors der Philosophie
vorgelegt der
Philosophisch-Naturwissenschaftlichen Fakultät
der Universität Basel

von

Jinming Wu

Basel, Schweiz, 2024

Genehmigt von der Philosophisch-Naturwissenschaftlichen Fakultät
auf Antrag von

Erstbetreuer: Prof. Dr. Jan Pieter Abrahams
Zusätzlicher Erstbetreuer: Dr. Jinghui Luo
Zweitbetreuer: Prof. Dr. Henning Stahlberg
Externer Experte: Prof. Dr. Peter Faller

Basel, den 18 October, 2022

Prof. Dr. Marcel Mayor, Dekan

Table of Contents

Abstract

As the global population is aging, the growing prevalence of progressive neurodegenerative diseases places a huge burden on our society. A wide range of amyloid-forming proteins or peptides, such as Alzheimer's amyloid-beta (Aβ) and Parkinson's α-Synuclein, have the inherent tendency to undergo protein homeostasis collapse under the misfolding conditions, in which these proteins or peptides fail to keep native conformations, followed by self-assembling into a diverse array of aggregates including the initial oligomers or protofibrils (or early aggregates) and mature fibrils. Though one of the hallmarks of these age-related diseases is the fibrillar deposits in the brain, numerous evidence has shown that it is the soluble early aggregates rather than these fibrils that are the main contributing factors to neurotoxicity. One of the prevalently accepted mechanisms states that early aggregates interact with lipid membranes, permeabilize and disrupt the integrity of cellular membranes, resulting in uncontrolled extracellular Ca^{2+} influx and imbalance of other biomolecules. However, these early aggregates are structurally heterogeneous, transient, and metastable, making them difficult to characterize their biophysical properties, such as the size distributions, the structural information, the interaction with other molecules (metal ions or extracellular globular proteins), and the permeabilization with cellular membranes.

To make a deep understanding of the above conspicuous feature of the toxicity-induced amyloid aggregates in the pathogenesis of neurodegenerative diseases, in this thesis, we discussed two main aspects of the involvement of different amyloid-forming proteins, that is amyloid oligomer formation in chapters 2-4 and oligomer interference in chapters 5-6 to discuss amyloid aggregation neurotoxic mechanisms, structural features, membrane permeabilization, and intermolecular interactions. In chapter 2, we proposed that single-molecule techniques can be taken as complementary tools for the characterization of heterogeneous amyloid aggregates and provide diagnostic perspectives for neurodegenerative diseases. Additionally, we showed a structurally and functionally relevant scaffold to stabilize Aβ oligomers in chapter 3, which enable us to determine the structure in a membrane-mimic environment, and we explored the membrane permeabilization mechanism of truncated prion protein in lipid membranes in chapter 4. Moreover, our results in chapters 5-6 reveal the effects of globular proteins on amyloid protein aggregation or the dynamic influence of lipids or metal ions on binding and unbinding to lipid membranes. Our results expand our knowledge about the toxic molecular mechanisms of amyloid aggregates and present the new directions to design

or screen the oligomer-based nanobody or antibody, which can further contribute to putting forward the diagnosis and drug design for subsequent therapy of these diseases.

Chapter 1

1 General introduction

1.1 Neurodegenerative diseases and amyloid proteins

In 2021, the United Nations released the highlights of *World Population Aging 2020* that people aged 60 years or over make up 12.3 percent of the global population, and the number is projected to reach 1.5 billion by 2050 (1). As the aging populations surge, the age-dependent physical deterioration and diseases also increase (2). Among all kinds of diseases encountered during aging, neurodegenerative diseases have become the most prevalent diseases for the middle-aged and older populations, largely affecting their life quality and healthy lifespan (3). Neurodegenerative disease is a generic term and includes Alzheimer's disease (AD, also called dementia), Parkinson's disease (PD), Huntington's disease (HD), Amyotrophic Lateral Sclerosis (ALS), and so on (4,5). The disparate neurodegenerative diseases display characteristics of the progressive loss of quantity, structure, or function of specific neurons in the human nervous system. In AD, memory loss or other forms of cognitive and behavior impairment are the general pathophysiological symptoms, and the neuro loss is most distributed in the neocortex and hippocampus cells. In PD, patients experience motor dysfunction like resting tremors, rigid muscles, and show movement (bradykinesia), which is characterized by the dopaminergic neuron deficits in the substantia nigra.

As the most notorious incurable and debilitating diseases that lead to disorders of our nervous system, neurodegenerative diseases not only bring patients the devasting physical torture but also bring an enormous economic burden to individuals, families, and the whole society. Taking dementia as an example, according to the *World report on aging and health* released in 2015 by World Health Organization (WHO), more than 47 million people worldwide got affected by dementia by 2015 and it is expected to reach over 220 million by 2050. The global cost of dementia care in 2020 was estimated to be US $ 604 billion and could rise to the US $ 1.2 trillion or more by 2030 (6). The huge number of patients and financial expenditure keep prompting researchers to constantly explore the underlying pathogenetic mechanisms and attempt effective clinical treatments against neurodegenerative diseases.

As the main risk factor for most neurodegenerative diseases, aging gradually changes the brain microenvironment such as loss of homeostasis (proteostasis), which is demonstrated to control protein synthesis, folding or unfolding, trafficking, aggregation, and degradation (7). Under normal conditions, the proteins associated with the nervous system are natively folded and thermodynamically stable with a specific three-dimensional structure to attain functionality in the organism (8). However, some internal and external factors, such as the genetic mutation, abnormal protein modifications, oxidative stress, and environmental pollution (9-11), trigger or even accentuate protein homeostasis impairment. These disease-related proteins or polypeptides fail to maintain their native conformation and tend to aggregate by exposing their hydrophobic amino acids and the unstructured backbone that are mostly buried in the native state (12). The result of intermolecular interaction of two or more non-native protein molecules leads to the formation of two large subsets of aggregates. One is the undefined amorphous structure; the other is the highly ordered fibrillar aggregates (called amyloid) with cross β-strands perpendicular to the long fibril axis (13,14). Both of them consist of thousands of individual amyloid protein molecules. The most thermodynamic stable amyloid fibrils are found to deposit into the patient brain with a wide range of neurodegenerative diseases. For example, in the cerebral cortex of AD patients' brains, the main core component of extracellular senile plaques is mainly made up of the insoluble amyloid-beta (Aβ) fibrils (15) and intracellular neurofibrillary tangles that contain protein Tau, which has become one of AD's pathological hallmarks (16). Though different neurodegenerative disorders consist of different amyloid proteins, such as the PD α-Synuclein (α-Syn) in the cytoplasm (17), prion proteins in Creutzfeldt–Jakob diseases (CJDs), and sclerosis's superoxide dismutase 1 (SOD1) in ALS (18), they share the 'amyloid fibrillar proteinaceous deposition' pathology, which means the deposition has similar histochemical properties and structural morphology. Human islet amyloid polypeptide (hIAPP), which is linked to the pathology of type-2 diabetes that is not classified into neurodegenerative diseases, also assembles and deposits into fibrils in the islet-β cells. Under denaturing conditions, many amyloid proteins can be easily accessed to the stable fibrillar structures, indicating their aggregation is not dependent on sequence but is an inherent property of the polypeptide chain alone (12,13).

1.2 Amyloid fibril formation

Since the term 'amyloid' was introduced as early as one century ago (19), the characterization of amyloid-forming or toxic pathogenic mechanisms and amyloid structure determination have

never stopped. According to the online *Pubmed* searching website, after typing 'amyloid review', over 16000 publications are listed from the year 2000 to now. In 1927, Divry and Florkin applied Congo red to stain an amyloid plaque from AD patients' brains and firstly viewed the apple-green birefringence under a polarized light (20). In 1959, under the electron microscope, Cohen *et al.* reported a linear, non-branching amyloid fibril with 80-100 Å diameter but the indeterminate length (21). The further applied X-ray fibril diffraction showed the ordered 4.7 Å cross-β conformation parallel to the fibril axis and 10-11 Å backbone perpendicular to the fibril axis (22). Combined with the solid-state NMR, cryo-electron imaging, and electron diffraction techniques, the high-resolution amyloid fibrils isolated from patients or formed *in vitro* both display the diverse and complex structural polymorphism (23-25) as well as the common cross-β architecture (26-31). The distinct polymorphs with the same protein sequence indicate a broad range of interactions to stabilize the amyloid core, suggesting the complicated molecular mechanisms of amyloid aggregation both *in vivo* and *in vitro*.

It is known that the amyloid fibril growing kinetic curves nicely fit the sigmoidal shape with three distinct phases: generally described as the lag (or nucleation) phase, elongation (or growth, exponential, polymerization) phase, and plateau (equilibrium or saturation) phase, which follows the 'nucleation-dependent' pathway without catalysis (18). The rates of the primary two phases (nucleation and elongation) predominantly determine the amyloid aggregation shape profile, and this process has been demonstrated to be nearly reproduced using the molecular crystallization-like model that only includes two parameters (nucleation and elongation) (32). In this nucleated polymerization model, the soluble homogeneous amyloid monomers convert into the low molecule weight prefibrillar oligomers or nuclei in the early stage of the nucleation period. This step is thermodynamically unfavorable and proceeds gradually. The elongation phase is more favorable the reason that the formed nuclei further act as templates or seeds to initiate and substantially speed up amyloid fibril formation. The small active oligomers/seeds (33) or monomers (34) growing at amyloid fibril ends is a general process to amplify fibril formation. Additionally, a range of secondary processes including fibril fragmentation and secondary nucleation reaction also plays an important role to accelerate the overall aggregation rate. In the fibril fragmentation process, a growing fibril breaks into several smaller parts and hence increases the number of fibrils. Furthermore, the surfaces of existing fibrils parallel to the cross-beta hydrogen bonds containing the active sites can catalyze the formation of new clusters of monomers acting as nuclei to facilitate the fibril formation (35), which is named the secondary nucleation reaction. This secondary process

system has been applied to explain a range of amyloid proteins such as Aβ (35,36), α-Syn (37), hIAPP (38), tau (39), and prion proteins (40).

Normally, the quantitative of amyloid fibril formation is to apply the light scattering or to add the Thioflavin-T (ThT) fluorescence probe into the solution at room temperature or more physiological-relevant conditions like 37 °C. ThT selectively binding to the cross-fibril structures makes ThT assay a robust and easy approach to characterize the fibril formation kinetics. The gradually enhancing fluorescence emission at 482 nm with the increasing number of fibrils enables the real-time monitoring of amyloid aggregation. Amyloid aggregation is significantly influenced by other proteins in the cellular environment. By applying the ThT-fluorescence assay at typical 37 °C, some extracellular chaperone (41-44), globular non-chaperone (45-47), and other amyloidogenic proteins (48-51) were all reported to modulate amyloid fibril formation. Popular molecular chaperones, such as clusterin (52,53), αB-crystallin (54), Bri2 (55-57), Brichos (58,59), and DNAJB6 (60), display strong anti-amyloid activity and also reduce oligomer-associated neurotoxicity by modulating specific aggregation mechanisms at the molecular level (61). Other globular non-chaperone proteins, like lysozyme and human serum albumin (HSA), can inhibit Aβ fibril formation, although the molecular interaction mechanisms remain to be explored (45,46).

1.3 Amyloid oligomer formation, structure, and toxicity

Several studies have indicated that the intermediate species (often termed oligomers or protofibrils) during the process of amyloid formation rather than the final-stage mature fibrils are the most toxic entities both *in vivo* (62) and *in vitro* (63), which make oligomers believed to be the initiating pathologic agents in the corresponding neurodegenerative diseases, such as Aβ/ tau oligomers in Alzheimer and α-Synuclein oligomers in Parkinson. This oligomer cascade hypothesis was based on the observation early as 1998 that diffusible, soluble, and nonfibrillar Aβ ligands were the potent neurotoxins to damage the central nervous system (63). The subsequent animal model experiments by *Walsh et al.* supported the toxic-oligomer statement by finding that naturally secreted Aβ oligomers in the absence of fibrils markedly inhibit the rat's hippocampal long-term potentiation, disrupt synaptic plasticity, and induce memory impairment (62). Since then, the elucidation of oligomer structural properties and the toxic mechanisms or species to cause cellular dysfunction has become very hot research topics. Over the last 20 years, more than 6000 articles including at least 900 reviews in terms of amyloid oligomers have been published.

Amyloid oligomers are structurally heterogeneous, widely ranging the size from dimers up to particles over one million daltons (64). Considering the high diversity of oligomeric species, one interesting question about the link between size and toxicity has been raised. Will the neurotoxicity of amyloid oligomers be size-dependent? It appears to be that the small size of misfolded oligomers is the potent neurotoxic fractions during the trigger of AD. Oligomeric Aβ42 dimers (65), trimers (66), tetramer (67), and Aβ-derived diffusible ligands (~17-42 kDa) (ADDLs) (63,68) are all reported to be capable of inducing mice memory formation impairment and neuronal damage. Bigger aggregates like the protofibrils (~100 kDa) (64,69), annular protofibrils (200-400 kDa) (70) and some big spherical aggregates (~ 670 kDa) (71) also show toxicity but have lower effects compared to the smaller ones. This result was supported by several reports that larger aggregates originated from the assembly of preformed amyloid oligomers in the presence of some molecular chaperones (42,72,73) or aromatic small molecules (74) significantly reduced the toxicity, demonstrating that the toxicity would decrease with increasing the size of oligomers. Smaller amyloid assemblies are likely to be more harmful, mainly due to their higher diffusion coefficient and surface-to-volume ratio, which allows them to diffuse more rapidly and to interact more aberrantly with some cellular components like membranes (42).

The broad size distributions of toxic amyloid oligomers call into question that size alone may not be sufficient to define toxicity. It has been reported that two types of Aβ42 with similar sizes show dissimilar toxicity (75). The more hydrophobic oligomeric species have the higher toxicity. This size-independent toxicity phenomenon was also observed in the non-pathological bacterial proteins (HypF-N), which is considered a valuable model system to study the structural association between misfolded protein oligomers and the induced cellular dysfunction, that two morphologically and pictorially similar HypF-N oligomeric species exhibited different cellular impairment (76). One of the plausible explanations lies in the different packing degrees from the core hydrophobic residues of peptides which are normally buried in proteins, resulting in different structural flexibility and solvent-exposed hydrophobic surfaces (77). Aβ42 (78), α-Synuclein (79), and prion-determining region Sup35(NM) (80) were all found to correlate the surface hydrophobicity directly with oligomer toxicity. A three-dimensional plot with the relationship of two structural important determinants (size and hydrophobicity) with toxicity has been plotted in the previous publication (77).

Due to neurodegenerative disease severity not linked tightly to the concentration of associated amyloid fibrils in the brain (81), more and more attention has been directed to understanding the connection between membrane-associated soluble toxic oligomers and their possible neurotoxicity. Up to now, the mechanism of how the misfolded oligomers result in cellular dysfunction in the pathogenesis of neurodegenerative diseases has not reached a consensus. A prevalently accepted molecular mechanism is the membrane depolarization and integrity disruption induced by active amyloid oligomers interacting with cellular membranes, resulting in aberrant Ca^{2+} flux and loss of cell homeostasis (5). A variety of amyloid intermediate species, including Aβ (82-87), α-Syn (88-90), and prion-associated proteins (91,92) were observed to penetrate the lipid bilayer, vesicles, or neuronal membranes, forming porous ion channels or pores upon oligomerization in membranes (93). The amyloid-pore model is analogous to the formation of transmembrane pore-forming toxins or antimicrobial peptides (94). Meanwhile, the dysregulation of cellular Ca^{2+} homeostasis was also considered to be one of the typical pathogenic features in several neurodegenerative diseases, including AD and PD (95-97).

The direct visualization of amyloid pore-shape oligomers reconstituted in lipid bilayers by atomic force (AFM) or electron transmission microscopy (TEM) showed strong support for the oligomeric pore hypothesis (93,98,99). Though the oligomer pores have been observed, the knowledge about the structural basis of oligomer-elicited neurotoxicity is still not enough. The transient, heterogeneous and unstable amyloid oligomers present difficulties for structural determination. Nuclear magnetic resonance (NMR) has revealed that membrane-mimicking Aβ42 tetramer and octamer insert as β-barrel pores into lipid membranes (100,101). Considering the highly heterogeneous property and the importance of a lipidic environment for oligomer characterization, it is still demanding to put up new methods to stabilize the transient and diverse amyloid oligomers in a membrane environment.

Metal homeostasis alterations have been reported in the patients suffering from neurodegenerative diseases including AD, PD, and CJDs (102-104). A high concentration of redox-active Cu (II) or Fe (III) and non-redox-active Zn (II) within the millimolar range has been observed in the insoluble plaques of AD patients' brains (105-107). In PD, raised Cu (II) and Fe (III) levels were found in the cerebrospinal-fluid (108) and Lewy bodies (109). Metal ions are known to bind to amyloid monomers. The N-terminal domain of Aβ (1-16 regions) (110) and α-Syn (1-52 regions) (111) both display a high affinity to Cu (II) (K_d ~1-50 nM and ~ 0.1 μM respectively). Zn (II) exhibits a lower binding ability to Aβ (112) or α-Synuclein

(113), followed by Fe (III) (113,114). The interaction with target proteins meanwhile modulates their aggregation and neurotoxicity (115,116). For α-Synuclein, the polyvalent metal ions accelerated the rate of α-Synuclein fibrillation *in vitro* (116) and induced higher neuronal toxicity (117). The N-terminal domain of α-Synuclein also shows a high affinity for the negatively-charged lipids bilayer (118) or vesicles (119), in which the loss of membrane integrity induced by the formed oligomers from lipids interaction with α-Syn is considered to be one of the underlying pathogenesis of PD (120). Both the metal ions and lipids as two significant factors contribute to the neurodegenerative disease's etiology.

1.4 Aim and scope of the thesis

As discussed above, the neurotoxicity-elicited amyloid oligomers are generally heterogeneous and structurally metastable, increasing the difficulty to determine the biophysical properties of oligomers, such as the size distribution, the atomic structure information, the interaction with cellular membranes, and so on. A lack of this information impedes the forward immune-based diagnostics and potential therapies for neurodegenerative diseases, such as antibody or nanobody development. The main goal of this thesis was to study the amyloid oligomer formation and interferences via several biophysical techniques and help shed light on the connection between amyloid assembly and toxicity, enabling us to put forward the diagnosis for neurodegenerative diseases.

The thesis work was split into two main parts as described below: amyloid oligomer formation from Chapters 2-4 and amyloid interferences from Chapters 5-6.

Some amyloidogenic proteins generally exist at an extremely low concentration (from picomolar to nanomolar range) under physiological conditions and vary between intracellular regions and brain cell types (121-125), which makes them below the detection ability of the conventional biophysical methods, such as circular dichroism (CD) for the peptide secondary structure analysis (126). Single-molecular techniques (STMs) hold unique advantages to require sample concentration close to endogenous level (127) and recording the dynamic behavior of individual molecules with a nanometer spatial and a microsecond temporal resolution (128). In **Chapter 2**, I mainly reviewed the application of three different kinds of SMTs to the characterization of biophysical properties of amyloid proteins. The overview of current molecular toxic mechanisms involved in amyloid misfolding by STMs and the perspectives of STMs for the diagnosis of amyloidosis is also presented in **Chapter 2**.

So far, the stoichiometry-defined and stable Aβ oligomers remain to be explored in a lipidic environment, which is important because of the potential value for the structure determination and conformation-specific antibody or nanobody development. Thus, an α-hemolysin (αHL) scaffold to stabilize and display the heterogeneous and transient Aβ42 oligomers was designed in a membrane environment. I further applied a series of biophysical methods to investigate the functional similarity between the stabilized and wild-type Aβ oligomers. Cryo-electron microscopy (cryo-EM) was further used for structure determination. The outcomes are presented in **Chapter 3.**

Since misfolded amyloid proteins can penetrate the cellular membranes, form ion channels, and induce the neurotoxicity (93), a deeper understanding of the role of different fragments of amyloid peptides on the channel activity and neurotoxicity helps shed light on the molecular mechanism of amyloid assembly and reveal new treatments for the neurodegenerative diseases. Thus, I investigated the influence of different prion protein fragments on the channel activity by using the single-channel recording. The results are shown in **Chapter 4.**

Amyloid fibril formation can be modulated by chaperones, non-chaperones, or other amyloidogenic proteins *in vitro* and *in vivo*. The fibrillation kinetic assays are typically carried out in *vitro*, where these proteins themselves are prone to the formation of mesoscopic amorphous aggregates due to a lack of proteostasis. In **Chapter 5**, a series of biochemical and biophysical techniques were applied to clarify the relationship between the amorphous aggregates and plaque deposits of the amyloid fibril, which are two typical forms observed in the AD brain. The results are presented in **Chapter 5.**

In addition to globular proteins, metal ions are also reported to bind to amyloid proteins and influence their folding or unfolding (129). Both metal ions and lipids trigger amyloid fibrillation *in vitro*, and it is still unclear how the metal ions influence amyloid peptides binding and unbinding to lipid membranes. In **Chapter** 6, the single-molecular nanopore technique described in **Chapter** 2 was used to study how different metal ions regulate α-Syn binding and unbinding to lipid membranes at the single-molecular level. The results are displayed in **Chapter 6.**

1.5 References

1. Economic, U. N. D. o., and Affairs, S. (2021) *World Population Ageing 2020: Highlights*, United Nations

2. Hou, Y., Dan, X., Babbar, M., Wei, Y., Hasselbalch, S. G., Croteau, D. L., and Bohr, V. A. (2019) Ageing as a risk factor for neurodegenerative disease. *Nat Rev Neurol* **15**, 565-581
3. Azam, S., Haque, M. E., Balakrishnan, R., Kim, I. S., and Choi, D. K. (2021) The Ageing Brain: Molecular and Cellular Basis of Neurodegeneration. *Front Cell Dev Biol* **9**, 683459
4. Gitler, A. D., Dhillon, P., and Shorter, J. (2017) Neurodegenerative disease: models, mechanisms, and a new hope. *Disease models & mechanisms* **10**, 499-502
5. Wu, J., Cao, C., Loch, R. A., Tiiman, A., and Luo, J. (2020) Single-molecule studies of amyloid proteins: from biophysical properties to diagnostic perspectives. *Q Rev Biophys* **53**, e12
6. World Health, O. (2015) *World report on ageing and health*, World Health Organization, Geneva
7. López-Otín, C., Blasco, M. A., Partridge, L., Serrano, M., and Kroemer, G. (2013) The hallmarks of aging. *Cell* **153**, 1194-1217
8. Greenwald, J., and Riek, R. (2010) Biology of amyloid: structure, function, and regulation. *Structure* **18**, 1244-1260
9. Jacobson, T., Priya, S., Sharma, S. K., Andersson, S., Jakobsson, S., Tanghe, R., Ashouri, A., Rauch, S., Goloubinoff, P., and Christen, P. (2017) Cadmium causes misfolding and aggregation of cytosolic proteins in yeast. *Molecular and cellular biology* **37**, e00490-00416
10. Sies, H., Berndt, C., and Jones, D. P. (2017) Oxidative stress. *Annual review of biochemistry* **86**, 715-748
11. Hipp, M. S., Kasturi, P., and Hartl, F. U. (2019) The proteostasis network and its decline in ageing. *Nature Reviews Molecular Cell Biology* **20**, 421-435
12. Hartl, F. U., and Hayer-Hartl, M. (2009) Converging concepts of protein folding in vitro and in vivo. *Nature Structural & Molecular Biology* **16**, 574-581
13. Dobson, C. M. (2003) Protein folding and misfolding. *Nature* **426**, 884-890
14. Rochet, J. C., and Lansbury, P. T., Jr. (2000) Amyloid fibrillogenesis: themes and variations. *Curr Opin Struct Biol* **10**, 60-68
15. Tagliavini, F., Giaccone, G., Frangione, B., and Bugiani, O. (1988) Preamyloid deposits in the cerebral cortex of patients with Alzheimer's disease and nondemented individuals. *Neuroscience Letters* **93**, 191-196
16. Selkoe, D. J. (2001) Alzheimer's Disease: Genes, Proteins, and Therapy. *Physiological Reviews* **81**, 741-766
17. Goedert, M. (2001) Alpha-synuclein and neurodegenerative diseases. *Nature Reviews Neuroscience* **2**, 492-501
18. Chiti, F., and Dobson, C. M. (2017) Protein Misfolding, Amyloid Formation, and Human Disease: A Summary of Progress Over the Last Decade. *Annu Rev Biochem* **86**, 27-68
19. Sipe, J. D., and Cohen, A. S. (2000) Review: History of the Amyloid Fibril. *Journal of Structural Biology* **130**, 88-98
20. Kyle, R. A. (2001) Amyloidosis: a convoluted story. *British Journal of Haematology* **114**, 529-538
21. Cohen, A. S., and Calkins, E. (1959) Electron Microscopic Observations on a Fibrous Component in Amyloid of Diverse Origins. *Nature* **183**, 1202-1203
22. EANES, E. D., and GLENNER, G. G. (1968) X-RAY DIFFRACTION STUDIES ON AMYLOID FILAMENTS. *Journal of Histochemistry & Cytochemistry* **16**, 673-677

23. Fitzpatrick, A. W., Falcon, B., He, S., Murzin, A. G., Murshudov, G., Garringer, H. J., Crowther, R. A., Ghetti, B., Goedert, M., and Scheres, S. H. (2017) Cryo-EM structures of tau filaments from Alzheimer's disease. *Nature* **547**, 185-190
24. Cao, Q., Boyer, D. R., Sawaya, M. R., Ge, P., and Eisenberg, D. S. (2019) Cryo-EM structures of four polymorphic TDP-43 amyloid cores. *Nature structural & molecular biology* **26**, 619-627
25. Qiang, W., Yau, W.-M., Lu, J.-X., Collinge, J., and Tycko, R. (2017) Structural variation in amyloid-β fibrils from Alzheimer's disease clinical subtypes. *Nature* **541**, 217-221
26. Gallardo, R., Ranson, N. A., and Radford, S. E. (2020) Amyloid structures: much more than just a cross-β fold. *Current Opinion in Structural Biology* **60**, 7-16
27. Serpell, L. C. (2000) Alzheimer's amyloid fibrils: structure and assembly. *Biochimica et Biophysica Acta (BBA) - Molecular Basis of Disease* **1502**, 16-30
28. Guerrero-Ferreira, R., Taylor, N. M. I., Arteni, A.-A., Kumari, P., Mona, D., Ringler, P., Britschgi, M., Lauer, M. E., Makky, A., Verasdonck, J., Riek, R., Melki, R., Meier, B. H., Böckmann, A., Bousset, L., and Stahlberg, H. (2019) Two new polymorphic structures of human full-length alpha-synuclein fibrils solved by cryo-electron microscopy. *eLife* **8**, e48907
29. Guerrero-Ferreira, R., Kovacik, L., Ni, D., and Stahlberg, H. (2020) New insights on the structure of alpha-synuclein fibrils using cryo-electron microscopy. *Curr Opin Neurobiol* **61**, 89-95
30. Li, B., Ge, P., Murray, K. A., Sheth, P., Zhang, M., Nair, G., Sawaya, M. R., Shin, W. S., Boyer, D. R., and Ye, S. (2018) Cryo-EM of full-length α-synuclein reveals fibril polymorphs with a common structural kernel. *Nature communications* **9**, 1-10
31. Gremer, L., Schölzel, D., Schenk, C., Reinartz, E., Labahn, J., Ravelli, R. B., Tusche, M., Lopez-Iglesias, C., Hoyer, W., and Heise, H. (2017) Fibril structure of amyloid-β (1–42) by cryo–electron microscopy. *Science* **358**, 116-119
32. Crespo, R., Rocha, F. A., Damas, A. M., and Martins, P. M. (2012) A Generic Crystallization-like Model That Describes the Kinetics of Amyloid Fibril Formation *[♦]. *Journal of Biological Chemistry* **287**, 30585-30594
33. Serio, T. R., Cashikar, A. G., Kowal, A. S., Sawicki, G. J., Moslehi, J. J., Serpell, L., Arnsdorf, M. F., and Lindquist, S. L. (2000) Nucleated Conformational Conversion and the Replication of Conformational Information by a Prion Determinant. *Science* **289**, 1317-1321
34. Collins, S. R., Douglass, A., Vale, R. D., Weissman, J. S., and Eisenberg, D. (2004) Mechanism of prion propagation: amyloid growth occurs by monomer addition. *PLoS biology* **2**, e321
35. Cohen, S. I., Linse, S., Luheshi, L. M., Hellstrand, E., White, D. A., Rajah, L., Otzen, D. E., Vendruscolo, M., Dobson, C. M., and Knowles, T. P. (2013) Proliferation of amyloid-β42 aggregates occurs through a secondary nucleation mechanism. *Proceedings of the National Academy of Sciences* **110**, 9758-9763
36. Jarrett, J. T., Berger, E. P., and Lansbury Jr, P. T. (1993) The carboxy terminus of the. beta. amyloid protein is critical for the seeding of amyloid formation: Implications for the pathogenesis of Alzheimer's disease. *Biochemistry* **32**, 4693-4697
37. Uversky, V. N., Li, J., and Fink, A. L. (2001) Evidence for a partially folded intermediate in α-synuclein fibril formation. *Journal of Biological Chemistry* **276**, 10737-10744

38. Padrick, S. B., and Miranker, A. D. (2002) Islet amyloid: phase partitioning and secondary nucleation are central to the mechanism of fibrillogenesis. *Biochemistry* **41**, 4694-4703
39. Ramachandran, G., and Udgaonkar, J. B. (2012) Evidence for the existence of a secondary pathway for fibril growth during the aggregation of tau. *Journal of molecular biology* **421**, 296-314
40. Masel, J., Jansen, V. A., and Nowak, M. A. (1999) Quantifying the kinetic parameters of prion replication. *Biophysical chemistry* **77**, 139-152
41. Wang, H., Lallemang, M., Hermann, B., Wallin, C., Loch, R., Blanc, A., Balzer, B. N., Hugel, T., and Luo, J. (2021) ATP Impedes the Inhibitory Effect of Hsp90 on Aβ40 Fibrillation. *Journal of Molecular Biology* **433**, 166717
42. Mannini, B., Cascella, R., Zampagni, M., Waarde-Verhagen, M. v., Meehan, S., Roodveldt, C., Campioni, S., Boninsegna, M., Penco, A., Relini, A., Kampinga, H. H., Dobson, C. M., Wilson, M. R., Cecchi, C., and Chiti, F. (2012) Molecular mechanisms used by chaperones to reduce the toxicity of aberrant protein oligomers. *Proceedings of the National Academy of Sciences* **109**, 12479-12484
43. Dedmon, M. M., Christodoulou, J., Wilson, M. R., and Dobson, C. M. (2005) Heat shock protein 70 inhibits α-synuclein fibril formation via preferential binding to prefibrillar species. *Journal of Biological Chemistry* **280**, 14733-14740
44. Arosio, P., Michaels, T. C. T., Linse, S., Månsson, C., Emanuelsson, C., Presto, J., Johansson, J., Vendruscolo, M., Dobson, C. M., and Knowles, T. P. J. (2016) Kinetic analysis reveals the diversity of microscopic mechanisms through which molecular chaperones suppress amyloid formation. *Nature Communications* **7**, 10948
45. Luo, J., Wärmländer, S. K. T. S., Gräslund, A., and Abrahams, J. P. (2014) Non-chaperone proteins can inhibit aggregation and cytotoxicity of Alzheimer amyloid β peptide. *The Journal of biological chemistry* **289**, 27766-27775
46. Luo, J., Wärmländer, S. K. T. S., Gräslund, A., and Abrahams, J. P. (2013) Human lysozyme inhibits the in vitro aggregation of Aβ peptides, which in vivo are associated with Alzheimer's disease. *Chemical Communications* **49**, 6507-6509
47. Assarsson, A., Hellstrand, E., Cabaleiro-Lago, C., and Linse, S. (2014) Charge Dependent Retardation of Amyloid β Aggregation by Hydrophilic Proteins. *ACS Chemical Neuroscience* **5**, 266-274
48. Luo, J., Wärmländer, S. K. T. S., Gräslund, A., and Abrahams, J. P. (2016) Reciprocal Molecular Interactions between the Aβ Peptide Linked to Alzheimer's Disease and Insulin Linked to Diabetes Mellitus Type II. *ACS Chemical Neuroscience* **7**, 269-274
49. Luo, J., Wärmländer, S. K. T. S., Gräslund, A., and Abrahams, J. P. (2016) Cross-interactions between the Alzheimer Disease Amyloid-β Peptide and Other Amyloid Proteins: A Further Aspect of the Amyloid Cascade Hypothesis. *The Journal of biological chemistry* **291**, 16485-16493
50. Wallin, C., Hiruma, Y., Wärmländer, S. K. T. S., Huvent, I., Jarvet, J., Abrahams, J. P., Gräslund, A., Lippens, G., and Luo, J. (2018) The Neuronal Tau Protein Blocks in Vitro Fibrillation of the Amyloid-β (Aβ) Peptide at the Oligomeric Stage. *Journal of the American Chemical Society* **140**, 8138-8146
51. Braun, G. A., Dear, A. J., Sanagavarapu, K., Zetterberg, H., and Linse, S. (2022) Amyloid-β peptide 37, 38 and 40 individually and cooperatively inhibit amyloid-β 42 aggregation. *Chemical Science* **13**, 2423-2439
52. Narayan, P., Meehan, S., Carver, J. A., Wilson, M. R., Dobson, C. M., and Klenerman, D. (2012) Amyloid-β Oligomers are Sequestered by both Intracellular and Extracellular Chaperones. *Biochemistry* **51**, 9270-9276

53. Yerbury, J. J., Poon, S., Meehan, S., Thompson, B., Kumita, J. R., Dobson, C. M., and Wilson, M. R. (2007) The extracellular chaperone clusterin influences amyloid formation and toxicity by interacting with prefibrillar structures. *The FASEB Journal* **21**, 2312-2322
54. Scheidt, T., Carozza, J. A., Kolbe, C. C., Aprile, F. A., Tkachenko, O., Bellaiche, M. M. J., Meisl, G., Peter, Q. A. E., Herling, T. W., Ness, S., Castellana-Cruz, M., Benesch, J. L. P., Vendruscolo, M., Dobson, C. M., Arosio, P., and Knowles, T. P. J. (2021) The binding of the small heat-shock protein αB-crystallin to fibrils of α-synuclein is driven by entropic forces. *Proceedings of the National Academy of Sciences* **118**, e2108790118
55. Willander, H., Askarieh, G., Landreh, M., Westermark, P., Nordling, K., Keränen, H., Hermansson, E., Hamvas, A., Nogee, L. M., Bergman, T., Saenz, A., Casals, C., Åqvist, J., Jörnvall, H., Berglund, H., Presto, J., Knight, S. D., and Johansson, J. (2012) High-resolution structure of a BRICHOS domain and its implications for anti-amyloid chaperone activity on lung surfactant protein C. *Proceedings of the National Academy of Sciences* **109**, 2325-2329
56. Chen, G., Abelein, A., Nilsson, H. E., Leppert, A., Andrade-Talavera, Y., Tambaro, S., Hemmingsson, L., Roshan, F., Landreh, M., Biverstål, H., Koeck, P. J. B., Presto, J., Hebert, H., Fisahn, A., and Johansson, J. (2017) Bri2 BRICHOS client specificity and chaperone activity are governed by assembly state. *Nature Communications* **8**, 2081
57. Chen, G., Andrade-Talavera, Y., Tambaro, S., Leppert, A., Nilsson, H. E., Zhong, X., Landreh, M., Nilsson, P., Hebert, H., Biverstål, H., Fisahn, A., Abelein, A., and Johansson, J. (2020) Augmentation of Bri2 molecular chaperone activity against amyloid-β reduces neurotoxicity in mouse hippocampus in vitro. *Communications Biology* **3**, 32
58. Willander, H., Presto, J., Askarieh, G., Biverstål, H., Frohm, B., Knight, S. D., Johansson, J., and Linse, S. (2012) BRICHOS Domains Efficiently Delay Fibrillation of Amyloid β-Peptide *. *Journal of Biological Chemistry* **287**, 31608-31617
59. Cohen, S. I. A., Arosio, P., Presto, J., Kurudenkandy, F. R., Biverstål, H., Dolfe, L., Dunning, C., Yang, X., Frohm, B., Vendruscolo, M., Johansson, J., Dobson, C. M., Fisahn, A., Knowles, T. P. J., and Linse, S. (2015) A molecular chaperone breaks the catalytic cycle that generates toxic Aβ oligomers. *Nature Structural & Molecular Biology* **22**, 207-213
60. Månsson, C., Arosio, P., Hussein, R., Kampinga, H. H., Hashem, R. M., Boelens, W. C., Dobson, C. M., Knowles, T. P. J., Linse, S., and Emanuelsson, C. (2014) Interaction of the Molecular Chaperone DNAJB6 with Growing Amyloid-beta 42 (Aβ42) Aggregates Leads to Sub-stoichiometric Inhibition of Amyloid Formation*. *Journal of Biological Chemistry* **289**, 31066-31076
61. Flagmeier, P., De, S., Michaels, T. C. T., Yang, X., Dear, A. J., Emanuelsson, C., Vendruscolo, M., Linse, S., Klenerman, D., Knowles, T. P. J., and Dobson, C. M. (2020) Direct measurement of lipid membrane disruption connects kinetics and toxicity of Aβ42 aggregation. *Nature Structural & Molecular Biology* **27**, 886-891
62. Walsh, D. M., Klyubin, I., Fadeeva, J. V., Cullen, W. K., Anwyl, R., Wolfe, M. S., Rowan, M. J., and Selkoe, D. J. (2002) Naturally secreted oligomers of amyloid β protein potently inhibit hippocampal long-term potentiation in vivo. *Nature* **416**, 535-539
63. Lambert, M. P., Barlow, A. K., Chromy, B. A., Edwards, C., Freed, R., Liosatos, M., Morgan, T. E., Rozovsky, I., Trommer, B., Viola, K. L., Wals, P., Zhang, C., Finch, C. E., Krafft, G. A., and Klein, W. L. (1998) Diffusible, nonfibrillar ligands derived from

Abeta1-42 are potent central nervous system neurotoxins. *Proceedings of the National Academy of Sciences* **95**, 6448-6453
64. Walsh, D. M., Lomakin, A., Benedek, G. B., Condron, M. M., and Teplow, D. B. (1997) Amyloid β-protein fibrillogenesis: detection of a protofibrillar intermediate. *Journal of Biological Chemistry* **272**, 22364-22372
65. Klyubin, I., Betts, V., Welzel, A. T., Blennow, K., Zetterberg, H., Wallin, A., Lemere, C. A., Cullen, W. K., Peng, Y., and Wisniewski, T. (2008) Amyloid β protein dimer-containing human CSF disrupts synaptic plasticity: prevention by systemic passive immunization. *Journal of Neuroscience* **28**, 4231-4237
66. Townsend, M., Shankar, G. M., Mehta, T., Walsh, D. M., and Selkoe, D. J. (2006) Effects of secreted oligomers of amyloid β-protein on hippocampal synaptic plasticity: a potent role for trimers. *The Journal of Physiology* **572**, 477-492
67. Bernstein, S. L., Dupuis, N. F., Lazo, N. D., Wyttenbach, T., Condron, M. M., Bitan, G., Teplow, D. B., Shea, J.-E., Ruotolo, B. T., Robinson, C. V., and Bowers, M. T. (2009) Amyloid-β protein oligomerization and the importance of tetramers and dodecamers in the aetiology of Alzheimer's disease. *Nature Chemistry* **1**, 326-331
68. Gong, Y., Chang, L., Viola, K. L., Lacor, P. N., Lambert, M. P., Finch, C. E., Krafft, G. A., and Klein, W. L. (2003) Alzheimer's disease-affected brain: Presence of oligomeric Aβ ligands (ADDLs) suggests a molecular basis for reversible memory loss. *Proceedings of the National Academy of Sciences* **100**, 10417-10422
69. Townsend, M., Shankar, G. M., Mehta, T., Walsh, D. M., and Selkoe, D. J. (2006) Effects of secreted oligomers of amyloid β-protein on hippocampal synaptic plasticity: a potent role for trimers. *The Journal of physiology* **572**, 477-492
70. Kayed, R., Pensalfini, A., Margol, L., Sokolov, Y., Sarsoza, F., Head, E., Hall, J., and Glabe, C. (2009) Annular protofibrils are a structurally and functionally distinct type of amyloid oligomer. *Journal of Biological Chemistry* **284**, 4230-4237
71. Hoshi, M., Sato, M., Matsumoto, S., Noguchi, A., Yasutake, K., Yoshida, N., and Sato, K. (2003) Spherical aggregates of beta-amyloid (amylospheroid) show high neurotoxicity and activate tau protein kinase I/glycogen synthase kinase-3β. *Proceedings of the National Academy of Sciences* **100**, 6370-6375
72. Ojha, J., Masilamoni, G., Dunlap, D., Udoff, R. A., and Cashikar, A. G. (2011) Sequestration of toxic oligomers by HspB1 as a cytoprotective mechanism. *Molecular and cellular biology* **31**, 3146-3157
73. Cascella, R., Conti, S., Mannini, B., Li, X., Buxbaum, J. N., Tiribilli, B., Chiti, F., and Cecchi, C. (2013) Transthyretin suppresses the toxicity of oligomers formed by misfolded proteins in vitro. *Biochimica et Biophysica Acta (BBA)-Molecular Basis of Disease* **1832**, 2302-2314
74. Ladiwala, A. R. A., Dordick, J. S., and Tessier, P. M. (2011) Aromatic small molecules remodel toxic soluble oligomers of amyloid β through three independent pathways. *Journal of Biological Chemistry* **286**, 3209-3218
75. Ladiwala, A. R. A., Litt, J., Kane, R. S., Aucoin, D. S., Smith, S. O., Ranjan, S., Davis, J., Van Nostrand, W. E., and Tessier, P. M. (2012) Conformational differences between two amyloid β oligomers of similar size and dissimilar toxicity. *Journal of Biological Chemistry* **287**, 24765-24773
76. Campioni, S., Mannini, B., Zampagni, M., Pensalfini, A., Parrini, C., Evangelisti, E., Relini, A., Stefani, M., Dobson, C. M., Cecchi, C., and Chiti, F. (2010) A causative link between the structure of aberrant protein oligomers and their toxicity. *Nature Chemical Biology* **6**, 140-147
77. Mannini, B., Mulvihill, E., Sgromo, C., Cascella, R., Khodarahmi, R., Ramazzotti, M., Dobson, C. M., Cecchi, C., and Chiti, F. (2014) Toxicity of Protein Oligomers Is

Rationalized by a Function Combining Size and Surface Hydrophobicity. *ACS Chemical Biology* **9**, 2309-2317
78. Kremer, J. J., Pallitto, M. M., Sklansky, D. J., and Murphy, R. M. (2000) Correlation of β-Amyloid Aggregate Size and Hydrophobicity with Decreased Bilayer Fluidity of Model Membranes. *Biochemistry* **39**, 10309-10318
79. Chen Serene, W., Drakulic, S., Deas, E., Ouberai, M., Aprile Francesco, A., Arranz, R., Ness, S., Roodveldt, C., Guilliams, T., De-Genst Erwin, J., Klenerman, D., Wood Nicholas, W., Knowles Tuomas, P. J., Alfonso, C., Rivas, G., Abramov Andrey, Y., Valpuesta José, M., Dobson Christopher, M., and Cremades, N. (2015) Structural characterization of toxic oligomers that are kinetically trapped during α-synuclein fibril formation. *Proceedings of the National Academy of Sciences* **112**, E1994-E2003
80. Krishnan, R., Goodman Jessica, L., Mukhopadhyay, S., Pacheco Chris, D., Lemke Edward, A., Deniz Ashok, A., and Lindquist, S. (2012) Conserved features of intermediates in amyloid assembly determine their benign or toxic states. *Proceedings of the National Academy of Sciences* **109**, 11172-11177
81. Selkoe, D. J., and Hardy, J. (2016) The amyloid hypothesis of Alzheimer's disease at 25 years. *EMBO molecular medicine* **8**, 595-608
82. Lin, H., Bhatia, R., and Lal, R. (2001) Amyloid β protein forms ion channels: implications for Alzheimer's disease pathophysiology. *The FASEB Journal* **15**, 2433-2444
83. Arispe, N., Diaz, J. C., and Simakova, O. (2007) Aβ ion channels. Prospects for treating Alzheimer's disease with Aβ channel blockers. *Biochimica et Biophysica Acta (BBA)-Biomembranes* **1768**, 1952-1965
84. Pollard, H. B., Arispe, N., and Rojas, E. (1995) Ion channel hypothesis for Alzheimer amyloid peptide neurotoxicity. *Cellular and molecular neurobiology* **15**, 513-526
85. Kourie, J. I., Henry, C. L., and Farrelly, P. (2001) Diversity of amyloid β protein fragment [1–40]-formed channels. *Cellular and molecular neurobiology* **21**, 255-284
86. Kourie, J. I. (2001) Mechanisms of amyloid β protein-induced modification in ion transport systems: implications for neurodegenerative diseases. *Cellular and molecular neurobiology* **21**, 173-213
87. Kawahara, M., and Kuroda, Y. (2000) Molecular mechanism of neurodegeneration induced by Alzheimer's β-amyloid protein: channel formation and disruption of calcium homeostasis. *Brain research bulletin* **53**, 389-397
88. Volles, M. J., Lee, S.-J., Rochet, J.-C., Shtilerman, M. D., Ding, T. T., Kessler, J. C., and Lansbury, P. T. (2001) Vesicle permeabilization by protofibrillar α-synuclein: implications for the pathogenesis and treatment of Parkinson's disease. *Biochemistry* **40**, 7812-7819
89. Kim, H.-Y., Cho, M.-K., Kumar, A., Maier, E., Siebenhaar, C., Becker, S., Fernandez, C. O., Lashuel, H. A., Benz, R., and Lange, A. (2009) Structural properties of pore-forming oligomers of α-synuclein. *Journal of the American Chemical Society* **131**, 17482-17489
90. Volles, M. J., and Lansbury, P. T. (2002) Vesicle permeabilization by protofibrillar α-synuclein is sensitive to Parkinson's disease-linked mutations and occurs by a pore-like mechanism. *Biochemistry* **41**, 4595-4602
91. Kourie, J. I., and Culverson, A. (2000) Prion peptide fragment PrP [106–126] forms distinct cation channel types. *Journal of Neuroscience Research* **62**, 120-133
92. Wu, B., McDonald, A. J., Markham, K., Rich, C. B., McHugh, K. P., Tatzelt, J., Colby, D. W., Millhauser, G. L., and Harris, D. A. (2017) The N-terminus of the prion protein is a toxic effector regulated by the C-terminus. *Elife* **6**, e23473

93. Quist, A., Doudevski, I., Lin, H., Azimova, R., Ng, D., Frangione, B., Kagan, B., Ghiso, J., and Lal, R. (2005) Amyloid ion channels: A common structural link for protein-misfolding disease. *Proceedings of the National Academy of Sciences* **102**, 10427-10432
94. Lashuel, H. A., and Lansbury, P. T. (2006) Are amyloid diseases caused by protein aggregates that mimic bacterial pore-forming toxins? *Quarterly reviews of biophysics* **39**, 167-201
95. Hajieva, P., Kuhlmann, C., Luhmann, H. J., and Behl, C. (2009) Impaired calcium homeostasis in aged hippocampal neurons. *Neuroscience Letters* **451**, 119-123
96. Mattson, M. P. (2000) Apoptosis in neurodegenerative disorders. *Nature reviews Molecular cell biology* **1**, 120-130
97. Mattson, M. P., and Chan, S. L. (2001) Dysregulation of cellular calcium homeostasis in Alzheimer's disease. *Journal of Molecular Neuroscience* **17**, 205-224
98. Lashuel, H. A., Hartley, D., Petre, B. M., Walz, T., and Lansbury, P. T. (2002) Amyloid pores from pathogenic mutations. *Nature* **418**, 291-291
99. Pountney, D. L., Lowe, R., Quilty, M., Vickers, J. C., Voelcker, N. H., and Gai, W. P. (2004) Annular α-synuclein species from purified multiple system atrophy inclusions. *Journal of Neurochemistry* **90**, 502-512
100. Usachev, K. S., Kolosova, O. A., Klochkova, E. A., Yulmetov, A. R., Aganov, A. V., and Klochkov, V. V. (2017) Oligomerization of the antimicrobial peptide Protegrin-5 in a membrane-mimicking environment. Structural studies by high-resolution NMR spectroscopy. *European Biophysics Journal* **46**, 293-300
101. Ciudad, S., Puig, E., Botzanowski, T., Meigooni, M., Arango, A. S., Do, J., Mayzel, M., Bayoumi, M., Chaignepain, S., Maglia, G., Cianferani, S., Orekhov, V., Tajkhorshid, E., Bardiaux, B., and Carulla, N. (2020) Aβ(1-42) tetramer and octamer structures reveal edge conductivity pores as a mechanism for membrane damage. *Nature Communications* **11**, 3014
102. Gerhardsson, L., Lundh, T., Londos, E., and Minthon, L. (2011) Cerebrospinal fluid/plasma quotients of essential and non-essential metals in patients with Alzheimer's disease. *Journal of Neural Transmission* **118**, 957-962
103. Gorell, J. M., Rybicki, B. A., Johnson, C. C., and Peterson, E. L. (1999) Occupational metal exposures and the risk of Parkinson's disease. *Neuroepidemiology* **18**, 303-308
104. Brown, D. R., Qin, K., Herms, J. W., Madlung, A., Manson, J., Strome, R., Fraser, P. E., Kruck, T., von Bohlen, A., Schulz-Schaeffer, W., Giese, A., Westaway, D., and Kretzschmar, H. (1997) The cellular prion protein binds copper in vivo. *Nature* **390**, 684-687
105. Lovell, M. A., Robertson, J. D., Teesdale, W. J., Campbell, J. L., and Markesbery, W. R. (1998) Copper, iron and zinc in Alzheimer's disease senile plaques. *Journal of the Neurological Sciences* **158**, 47-52
106. Dong, J., Atwood, C. S., Anderson, V. E., Siedlak, S. L., Smith, M. A., Perry, G., and Carey, P. R. (2003) Metal Binding and Oxidation of Amyloid-β within Isolated Senile Plaque Cores: Raman Microscopic Evidence. *Biochemistry* **42**, 2768-2773
107. Miller, L. M., Wang, Q., Telivala, T. P., Smith, R. J., Lanzirotti, A., and Miklossy, J. (2006) Synchrotron-based infrared and X-ray imaging shows focalized accumulation of Cu and Zn co-localized with β-amyloid deposits in Alzheimer's disease. *Journal of Structural Biology* **155**, 30-37
108. Pall, H. S., Blake, D. R., Gutteridge, J. M., Williams, A. C., Lunec, J., Hall, M., and Taylor, A. (1987) RAISED CEREBROSPINAL-FLUID COPPER CONCENTRATION IN PARKINSON'S DISEASE. *The Lancet* **330**, 238-241

109. Castellani, R. J., Siedlak, S. L., Perry, G., and Smith, M. A. (2000) Sequestration of iron by Lewy bodies in Parkinson's disease. *Acta Neuropathologica* **100**, 111-114
110. Wärmländer, S., Tiiman, A., Abelein, A., Luo, J., Jarvet, J., Söderberg, K. L., Danielsson, J., and Gräslund, A. (2013) Biophysical Studies of the Amyloid β-Peptide: Interactions with Metal Ions and Small Molecules. *ChemBioChem* **14**, 1692-1704
111. Binolfi, A., Rasia, R. M., Bertoncini, C. W., Ceolin, M., Zweckstetter, M., Griesinger, C., Jovin, T. M., and Fernández, C. O. (2006) Interaction of α-Synuclein with Divalent Metal Ions Reveals Key Differences: A Link between Structure, Binding Specificity and Fibrillation Enhancement. *Journal of the American Chemical Society* **128**, 9893-9901
112. Tõugu, V., Karafin, A., and Palumaa, P. (2008) Binding of zinc(II) and copper(II) to the full-length Alzheimer's amyloid-β peptide. *Journal of Neurochemistry* **104**, 1249-1259
113. Moons, R., Konijnenberg, A., Mensch, C., Van Elzen, R., Johannessen, C., Maudsley, S., Lambeir, A.-M., and Sobott, F. (2020) Metal ions shape α-synuclein. *Scientific Reports* **10**, 16293
114. Bisaglia, M., Tessari, I., Mammi, S., and Bubacco, L. (2009) Interaction Between α-Synuclein and Metal Ions, Still Looking for a Role in the Pathogenesis of Parkinson's Disease. *NeuroMolecular Medicine* **11**, 239-251
115. Wärmländer, S. K. T. S., Österlund, N., Wallin, C., Wu, J., Luo, J., Tiiman, A., Jarvet, J., and Gräslund, A. (2019) Metal binding to the amyloid-β peptides in the presence of biomembranes: potential mechanisms of cell toxicity. *JBIC Journal of Biological Inorganic Chemistry* **24**, 1189-1196
116. Uversky, V. N., Li, J., and Fink, A. L. (2001) Metal-triggered Structural Transformations, Aggregation, and Fibrillation of Human α-Synuclein: A POSSIBLE MOLECULAR LINK BETWEEN PARKINSON′S DISEASE AND HEAVY METAL EXPOSURE *. *Journal of Biological Chemistry* **276**, 44284-44296
117. (2016) Alpha-Synuclein Oligomers Interact with Metal Ions to Induce Oxidative Stress and Neuronal Death in Parkinson's Disease. *Antioxidants & Redox Signaling* **24**, 376-391
118. Jo, E., McLaurin, J., Yip, C. M., St. George-Hyslop, P., and Fraser, P. E. (2000) α-Synuclein Membrane Interactions and Lipid Specificity *. *Journal of Biological Chemistry* **275**, 34328-34334
119. Rhoades, E., Ramlall, T. F., Webb, W. W., and Eliezer, D. (2006) Quantification of α-synuclein binding to lipid vesicles using fluorescence correlation spectroscopy. *Biophysical journal* **90**, 4692-4700
120. Musteikytė, G., Jayaram, A. K., Xu, C. K., Vendruscolo, M., Krainer, G., and Knowles, T. P. J. (2021) Interactions of α-synuclein oligomers with lipid membranes. *Biochimica et Biophysica Acta (BBA) - Biomembranes* **1863**, 183536
121. Hannestad, J. K., Rocha, S., Agnarsson, B., Zhdanov, V. P., Wittung-Stafshede, P., and Höök, F. (2020) Single-vesicle imaging reveals lipid-selective and stepwise membrane disruption by monomeric α-synuclein. *Proceedings of the National Academy of Sciences* **117**, 14178-14186
122. Lue, L.-F., Kuo, Y.-M., Roher, A. E., Brachova, L., Shen, Y., Sue, L., Beach, T., Kurth, J. H., Rydel, R. E., and Rogers, J. (1999) Soluble Amyloid β Peptide Concentration as a Predictor of Synaptic Change in Alzheimer's Disease. *The American Journal of Pathology* **155**, 853-862
123. McLean, C. A., Cherny, R. A., Fraser, F. W., Fuller, S. J., Smith, M. J., Vbeyreuther, K., Bush, A. I., and Masters, C. L. (1999) Soluble pool of Aβ amyloid as a determinant

of severity of neurodegeneration in Alzheimer's disease. *Annals of Neurology* **46**, 860-866

124. Mollenhauer, B., Cullen, V., Kahn, I., Krastins, B., Outeiro, T. F., Pepivani, I., Ng, J., Schulz-Schaeffer, W., Kretzschmar, H. A., McLean, P. J., Trenkwalder, C., Sarracino, D. A., VonSattel, J.-P., Locascio, J. J., El-Agnaf, O. M. A., and Schlossmacher, M. G. (2008) Direct quantification of CSF α-synuclein by ELISA and first cross-sectional study in patients with neurodegeneration. *Experimental Neurology* **213**, 315-325
125. Mehta, P. D., Pirttilä, T., Mehta, S. P., Sersen, E. A., Aisen, P. S., and Wisniewski, H. M. (2000) Plasma and cerebrospinal fluid levels of amyloid beta proteins 1-40 and 1-42 in Alzheimer disease. *Arch Neurol* **57**, 100-105
126. Whitmore, L., and Wallace, B. A. (2008) Protein secondary structure analyses from circular dichroism spectroscopy: Methods and reference databases. *Biopolymers* **89**, 392-400
127. Holzmeister, P., Acuna, G. P., Grohmann, D., and Tinnefeld, P. (2014) Breaking the concentration limit of optical single-molecule detection. *Chem Soc Rev* **43**, 1014-1028
128. Greenleaf, W. J., Woodside, M. T., and Block, S. M. (2007) High-Resolution, Single-Molecule Measurements of Biomolecular Motion. *Annual Review of Biophysics and Biomolecular Structure* **36**, 171-190
129. Gaeta, A., and Hider, R. C. (2005) The crucial role of metal ions in neurodegeneration: the basis for a promising therapeutic strategy. *British journal of pharmacology* **146**, 1041-1059

Chapter 2

Single-molecule studies of amyloid proteins: from biophysical properties to diagnostic perspectives

Jinming Wu[1], Chan Cao[2,3], Rolf Antonie Loch[1], Ann Tiiman[4], Jinghui Luo[1,*]

1. Department of Biology and Chemistry, Paul Scherrer Institute, 5232 Villigen, Switzerland
2. Institute of Bioengineering, School of Life Sciences, Ecole Polytechnique Fédérale de Lausanne (EPFL), 1015 Lausanne, Switzerland.
3. Swiss Institute of Bioinformatics (SIB), 1015 Lausanne, Switzerland.
4. Department of Clinical Neuroscience (CNS), Center for Molecular Medicine CMM L8:01, Karolinska Institute, 17176 Stockholm, Sweden.

*Corresponding author: Jinghui.luo@psi.ch

Accept by ***Quarterly Reviews of Biophysics.***

DOI: https://doi.org/10.1017/S0033583520000086

2.1 Abstract

In neurodegenerative diseases, a wide range of amyloid proteins or peptides such as amyloid–beta and α-synuclein fail to keep native functional conformations, followed by misfolding and self-assembling into a diverse array of aggregates. The aggregates further exert toxicity leading to the dysfunction, degeneration and loss of cells in the affected organs. Due to the disordered structure of the amyloid proteins, endogenous molecules, such as lipid membranes, are prone to interact with amyloid proteins at a low concentration and influence amyloid cytotoxicity. The heterogeneity of amyloid aggregates complicates the understanding on the amyloid cytotoxicity when relying only on the conventional bulk and ensemble techniques. As complementary tools, single-molecule techniques (SMTs) provide novel insight into the different subpopulations of a heterogeneous amyloid mixture as well as the cytotoxicity, in particular as involved in lipid membranes. This review focuses on the recent advances of a series of SMTs, including single-molecule fluorescence imaging, single-molecule force spectroscopy and single-nanopore electrical recording, for the understanding of the amyloid molecular mechanism. The working principles, benefits and limitations of each technique are discussed and compared, as well as the contributions of SMTs to the enhanced understanding of the amyloid molecular mechanisms. We also discuss why SMTs show great potential and are worthy of further investigation with feasibility studies as diagnostic tools of neurodegenerative diseases and which limitations are to be addressed.

Keywords: Amyloid protein; Single-molecule fluorescence imaging; single-molecule force spectroscopy; Single-nanopore electrical recording.

2.2 Introduction

Neurodegenerative disease, characterized by the loss of structure, function or quantity of specific neurons in the human brain, is a generic term covering a range of incurable and debilitating conditions that progressively lead to disorders of our nervous system. A series of pathophysiological symptoms include memory/cognitive impairment and motor dysfunction, caused by diseases such as Alzheimer's (AD), Parkinson's (PD), Huntington's diseases (HD) and Amyotrophic Lateral Sclerosis (ALS) (1,2). The onset of the diseases is prone to be prevalent in the middle-aged and elderly at an increasing rate (3). Though many approaches have been introduced with the potential to understand and treat these neurodegenerative diseases, the outcomes of the clinical research have yet to be assessed. Therefore, novel

experimental approaches and insights are essential to better understand the pathogenesis and to find new therapeutic agents against the diseases.

When loss of protein homeostasis (proteostasis) occurs, the proteins associated with the nervous system fail to sustain their native conformation, start to aggregate and deposit in the brain through two different aggregation routes (4,5). The first route is to form amorphous aggregates, which are usually present in undefined structures. Alternatively, monomeric proteins aggregate into soluble oligomers and then form highly ordered amyloid fibrils (6-8). One of the pathological hallmarks of AD is the finding of senile plaques deposited in the brain. The core component of the plaques was demonstrated to be the insoluble amyloid-beta (Aβ) fibrils (9,10). Numerous other neurodegenerative disorders share this common pathology with amyloid proteins, such as Parkinson's α-synculein (α-syn), Creutzfeldt–Jakob disease's prion protein, and amyotrophic lateral sclerosis's superoxide dismutase 1 (SOD1) (11). Although most disease-related amyloids are assumed to be non-functional, there are some amyloids, found from microbes to humans that are functional, and even disease-related amyloids can, sometimes, possess functions (12-14). Therefore, amyloid proteins can be both protective and destructive, critically dependent upon the amyloid homeostasis (15), which involves protein synthesis and folding, conformational maintenance and degradation (4,12).

Amyloid fibril formation has been proposed as a "nucleation-dependent polymerization" process (16), where the kinetics falls into three phases: the lag phase, the elongation and the final plateau. First, toxic oligomers form in the initial lag period and may act as a template to nucleate amyloid fibril formation in the latter phases. Likewise, amyloid fibrils facilitate the formation of new fibrils through a process of secondary nucleation (17-19). A number of studies have indicated that soluble oligomers or protofibrils are the main contributing factor of the cellular toxicity rather than the final-step mature fibrils (20-22). Although consensus has not been reached on the pathogenesis of amyloids, a prevalently accepted mechanism states that the early aggregates interact with lipid membranes, disrupt the integrity of cell membranes, resulting in uncontrolled extracellular Ca^{2+} influx and imbalance of other biomolecules (23-25). However, several questions remain to be answered. For example, what sizes of the aggregates are responsible for the damage to cellular membranes? What are the toxic mechanisms by which amyloid oligomers can disrupt cellular membranes? Do these aggregates thin the membranes, form pores or step-wise increase membrane permeability, or a combination?

There are several reasons why these questions remain unanswered. First, it is difficult to detect individual oligomers, because the fibrillation process is a dynamic equilibrium process, giving rise to a highly heterogeneous mixture. The heterogeneity hinders the analysis of the size, conformation and structure of the neurotoxic aggregates. In addition, monomers and small aggregates (from dimers to hexamers) *in vivo* are likely to interconvert in a dynamic equilibrium (20,26,27). Moreover, at physiological conditions, amyloidogenic proteins exist at a low concentration and vary between intracellular regions and brain cell types. For example, concentrations of intercellular a-syn might be likely in the low nanomolar range (28), while the soluble Aβ42 were only found at the picomolar levels in human AD brain entorhinal cortex and superior frontal gyrus regions (29-31). Such low concentration are below the detection capability of conventional biophysical assays. Using higher (non-physiological) concentration in the assays may result in completely different interactions or pathways that may not be the correct representation of the *in vivo* processes. In addition, the conventional biophysical techniques such as fluorescence assays and circular dichroism (CD) (32-34), represent the averaged data of whole populations, smoothing out the low 'noise' signal from an individual aggregate (35). These ensemble methods are therefore not ideal for the investigation of the energetically metastable, heterogeneous states of amyloid proteins. To overcome some of these limitations, single-molecule amyloid characterization at the physiological concentration is thus of great importance.

Single-molecule techniques (SMTs) have unique advantages of recording the behavior of individual molecules in a heterogeneous sample (36,37). The required concentration for most SMTs is close to the endogenous level (pM to nM). Such conditions assist in the formation of stabilized heterogeneous and transient oligomers at a time that allows to study their structures and dynamics, which are easily hampered or altered at higher concentrations (38). Moreover, the experimental parameters of SMTs can reach a nanometer spatial resolution and a microsecond temporal resolution (39). SMTs may give the appropriate and accurate analysis of transient amyloid aggregates at the single-molecule level. SMTs can be classified into three types: single-molecule fluorescence-based imaging (SMFI), single-molecule force spectroscopy (SMFS) and single-nanopore electrical systems (SNS). SMFI methods are localization-based imaging techniques that can normally track fluorophore-tagged single particles or vesicles without perturbation (28,40). SMFS generally applies the tension or torsion to investigate the mechanical responses of biological systems (41). SNS allow to analyze the behavior of both small and large sized oligomers in a single nanopore system by recording the

dwell time and residual current when they assemble into nanopore (42,43). The principles of these techniques and their applications on amyloids will be discussed in further detail in section 2.3.

Our paper aims to give an overview of the current understanding of the molecular mechanisms involved in amyloid misfolding, by focusing on single-molecule approaches in contrast to the more commonly used bulk or ensemble methods. In particular, we focus on the application of the three main types of SMTs mentioned above for the characterization of the biophysical properties of amyloid proteins. Here, we will briefly state the working principles, benefits and limitations of each single-molecule technique, and combined single-molecule dual measurements will be briefly discussed in this review. We will also summarize the detailed insights they can give for different species of amyloid proteins, the interaction with membranes and their roles in amyloid diseases. In addition, our paper covers the perspectives of each single-molecule technique for the diagnosis of amyloidosis.

2.3 Single-molecule techniques for biophysical studies of amyloid proteins

In comparison to the conventional methods studying ensemble systems, single-molecule approaches can provide insights in the heterogeneity of amyloid proteins and distinguish contributions of different oligomers, and therefore hold the potential to gain a deeper understanding of structure and function of different amyloid morphologies. We subsequently discuss three main types of SMTs and their variants in three separate sections, and show how these techniques have been relevant to amyloid protein studies at the molecular level.

2.3.1 Single-molecule fluorescence imaging (SMFI)

Fluorescence imaging is based on the emission of light by a fluorophore. After the excitation of an electron to a higher energy state, the fluorophore relaxes back to the ground state and re-emits a new photon. A protein of interest can be directly observed with a non-covalent fluorophore or covalent fluorophore after a conjunction with a probe (44,45). SMFI techniques visualize the changes of fluorescent properties of labelled proteins such as fluorescence lifetime, quantum yield or polarization to reveal intermolecular interactions, reaction kinetics and conformational dynamics.

Total internal reflection fluorescence (TIRF), fluorescence resonance energy transfer (FRET), two color coincidence detection (TCCD), fluorescence recovery after photobleaching (FRAP)

and fluorescence correlation spectroscopy (FCS) are common fluorescence-based methods for tracking single particles. For an overview on the history and some of the recent discoveries in the life sciences made via SMFI, we refer to the review by Shashkova and Leake (40). In this review, we will focus on the implementation of these techniques for amyloid protein studies.

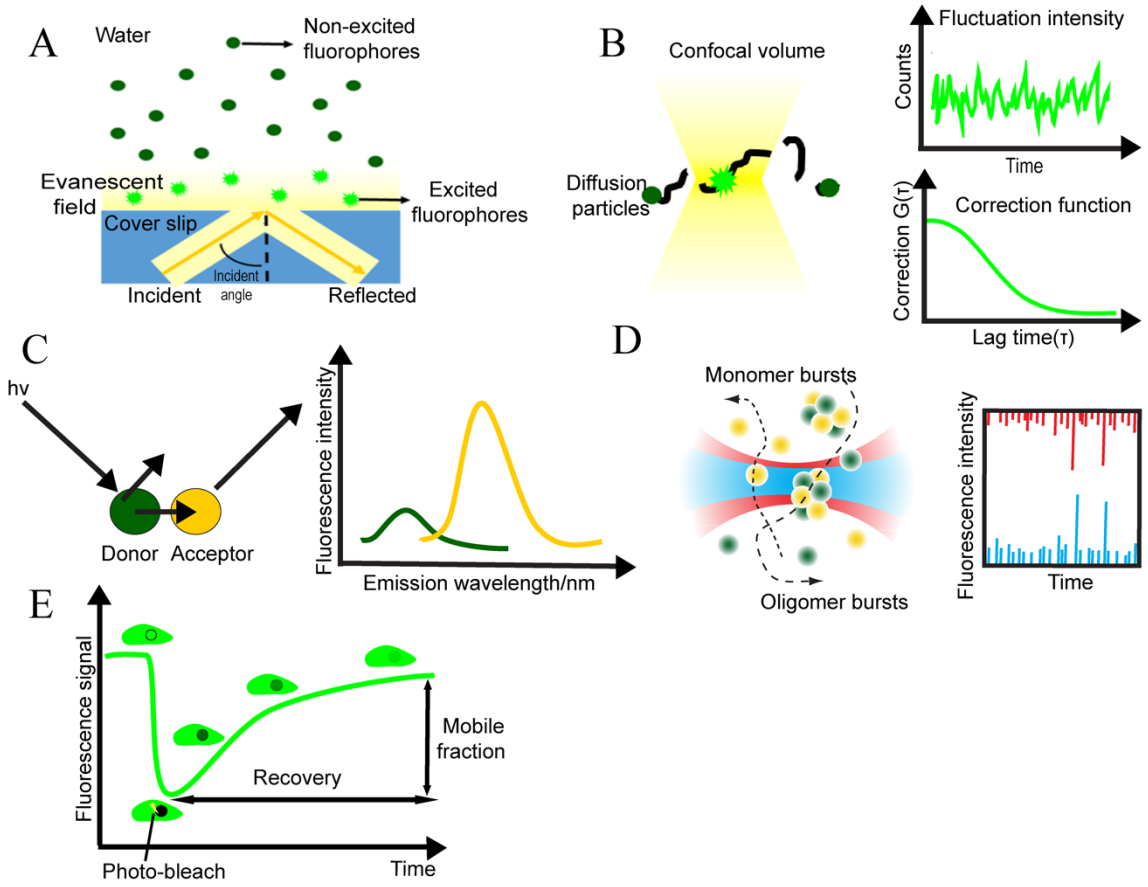

Figure 1. Schematic illustrations of the basic concept of SMFI techniques. (A) TIRF uses total internal reflection at the interface where an 'evanescent field' is produced and the fluorophores close to the glass surface are efficiently excited by the evanescent field. (B) In FCS method, fluorescent molecules diffuse through a tiny confocal volume and the fluctuations of fluorescence intensity are detected to determine the number of particles in this area. The autocorrelation function provides information about the concentration and the thermodynamic and kinetic parameters. (C) FRET represents a non-radiative energy transfer between a donor and an acceptor chromophore molecule via the long-range dipole–dipole coupling when these molecules are in close proximity (left). The donor fluorescence is quenching while the emission of the acceptor is increasing (right). (D) TCCD is based on oligomers with two distinct fluorophores but cannot exhibit high FRET give coincident fluorescent bursts after emitting the photons (left). The fluorescence intensity derived from the two-color channels (red and

blue) presents the numbers of monomers that are labeled in one oligomer (right). (E) FRAP can be used to quantify the recovery of fluorescence intensity over time after a region of interest in a cell or tissue is photo-bleached with a high-intensity laser and subsequently probed by a low-power laser.

TIRF imaging

TIRF (Total internal reflection fluorescence) imaging is now one of the most common fluorescence microscopic imaging to track single particles by selectively illuminating one area to minimize background signal. The innovation of TIRF has greatly enhanced the signal-to-noise ratio by reducing the background fluorescence, resulting in better contrast for detecting single molecules (46). For TIRF, a solid-liquid interface with different refractive indexes, such as a glass coverslip/slide and a water-based physiological solution, are needed (Figure 1A) (40). The incidence angle with a 90° refraction is called a 'critical angle'. At larger angles than the critical angle, the excitation light will not transmit through the liquid surface, instead total internal reflection of the incident light occurs at the interface and an 'evanescent field' is created. The intensity from this field drops off exponentially with the increasing distance from the interface whereas the depth of penetration can actually be adjusted over a wide range. Therefore, TIRF imaging can restrict the excitation to fluorophores that are positioned close to the surface, making this technique particularly suitable for identifying molecules integrated into membranes.

TIRF has been applied for the direct visualization of amyloid aggregates. As using covalently labelling proteins might affect the aggregation process (47) and it is challenging to tag samples extracted from *in vivo* sources, Horrocks *et al.* relied on addition of a dye (Thioflavin-T, ThT) that noncovalently binds to oligomers and fibrils with β-sheet structures (48). Small β-sheet aggregates of α-syn, Aβ and tau *in vitro* are observed with the sizes lower than 250 nm in the beginning of aggregation and the enriched oligomers contain on average 25 monomers. Amyloid fibrillation kinetics can be tracked as well. In the presence of ThT, Yuji's group (49) clearly observed the real-time individual Aβ40 fibrils growth with a seed-dependent manner and found the constant rate of fibril growth is similar with the steady-state enzymatic kinetics. Another study showed that glucagon fibrils grow exclusively by forming branches along sides of the parent fibril with an angle of 35-40 degrees (50), which differs from Aβ fibrils that extend themselves from the end of the preformed seeds in a linear elongation. By using TIRF, Patil *et al*. revealed three different hIAPP aggregation patterns that demonstrate the role of

secondary nucleation mechanisms where the preformed fibrils serve as a new template for fibril formation (51). All these studies illustrate that TIRF microscopy is an effective tool to visualize entire aggregates and fibril growth kinetics.

TIRF was also applied to depict permeation of single vesicles or cells filled with fluorescent dye by measuring the Ca^{2+} influx induced by oligomers on the membranes. After the penetration of synthetic Aβ oligomers (down to 200 pM) into the live neuronal astrocyte cells (52,53), tetramers or larger oligomers were found as the most toxic Aβ oligomer aggregates across the membranes. This suggests that the membrane permeabilization is one of the toxic mechanisms induced by oligomers. The extracellular chaperone clusterin, antibody or nanobody that specifically binds to oligomers could prevent Ca^{2+} influx induced by synthetic Aβ oligomers (54), whereas these inhibition effects are not obvious under CSF conditions. This implies that these single-molecule assays might be a cost- and time-effective approach before clinical trials. Recently, with TIRF, Tanaka and coworkers showed that Aβ42 oligomers on the surface of live hippocampal neurons impair the ability of learning and memory in the early stage of AD via suppressing the increase of fluorescently labeled (glutamate receptor) GluA1 number and GluA1 exocytosis frequency in both postsynaptic and extrasynaptic membranes (55). The increase of GluA1 is important for cellular basis of synaptic plasticity (56). Based on this result, a feasible therapy to recover mild memory impairment could be to target the increase of exocytic GluA1 on neuronal cells and TIRF could be the effective imaging tool to validate this potential.

A novel approach, label-free scattering microscopy has been used to image the surface-bound lipids and detect the specific protein-binding to single vesicles without labelling the lipids (57). Scattering microscopy produce the ‘evanescent field ’by optical waveguide instead of using the objective in TIRF. In this method, a more uniform illumination profile is obtained. Recently, Hannestad *et al.* investigated the kinetics of monomeric α-syn interaction with different lipid vesicles under both fluorescence and light-scattering emission at the single-vesicle level. They found α-syn induces obvious step-wise structural changes and asymmetric membrane deformation of individual phosphatidylglycerol (PG) vesicles with a very low α-syn concentration 10 nM (~100 proteins/vesicle) (28). The pore formation mechanism was not concluded to result in membrane leakage when α-syn binds to the vesicles. This finding might enlighten the abnormal behavior of monomeric α-syn *in vivo*. Scattering microscopy was also used to distinguish misfolded proteins from normal ones in Aβ plaques of an AD mouse brain model (58). Aβ plaques were found to form a typical core-shell structure which is surrounded

by a halo-like shell of lipid-rich deposits (59). This result indicates the ability of scattering microscopy in providing the novel perspectives into biochemical constitution of pathological structures.

FCS Method

FCS (Fluorescence correlation spectroscopy) is a quantitative analysis method with the ultimate single-molecule sensitivity for the detection of fluorescent molecules (60,61). In FCS, the fluctuations of fluorescence intensity, originating from the diffusion of fluorescent molecules (physiological nanomolar to picomolar) through a very tiny confocal volume (~1 μm^3) is measured with a high temporal resolution (nanosecond time scale) (Figure 1B). The detected fluorescence real-time fluctuations and autocorrelation function provide the thermodynamic or kinetic parameters such as diffusion coefficient or time, nucleation boundary radius and the free energy barrier for nucleation (62-64). Knowing these parameters can assist in developing an exact thermodynamic model of Aβ aggregation. Moreover, understanding the energy landscape of amyloids may estimate the stability of intermediates, which could help the quest for a method to reduce its population (65).

FCS has been used to characterize amyloids aggregation process and determine the presence of different oligomeric species, both in well-equilibrated systems *in vitro* and more complicated environments *in vivo* (66-68). Mittag *et al.* fitted FCS data to Gaussian distribution models to clearly distinguish different Aβ oligomeric species *in vitro* (69). They estimated the sizes of different amyloid types, including monomer (<1 nm) and low molecular weight oligomers (1-5 nm), high molecule weight oligomers (5-40 nm), protofibrils (40-4000 nm) and fibrils (4000-20000 nm). Additionally, Rigler's group observed that Aβ peptides have a highly cooperative polymerization process where the fibril is predominantly built up from monomers or dimers rather than free oligomers (70). The size of small Aβ aggregate particles *in vitro* is 1.7-2.1 nm and big aggregates have sizes of 100 nm or higher (71). Tiiman *et al*. later suggested that the smallest ThT-visible Aβ aggregates *in vitro* with a diffuse time ~ 200 μs, is comprised of 40-70 Aβ monomers (66). By directly tracking Aβ42 concentration changes, Novo *et al.* found that the critical aggregation concentration (CAC) of Aβ42 to form oligomers is about 90 nM (72). Based on this, they suggested that the assembly process is spontaneous and cooperative which is similar to the process of surfactants self-assembling, and produces the stable micelle-like oligomers formed from 50 monomers (hydrodynamic radius, Rh, 7-11 nm). In terms of complex samples, with FCS, Pitschke and coworkers detected the very large

multimers of single Aβ aggregates in all CSF samples from 15 AD patients but in none of the 19 age-matched healthy controls (73). Funke *et al.* also easily differentiated three CSF AD samples from the control ones by the presence of Aβ aggregates (74). FCS is also suitable for identifying the inhibitors of initial formation of amyloid oligomers by analyzing the average size and number of oligomeric particles. D-enantiomeric amino acid peptides were demonstrated to reduce the average size of Aβ aggregates but increases their number (75). These results demonstrate the effectiveness of FCS on determining heterogeneous oligomeric species.

FCS can also be used to quantitatively investigate the binding of amyloid proteins on membranes. Fluorescently labeled α-syn has been demonstrated to preferentially bind to acidic vesicles (76). Less bulky headgroups of anionic lipids enhance this binding possibly due to the anionic lipids being able to pack more closely together, thus producing a high charge density (77,78). A minimum of 30 lipid molecules or 60-molecule bilayer patch is required to bind a single α-syn molecule (77). Additionally, α-syn prefers to bind small vesicles such as synaptic vesicles, over large multilamellar vesicles. It was suggested that the ideal match of vesicle curvature with α -syn would be as found in the N-terminal helix (78). Another study showed that labeled Aβ40 and Aβ42 oligomers exhibit stronger binding to neuronal and somatic cell membranes than monomers at physiological concentrations (250 nM) (79). The negligible binding to cell membranes by monomers explains why they are non-toxic. Additionally, on mammalian cell membranes the size distribution of small Aβ40 aggregates (2.3 nm average R_h) peaks at both tested concentrations of 150 and 350 nM, while only large assemblies of Aβ40 (>>10 nm average R_h) appear at a concentration of 350 nM (80). These results indicate that the formation of large Aβ complexes on living cells relies on Aβ concentration. This discovery might partially explain why the Aβ targeting drugs fail in clinical trials since much higher physiological concentration of Aβ is used *in vitro*. Recently, Simpson *et al.* identified differences of Aβ aggregation and cytotoxicity between 2D *in vitro* models (typically culture cells on flat plastic or glass substrates) and 3D environments, such as collagen hydrogels in tissue culture models (81). Combined with FCS, they found that the size of Aβ aggregates in 3D collagen hydrogel is 25 to 200 times larger in diameter compared to 2D culture, suggesting a vastly different aggregation process. It appears that the cytotoxicity of Aβ gets attenuated in 3D compared to 2D environments. The difference in crowding and confinement are the main contributions. This discovery might provide another reason for failed Aβ drugs screening models that might miss these two factors.

FCCS (Fluorescence cross-correlation spectroscopy), which is an extension of FCS, was developed by Schwille *et al* (82). In FCCS there are two differently labeled fluorescent species whose concentration and diffusion characteristics are measured in parallel. In addition, information about whether the two molecules interact can be obtained. The principle is the same as FCS, but there are two different lasers focused onto the same spot, thereby resulting in overlapping diffraction-limited confocal volumes. FCCS has been used to study the interaction of aggregation inhibitors such as antibodies (83) and kinesin-1 (84) with Aβ peptide. Two kinesin-1 subunits, KLC-E and E-KLC were tagged to determine the interaction of kinesin-1 on Aβ peptide at the single-molecule level (84). Data revealed both KLC-E and E-KLC have an inhibitory effect on Aβ42 aggregation over a period of time, and KLC-E shows a much higher binding affinity than E-KLC, which might result from the spatial conformation of KLC-E.

FRET, TCCD and FRAP Techniques

FRET (Fluorescence resonance energy transfer) is one of the most commonly used techniques when studying physical interactions between two molecules within several nanometers (30–70 Å range), a distance sufficiently close for intermolecular interactions to occur (85,86). The principle of FRET is based on the excitation energy transfer from a donor to an acceptor chromophore molecule with the reduced donor fluorescence/lifetime and increased emission of acceptor fluorescence/lifetime. For protein interaction studies, fluorophore-tagged antibodies or fusion proteins are the two common methods to adhere the fluorophores to the interacting proteins.

Based on the direct observation of coincident bursts of oligomer fluorescence, two distinct structural types of α-syn oligomers were inferred during α-syn aggregation *in vitro* (87). Oligomers of type A and B, with medium and higher FRET efficiencies respectively, were found at α-syn aggregation different stages. Type B oligomers with a more compact structure and proteinase-K resistance were monitored in later aggregation stage, indicating type A might undergo a structural reorganization to form type B. Structural conversion has been assumed to be the key step of α-syn aggregation. This result is consistent with the hypothesis of sequential finding of discrete oligomeric intermediates in the early stage of α-syn aggregation (88). Additionally, they detected toxic α-syn oligomers originating from disaggregation of mature α-syn fibrils, suggesting that the disaggregation of fibrils can also be a source of toxic species and result in toxicity (87). This implies that attention should also be paid to the disaggregation

of fibrils at the final stage besides the toxic forms in the early stage of the aggregation process. Later, Horrocks and co-workers combined a fast flow microfluidics with FRET to investigate the oligomerization of α-syn (89). Isolating type A from type B oligomers by dilution, they discovered that type A dissociates but type B stabilizes in the lower ionic strength of the solution. Moreover, type-B oligomers from two α-syn mutant forms (A53T and A30P) displayed different FRET efficiencies, suggesting that the variants contribute to the structural diversity of oligomeric ensembles (90). By systematic analysis of the FRET efficiency values in a wide range of starting α-syn monomer concentration (from 0.5 to 140 μM), the required number of seeds to affect the initial aggregation was predicted to be in the order of 10^4 species in a single cell $(10\ \mu m)^3$ (91). This demonstrates that FRET is suitable to quantitatively explore the seeding process of amyloid aggregation. The same setup also demonstrated that tau protein has a similar structural trajectory evolving from type A to type B oligomers prior to fibril formation (92). Combining FRET with FCS method, the fraction of small Aβ oligomer containing less than 10 Aβ molecules were detectable as low as 2 ± 2% in solution at physiological concentrations (93). Additionally, Kaminski Schierle *et al.* found that labelled α-syn in living worm *Caenorhabditis elegans* (*C. elegans*) has the slowest decrease in fluorescence lifetime, followed by *in vitro* samples, then by neuronal cells (94). It indicates that the aggregation rate of α-syn is environmentally-dependent with the fastest rate of aggregation in cells. This result shows that FRET is an effective tool to track the kinetics of α-syn self-assembly *in vitro* and *in vivo*, and the molecular environment should be taken into consideration when revealing the nature of aggregation species.

Recently, FRET has been used to identify the binding of Aβ oligomers to the cholinergic nicotinic ACh receptor α7 (α7nAChR) (95). Loss of activity of α7nAChR is believed to impair cognitive performance in AD (96). The result showed that the Aβ binding site on α7nAChR overlaps with the orthosteric ligand binding sites comprising loop C with a high binding affinity (pK_D 10.3 ± 0.2). FRET was also used to evaluate different α7nAChR-related compounds of interfering the binding abilities of Aβ to α7nAChR (95). In addition, FRET was applied for the screening of various compounds against Zn^{2+}-Aβ interaction (97). Eight natural inhibitors (out of 145 compounds) were demonstrated to have efficient inhibition effects (>80%) and six of them are capable of decreasing the toxicity induced by Zn^{2+}-Aβ on living cells. The two studies indicate that FRET is suitable for measuring the binding activity of peptides/metal ions to amyloid proteins and very effective to assess potential drug candidates against neurodegenerative disorders. Zadorsky's group used FRET to demonstrate that the newly

found amyloid protein Toh1, which is localized in the yeast cell wall, could interact with other prion proteins Rnq1 and Sup35. The result highlighted that the interactions among different amyloid proteins not only occur between molecules with a similar primary structure, but also between proteins that have a close secondary structure and conformational folds (98).

Besides investigating the interactions of two molecules, FRET is also suitable to explore the interaction of membranes and amyloid proteins. Reynolds *et al.* found that α-syn aggregation appears to extract lipids from the membranes making them thinner. These extracted lipids could be initial step to more intense disruption of the membrane integrity. Larger damage to membranes was observed at higher α-syn concentrations, demonstrating the concentration dependency of α-syn aggregates on membrane toxicity (99). Terzi *et al.* reported that Aß preferentially interacts with anionic membranes (100) and Wong *et al.* found more net negative charge increases the binding affinity of low-molecular mass species of Aß40 (<10mer) with membranes. The very weak interaction of Aß40 with the pure DPPC (Dipalmitoylphosphatidylcholine) neutral liposomes confirms that Aß40 membrane insertion is highly dependent on the negative charge of membrane (101). The tight binding of Aß40 to anionic membranes was further confirmed by TIRF imaging but with a much lower dissociation constant of the peptide from the membrane (<470 pM) (102), compared to Wong's report (38.8±7.0 μM). The main reason is the very low peptide concentration in the latter case (sub-nanomolar), which leads to very low peptide/lipid ratio. This result indicates that the ratio of peptide/lipid concentration should be considered when calculating the binding affinities of amyloid proteins with lipid membranes.

In addition to the interaction of membranes with oligomers, the fluorescent lipid membranes was found to directly bind to fibrils and accelerate fibril formation (103,104). The vesicle lipid-fibril interaction reinforces Aβ42 secondary nucleation at the surface of existing Aβ fibrils (103). The charged plain lipid membrane has the similar effect on Aβ fibrillation. Additionally, Widenbrant *et al.* found the Aβ aggregates bind to the giant vesicle membrane, rapidly cross the vesicle bilayer, then incorporate into the interior small vesicle membrane (105). Meanwhile, the incorporated membrane was found to possess reduced membrane fluidity, which is indicative for pathophysiology of disease-affected cells. The reason for membrane penetrations and finally cell death was suggested to be due to induced membrane leakage by the localized aggregates, not due to pore formation mechanisms.

TCCD (Two color coincidence detection) technique uses two fluorophores that cannot exhibit high FRET and which are illuminated by two lasers compared to one laser for FRET (106). Monomers tagged with a single color are only detected by one of the detecting channels while the oligomers with two distinct fluorophores result in coincident fluorescent bursts after emitting the photons (Figure 1D, left). The signal of fluorescence intensity derived from the two-color channels present the numbers of monomers that are labelled in one oligomer (Figure 1D, right). As different oligomers show different coincident bursts of fluorescence when they diffuse through the confocal volume, TCCD is sensitive and quantitative to provide the information about the concentration and the stoichiometries of associated molecules in a heterogeneous environment. Klenerman's group used TCCD to trace the oligomer ensemble of SH3 domain from bovine phosphatidylinositol-3-kinase (PI3) (107). The heterogeneous oligomeric species of SH3 with the most cytotoxic properties have a median size of 38±10 molecules. The size distribution of these oligomers remains constant while their stability is gradually increasing during aggregation. TCCD method was also applied to determine the interaction of Aβ peptide with neuroserpin, a member of the serine protease inhibitor which can suppress the toxicity of Aβ peptides (108). It was found that Aβ increases the rate of neuropserpin's polymerization by forming a weak complex with neuroserpin. As Aβ is later released from the complex and not incorporated into the neuroserpin polymers, it was suggested that Aβ40 acts as a catalyst to enhance polymerization. IIjina *et al.* quantitively determined the composition of self- or co-oligomer formation of Aβ40 and Aβ42 at physiological conditions (109). The main oligomers are Aβ40 at the physiologically relevant ratio of 9:1 of Aβ40 to Aβ42. Dimers are the predominant oligomers when the total Aβ concentration is ~1 nM. The oligomerization of α-syn as well as their co-aggregation with Aβ40, Aβ42 and tau was also determined by TCCD (110). At a very low concentration, close to the physiological conditions, co-oligomerization is more favorable than pure α-syn oligomer formation, but co-oligomers also showed lower lipid membrane disruption than α-syn assembled oligomers.

FRAP (Fluorescence recovery after photobleaching) is another SMFI technique to measure molecular mobility and turnover processes. The basic principle of FRAP is that a region of interest in a cell or tissue is photo-bleached with a high-intensity laser and subsequently probed by a low-power laser to quantify the recovery of fluorescence intensity over time (Figure 1E). The recovery curve provides information about the mobile fraction and the diffusion coefficient (DC) of the labelled component (111). Nonetheless, specific interactions, membrane topology

and viscosity can also lead to differences in diffusion coefficients (112). Thus, great considerations should be taken when performing FRAP experiments in different cell lines or compartments to compare diffusion coefficients and mobile fractions.

By counting the number of photobleaching steps, FRAP can directly distinguish the labelled Aβ oligomers with different number of subunits at a very low concentration (1 nM). Combined with confocal microscopy, Ding *et al.* differentiated labelled Aβ40 oligomers that were deposited onto a cover glass, and found the size vary from dimers to hexamers, but mainly the dimers, trimers and tetramers. This result is in agreement with the peak estimation from gel filtration chromatography (113). Nevertheless, some oligomer species such as pentamers and hexamers are only observed by FRAP but not the gel filtration method, indicating the advantage of single-molecule techniques on quantitatively measuring oligomer species. Additionally, the determination of Aβ oligomer species on lipid membranes can also be obtained by forming the lipids on the clean coverglass. It was shown that the sizes of formed oligomers highly depend on the concentration of amyloids on lipid membranes. At close to physiological concentration (2 nM), a large fraction of Aβ species (34%) on supported anionic lipid membranes are trimer/tetramer (102). Similar smaller pore-forming oligomers were observed directly by high-resolution atomic force microscopy (42), indicating these species might be the smallest species in the membrane and the source of pre-pore forming oligomers and neurotoxicity. At relatively high concentration (100 nM), faster oligomer formation and larger size distribution with a very wide range from around pentamers to 60mers were observed. In this situation, the fast forming oligomers might serve as the nuclei for the direct insertion into a membrane or for initial formation of fibrils and then lead to membrane permeabilization (102). Additionally, combined with TIRF, they found the binding to anionic lipid membranes starts with the monomers and the subsequent incubation leads to the formation of oligomers in the membranes. To get a more detailed picture of the toxic mechanism at the single-molecule level, Schauerte *et al.* combined membrane conductivity measurements with FRAP to identify the structure of amyloid proteins when causing membrane-permeabilization (114). The ability of the oligomers to permeabilize the membrane was determined by simultaneously measuring the conductance as well as their size distributions. At low concentration below 10 nM, labelled Aβ monomers uniformly bind to the membrane while they do not induce any detectable conductance. At intermediate concentrations (from 10 nM to 100 nM), small oligomeric Aβ species (mainly dimers to 14mers) are identified and the smallest size of oligomers to show a detectable conductivity are hexamers but not dimers.

When the concentration is higher than 100 nM, large Aβ structures and large conductance are detected, indicating the serious interruption of these aggregates on membranes. This observation supports the pore-formation model where monomers interact with the membrane surface followed by surface diffusion and then assemble into pore structures.

By analyzing DC curves, the change of membrane fluidity which is important for biological functions in cell membranes (115,116), can also be determined when membranes interact with the amyloid peptides (117-119). hIAPP shows a more dramatic change of average DC signal before and after adding it into the lipid bilayer (from 1.07±0.2 to 0.004±0.004 $\mu m^2/s$), compared to Aβ42 peptide (from 0.99 ± 0.1 to 0.07 ± 0.01 $\mu m^2/s$) (117,118). The deposition of hIAPP on the surfaces of bilayers results in the insertion to the bilayers (120). The membrane mobility decreases considerably when Aβ42 concentration increases from 10 to 20 μM (121). These results address the involvements of lipids in amyloid aggregation when proteins penetrate into the fluid membranes. FRAP has proved also useful for assessing the molecular mobility in living cells. α-syn aggregates in the SH-SY5Y human neuroblastoma cells showed a very low fluorescence recovery signal compared with the area without aggregates which showed complete signal recovery (122). The diffusion constant of α-syn is relatively small (0.03–0.04 $\mu m^2/s$) in living cells, suggesting that the α-syn aggregates remain predominantly immobile. These results demonstrate that FRAP is powerful to investigate the effects of amyloid protein on membrane fluidity and function.

2.3.2 Single-molecule force (SMF) microscopy

Force microscopy (widely, though inappropriately, named as force spectroscopy) is a set of techniques used for the study of individual molecule interactions and the binding forces, that include atomic force microscopy (AFM), optical tweezers/traps (OTs) and magnetic tweezers (MTs), which have been extensively reviewed before (41,123). Here we focus on the techniques that have been used and will be of specific relevance in the future to study single amyloid molecules and their interactions.

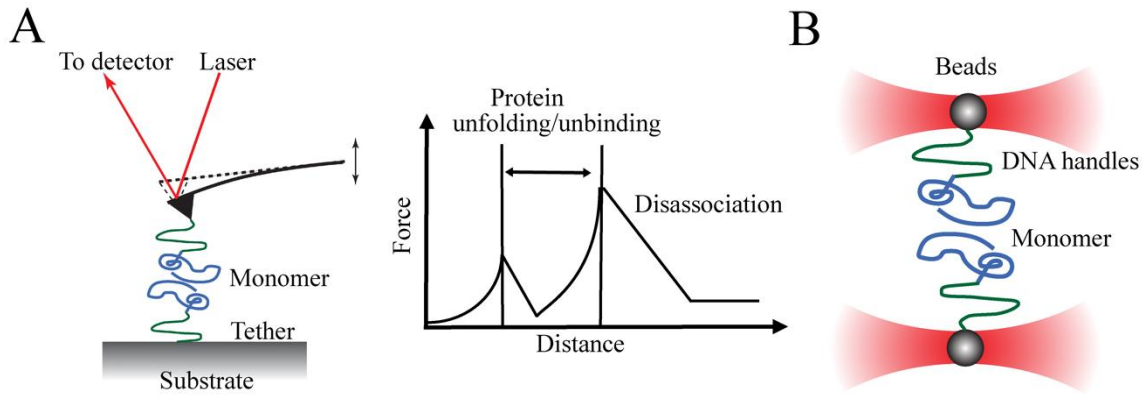

Figure 2. Schematic examples of the basic principles of SMF techniques. (A) One single amyloid protein is attached to the functionalized AFM tip and a mica surface separately. When the probe approaches and retracts from the substrate in the vertical direction, the force-distance curve that is systematically recorded reveals the protein unfolding pathways. (B) Two single amyloid proteins are tethered to two beads constricted in traps. SMF–OTs exert extremely small forces via a highly focused laser beam that generates a very strong electric field gradient.

SMF-AFM

AFM (atomic force microscopy) is a type of scanning probe microscopy with a nanometer resolution, which mainly relies on Van der Waals interactions and Coulomb repulsions resulting in a weak deformation of the AFM micro-cantilever with respect to the sample surface (124). When the probe approaches and retracts from the substrate in the vertical direction, the changes of cantilever position will be systematically recorded and represented in a force-distance curve (Figure 2A). These forces reflect the surface topography and structure of the biological sample. AFM enables the visualization of the microscopic surface of heterogeneous amyloid oligomers and fibrils in ambient atmospheric and liquid conditions, thereby provide information about parameters such as height, diameter and morphology (123,125,126). For example, AFM imaging has been utilized to observe different shapes of amyloid aggregates in atmospheric conditions, including pore-like and spherical shaped Aβ oligomers (127,128). It was also found that the height of α-syn oligomers varies from 2-12 nm and was dependent on salt concentration (129), whereas the height of primarily formed Aβ oligomers varies from 2-8 nm (130). The height of α-syn fibrils in air is 17 % lower than those of same fibrils imaged in liquids and the C-terminal tails of α-syn fibrils in liquids show different conformation in different ion concentrations (131). Additionally, AFM in liquids can monitor real time amyloid protein aggregation in buffer and in membranes and investigate the effect of lipid composition on amyloids binding to membranes. Aβ42 was observed to form small oligomers and short

protofibrils but not the long fibrils, correlating well with the higher neurotoxicity of oligomers compared to fibrils (132). In fluid phase, positively and neutrally charged lipid bilayers have stronger interference with Aβ42, compared to the negatively and zwitterionic ones (133). Lipid rafts cholesterol and ganglioside GM1 promote the harmful membrane interactions with Aβ (Azouz et al., 2019). All these results demonstrate that conventional AFM has the irreplaceable advantage on providing morphological information of amyloids. However, traditional AFM imaging cannot show how two molecules interacting with each other affects aggregation morphology. By tethering individual amyloid peptides/proteins to the substrate and probe respectively, single-molecule force AFM (SMF-AFM) measures the internal mechanical features of small heterogeneous amyloid oligomers (dimer to tetramers). SMF-AFM mechanically unfolds the native molecule at a single-molecule level with pN resolution (134-136). The obtained force curves can be used to characterize the interaction forces between them or to reveal the unfolding pathway of oligomers (137-140). Lyubchenko's group has covalently immobilized the C-terminal of a series of cysteine-modified amyloid proteins on both probe and substrate surface (141,142). The pulling strength/rupture forces of monomers between the probe and substrate can provide information about the spontaneous dissociation and the resulting off-rate constant, indicative of the degree of intermolecular interactions and the self-assembly of an amyloid protein dimer (143). It has been reported that α-syn dimer has two different dissociation rates (0.25 and 13.2 s^{-1}), implying there might be two distinct pathways of forming α-syn dimers (144). For Aβ40 dimers, four close rupture forces (~ 120 pN) with different rupture positions from 25 nm to 45 nm were observed (138). It suggested the formation of different transient misfolded states. Aβ42 and Aβ40 display similar rupture forces and rupture position when probed by SMF-AFM (145). The approach further reveals a set of transients of Aβ dimers with different conformations, representing diverse misfolding pathways of Aβ dimers. In addition, the dimer lifetime was quantified by combining dynamics force spectroscopy. Compared to dynamic monomeric states, the dimer lifespan of α-syn and Aβ is unexpectedly high within the range of seconds (138,140,145), indicating that the stable dimers may act as nuclei in the aggregation process. Also, the amyloid dimer lifetime value is pH-dependent. α-syn has two different lifetimes at acid pH conditions (4 s and 0.8 s at pH 2.7, 1.35 s and 0.05 s at pH 3.7) (140), demonstrating two different pH-dependent α-syn aggregation processes. As for Aβ40 dimer, the lifetime is 0.46 s at pH 7.0 and 2.5 s at pH 2.7 respectively (138). Aβ42 has slightly different lifetimes (0.1 s at pH 7.0 and 2.7 s at pH 2.7) (145). The results suggest that experimental conditions play a vital role in the aggregation process. As protein interactions highly depend on their conformational changes, SMF-AFM is

suitable for directly detecting the rupture forces to indicate conformational changes of amyloid proteins. It has been shown that the pulling strength of α-syn and Aβ is the weakest at neutral pH, indicating a random coil structure. At an acidic pH, a higher pulling strength revealed the rapid conformation conversion to a more ordered, predominantly β-sheet structure (146). Furthermore, SMF-AFM was applied to study Aβ14-23 trimers where a larger rupture force is required to unravel trimers, compared to that of dimers (147). This explains the different folding arrangements within trimers and dimers. Yu *et al*. revealed a dramatic increase of rupture events of α-syn interactions in the presence of Al^{3+} and Zn^{2+}, demonstrating the supportive effect of metal ions on α-syn misfolding. In addition, dopamine does not increase the rupture events and forces, which suggests dopamine may not involve in the α-syn dimerization (148). Based on these results, SMF-AFM can be used as an efficient tool to screen drugs or biomolecules that interfere with amyloid aggregation in the early stages of the aggregation. Another advantage is that SMF-AFM can be conducted in a broad pH distribution, which is important as it has been shown that acidic pH dramatically facilitates amyloid aggregation and amyloid monomers and oligomers *in vivo* normally occur in an acidic environment (149).

As trimers, tetramers and larger oligomers also contribute to the heterogeneity of amyloid oligomers in the aggregation process, flexible nanoarrays (FNA), an extension of SMF-AFM, was developed to investigate the intermolecular interactions of higher oligomeric structures (150-152). In the FNA setup, amyloid proteins (dimer or monomer) are covalently immobilized within a highly flexible, linear PEG-type polymer on which the tethered proteins can interact and form the higher complex (153). The two functionalized ends of the FNA-polymer are linked to AFM tip and substrate respectively. As the synthesis process of the polymer can control incorporation of the monomers, the attached amyloid molecules can be anchored to the desired positions within the polymer (Krasnoslobodtsev et al., 2015). Then different scenarios can be studied. For example, dimer construct can interact with another monomer of which is tethered to the flexible polymer, and this creates a trimer model to explore the dimer-monomer intermolecular interaction. Analysis of the dissociation force of Aβ14–23 trimers showed that the first rupture force of the monomer is ~48±2.4 pN, which is slightly lower as compared with the second step of rupturing the dimers (~53±3.2 pN) (154). This demonstrated that the dimers are at a more stable state than the dynamic monomers in the early stage of aggregation. Another example is where a dimer construct forms at the end of the flexible polymer, which allows dimer-dimer interactions to be studied (150). The results of rupture force and lifetime of Aβ14–

23 tetramer are close to these of trimers at the neutral pH. However, the acid condition affects the oligomer behaviors with different rupture forces and lifetimes. At pH 3.7, the lifetime histogram of the tetramer and trimer has a broad distribution and each fits three Gaussian peaks. Different sets of lifetimes indicate different intermolecular interactions with distinct structures. A similar change due to an altered pH was found for the strengths of the bonds. These results are consistent with the known heterogeneity of amyloid oligomers and suggest they can follow different aggregation pathways that are pH-dependent. In a similar way, the intermolecular interaction of higher order oligomerization such as pentamers and hexamers might be studied. FNA allows to dissociate the organized oligomers in a stepwise way and provides a good way to reveal the interaction of different states of oligomers, which can contribute greatly to the understanding of the mechanisms involved in amyloid aggregation.

SMF-OTs

Compared to SMF-AFM that probes biomolecules directly, SMF-OTs (optical tweezers/traps) indirectly manipulate and trap sub-nanometer to micron-sized dielectric particles by exerting extremely small forces via a highly focused laser beam that generates a very strong electric field gradient. SMF-OTs uses a high numerical aperture (NA>1) microscope objective to create the stable optical trap to stabilize the vicinal dielectric microparticles. The working principle is illustrated in figure 2B. A single molecule, such as a DNA strand, a peptide or protein, is attached to a microparticle (155). SMF-OTs exert a force of up to 100 pN on particles with a 10^{-8} N force accuracy and a 10^{-4} s temporal resolution and 10^{-9} m spatial resolution. By adjusting the position of the traps, the force on the molecule can be indirectly obtained through the real-time measurement of three-dimensional displacement of the particles. In Woodside's group, Syrian hamster prion protein (PrP) was linked to DNA handles and connected to the polystyrene beads (156). A single PrP molecule is trapped and then the end-to-end extension is traced by exerting the denaturing tension on the PrP protein. The traps are taken apart at a constant rate to ramp up the force until the monomer PrP is totally stretched out. Under force-extension, PrP shows conformational fluctuations in the folding process with high precision. No partially folded intermediate is found to regulate the misfolding event during the native folding process. It suggests that the native state or the on-pathway intermediate is not the important factor for PrP misfolding. Instead, the unfolded states are found to involve three different misfolding off-pathways, which indicates these unfolded states serve as intermediates in the misfolding process. SMF-OTs allow the observation of the transient transitions from the

unabiding structural fluctuations of single-molecule folding trajectory, which makes SMF-OTs a powerful tool to explore the different aspects of amyloid protein misfolding mechanisms.

Based on the above SMF-OTs setup, Neupane *et al.* found different intermediates with various sizes and stabilities during α-syn aggregation (157). They reported that many metastable α-syn structures are formed from small oligomers and that these have a wide range of sizes. By monitoring the folding kinetics of a single α-syn monomer, small parts of discrete unfolding events were analyzed by fitting the force-extension curves. The change of contour length in the conformational transitions upon unfolding vary from 10 nm to 36 nm. These separate unfolding transitions are also observed in α-syn dimers and tetramers, indicating the formation of unfolding intermediates with several distinct structures. Furthermore, the unfolding forces which reflect the structural stability and the height of energy barrier to unfolding were compared with the monomers, dimers and tetramers. It shows that the unfolding forces increase with the growing size of the oligomer, confirming that larger oligomers of α-syn have higher structural complexity.

Unlike a single amyloid monomer, it is difficult to manipulate one single fibril by optical-trapping experiment as amyloid fibrils are highly flexible. Dong and co-workers introduced a new method to tether Sup35 prion protein fibrils (158). They first attached the N-domain of prion monomer variant NM, which only contains prion N and M regions, onto the glass. Then these tethered monomers exert the self-recognition feature to capture prion fibrils in which the attachment happens at the end of fibrils. The polystyrene bead was used to capture the other end of the fibrils. After applying normal pulling strength, prion fibrils showed resistance to disruption and maintained fibril integrity. When exerting much higher forces of up to 250 pN, some force-dropping events were monitored before the fibril ruptured and it suggests that dropping events result from the prion intrinsic fold properties rather than from extrinsic surface attachments. SMF-OTs results support the β-helix model structure for prion fibrils rather than β-pleated-sheet model. Based on this method, the mechanical properties of NM from prion fibrils were explored and showed that the persistence length of NM is much shorter than that of insulin and Aβ fibrils (159). This result means that NM fibrils are much less resistant to bending compared to the other amyloids. The formation of point defects (hinges) of prion fibril structure greatly reduces the bending stiffness. Goldmann previously reported that actin becomes more susceptible to fragmentation when bending decreases (160). Thus, SMF-OTs results support the hypothesis that prion fibrils are not rigid enough to be fragmented, producing more seeds to function as protein-based elements of inheritance and leading to

stronger prion phenotypes *in vivo* (159). Other mechanical parameters such as the axial and torsional stiffness are also deduced by the SMF-OTs method. These results provide meaningful guidance for designing novel amyloid-based nanomaterials including scaffolds and biosensors. Recently, Fränzl *et al.* designed a thermophoretic trap to observe the single amyloid fibril growth over rather long periods of time (161). Analogous to the electric field gradient in the SMF-OTs, the temperature filed gradient was created by heating an optically heated, 10-μm-sized chrome ring via a focused laser beam. The trapped single amyloid fibril showed the rare fibril fracture events, confirming the idea of existing secondary processes during the growth of amyloid fibrils. With a similar concept as SMF-OTs, magnetic tweezers (MTs) use the gradient of a magnetic field to manipulate paramagnetic beads (162,163). There are several reviews detailing the principles of MTs and its application at the single-molecule level (41,163,164). Though the technique of MTs is mature to handle, to the best of our knowledge, there is no report where MTs are applied to characterize amyloid proteins.

2.3.3 Single-nanopore electrical systems (SNS)

Single-nanopore electrical recording has been developing into a powerful single-molecule approach to characterize the properties of amyloid proteins (such as structure, aggregation, abundance and interaction with other molecules) within an aqueous solution. There are three classes of nanopores: biological protein nanopores embedded in lipid layers (such as α-hemolysin (α-HL), aerolysin, Mycobacterium smegmatis porin A (MspA), and DNA packaging motors), synthetic solid-state nanopores (usually in a SiNx, SiO_2, Al_2O_3, TiO_2 or graphene membrane) or a hybrid of these that consists of a protein channel set in the synthetic membrane. The nanopore system confines the disordered protein in a nanoscopic environment of the pores, providing a method to detect the dynamics of a single protein in a nano confinement (165). Here, we mainly talk about the application of biological and solid nanopores for the detection of intrinsically disordered proteins.

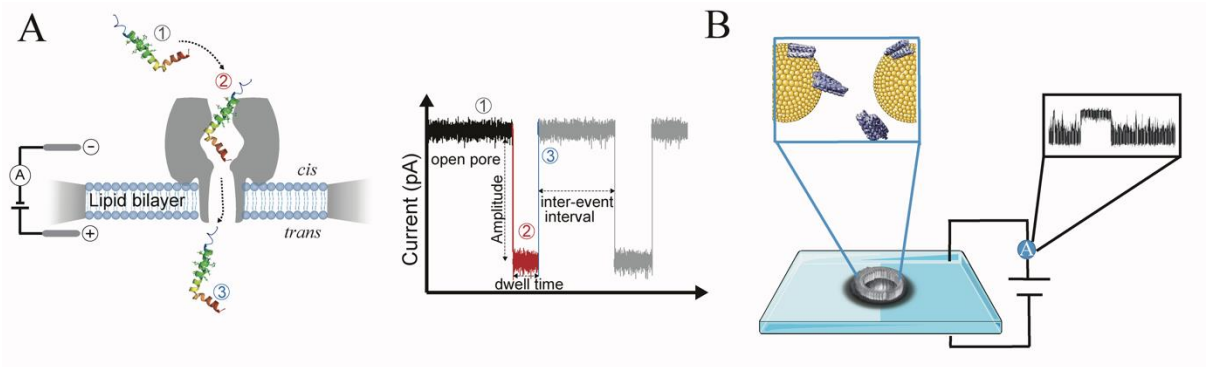

Figure 3. Illustration of single-nanopore measurements. (A) The process of single amyloid protein translocation the biological nanopore system (using α-HL as an example) (Left). (Right) Typical current trace of a single protein across a nanopore. After applying a constant voltage, an open pore current is recorded (①); once a single molecule has been captured and sliding inside the pore, the current value drops to a lower state (②); the current back to the open pore state when the molecule completely translocates the pore (③). (B) Solid-state nanopore setup with fluid access channels to a nanopore across a silicon nitride membrane. A typical current event is recorded. The components of (B) are from Servier Medical Art.

Biological Nanopores

The transportation of ions or molecules into and out of cells depend on channels, which are protein pores in the cell membrane with a size range of 0.3-10 nm. The typical biological nanopore apparatus is composed of two chambers or reservoirs (*cis* and *trans*, as illustrated in Figure 3A) immersed in an electrolyte solution separated by a lipid bilayer film that is formed across an orifice, the nanopore. An electric potential applied between the two chambers generates an electric field across the nanopore, which drives charged ions or molecules to pass through the nanopore (166). For small unfolded molecules, they are easy to translocate the pore, whereas molecules with large sizes, such as aggregates, fibrils or folded proteins, tend to simply clog the pore or bump into the pore and then diffuse away (167). By analyzing the amplitudes, durations and shapes of the events, the size, conformational changes and interactions with other molecules can be determined at a single-molecule level. Recently, single-nanopore technologies have shown a great potential for the characterization of individual amyloid proteins (168), which will be further discussed.

Zhao *et al.* studied the translocation of Aβ10-20 and various short peptides through an engineered α-HL nanopore (169). Both the dwell time and the change in the amplitude of current blockades increase as the length of the sequence increases. A stronger binding affinity was observed between peptides and pores when more aromatic binding sites were engineered to be present inside the lumen of the pore. Based on the characteristic currents caused by different lengths and structures of the peptides, biological nanopores make it possible to study structural changes when Aβ peptides interact with small molecules. Wang *et al*. probed the different aggregation transitions of Aβ42 in the presence of an aggregation promoter (β-cyclodextrin, β-CD) and an inhibitor (Congo red, CR) using α-HL nanopores to differentiate between fibrils and oligomers (170). Two populations were observed of Aβ42-CR, namely,

one current amplitude is the same as the events caused by Aβ42 alone, while the other current is slightly higher, indicating that after the incubation with the CR, a new structure emerged in the Aβ42 protein. For Aβ42-β-CD, barely any events were observed, and the current distribution is in a wide range, suggesting that the detected protein structure is bigger than the α-HL and thus cannot be captured effectively. Therefore, only bumping events were recorded as would be expected from large aggregates. Madampage *et al.* also got similar results when Aβ42 is aggregated and they investigated the effect of mutation on the conformational changes and aggregation propensities (167). Aβ40 translocation experiments showed recognizable events corresponding to α-helical structures whereas Aβ40 mutant protein, D23N has typical folded β-sheet signals. Two mutants (A30P and A53T) but not the E46K mutant of α-syn caused more bumping events than wild type α-syn, suggesting the two former mutations increase the propensity for misfolding and aggregation whereas the latter does not. Hu *et al.* characterized the preliminary structural aspects during the aggregation process of Aβ25–35 and its reversed sequence Aβ35–25 in a time-dependent way (171). Their results showed that Aβ35–25 conforms into a random coil structure while Aβ25–35 comprises both random coil and β-sheet structures, which is consistent with the CD spectra measurements. As the nanopore-based detection is performed in aqueous solution, it is well-suited for studying the kinetic interactions between metals and Aβ proteins. Asandei *et al.* compared the Cu^{2+} binding affinity of Aβ16 derived from human and rat tissues (172). Compared to peptides from humans, Cu^{2+} binding of Aβ16 peptides from rats showed higher association and dissociation kinetics of the peptides reversible interaction with the pore (173). In addition, based on single-nanopore experiments the binding affinity of metals to Aβ16 obeyed the following order: $Cu^{2+} > Zn^{2+} > Fe^{3+} > Al^{3+}$.

Gurnev *et al.* utilized α-HL nanopore to explore how α-syn interacts with the membranes at a single-molecule level (165). It showed the N-terminus of α-syn first binds to the lipid membrane, then the C terminus enters and finally passes through the nanopore. Additionally, their study of the interaction affinity between α-syn and voltage-dependent anion channels (VDAC) channels revealed a previously unknown mechanism of mitochondrial outer membrane permeability regulation induced by α-syn (174). α-syn is able to block VDAC in a concentration and voltage dependent manner and cross the mitochondrial outer membrane into the intermembrane space when the voltage is above 43 mV. Biological nanopore technologies have been demonstrated to hold the potential for applications in the design of drug screening assays and gaining a deeper understanding of the aggregation mechanisms of amyloid proteins

when investigating their interactions with lipid membranes as well as biomolecules such as chaperones and metal ions at the early stage of aggregation.

Solid-state Nanopores

Although biological nanopores possess an extremely high sensitivity and specificity to study structural variations of monomeric amyloid proteins, it remains a challenge to monitor the whole process of amyloid protein aggregation due to the small volume of a biological nanopore, their mechanically fragile nature and their poor chemical, thermal and mechanical stability in extreme solution conditions (175). To overcome these limitations, solid-state nanopores, fabricated from synthetic materials, are rapidly becoming an inexpensive and highly versatile alternative due to their tunable size and shape, ability to be fabricated as high-density arrays, and possibility of integrating them with either an optical detection platform, or nanofluidic or other nanodevices (176). Different fabrication techniques have been reviewed by Chen and Liu (166). Yusko and co-workers first reported the use of silicon nitride to detect amyloid proteins (177). They coated a solid-nanopore with a fluid lipid bilayer and controlled the translocation speed of proteins via increasing the viscosity of the coated lipid membrane. More importantly, this enables to translocate Aβ oligomers and fibrils without clogging the nanopores. Four distinct Aβ clusters could be clearly distinguished via this solid nanopore, which represent spherical oligomers, protofibrils shorter than the effective pore length, protofibrils longer than effective pore length, and mature fibers (178). It proved the tremendous heterogeneity of the sizes of Aβ aggregates. Besides lipid coated nanopores, Martyushenko *et al.* used quartz glass nanopores to observe the translocation events of lysozyme fibrils at a low pH and low salt concentration. Due to the robustness of these solid-state nanopores over period of 24 hours, tracking the development of protein aggregation over a longer time period becomes possible (179). Yu *et al.* applied the glass nanopore to study the dynamic amyloidosis process of Aβ42 peptides(180) . However, there is a crucial question about the differences in protein adsorption at the solid-liquid interface without a lipid coating in such non-physiological conditions. To address this problem, Balme and co-workers characterized the adsorption influence of three proteins (avidin, lysozyme, and IgG) on silicon nitride nanopore surfaces (181). The data showed that only lysozyme has no specific adsorption and can be totally neglected. Five parameters of proteins could be analyzed simultaneously, namely the shape, volume, charge, rotational diffusion coefficient and dipole moment (182). It demonstrated solid-state nanopores system is a valuable approach for characterizing amyloid aggregates or fibrils.

2.3.4 Single-molecule dual measurements

Combining the benefits of two or more single-molecule techniques can provide additional information about the biological system under investigation. Multiparametric analysis can further deepen the collective understanding and possibly initiate different solutions to diagnose and treat amyloid-based diseases such as AD and PD.

A first example of a dual technique is the High-Resolution "Fleezers", which combines an optical tweezers with fluorescence imaging to simultaneously obtain sub-nanometer displacements, sub-piconewton forces, and fluorescence signals. Marqusee's group introduced fluorescent imaging to visualize a single prion fibril which was stretched by high force optical trapping (155). After a single prion fibril was tethered to the glass surface via the self-templating feature, the imaging method allows to observe the behaviors of the uniform and unbranched single fibrils under various optical forces. Simultaneous imaging contributes to confirm the force-dropping events originated from the breaking of the fibril itself. Moreover, the microstructures of the constructed single prion fibril generally shows structural non-uniformity such as the inhomogeneous static curvature of local regions, despite the single fibril being obtained in a biologically homogeneous way (159). Together with TIRF imaging, SMF-AFM has been implemented to investigate intermolecular interactions of dimers or tetramers of the Aβ14-23 peptides (150). In an example of the trimer, the fluorescence burst occurs once the attached dimer binds to the monomer. The fluorescence duration that represents trimer stability can be monitored by using TIRF microscopy and the rupture force exerted by SMF-AFM would be subsequently recorded. Dimer-dimer interaction has been investigated in the same way as trimers to assemble tetramers. At neutral pH, the lifetime and rupture force of trimers are similar to these of tetramers, suggesting a similar structure and assembly process for trimers and tetramers (150).

Another dual-measurement experiment was carried out by combining the highly sensitive TCCD with TIRF microscopy to study chaperone interaction with amyloid proteins (183). TCCD distinguishes the different species of oligomers by the coincident fluorescence bursts in solution, based on the principle that the numbers of oligomers contribute to sizes of oligomers with distinct fluorescence brightness signal. These isolated species are then deposited onto a surface for imaging by TIRF. For example, two chaperone proteins (clusterin and αB-crystallin) show strong interaction with small Aβ40 oligomers by forming a stable and long-life complex (183,184). By observing the persistent oligomer populations when the chaperone

dissociates/degrades the fibrils, αB-crystallin-Aβ40 oligomer complex was found to have a 17±2 h half time which is much shorter than that of clusterin with 50±10 h. It suggests that clusterin has a higher binding affinity to Aβ40 compared to αB-crystallin. Moreover, the complex of αB-crystallin formed in the disaggregation (degradation) is more stable than that formed in the early stage of the aggregation, suggesting a structural difference between the two oligomers. Not only to Aβ, clusterin and α2-macroglobulin also bind directly to α-syn oligomers. Each protein possesses different binding abilities, which was explained by the formation of two different types of α-syn oligomers in the process of aggregation (185). Aside from chaperone proteins, the interaction between Aβ and the specific receptor-PrP on live hippocampal cells was also investigated using the TCCD-TIRF combination (186). It indicated that mainly the small Aβ oligomers (dimers and trimers) bind to PrP. These examples prove that this combination of techniques provides a good way to visualize the amyloid protein interactions with other molecules at the single-molecule level, in particular the inhibition process of chaperone proteins that appear to interact with the small oligomers. Furthermore, the protective role of the chaperone proteins reminds us that keeping a normal level of chaperone proteins in the brain is a potential therapeutic approach against the development of AD.

TIRF imaging has been integrated with single-channel electrical recording to detect single molecule diffusion on the lipid membrane. This combination was firstly developed by Toru and Toshio to detect the moving paths of single lipid molecules on an artificial lipid membrane (187). To overcome the problem of unsupported bilayers which would result in high lateral mobility of lipids and short bilayer lifetime, glass, gels or polymers supporting substrates were designed (188-190). Currently, droplet/hydrogel interfaces (DHB) have been utilized to study the membrane protein diffusion in combination with TIRF microscopy (191) whereas droplet interface bilayers (DIB) are too far from the surface to allow visualization by TIRF microscopy. This combination provides a good example of how to possibly study protein diffusion in the lipid bilayers. Yet, the applications remain to be explored for amyloid proteins.

2.4 Comparisons of single-molecule optical, force, and electrical approaches

Besides the working principles and applications mentioned in the previous sections, we summarize and compare benefits and limits of single-molecule mechanical, electrical and optical approaches for amyloid protein studies in table 1. Like other conventional biophysical

methods, single-molecule approaches possess inherent limits and only disclose a few aspects of the complexity of amyloid aggregation. Particularly, the fluorescent label attached to the amyloid peptide/protein may alter the traits of the peptide/protein and influence the detailed aggregation process. With real-time and label-free probing, single-nanopore electrical measurements are mainly limited by spatial resolution through the single nanopore and need sufficient data collection for statistically robust conclusions. In the single-molecule mechanical measurement, high-resolution optical trapping is not strictly limited to any dielectric particle and therefore requests highly homogenous sample preparation, which remains challenging for amyloid peptides/proteins. The discrimination between interactions of the AFM cantilever with different domains of amyloid protein is still challenging. The stiffness of the AFM cantilever and optical trap may also limit single-molecule studies of amyloid protein where particular care must be exercised in physiological conditions. Some of these limits shown in table 1 may be overcome by single-molecule dual measurements discussed in section 4.

Table 1. The benefits and limits of single-molecule methods and the main application on amyloid proteins

Technique	Benefits	Limits	Application on amyloids
TIRF	1. Improved axial resolution 2. Minimal out-of-focus fluorescence and lowest background 3. Less bleaching and light stress for living cells	1. Only for molecules near the coverslip 2. Limited image acquisition speed 3. Requirement of a fluorescent tag or component	1. Fibrillation kinetics 2. Oligomer size distribution 3. Molecule diffusion rates 4. Binding kinetics
FCS	1. Dierect measurement of stoichiometry 2. Broadened dynamic range for determining dissociation constants 3. Single-molecule sensitivity 4. No requirement of physical sample seperation	1. More susceptible to chromatic aberration and autofluorescence 2. Requirement of a fluorescence tag or component	1. Fibrillation kinetics 2. Distinguishing oligomeric species 3. Binding kinetics 4. Complex stoichiometry
FRET	1. High-spatial resolution for measuring intermolecular interaction	1. Need of photostable acceptor 2. More influences of environment on photobleaching 3. Proximity assay	1. Distinguishing oligomeric species 2. Binding kinetics
TCCD	1. No restriction of position placement for fluorophores 2. No requirement of physicl sample separation	1. Production of non-associated molecules in low concentration 2. Complex data fitting 3. Requirement of a fluorescence tag	1. Oligomer size distribution 2. Binding kinetics
FRAP	1. Quantitive measurement of molecular mobility in living cells 2. Suitable for different membrane systems	1. Influence of the intrinsic photobleaching on signals 2. Unsuitable for large aggregates 3. Membrane topology and viscosity effects 4. Requirement of a fluorescence tag	1. Molecule diffusion rates 2. Identifying oligomer species 3. Protein mobility on membranes 4. Binding kinetics
SMF-AFM	1. No requirement of a fluorescent tag or component 2. Easy sample preparation and no damage for the samples 3. Higher lateral resolution	1 Low throughput 2. Not suitable for characterizing big aggregates 3. The stiffness of cantilever	1. Folding and unfolding kinetics 2. Structure changes 3. Oligomer lifetime
SMF-OTs	1. No requirement of a fluorescent tag or component 2. Manipulation of single molecules without direct contact 3. Independent on testing environment	1. Sample heating and photodamage 2. Not suitable for characterizing big aggregates 3. The stiffness of traps	1. Folding and unfolding kinetics 2. Identifying oligomer species 3. Mechanical properties of fibrils
Biological nanopores	1. No requirement of fluorescent tag or component 2. Low cost 3. Excellent signal to noise ratio	1. Strict environmental requirements for nanopores 2. Requirement of the stable lipid bilayers 3. Fibrils and big aggregates easily clog the pore 4. Size of the pore is fixed	1. Interaction sites with lipid membranes 2. Binding kinetics 3. Identifying oligomer species
Solid-state nanopores	1. No requirement of fluorescent tag or component 2 Low cost 3. Suitable for bigger aggregates or fibrils 4. Adjustable pore size	1. Lipid bilayer is not physiological relevant 2. Lower electric performance and low signal to noise ratio	1. Interaction sites with lipid membranes 2. Binding kinetics 3. Identifying oligomer species

2.5 Contributions to the understanding of amyloid toxicity in lipid membranes

Using ensemble techniques, the toxicity on lipid membranes by amyloid proteins has been proposed to be due to the formation of a ring-like amyloid oligomer that forms a pore in lipid membranes (42). Various amyloid proteins, including Aβ40, α-syn, ABri, ADan, serum amyloid A and IAPP, show a pore-like morphology as revealed by atomic force microscopy and electron microscopy EM (Lashuel et al., 2002).These results may explain the pore-like activity of amyloid proteins towards lipid vesicles and planar bilayers. In the early 90's, Arispe and colleagues first incorporated freshly prepared Aβ into liposomes and observed voltage-dependent ion channel activity after the liposomes were fused with planar lipid 1-palmitoyl-2-oleoyl-sn-glycero-3-phosphoethanolamine (POPE) bilayer (Arispe et al., 1993a; Arispe et al., 1996; Arispe et al., 1993b). The channels exhibited various fluctuations (192). Also, other freshly prepared amyloid proteins, including IAPP (193), β2-microglobulin (194), and a prion protein fragment (195), possess very similar characteristics in the measured currents as with the Aβ in the planar bilayers. These fluctuating and poor reproducible features of electrical signals cannot be attributed to the currents from individual events that may be explored by single-molecule approaches.

The single-molecule approaches mentioned in the previous sections, enable the time-resolved detection of individual amyloid interaction with lipid membranes, with a possibility to distinguish specific pore formation and step-wise membrane permeabilization. Both pore formation and step-wise membrane permeabilization, as schematically illustrated in figure, 4 have been observed by different single-molecule methods. For example, Hannestad *et al.* found that α-syn induces a step-wise disruption and asymmetric membrane deformation of DOPG (28). Aβ aggregates cause the leakage of the vesicle bilayer and rapidly cross the vesicle (105). As shown in the step 1-2 of figure 4, these illustrate the step-wise membrane permeabilization by local amyloid proteins rather than a specific pore structure. On the contrary, small amyloid oligomers may act as a preformed pore to insert into lipid membranes (as illustrated in step 3) (102). FRAP experiments suggested that amyloid beta monomers interact and diffuse within membrane surfaces to cause pore formation in lipid membranes (steps 1, 4) (114).

To further understand the interaction of amyloid proteins with membranes, we may compare amyloid proteins with antimicrobial peptides (AMP) (196). Comparable to amphipathic AMPs, amyloid proteins show a strong binding preference to lipid membranes at a μM range (197,198) this binding results in packing defects and increases surface pressure in lipid membranes (199,200). For instance, the thinning of the outer acyl chain layer of lipid membranes has been observed in the presence of α-syn, IAPP and Aβ (201-204). Presumably, the thinning of lipid

membranes decreases the entropy and tension of the head and acyl regions of lipid membranes. Therefore, amyloid proteins theoretically exert the thinning of the acyl region to reduce the tension of the bilayer. Upon individual amphipathic peptides/protein (such as amyloid protein or AMP) binding to the lipid membranes, its permeabilization occurs spontaneously, possibly, promoted by favorable but not necessarily conformational specific oligomeric pores. In summary, the hydrophilic part of amyloid protein interacts with the head group of lipid membranes. Once the integrity of lipid membrane is affected, specific oligomers form and interact with the lipid membrane followed by pore formation. However, if an asymmetric and instable pore is formed, membrane permeabilization can be enlarged by extra amyloid proteins.

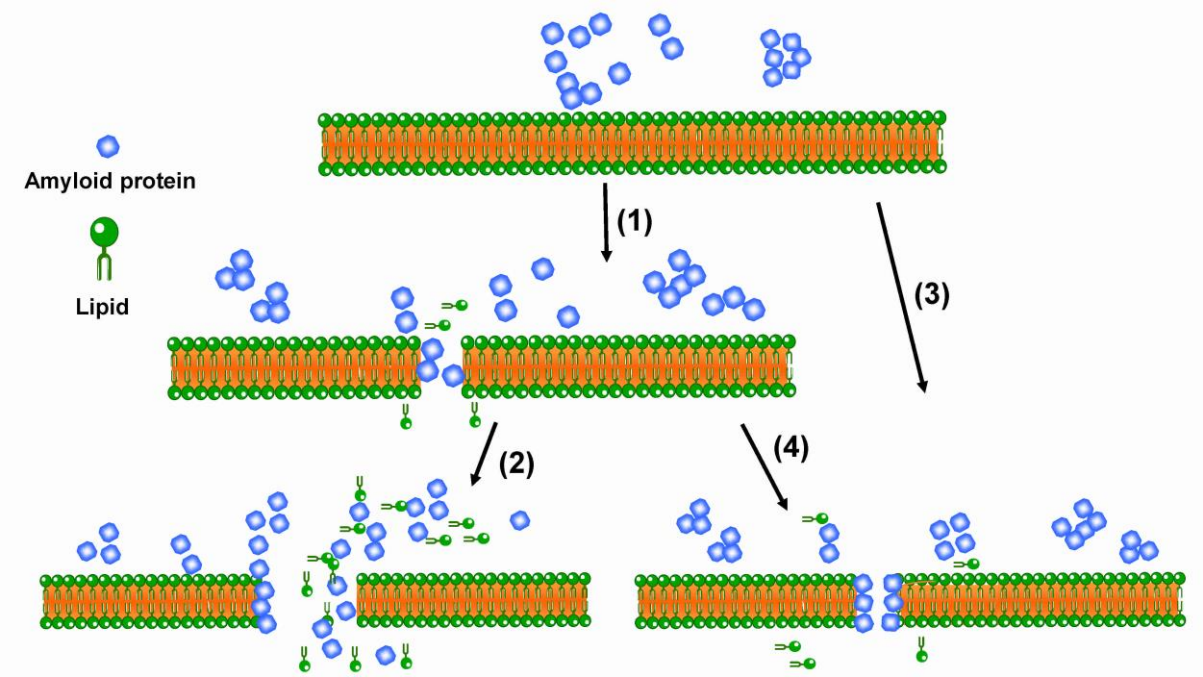

Figure 4. Illustrated mechanisms for amyloid toxicity in lipid membranes. Amyloid monomers or unstable oligomers interact with the polar head group of lipids and then thin the acyl chain layer in stepwise membrane permeabilization (steps 1–2). Alternatively, a specific pore forms in lipid membranes (steps 3–4).

2.6 Application of single-molecule techniques for amyloidosis diagnosis

There is a need for the development of reliable biochemical markers that allow to identify the onset of amyloid diseases such as the progression from mild cognitive impairment (MCI) to AD dementia (205,206). As the most reliable tool for the standard diagnostic procedures (207), CSF biomarkers (Aβ42, total Tau (T-tau), phosphorylated tau (P-tau)) have tremendously

contributed to the clinical diagnosis of MCI to AD due to the high sensitivity and specificity (208,209). It is clear that in AD patients, the level of monomeric Aβ42 is normally reduced due to cortical deposits and the level of Tau is increased due to cortical neuronal loss (T-tau) and tangle formation (P-tau) (208). Though the enzyme-linked immunosorbent assay (ELISA) has been widely used to determine CSF oligomer levels in AD (210), the measured level still show large variability between different studies and individual patients (211). This decreases the diagnostic accuracy of CSF biomarkers, thus hinders the use and integration of these biomarkers as the routine clinical diagnostics. To enhance the accuracy of CSF biomarkers, we propose to analyze the size distributions of these biomarkers and their response to toxicities (such as inflammation response, Ca^{2+} influx, neuronal death), in addition to the detection of the overall levels of CSF biomarker. Our suggestion is based on the increasing reports that show no significant difference in the total number of aggregated species among AD or PD and control CSF samples (212-214). It indicates that the overall level of aggregates might remain constant over long periods of time. However, in different stages of neurodegenerative disease, aggregates do vary with structures or sizes, resulting in different toxicities. Detecting these structural specific and toxic various aggregates can improve the diagnostic accuracy as well as the utilization rate of biomarkers. It is laboratorial available since single-molecule techniques (SMTs) have ultra-sensitivity for identifying the heterogeneous oligomers and handling the small CSF volumes and low working concentrations. Recently, with TIRF microscopy, De *et al.* found that compared to the control CSF, CSF from patients with MCI have a higher amount of small Aβ42 aggregates (<50 nm) that could induce higher membrane permeabilization, while the CSF from AD patients show a larger number of longer and matured aggregates (size 40-200 nm) that could trigger higher inflammation response in microglial cells (212). Horrocks *et al.* also showed no significant difference in total α-syn concentration in the CSF of PD patients and healthy controls via ELISA, nevertheless, with TIRF, they observed there is a different number distribution of aggregates with β-sheet structure (48). These results demonstrate that SMTs can assist in the feasibility studies to implement size distributions as a complementary diagnostic criteria, besides the existing overall aggregate level in CSF biomarker.

Additionally, statistical significance is important for establishing any standard diagnostic criteria. High-throughput methods are required when handing multiple samples. Up to now, a high-throughput for determining oligomers via SMTs alone has not been reported, but combining FRET with high-throughput flow cytometry, Santos and coworkers measured Aβ

oligomers in 174 CSF samples of various neurological disorders but non-demented control patients (215). They confirmed the great variability of oligomer concentration. Another example to improve the time resolution of SMTs is combining FRET with fast-flow microfluidics (89), the measurement time of α-syn oligomers *in vitro* is tremendously decreased from 3 hours to only 5 minutes. Although these methods have not yet been applied as clinical diagnostic tools, the enhanced efficiency could help further establish potential diagnostic criteria in a very efficient way.

It could be effective to implement CSF biomarkers as a strategy to perform the early clinical diagnosis. However, lumbar puncture to collect CSF samples is an invasive procedure, which is the other main reason to prevent the broad dissemination of CSF biomarkers in the routine. A minimally invasive, cost-effective blood-based biomarker was suggested as an alternative to CSF analysis for prediction of early stage of AD (216). However, it has been reported that plasma Aβ42 or Aβ40 level through ELISA between AD and controls has no significant difference (217), while Janelidze *et al.* found the reduced plasma Aβ42 and Aβ40 in AD dementia stages, compared with cognitively healthy control individuals (218). The inconsistent data could attribute to, at least in part, the limits of sensitivity of analytical methods. Additionally, the blood-brain barrier also leads to very low Aβ concentration in blood (35 pg/ml), compared to that in CSF (350 pg/ml) (219). Thus, ultrasensitive analytical methods are needed to improve the accuracy of blood-based biomarkers for early-stage AD prediction. Recently, Tiiman *et al.* identified the Aβ aggregates in blood serum from AD patients and found a higher concentration and larger size of ThT-reactive amyloidogenic nanoplaque compared to healthy controls through single-molecule FCS-ThT method (220). This result demonstrated the feasibility of detecting the actual amyloid states in blood that corresponds to the fibrils in the brain. Though only big aggregates (40mers) were detected in this method, SMTs could be further applied to determine the size of smaller oligomers in the blood. Plasma Aβ40/Aβ42 ratio was also reported as a possible surrogate biomarker of cortical Aβ deposition (221), yet no single-molecule techniques have been applied to characterize the levels. For mild PD clinical prediction, assessing plasma/serum α-syn monomer concentration shows differences between PD patients and controls (222). Thus, the accurate determination of oligomers of plasma α-syn seems more promising. As the ultrasensitive methods, SMTs can contribute to driving this process. Recently, the presence of α-syn in saliva and tears has been proposed as the new potential biofluid biomarkers for PD diagnosis (223,224). Although their

clinical feasibilities need more verification, SMTs provide the possibility to detect the low concentrations of heterogeneous amyloid aggregates.

2.7 Summary and future perspectives

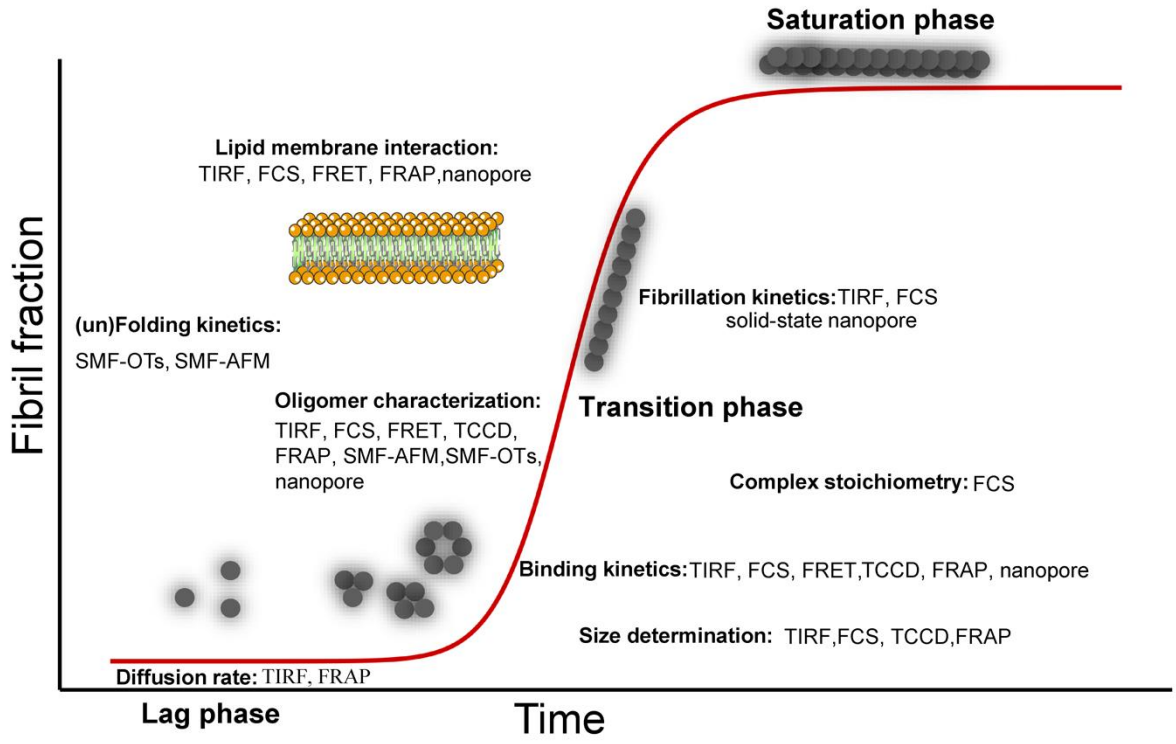

Figure 5. Illustrated amyloid fibrillation pathway and SM studies of amyloidogenesis. Oligomers are formed from disordered amyloid monomers in the lag phase, subsequently assembling into protofibrils and growing into mature fibrils. This process and relevant aggregates can be determined by several physical-chemical parameters, such as diffusion rate, folding kinetics, fibrillation kinetics, and binding kinetics, which are characterized by SM electrical, optical, and mechanical approaches.

Single-molecule techniques (SMTs) have been increasingly employed to characterize individual heterogeneous amyloid aggregates. In the context of neurodegenerative diseases, we have discussed how the different optical, electrical and mechanical single-molecule methods provide great insight into the physical-chemical behaviors of amyloid proteins in heterogenic samples. The working principles, benefits and limitations of the different available techniques were explained and the outcomes of experiments performed by others summarized. As ideal complementary techniques to the regularly used bulk sample techniques and overcome some of their limitations, SMTs determine the size distribution and transient aggregates to

correspond the toxicity in different stages of neurodegenerative diseases. In CSF samples from MCI patients, the toxicity is mainly due to aggregates with size smaller than 50 nm which disturb the Ca^{2+} homeostasis. On the contrary, in AD samples, mainly aggregates between 40-200 nm are responsible for the increased inflammatory response (212). As for CSF sampled from PD patients, it was shown that oligomers and short protofibrils with the size <250 nm increase reactive oxygen species and finally induce highly cytotoxicity to neuronal cells (48,87). Conventional gel chromatography method can also be used to measure the oligomer size distribution, but with larger ambiguity, as elution fractions do not match the individual oligomers precisely and it cannot determine larger oligomers (>10 mers) (113). Additionally, the single-molecule fluorescence and nano-pore systems monitor the structural conversion of oligomers in a more dynamic process that barely be observed by the bulk method circular dichroism (CD). A very typical example is the finding of conformational convention of initially formed α-syn oligomer A to stable and more compact proteinase-K-resistant oligomer B through FRET (87). This result demonstrates the important role of structural conversion in α-syn aggregation. SMTs can also identify dynamic small fibril formation including α-syn, tau and Aβ (<250 nm) (48), however, for the larger fibrils and long-time observation, the traditional methods for kinetics such as the fluorescence assay (ThT assay) might be more suitable. For observing the shape (height or diameter) of the fibrils or big aggregates, conventional AFM exerts more advantages, as the structures of samples are stable and large enough to monitor by the bulk method. Nevertheless, SMF-AFM focuses on the intermolecular interaction between two monomers or dimers, contributing to explaining the initial folding and unfolding process at the single-molecule level. Additionally, by characterizing the oligomers binding to membranes, SMTs provide a series of evidence to manifest that the permeabilization of cellular membrane induced by amyloid oligomers might be the main reason for disrupting cellular homeostasis. For example, by measuring the Ca^{2+} influx, smaller amyloid oligomers are demonstrated to cross the neuronal and CSF membrane (52,54). This supports the hypothesis that the damaged membrane facilitates the transport of the small molecules across the membrane. However, it remains unclear whether these species assemble onto the surface of membranes to make the tightly packed lipids thinner or they incorporate the membrane by forming transmembrane pore. By combining FRAP with the conductivity experiment, these toxic oligomers are shown to have detectable conductance with the value proportional with the size of oligomers (114). The small oligomers from tetramers to octamer might be the origin of forming the pores. Nevertheless, the reported step-wise structural changes and asymmetric membrane leakage induced by α-syn on vesicles do not support the pore model (28) and the

measurement of lower membrane fluidity induced by hIAPP oligomers is an evidence of membrane thinning (225). All these results demonstrate SMTs are very helpful tools to gain a deeper understanding of the membrane-involved toxicity induced by amyloid proteins at the single-molecule level.

In summary, to provide more institutive application of SMTs on different amyloid aggregation processes, we illustrated figure 5 to show where certain SMTs have most beneficial use. Monomeric amyloid proteins diffuse, unfold and assemble into oligomers over the lag phase as characterized by TIRF, FRAP, SMF-OTs and other single-molecule techniques. Cellular membranes contribute to the complex behaviors of amyloid proteins, which can be revealed by FRAP and nanopores. In the presence of lipid membranes, cellular toxic oligomers subsequently aggregate into amyloid protofibrils and fibrils that kinetically and mechanically can be investigated by SMF-OTs, TIRF and many other single-molecule techniques (see figure 5). Small molecules, as well as lipids that may react with amyloid proteins and affect binding kinetics and interaction complex stoichiometry and other physical-chemical factors, have been discussed in the application part. All of these demonstrate that SMTs enhance our understanding of the complicated interaction mechanism of transient, heterogeneous amyloid aggregates with lipids at the single-molecule level, enabling us to put forward the diagnosis of Alzheimer's and Parkinson's diseases. In spite of distinct clinical symptoms behind each disease, amyloid proteins share many above-mentioned structural and dynamic features, possibly damage cells and cause inflammation or other immune responses in a similar manner. We anticipate that these amyloid protein-related responses will be further explored by SMTs in the future. Overall, electrical, optical, and mechanical single-molecule methods have been indispensable in characterizing the physical-chemical complexity of amyloid proteins, and contributed tremendously to the knowledge and detailed understanding of amyloid assembly and toxicity.

In the near future, technological and analytical developments in single-molecule methods, as well as combined computational modeling, may permit a complete understanding of the complexity of amyloid protein assembly and further shed light on other applications such as structure determination. One important future application of single-molecule approaches will be to characterize amyloid aggregates of *ex vivo* samples providing an important determinant for the toxicity of biological samples and the diagnosis and subsequent therapy of neurodegenerative diseases.

2.8 Abbreviations

AD Alzheimer’s disease

PD Parkinson’s disease

HD Huntington's diseases

ALS Amyotrophic Lateral Sclerosis

CJD Creutzfeldt–Jakob

SOD1 Superoxide dismutase 1

CD Circular dichroism

SMTs Single-molecule techniques

SMFI Single-molecule fluorescence-based imaging

SMFS Single-molecule force spectroscopy

SNS Single-nanopore electrical systems

TIRF Total internal reflection fluorescence

FRET Fluorescence resonance energy transfer

TCCD Two color coincidence detection

FRAP Fluorescence recovery after photobleaching

FCS Fluorescence correlation spectroscopy

CSF Cerebrospinal fluid

SMF Single-molecule force

AFM Atomic force microscopy

OTs Optical tweezers/traps

MTs Magnetic tweezers

FNA Flexible nanoarrays

hIAPP Human islet amyloid polypeptide

ThT Thioflavin-T

β2-m β2-microgobulin

cac Critical aggregation concentration

R_h Hydrodynamic radius

C. elegans Caenorhabditis elegans

DC Diffusion coefficient

NA Numerical aperture

PrP Prion protein

NM N-domain of prion monomer variant

α-HL α-hemolysin

MspA Mycobacterium smegmatis porin A

β-CD β-cyclodextrin

VDAC Voltage-dependent anion channels

DIB Droplet interface bilayers

DHB Droplet/hydrogel interfaces

PG Phosphatidylglycerol

DPPC Dipalmitoylphosphatidylcholine

POPE 1-palmitoyl-2-oleoyl-sn-glycero-3-phosphoethanolamine

AMP Antimicrobial peptide

2.9 Acknowledgements

We thank Prof. Astrid Gräslund (Stockholm University, Sweden) and Prof. Guy Lippens (Université de Toulouse, France) for invaluable insights as well as critical advices of the manuscript.

2.10 References

1. Gitler, A. D., Dhillon, P., and Shorter, J. (2017) Neurodegenerative disease: models, mechanisms, and a new hope. *Disease Models & Mechanisms* **10**, 499-502
2. Kumar, A., Singh, A., and Ekavali. (2015) A review on Alzheimer's disease pathophysiology and its management: an update. *Pharmacological Reports* **67**, 195-203
3. Jaul, E., and Barron, J. (2017) Age-Related Diseases and Clinical and Public Health Implications for the 85 Years Old and Over Population. *Front Public Health* **5**, 335-335
4. Hipp, M. S., Kasturi, P., and Hartl, F. U. (2019) The proteostasis network and its decline in ageing. *Nature Reviews Molecular Cell Biology* **20**, 421-435
5. Greenwald, J., and Riek, R. (2010) Biology of amyloid: structure, function, and regulation. *Structure* **18**, 1244-1260
6. Adamcik, J., and Mezzenga, R. (2018) Amyloid Polymorphism in the Protein Folding and Aggregation Energy Landscape. *Angewandte Chemie International Edition* **57**, 8370-8382
7. Dobson, C. M. (2003) Protein folding and misfolding. *Nature* **426**, 884-890
8. Selkoe, D. J. (2003) Folding proteins in fatal ways. *Nature* **426**, 900-904
9. Tagliavini, F., Giaccone, G., Frangione, B., and Bugiani, O. (1988) Preamyloid deposits in the cerebral cortex of patients with Alzheimer's disease and nondemented individuals. *Neuroscience Letters* **93**, 191-196
10. Fukumoto, H., Asami-Odaka, A., Suzuki, N., and Iwatsubo, T. (1996) Association of A beta 40-positive senile plaques with microglial cells in the brains of patients with Alzheimer's disease and in non-demented aged individuals. *Neurodegeneration* **5**, 13-17
11. Chiti, F., and Dobson, C. M. (2017) Protein Misfolding, Amyloid Formation, and Human Disease: A Summary of Progress Over the Last Decade. *Annual Review of Biochemistry* **86**, 27-68
12. Fowler, D. M., Koulov, A. V., Balch, W. E., and Kelly, J. W. (2007) Functional amyloid--from bacteria to humans. *Trends in Biochemical Sciences* **32**, 217-224
13. Pham, C. L., Kwan, A. H., and Sunde, M. (2014) Functional amyloid: widespread in Nature, diverse in purpose. *Essays in Biochemistry* **56**, 207-219
14. Brothers, H. M., Gosztyla, M. L., and Robinson, S. R. (2018) The Physiological Roles of Amyloid-beta Peptide Hint at New Ways to Treat Alzheimer's Disease. *Frontiers in Aging Neuroscience* **10**, 118
15. Chen, G. F., Xu, T. H., Yan, Y., Zhou, Y. R., Jiang, Y., Melcher, K., and Xu, H. E. (2017) Amyloid beta: structure, biology and structure-based therapeutic development. *Acta Pharmacologica Sinica* **38**, 1205-1235
16. Butterfield, S. M., and Lashuel, H. A. (2010) Amyloidogenic protein-membrane interactions: mechanistic insight from model systems. *Angewandte Chemie International Edition in English* **49**, 5628-5654
17. Jahn, T. R., and Radford, S. E. (2008) Folding versus aggregation: polypeptide conformations on competing pathways. *Archives of Biochemistry and Biophysics* **469**, 100-117
18. Eichner, T., and Radford, S. E. (2011) A diversity of assembly mechanisms of a generic amyloid fold. *Molecular Cell* **43**, 8-18
19. Tipping, K. W., van Oosten-Hawle, P., Hewitt, E. W., and Radford, S. E. (2015) Amyloid Fibres: Inert End-Stage Aggregates or Key Players in Disease? *Trends in Biochemical Sciences* **40**, 719-727
20. Klein, W. L., Krafft, G. A., and Finch, C. E. (2001) Targeting small Abeta oligomers: the solution to an Alzheimer's disease conundrum? *Trends in Neurosciences* **24**, 219-224
21. Walsh, D. M., and Selkoe, D. J. (2007) A beta oligomers - a decade of discovery. *Journal of Neurochemistry* **101**, 1172-1184

22. Benilova, I., Karran, E., and De Strooper, B. (2012) The toxic Abeta oligomer and Alzheimer's disease: an emperor in need of clothes. *Nature Neuroscience* **15**, 349-357
23. Williams, T. L., and Serpell, L. C. (2011) Membrane and surface interactions of Alzheimer's Abeta peptide--insights into the mechanism of cytotoxicity. *The FEBS Journal* **278**, 3905-3917
24. Lee, J., Kim, Y. H., F, T. A., Gillman, A. L., Jang, H., Kagan, B. L., Nussinov, R., Yang, J., and Lal, R. (2017) Amyloid beta Ion Channels in a Membrane Comprising Brain Total Lipid Extracts. *ACS Chemical Neuroscience* **8**, 1348-1357
25. Lashuel, H. A., and Lansbury, P. T., Jr. (2006) Are amyloid diseases caused by protein aggregates that mimic bacterial pore-forming toxins? *Quarterly Reviews of Biophysics* **39**, 167-201
26. Cipriani, G., Dolciotti, C., Picchi, L., and Bonuccelli, U. (2011) Alzheimer and his disease: a brief history. *Neurological Sciences* **32**, 275-279
27. Johnson, R. D., Steel, D. G., and Gafni, A. (2014) Structural evolution and membrane interactions of Alzheimer's amyloid-beta peptide oligomers: new knowledge from single-molecule fluorescence studies. *Protein Science* **23**, 869-883
28. Hannestad, J. K., Rocha, S., Agnarsson, B., Zhdanov, V. P., Wittung-Stafshede, P., and Höök, F. (2020) Single-vesicle imaging reveals lipid-selective and stepwise membrane disruption by monomeric α-synuclein. *Proceedings of the National Academy of Sciences* **117**, 14178-14186
29. McLean, C. A., Cherny, R. A., Fraser, F. W., Fuller, S. J., Smith, M. J., Beyreuther, K., Bush, A. I., and Masters, C. L. (1999) Soluble pool of Abeta amyloid as a determinant of severity of neurodegeneration in Alzheimer's disease. *Annals of Neurology* **46**, 860-866
30. Lue, L. F., Kuo, Y. M., Roher, A. E., Brachova, L., Shen, Y., Sue, L., Beach, T., Kurth, J. H., Rydel, R. E., and Rogers, J. (1999) Soluble amyloid beta peptide concentration as a predictor of synaptic change in Alzheimer's disease. *The American Journal of Pathology* **155**, 853-862
31. Mollenhauer, B., Cullen, V., Kahn, I., Krastins, B., Outeiro, T. F., Pepivani, I., Ng, J., Schulz-Schaeffer, W., Kretzschmar, H. A., McLean, P. J., Trenkwalder, C., Sarracino, D. A., VonSattel, J.-P., Locascio, J. J., El-Agnaf, O. M. A., and Schlossmacher, M. G. (2008) Direct quantification of CSF α-synuclein by ELISA and first cross-sectional study in patients with neurodegeneration. *Experimental Neurology* **213**, 315-325
32. Whitmore, L., and Wallace, B. A. (2008) Protein secondary structure analyses from circular dichroism spectroscopy: methods and reference databases. *Biopolymers* **89**, 392-400
33. Ruggeri, F. S., Adamcik, J., Jeong, J. S., Lashuel, H. A., Mezzenga, R., and Dietler, G. (2015) Influence of the β-sheet content on the mechanical properties of aggregates during amyloid fibrillization. *Angewandte Chemie International Edition in English* **54**, 2462-2466
34. Zandomeneghi, G., Krebs, M. R., McCammon, M. G., and Fändrich, M. (2004) FTIR reveals structural differences between native beta-sheet proteins and amyloid fibrils. *Protein Science* **13**, 3314-3321
35. Lord, S. J., Lee, H. L., and Moerner, W. E. (2010) Single-molecule spectroscopy and imaging of biomolecules in living cells. *Analytical Chemistry* **82**, 2192-2203
36. Zhang, Y., Ha, T., and Marqusee, S. (2018) Editorial Overview: Single-Molecule Approaches up to Difficult Challenges in Folding and Dynamics. *Journal of Molecular Biology* **430**, 405-408
37. Seisenberger, G., Ried, M. U., Endreß, T., Büning, H., Hallek, M., and Bräuchle, C. (2001) Real-Time Single-Molecule Imaging of the Infection Pathway of an Adeno-Associated Virus. *Science* **294**, 1929-1932
38. Mukhopadhyay, S., Krishnan, R., Lemke, E. A., Lindquist, S., and Deniz, A. A. (2007) A natively unfolded yeast prion monomer adopts an ensemble of collapsed and rapidly fluctuating structures. *Proceedings of the National Academy of Sciences* **104**, 2649-2654
39. Greenleaf, W. J., Woodside, M. T., and Block, S. M. (2007) High-resolution, single-molecule measurements of biomolecular motion. *Annu Rev Biophys Biomol Struct* **36**, 171-190
40. Shashkova, S., and Leake, M. C. (2017) Single-molecule fluorescence microscopy review: shedding new light on old problems. *Bioscience Reports* **37**
41. Neuman, K. C., and Nagy, A. (2008) Single-molecule force spectroscopy: optical tweezers, magnetic tweezers and atomic force microscopy. *Nature Methods* **5**, 491-505

42. Quist, A., Doudevski, I., Lin, H., Azimova, R., Ng, D., Frangione, B., Kagan, B., Ghiso, J., and Lal, R. (2005) Amyloid ion channels: a common structural link for protein-misfolding disease. *Proceedings of the National Academy of Sciences* **102**, 10427-10432
43. Jang, H., Arce, F. T., Ramachandran, S., Kagan, B. L., Lal, R., and Nussinov, R. (2014) Disordered amyloidogenic peptides may insert into the membrane and assemble into common cyclic structural motifs. *Chemical Society Reviews* **43**, 6750-6764
44. Jaiswal, J. K., Mattoussi, H., Mauro, J. M., and Simon, S. M. (2003) Long-term multiple color imaging of live cells using quantum dot bioconjugates. *Nature Biotechnology* **21**, 47-51
45. Keppler, A., Gendreizig, S., Gronemeyer, T., Pick, H., Vogel, H., and Johnsson, K. (2003) A general method for the covalent labeling of fusion proteins with small molecules in vivo. *Nature Biotechnology* **21**, 86-89
46. Schneckenburger, H. (2005) Total internal reflection fluorescence microscopy: technical innovations and novel applications. *Current Opinion in Biotechnology* **16**, 13-18
47. Zheng, Y., Xu, L., Yang, J., Peng, X., Wang, H., Yu, N., Hua, Y., Zhao, J., He, J., and Hong, T. (2018) The effects of fluorescent labels on Aβ(42) aggregation detected by fluorescence correlation spectroscopy. *Biopolymers* **109**, e23237
48. Horrocks, M. H., Lee, S. F., Gandhi, S., Magdalinou, N. K., Chen, S. W., Devine, M. J., Tosatto, L., Kjaergaard, M., Beckwith, J. S., Zetterberg, H., Iljina, M., Cremades, N., Dobson, C. M., Wood, N. W., and Klenerman, D. (2016) Single-Molecule Imaging of Individual Amyloid Protein Aggregates in Human Biofluids. *ACS Chemical Neuroscience* **7**, 399-406
49. Ban, T., Hoshino, M., Takahashi, S., Hamada, D., Hasegawa, K., Naiki, H., and Goto, Y. (2004) Direct observation of Abeta amyloid fibril growth and inhibition. *Journal of Molecular Biology* **344**, 757-767
50. Andersen, C. B., Yagi, H., Manno, M., Martorana, V., Ban, T., Christiansen, G., Otzen, D. E., Goto, Y., and Rischel, C. (2009) Branching in amyloid fibril growth. *Biophysical Journal* **96**, 1529-1536
51. Patil, S. M., Mehta, A., Jha, S., and Alexandrescu, A. T. (2011) Heterogeneous amylin fibril growth mechanisms imaged by total internal reflection fluorescence microscopy. *Biochemistry* **50**, 2808-2819
52. Drews, A., Flint, J., Shivji, N., Jönsson, P., Wirthensohn, D., De Genst, E., Vincke, C., Muyldermans, S., Dobson, C., and Klenerman, D. (2016) Individual aggregates of amyloid beta induce temporary calcium influx through the cell membrane of neuronal cells. *Scientific Reports* **6**, 31910
53. Flagmeier, P., De, S., Wirthensohn, D. C., Lee, S. F., Vincke, C., Muyldermans, S., Knowles, T. P. J., Gandhi, S., Dobson, C. M., and Klenerman, D. (2017) Ultrasensitive Measurement of Ca2+ Influx into Lipid Vesicles Induced by Protein Aggregates. *Angewandte Chemie International Edition in English* **56**, 7750 - 7754
54. Drews, A., De, S., Flagmeier, P., Wirthensohn, D. C., Chen, W. H., Whiten, D. R., Rodrigues, M., Vincke, C., Muyldermans, S., Paterson, R. W., Slattery, C. F., Fox, N. C., Schott, J. M., Zetterberg, H., Dobson, C. M., Gandhi, S., and Klenerman, D. (2017) Inhibiting the Ca(2+) Influx Induced by Human CSF. *Cell Reports* **21**, 3310-3316
55. Tanaka, H., Sakaguchi, D., and Hirano, T. (2019) Amyloid-β oligomers suppress subunit-specific glutamate receptor increase during LTP. *Alzheimer's & Dementia: Translational Research & Clinical Interventions* **5**, 797-808
56. Jarosz-Griffiths, H. H., Noble, E., Rushworth, J. V., and Hooper, N. M. (2016) Amyloid-β Receptors: The Good, the Bad, and the Prion Protein. *J Biol Chem* **291**, 3174-3183
57. Agnarsson, B., Lundgren, A., Gunnarsson, A., Rabe, M., Kunze, A., Mapar, M., Simonsson, L., Bally, M., Zhdanov, V. P., and Höök, F. (2015) Evanescent Light-Scattering Microscopy for Label-Free Interfacial Imaging: From Single Sub-100 nm Vesicles to Live Cells. *ACS Nano* **9**, 11849-11862
58. Ji, M., Arbel, M., Zhang, L., Freudiger, C. W., Hou, S. S., Lin, D., Yang, X., Bacskai, B. J., and Xie, X. S. (2018) Label-free imaging of amyloid plaques in Alzheimer's disease with stimulated Raman scattering microscopy. *Science Advances* **4**, eaat7715

59. Schweikhard, V., Baral, A., Krishnamachari, V., Hay, W. C., and Fuhrmann, M. (2019) Label-free characterization of Amyloid-β-plaques and associated lipids in brain tissues using stimulated Raman scattering microscopy. *bioRxiv*, 789248
60. Rigler, R. (2010) Fluorescence and single molecule analysis in cell biology. *Biochemical and Biophysical Research Communications* **396**, 170-175
61. Elson, E. L. (2018) Introduction to fluorescence correlation Spectroscopy-Brief and simple. *Methods* **140-141**, 3-9
62. Medina, M. A., and Schwille, P. (2002) Fluorescence correlation spectroscopy for the detection and study of single molecules in biology. *Bioessays* **24**, 758-764
63. Kitamura, A., and Kinjo, M. (2018) State-of-the-Art Fluorescence Fluctuation-Based Spectroscopic Techniques for the Study of Protein Aggregation. *International Journal of Molecular Sciences* **19**
64. Garai, K., Sahoo, B., Sengupta, P., and Maiti, S. (2008) Quasihomogeneous nucleation of amyloid beta yields numerical bounds for the critical radius, the surface tension, and the free energy barrier for nucleus formation. *The Journal of Chemical Physics* **128**, 045102
65. Garai, K., Sengupta, P., Sahoo, B., and Maiti, S. (2006) Selective destabilization of soluble amyloid β oligomers by divalent metal ions. *Biochemical and Biophysical Research Communications* **345**, 210-215
66. Tiiman, A., Jarvet, J., Gräslund, A., and Vukojević, V. (2015) Heterogeneity and Turnover of Intermediates during Amyloid-β (Aβ) Peptide Aggregation Studied by Fluorescence Correlation Spectroscopy. *Biochemistry* **54**, 7203-7211
67. Liang, Y., Lynn, D. G., and Berland, K. M. (2010) Direct observation of nucleation and growth in amyloid self-assembly. *Journal of the American Chemical Society* **132**, 6306-6308
68. Guan, Y., Cao, K. J., Cantlon, A., Elbel, K., Theodorakis, E. A., Walsh, D. M., Yang, J., and Shah, J. V. (2015) Real-Time Monitoring of Alzheimer's-Related Amyloid Aggregation via Probe Enhancement-Fluorescence Correlation Spectroscopy. *ACS Chemical Neuroscience* **6**, 1503-1508
69. Mittag, J. J., Milani, S., Walsh, D. M., Rädler, J. O., and McManus, J. J. (2014) Simultaneous measurement of a range of particle sizes during Aβ1-42 fibrillogenesis quantified using fluorescence correlation spectroscopy. *Biochemical and Biophysical Research Communications* **448**, 195-199
70. Tjernberg, L. O., Pramanik, A., Björling, S., Thyberg, P., Thyberg, J., Nordstedt, C., Berndt, K. D., Terenius, L., and Rigler, R. (1999) Amyloid beta-peptide polymerization studied using fluorescence correlation spectroscopy. *Chemistry & Biology* **6**, 53-62
71. Garai, K., Sureka, R., and Maiti, S. (2007) Detecting Amyloid-β Aggregation with Fiber-Based Fluorescence Correlation Spectroscopy. *Biophysical Journal* **92**, L55-L57
72. Novo, M., Freire, S., and Al-Soufi, W. (2018) Critical aggregation concentration for the formation of early Amyloid-β (1-42) oligomers. *Scientific reports* **8**, 1783-1783
73. Pitschke, M., Prior, R., Haupt, M., and Riesner, D. (1998) Detection of single amyloid β-protein aggregates in the cerebrospinal fluid of Alzheimer's patients by fluorescence correlation spectroscopy. *Nature Medicine* **4**, 832-834
74. Funke, S. A., Birkmann, E., Henke, F., Görtz, P., Lange-Asschenfeldt, C., Riesner, D., and Willbold, D. (2007) Single particle detection of Aβ aggregates associated with Alzheimer's disease. *Biochemical and Biophysical Research Communications* **364**, 902-907
75. Wiesehan, K., Stöhr, J., Nagel-Steger, L., van Groen, T., Riesner, D., and Willbold, D. (2008) Inhibition of cytotoxicity and amyloid fibril formation by a D-amino acid peptide that specifically binds to Alzheimer's disease amyloid peptide. *Protein Engineering, Design and Selection* **21**, 241-246
76. Miraglia, F., Ricci, A., Rota, L., and Colla, E. (2018) Subcellular localization of alpha-synuclein aggregates and their interaction with membranes. *Neural Regen Res* **13**, 1136-1144
77. Rhoades, E., Ramlall, T. F., Webb, W. W., and Eliezer, D. (2006) Quantification of alpha-synuclein binding to lipid vesicles using fluorescence correlation spectroscopy. *Biophysical Journal* **90**, 4692-4700
78. Middleton, E. R., and Rhoades, E. (2010) Effects of curvature and composition on α-synuclein binding to lipid vesicles. *Biophysical journal* **99**, 2279-2288

79. Sarkar, B., Das, A., and Maiti, S. (2013) Thermodynamically stable amyloid-β monomers have much lower membrane affinity than the small oligomers. *Frontiers in Physiology* **4**
80. Nag, S., Chen, J., Irudayaraj, J., and Maiti, S. (2010) Measurement of the attachment and assembly of small amyloid-β oligomers on live cell membranes at physiological concentrations using single-molecule tools. *Biophysical journal* **99**, 1969-1975
81. Simpson, L. W., Szeto, G. L., Boukari, H., Good, T. A., and Leach, J. B. (2020) Collagen hydrogel confinement of Amyloid-β (Aβ) accelerates aggregation and reduces cytotoxic effects. *Acta Biomaterialia* **112**, 164-173
82. Schwille, P., Meyer-Almes, F. J., and Rigler, R. (1997) Dual-color fluorescence cross-correlation spectroscopy for multicomponent diffusional analysis in solution. *Biophysical Journal* **72**, 1878-1886
83. Bonito-Oliva, A., Schedin-Weiss, S., Younesi, S. S., Tiiman, A., Adura, C., Paknejad, N., Brendel, M., Romin, Y., Parchem, R. J., Graff, C., Vukojević, V., Tjernberg, L. O., Terenius, L., Winblad, B., Sakmar, T. P., and Graham, W. V. (2019) Conformation-specific antibodies against multiple amyloid protofibril species from a single amyloid immunogen. *Journal of Cellular and Molecule Medicine* **23**, 2103-2114
84. Zheng, Y., Tian, S., Peng, X., Yang, J., Fu, Y., Jiao, Y., Zhao, J., He, J., and Hong, T. (2016) Kinesin-1 inhibits the aggregation of amyloid-β peptide as detected by fluorescence cross-correlation spectroscopy. *FEBS Letters* **590**, 1028-1037
85. Schuler, B., and Eaton, W. A. (2008) Protein folding studied by single-molecule FRET. *Current Opinion in Structural Biology* **18**, 16-26
86. Roy, R., Hohng, S., and Ha, T. (2008) A practical guide to single-molecule FRET. *Nature Methods* **5**, 507-516
87. Cremades, N., Cohen, S. I., Deas, E., Abramov, A. Y., Chen, A. Y., Orte, A., Sandal, M., Clarke, R. W., Dunne, P., Aprile, F. A., Bertoncini, C. W., Wood, N. W., Knowles, T. P., Dobson, C. M., and Klenerman, D. (2012) Direct observation of the interconversion of normal and toxic forms of α-synuclein. *Cell* **149**, 1048-1059
88. Conway, K. A., Lee, S. J., Rochet, J. C., Ding, T. T., Williamson, R. E., and Lansbury, P. T., Jr. (2000) Acceleration of oligomerization, not fibrillization, is a shared property of both alpha-synuclein mutations linked to early-onset Parkinson's disease: implications for pathogenesis and therapy. *Proceedings of the National Academy of Sciences* **97**, 571-576
89. Horrocks, M. H., Tosatto, L., Dear, A. J., Garcia, G. A., Iljina, M., Cremades, N., Dalla Serra, M., Knowles, T. P., Dobson, C. M., and Klenerman, D. (2015) Fast flow microfluidics and single-molecule fluorescence for the rapid characterization of α-synuclein oligomers. *Analytical Chemistry* **87**, 8818-8826
90. Tosatto, L., Horrocks, M. H., Dear, A. J., Knowles, T. P., Dalla Serra, M., Cremades, N., Dobson, C. M., and Klenerman, D. (2015) Single-molecule FRET studies on alpha-synuclein oligomerization of Parkinson's disease genetically related mutants. *Scientific Reports* **5**, 16696
91. Iljina, M., Garcia, G. A., Horrocks, M. H., Tosatto, L., Choi, M. L., Ganzinger, K. A., Abramov, A. Y., Gandhi, S., Wood, N. W., Cremades, N., Dobson, C. M., Knowles, T. P., and Klenerman, D. (2016) Kinetic model of the aggregation of alpha-synuclein provides insights into prion-like spreading. *Proceedings of the National Academy of Sciences* **113**, E1206-1215
92. Shammas, S. L., Garcia, G. A., Kumar, S., Kjaergaard, M., Horrocks, M. H., Shivji, N., Mandelkow, E., Knowles, T. P., Mandelkow, E., and Klenerman, D. (2015) A mechanistic model of tau amyloid aggregation based on direct observation of oligomers. *Nature Communications* **6**, 7025
93. Wennmalm, S., Chmyrov, V., Widengren, J., and Tjernberg, L. (2015) Highly Sensitive FRET-FCS Detects Amyloid β-Peptide Oligomers in Solution at Physiological Concentrations. *Analytical Chemistry* **87**, 11700-11705
94. Kaminski Schierle, G. S., Bertoncini, C. W., Chan, F. T. S., van der Goot, A. T., Schwedler, S., Skepper, J., Schlachter, S., van Ham, T., Esposito, A., Kumita, J. R., Nollen, E. A. A., Dobson, C. M., and Kaminski, C. F. (2011) A FRET sensor for non-invasive imaging of amyloid formation in vivo. *Chemphyschem* **12**, 673-680

95. Cecon, E., Dam, J., Luka, M., Gautier, C., Chollet, A. M., Delagrange, P., Danober, L., and Jockers, R. (2019) Quantitative assessment of oligomeric amyloid β peptide binding to α7 nicotinic receptor. *British Journal of Pharmacology* **176**, 3475-3488
96. Bertrand, D., Lee, C. H., Flood, D., Marger, F., and Donnelly-Roberts, D. (2015) Therapeutic Potential of α7 Nicotinic Acetylcholine Receptors. *Pharmacological Reviews* **67**, 1025-1073
97. Lee, H. J., Lee, Y. G., Kang, J., Yang, S. H., Kim, J. H., Ghisaidoobe, A. B. T., Kang, H. J., Lee, S. R., Lim, M. H., and Chung, S. J. (2019) Monitoring metal-amyloid-β complexation by a FRET-based probe: design, detection, and inhibitor screening. *Chemical Science* **10**, 1000-1007
98. Sergeeva, A. V., Sopova, J. V., Belashova, T. A., Siniukova, V. A., Chirinskaite, A. V., Galkin, A. P., and Zadorsky, S. P. (2019) Amyloid properties of the yeast cell wall protein Toh1 and its interaction with prion proteins Rnq1 and Sup35. *Prion* **13**, 21-32
99. Reynolds, N. P., Soragni, A., Rabe, M., Verdes, D., Liverani, E., Handschin, S., Riek, R., and Seeger, S. (2011) Mechanism of Membrane Interaction and Disruption by α-Synuclein. *Journal of the American Chemical Society* **133**, 19366-19375
100. Terzi, E., Hölzemann, G., and Seelig, J. (1995) Self-association of β-Amyloid Peptide (1–40) in Solution and Binding to Lipid Membranes. *Journal of Molecular Biology* **252**, 633-642
101. Wong, P. T., Schauerte, J. A., Wisser, K. C., Ding, H., Lee, E. L., Steel, D. G., and Gafni, A. (2009) Amyloid-β Membrane Binding and Permeabilization are Distinct Processes Influenced Separately by Membrane Charge and Fluidity. *Journal of Molecular Biology* **386**, 81-96
102. Ding, H., Schauerte, J. A., Steel, D. G., and Gafni, A. (2012) β-Amyloid (1-40) peptide interactions with supported phospholipid membranes: a single-molecule study. *Biophysical Journal* **103**, 1500-1509
103. Lindberg, D. J., Wesén, E., Björkeroth, J., Rocha, S., and Esbjörner, E. K. (2017) Lipid membranes catalyse the fibril formation of the amyloid-β (1–42) peptide through lipid-fibril interactions that reinforce secondary pathways. *Biochimica et Biophysica Acta (BBA) - Biomembranes* **1859**, 1921-1929
104. Gorbenko, G., Trusova, V., Girych, M., Adachi, E., Mizuguchi, C., Akaji, K., and Saito, H. (2015) FRET evidence for untwisting of amyloid fibrils on the surface of model membranes. *Soft Matter* **11**, 6223-6234
105. Widenbrant, M. J. O., Rajadas, J., Sutardja, C., and Fuller, G. G. (2006) Lipid-Induced β-Amyloid Peptide Assemblage Fragmentation. *Biophysical Journal* **91**, 4071-4080
106. Orte, A., Clarke, R., and Klenerman, D. (2010) Single-molecule two-colour coincidence detection to probe biomolecular associations. *Biochemical Society Transactions* **38**, 914-918
107. Orte, A., Birkett, N. R., Clarke, R. W., Devlin, G. L., Dobson, C. M., and Klenerman, D. (2008) Direct characterization of amyloidogenic oligomers by single-molecule fluorescence. *Proceedings of the National Academy of Sciences* **105**, 14424-14429
108. Chiou, A., Hägglöf, P., Orte, A., Chen, A. Y., Dunne, P. D., Belorgey, D., Karlsson-Li, S., Lomas, D. A., and Klenerman, D. (2009) Probing neuroserpin polymerization and interaction with amyloid-beta peptides using single molecule fluorescence. *Biophysical Journal* **97**, 2306-2315
109. Iljina, M., Garcia, G. A., Dear, A. J., Flint, J., Narayan, P., Michaels, T. C., Dobson, C. M., Frenkel, D., Knowles, T. P., and Klenerman, D. (2016) Quantitative analysis of co-oligomer formation by amyloid-beta peptide isoforms. *Scientific Reports* **6**, 28658
110. Iljina, M., Dear, A. J., Garcia, G. A., De, S., Tosatto, L., Flagmeier, P., Whiten, D. R., Michaels, T. C. T., Frenkel, D., Dobson, C. M., Knowles, T. P. J., and Klenerman, D. (2018) Quantifying Co-Oligomer Formation by α-Synuclein. *ACS Nano* **12**, 10855-10866
111. Axelrod, D., Koppel, D. E., Schlessinger, J., Elson, E., and Webb, W. W. (1976) Mobility measurement by analysis of fluorescence photobleaching recovery kinetics. *Biophysical Journal* **16**, 1055-1069
112. Reits, E. A., and Neefjes, J. J. (2001) From fixed to FRAP: measuring protein mobility and activity in living cells. *Nature Cell Biology* **3**, E145-147
113. Ding, H., Wong, P. T., Lee, E. L., Gafni, A., and Steel, D. G. (2009) Determination of the oligomer size of amyloidogenic protein beta-amyloid(1-40) by single-molecule spectroscopy. *Biophysical Journal* **97**, 912-921

114. Schauerte, J. A., Wong, P. T., Wisser, K. C., Ding, H., Steel, D. G., and Gafni, A. (2010) Simultaneous single-molecule fluorescence and conductivity studies reveal distinct classes of Abeta species on lipid bilayers. *Biochemistry* **49**, 3031-3039
115. Vereb, G., Szöllosi, J., Matkó, J., Nagy, P., Farkas, T., Vigh, L., Mátyus, L., Waldmann, T. A., and Damjanovich, S. (2003) Dynamic, yet structured: The cell membrane three decades after the Singer-Nicolson model. *Proceedings of the National Academy of Sciences* **100**, 8053-8058
116. Marguet, D., Lenne, P. F., Rigneault, H., and He, H. T. (2006) Dynamics in the plasma membrane: how to combine fluidity and order. *The Embo journal* **25**, 3446-3457
117. Sasahara, K., Morigaki, K., Okazaki, T., and Hamada, D. (2012) Binding of islet amyloid polypeptide to supported lipid bilayers and amyloid aggregation at the membranes. *Biochemistry* **51**, 6908-6919
118. Sasahara, K., Morigaki, K., and Shinya, K. (2013) Effects of membrane interaction and aggregation of amyloid β-peptide on lipid mobility and membrane domain structure. *Physical Chemistry Chemical Physics* **15**, 8929-8939
119. Schreiber, A., Fischer, S., and Lang, T. (2012) The amyloid precursor protein forms plasmalemmal clusters via its pathogenic amyloid-β domain. *Biophysical Journal* **102**, 1411-1417
120. Sasahara, K., Morigaki, K., and Shinya, K. (2014) Amyloid aggregation and deposition of human islet amyloid polypeptide at membrane interfaces. *The FEBS Journal* **281**, 2597-2612
121. Meker, S., Chin, H., Sut, T. N., and Cho, N. J. (2018) Amyloid-β Peptide Triggers Membrane Remodeling in Supported Lipid Bilayers Depending on Their Hydrophobic Thickness. *Langmuir* **34**, 9548-9560
122. Roberti, M. J., Jovin, T. M., and Jares-Erijman, E. (2011) Confocal fluorescence anisotropy and FRAP imaging of α-synuclein amyloid aggregates in living cells. *PLoS One* **6**, e23338
123. Adamcik, J., and Mezzenga, R. (2012) Study of amyloid fibrils via atomic force microscopy. *Current Opinion in Colloid & Interface Science* **17**, 369-376
124. Binnig, G., Quate, C. F., and Gerber, C. (1986) Atomic Force Microscope. *Physical Review Letters* **56**, 930-933
125. Ruggeri, F. S., Benedetti, F., Knowles, T. P. J., Lashuel, H. A., Sekatskii, S., and Dietler, G. (2018) Identification and nanomechanical characterization of the fundamental single-strand protofilaments of amyloid α-synuclein fibrils. *Proceedings of the National Academy of Sciences* **115**, 7230
126. Adamcik, J., Jung, J.-M., Flakowski, J., De Los Rios, P., Dietler, G., and Mezzenga, R. (2010) Understanding amyloid aggregation by statistical analysis of atomic force microscopy images. *Nature Nanotechnology* **5**, 423-428
127. Connelly, L., Jang, H., Arce, F. T., Capone, R., Kotler, S. A., Ramachandran, S., Kagan, B. L., Nussinov, R., and Lal, R. (2012) Atomic force microscopy and MD simulations reveal pore-like structures of all-D-enantiomer of Alzheimer's β-amyloid peptide: relevance to the ion channel mechanism of AD pathology. *The Journal of Physical Chemistry B* **116**, 1728-1735
128. Nirmalraj, P. N., List, J., Battacharya, S., Howe, G., Xu, L., Thompson, D., and Mayer, M. (2020) Complete aggregation pathway of amyloid β (1-40) and (1-42) resolved on an atomically clean interface. *Science Advances* **6**, eaaz6014
129. Hong, D. P., Han, S., Fink, A. L., and Uversky, V. N. (2011) Characterization of the non-fibrillar α-synuclein oligomers. *Protein & Peptide Letters* **18**, 230-240
130. Mastrangelo, I. A., Ahmed, M., Sato, T., Liu, W., Wang, C., Hough, P., and Smith, S. O. (2006) High-resolution atomic force microscopy of soluble Abeta42 oligomers. *Journal of Molecular Biology* **358**, 106-119
131. Sweers, K. K. M., van der Werf, K. O., Bennink, M. L., and Subramaniam, V. (2012) Atomic Force Microscopy under Controlled Conditions Reveals Structure of C-Terminal Region of α-Synuclein in Amyloid Fibrils. *ACS Nano* **6**, 5952-5960
132. Hane, F. T., Lee, B. Y., Petoyan, A., Rauk, A., and Leonenko, Z. (2014) Testing synthetic amyloid-β aggregation inhibitor using single molecule atomic force spectroscopy. *Biosensors and Bioelectronics* **54**, 492-498

133. Hane, F., Drolle, E., Gaikwad, R., Faught, E., and Leonenko, Z. (2011) Amyloid-β aggregation on model lipid membranes: an atomic force microscopy study. *Journal of Alzheimer's Disease* **26**, 485-494
134. Rief, M., Oesterhelt, F., Heymann, B., and Gaub, H. E. (1997) Single Molecule Force Spectroscopy on Polysaccharides by Atomic Force Microscopy. *Science* **275**, 1295-1297
135. Li, H., Zhang, W., Zhang, X., Shen, J., Liu, B., Gao, C., and Zou, G. (1998) Single molecule force spectroscopy on poly(vinyl alcohol) by atomic force microscopy. *Macromolecular Rapid Communications* **19**, 609-611
136. Hugel, T., Grosholz, M., Clausen-Schaumann, H., Pfau, A., Gaub, H., and Seitz, M. (2001) Elasticity of Single Polyelectrolyte Chains and Their Desorption from Solid Supports Studied by AFM Based Single Molecule Force Spectroscopy. *Macromolecules* **34**, 1039-1047
137. Yu, H., Dee, D. R., and Woodside, M. T. (2013) Single-molecule approaches to prion protein misfolding. *Prion* **7**, 140-146
138. Kim, B. H., Palermo, N. Y., Lovas, S., Zaikova, T., Keana, J. F., and Lyubchenko, Y. L. (2011) Single-molecule atomic force microscopy force spectroscopy study of Aβ-40 interactions. *Biochemistry* **50**, 5154-5162
139. Trexler, A. J., and Rhoades, E. (2010) Single molecule characterization of α-synuclein in aggregation-prone states. *Biophysical Journal* **99**, 3048-3055
140. Yu, J., Malkova, S., and Lyubchenko, Y. L. (2008) alpha-Synuclein misfolding: single molecule AFM force spectroscopy study. *Journal of Molecular Biology* **384**, 992-1001
141. Maity, S., and Lyubchenko, Y. L. (2020) AFM Probing of Amyloid-Beta 42 Dimers and Trimers. *Frontiers in Molecular Biosciences* **7**, 69
142. Krasnoslobodtsev, A. V., Volkov, I. L., Asiago, J. M., Hindupur, J., Rochet, J. C., and Lyubchenko, Y. L. (2013) α-Synuclein misfolding assessed with single molecule AFM force spectroscopy: effect of pathogenic mutations. *Biochemistry* **52**, 7377-7386
143. Kransnoslobodtsev, A. V., Shlyakhtenko, L. S., Ukraintsev, E., Zaikova, T. O., Keana, J. F., and Lyubchenko, Y. L. (2005) Nanomedicine and protein misfolding diseases. *Nanomedicine* **1**, 300-305
144. Yu, J., and Lyubchenko, Y. L. (2009) Early stages for Parkinson's development: alpha-synuclein misfolding and aggregation. *Journal of Neuroimmune Pharmacology* **4**, 10-16
145. Kim, B. H., and Lyubchenko, Y. L. (2014) Nanoprobing of misfolding and interactions of amyloid β 42 protein. *Nanomedicine* **10**, 871-878
146. McAllister, C., Karymov, M. A., Kawano, Y., Lushnikov, A. Y., Mikheikin, A., Uversky, V. N., and Lyubchenko, Y. L. (2005) Protein interactions and misfolding analyzed by AFM force spectroscopy. *Journal of Molecular Biology* **354**, 1028-1042
147. Maity, S., and Lyubchenko, Y. L. (2016) Probing of Amyloid Aβ (14-23) Trimers by Single-Molecule Force Spectroscopy. *Jacobs Journal of Molecular and Translational Medicine* **1**
148. Yu, J., Warnke, J., and Lyubchenko, Y. L. (2011) Nanoprobing of α-synuclein misfolding and aggregation with atomic force microscopy. *Nanomedicine* **7**, 146-152
149. Pasternak, S. H., Callahan, J. W., and Mahuran, D. J. (2004) The role of the endosomal/lysosomal system in amyloid-beta production and the pathophysiology of Alzheimer's disease: reexamining the spatial paradox from a lysosomal perspective. *Journal of Alzheimer's Disease* **6**, 53-65
150. Maity, S., Viazovkina, E., Gall, A., and Lyubchenko, Y. L. (2017) Single-molecule probing of amyloid nano-ensembles using the polymer nanoarray approach. *Physical Chemistry Chemical Physics* **19**, 16387-16394
151. Tong, Z., Mikheikin, A., Krasnoslobodtsev, A., Lv, Z., and Lyubchenko, Y. L. (2013) Novel polymer linkers for single molecule AFM force spectroscopy. *Methods* **60**, 161-168
152. Krasnoslobodtsev, A. V., Zhang, Y., Viazovkina, E., Gall, A., Bertagni, C., and Lyubchenko, Y. L. (2015) A flexible nanoarray approach for the assembly and probing of molecular complexes. *Biophysical Journal* **108**, 2333-2339
153. Maity, S., Viazovkina, E., Gall, A., and Lyubchenko, Y. (2016) A Metal-free Click Chemistry Approach for the Assembly and Probing of Biomolecules. *Journal of Nature and Science* **2**

154. Maity, S., Pramanik, A., and Lyubchenko, Y. L. (2018) Probing Intermolecular Interactions within the Amyloid β Trimer Using a Tethered Polymer Nanoarray. *Bioconjugate Chemistry* **29**, 2755-2762
155. Jagannathan, B., and Marqusee, S. (2013) Protein folding and unfolding under force. *Biopolymers* **99**, 860-869
156. Yu, H., Liu, X., Neupane, K., Gupta, A. N., Brigley, A. M., Solanki, A., Sosova, I., and Woodside, M. T. (2012) Direct observation of multiple misfolding pathways in a single prion protein molecule. *Proceedings of the National Academy of Sciences* **109**, 5283-5288
157. Neupane, K., Solanki, A., Sosova, I., Belov, M., and Woodside, M. T. (2014) Diverse metastable structures formed by small oligomers of α-synuclein probed by force spectroscopy. *PLoS One* **9**, e86495
158. Dong, J., Castro, C. E., Boyce, M. C., Lang, M. J., and Lindquist, S. (2010) Optical trapping with high forces reveals unexpected behaviors of prion fibrils. *Nature Structural & Molecular Biology* **17**, 1422-1430
159. Castro, C. E., Dong, J., Boyce, M. C., Lindquist, S., and Lang, M. J. (2011) Physical properties of polymorphic yeast prion amyloid fibers. *Biophysical Journal* **101**, 439-448
160. Goldmann, W. H. (2000) Binding of tropomyosin-troponin to actin increases filament bending stiffness. *Biochemical and Biophysical Research Communications* **276**, 1225-1228
161. Fränzl, M., Thalheim, T., Adler, J., Huster, D., Posseckardt, J., Mertig, M., and Cichos, F. (2019) Thermophoretic trap for single amyloid fibril and protein aggregation studies. *Nature Methods* **16**, 611-614
162. Strick, T. R., Allemand, J. F., Bensimon, D., Bensimon, A., and Croquette, V. (1996) The elasticity of a single supercoiled DNA molecule. *Science* **271**, 1835-1837
163. Gosse, C., and Croquette, V. (2002) Magnetic tweezers: micromanipulation and force measurement at the molecular level. *Biophysical Journal* **82**, 3314-3329
164. Sarkar, R., and Rybenkov, V. V. (2016) A Guide to Magnetic Tweezers and Their Applications. *Frontiers in Physics* **4**
165. Gurnev, P. A., Yap, T. L., Pfefferkorn, C. M., Rostovtseva, T. K., Berezhkovskii, A. M., Lee, J. C., Parsegian, V. A., and Bezrukov, S. M. (2014) Alpha-synuclein lipid-dependent membrane binding and translocation through the α-hemolysin channel. *Biophysical Journal* **106**, 556-565
166. Chen, Q., and Liu, Z. (2019) Fabrication and Applications of Solid-State Nanopores. *Sensors (Basel)* **19**
167. Madampage, C., Tavassoly, O., Christensen, C., Kumari, M., and Lee, J. S. (2012) Nanopore analysis: An emerging technique for studying the folding and misfolding of proteins. *Prion* **6**, 116-123
168. Houghtaling, J., List, J., and Mayer, M. (2018) Nanopore-Based, Rapid Characterization of Individual Amyloid Particles in Solution: Concepts, Challenges, and Prospects. *Small* **14**, e1802412
169. Zhao, Q., Jayawardhana, D. A., Wang, D., and Guan, X. (2009) Study of peptide transport through engineered protein channels. *The Journal of Physical Chemistry B* **113**, 3572-3578
170. Wang, H. Y., Ying, Y. L., Li, Y., Kraatz, H. B., and Long, Y. T. (2011) Nanopore analysis of β-amyloid peptide aggregation transition induced by small molecules. *Analytical Chemistry* **83**, 1746-1752
171. Hu, Y. X., Ying, Y. L., Gu, Z., Cao, C., Yan, B. Y., Wang, H. F., and Long, Y. T. (2016) Single molecule study of initial structural features on the amyloidosis process. *Chemical Communications* **52**, 5542-5545
172. Asandei, A., Schiopu, I., Iftemi, S., Mereuta, L., and Luchian, T. (2013) Investigation of Cu2+ binding to human and rat amyloid fragments Aβ (1-16) with a protein nanopore. *Langmuir* **29**, 15634-15642
173. Asandei, A., Iftemi, S., Mereuta, L., Schiopu, I., and Luchian, T. (2014) Probing of various physiologically relevant metals-amyloid-β peptide interactions with a lipid membrane-immobilized protein nanopore *The Journal of Membrane Biology* **247**, 523-530
174. Rostovtseva, T. K., Gurnev, P. A., Protchenko, O., Hoogerheide, D. P., Yap, T. L., Philpott, C. C., Lee, J. C., and Bezrukov, S. M. (2015) α-Synuclein Shows High Affinity Interaction with

Voltage-dependent Anion Channel, Suggesting Mechanisms of Mitochondrial Regulation and Toxicity in Parkinson Disease. *Journal of Biological Chemistry* **290**, 18467-18477

175. Haque, F., Li, J., Wu, H. C., Liang, X. J., and Guo, P. (2013) Solid-State and Biological Nanopore for Real-Time Sensing of Single Chemical and Sequencing of DNA. *Nano Today* **8**, 56-74
176. Talaga, D. S., and Li, J. (2009) Single-molecule protein unfolding in solid state nanopores. *Journal of the American Chemical Society* **131**, 9287-9297
177. Yusko, E. C., Johnson, J. M., Majd, S., Prangkio, P., Rollings, R. C., Li, J., Yang, J., and Mayer, M. (2011) Controlling protein translocation through nanopores with bio-inspired fluid walls. *Nature Nanotechnology* **6**, 253-260
178. Yusko, E. C., Prangkio, P., Sept, D., Rollings, R. C., Li, J., and Mayer, M. (2012) Single-particle characterization of Aβ oligomers in solution. *ACS Nano* **6**, 5909-5919
179. Martyushenko, N., Bell, N. A., Lamboll, R. D., and Keyser, U. F. (2015) Nanopore analysis of amyloid fibrils formed by lysozyme aggregation. *Analyst* **140**, 4882-4886
180. Yu, R. J., Lu, S. M., Xu, S. W., Li, Y. J., Xu, Q., Ying, Y. L., and Long, Y. T. (2019) Single molecule sensing of amyloid-β aggregation by confined glass nanopores. *Chemical Science* **10**, 10728-10732
181. Balme, S., Coulon, P. E., Lepoitevin, M., Charlot, B., Yandrapalli, N., Favard, C., Muriaux, D., Bechelany, M., and Janot, J. M. (2016) Influence of Adsorption on Proteins and Amyloid Detection by Silicon Nitride Nanopore. *Langmuir* **32**, 8916-8925
182. Yusko, E. C., Bruhn, B. R., Eggenberger, O. M., Houghtaling, J., Rollings, R. C., Walsh, N. C., Nandivada, S., Pindrus, M., Hall, A. R., Sept, D., Li, J., Kalonia, D. S., and Mayer, M. (2017) Real-time shape approximation and fingerprinting of single proteins using a nanopore. *Nature Nanotechnology* **12**, 360-367
183. Narayan, P., Orte, A., Clarke, R. W., Bolognesi, B., Hook, S., Ganzinger, K. A., Meehan, S., Wilson, M. R., Dobson, C. M., and Klenerman, D. (2011) The extracellular chaperone clusterin sequesters oligomeric forms of the amyloid-β(1-40) peptide. *Nature Structural & Molecular Biology* **19**, 79-83
184. Narayan, P., Meehan, S., Carver, J. A., Wilson, M. R., Dobson, C. M., and Klenerman, D. (2012) Amyloid-β oligomers are sequestered by both intracellular and extracellular chaperones. *Biochemistry* **51**, 9270-9276
185. Whiten, D. R., Cox, D., Horrocks, M. H., Taylor, C. G., De, S., Flagmeier, P., Tosatto, L., Kumita, J. R., Ecroyd, H., Dobson, C. M., Klenerman, D., and Wilson, M. R. (2018) Single-Molecule Characterization of the Interactions between Extracellular Chaperones and Toxic α-Synuclein Oligomers. *Cell Reports* **23**, 3492-3500
186. Ganzinger, K. A., Narayan, P., Qamar, S. S., Weimann, L., Ranasinghe, R. T., Aguzzi, A., Dobson, C. M., McColl, J., St George-Hyslop, P., and Klenerman, D. (2014) Single-molecule imaging reveals that small amyloid-β1-42 oligomers interact with the cellular prion protein (PrP(C)). *Chembiochem* **15**, 2515-2521
187. Ide, T., and Yanagida, T. (1999) An artificial lipid bilayer formed on an agarose-coated glass for simultaneous electrical and optical measurement of single ion channels. *Biochemical and Biophysical Research Communications* **265**, 595-599
188. Wagner, M. L., and Tamm, L. K. (2001) Reconstituted syntaxin1a/SNAP25 interacts with negatively charged lipids as measured by lateral diffusion in planar supported bilayers. *Biophysical Journal* **81**, 266-275
189. Goennenwein, S., Tanaka, M., Hu, B., Moroder, L., and Sackmann, E. (2003) Functional incorporation of integrins into solid supported membranes on ultrathin films of cellulose: impact on adhesion. *Biophysical Journal* **85**, 646-655
190. Tanaka, M., and Sackmann, E. (2005) Polymer-supported membranes as models of the cell surface. *Nature* **437**, 656-663
191. Bayley, H., Cronin, B., Heron, A., Holden, M. A., Hwang, W. L., Syeda, R., Thompson, J., and Wallace, M. (2008) Droplet interface bilayers. *Mol Biosyst* **4**, 1191-1208
192. Arispe, N., Pollard, H. B., and Rojas, E. (1993a) Giant multilevel cation channels formed by Alzheimer disease amyloid beta-protein A beta 1-40 in bilayer membranes. *Proceedings of the National Academy of Sciences* **90**, 10573-10577

193. Mirzabekov, T. A., Lin, M. C., and Kagan, B. L. (1996) Pore formation by the cytotoxic islet amyloid peptide amylin. *Journal of Biological Chemistry* **271**, 1988-1992
194. Hirakura, Y., and Kagan, B. L. (2001) Pore formation by beta-2-microglobulin: a mechanism for the pathogenesis of dialysis associated amyloidosis. *Amyloid* **8**, 94-100
195. Lin, M. C., Mirzabekov, T., and Kagan, B. L. (1997) Channel formation by a neurotoxic prion protein fragment. *Journal of Biological Chemistry* **272**, 44-47
196. Last, N. B., and Miranker, A. D. (2013) Common mechanism unites membrane poration by amyloid and antimicrobial peptides. *Proceedings of the National Academy of Sciences* **110**, 6382-6387
197. Galvagnion, C., Buell, A. K., Meisl, G., Michaels, T. C., Vendruscolo, M., Knowles, T. P., and Dobson, C. M. (2015) Lipid vesicles trigger α-synuclein aggregation by stimulating primary nucleation. *Nature Chemical Biology* **11**, 229-234
198. Matsuzaki, K. (2007) Physicochemical interactions of amyloid beta-peptide with lipid bilayers. *Biochimica et Biophysica Acta* **1768**, 1935-1942
199. Li, S., Micic, M., Orbulescu, J., Whyte, J. D., and Leblanc, R. M. (2012) Human islet amyloid polypeptide at the air-aqueous interface: a Langmuir monolayer approach. *Journal of the Royal Society Interface* **9**, 3118-3128
200. Chaari, A., Horchani, H., Frikha, F., Verger, R., Gargouri, Y., and Ladjimi, M. (2013) Surface behavior of α-Synuclein and its interaction with phospholipids using the Langmuir monolayer technique: a comparison between monomeric and fibrillar α-Synuclein. *International Journal of Biological Macromolecules* **58**, 190-198
201. Hellstrand, E., Grey, M., Ainalem, M. L., Ankner, J., Forsyth, V. T., Fragneto, G., Haertlein, M., Dauvergne, M. T., Nilsson, H., Brundin, P., Linse, S., Nylander, T., and Sparr, E. (2013) Adsorption of α-synuclein to supported lipid bilayers: positioning and role of electrostatics. *ACS Chemical Neuroscience* **4**, 1339-1351
202. Hebda, J. A., and Miranker, A. D. (2009) The interplay of catalysis and toxicity by amyloid intermediates on lipid bilayers: insights from type II diabetes. *Annual Review of Biophysics* **38**, 125-152
203. Li, X., Wan, M., Gao, L., and Fang, W. (2016) Mechanism of Inhibition of Human Islet Amyloid Polypeptide-Induced Membrane Damage by a Small Organic Fluorogen. *Scientific Reports* **6**, 21614
204. Korshavn, K. J., Satriano, C., Lin, Y., Zhang, R., Dulchavsky, M., Bhunia, A., Ivanova, M. I., Lee, Y. H., La Rosa, C., Lim, M. H., and Ramamoorthy, A. (2017) Reduced Lipid Bilayer Thickness Regulates the Aggregation and Cytotoxicity of Amyloid-β. *Journal of Biological Chemistry* **292**, 4638-4650
205. Molinuevo, J. L., Blennow, K., Dubois, B., Engelborghs, S., Lewczuk, P., Perret-Liaudet, A., Teunissen, C. E., and Parnetti, L. (2014) The clinical use of cerebrospinal fluid biomarker testing for Alzheimer's disease diagnosis: a consensus paper from the Alzheimer's Biomarkers Standardization Initiative. *Alzheimers Dement* **10**, 808-817
206. Trojanowski, J. Q., Vandeerstichele, H., Korecka, M., Clark, C. M., Aisen, P. S., Petersen, R. C., Blennow, K., Soares, H., Simon, A., Lewczuk, P., Dean, R., Siemers, E., Potter, W. Z., Weiner, M. W., Jack, C. R., Jr., Jagust, W., Toga, A. W., Lee, V. M., and Shaw, L. M. (2010) Update on the biomarker core of the Alzheimer's Disease Neuroimaging Initiative subjects. *Alzheimers Dement* **6**, 230-238
207. Mattsson, N., Andreasson, U., Persson, S., Carrillo, M. C., Collins, S., Chalbot, S., Cutler, N., Dufour-Rainfray, D., Fagan, A. M., Heegaard, N. H., Robin Hsiung, G. Y., Hyman, B., Iqbal, K., Kaeser, S. A., Lachno, D. R., Lleó, A., Lewczuk, P., Molinuevo, J. L., Parchi, P., Regeniter, A., Rissman, R. A., Rosenmann, H., Sancesario, G., Schröder, J., Shaw, L. M., Teunissen, C. E., Trojanowski, J. Q., Vanderstichele, H., Vandijck, M., Verbeek, M. M., Zetterberg, H., and Blennow, K. (2013) CSF biomarker variability in the Alzheimer's Association quality control program. *Alzheimers Dement* **9**, 251-261
208. Olsson, B., Lautner, R., Andreasson, U., Öhrfelt, A., Portelius, E., Bjerke, M., Hölttä, M., Rosén, C., Olsson, C., Strobel, G., Wu, E., Dakin, K., Petzold, M., Blennow, K., and Zetterberg, H. (2016) CSF and blood biomarkers for the diagnosis of Alzheimer's disease: a systematic review and meta-analysis. *The Lancet Neurology* **15**, 673-684

209. Blennow, K., and Hampel, H. (2003) CSF markers for incipient Alzheimer's disease. *The Lancet Neurology* **2**, 605-613
210. Savage, M. J., Kalinina, J., Wolfe, A., Tugusheva, K., Korn, R., Cash-Mason, T., Maxwell, J. W., Hatcher, N. G., Haugabook, S. J., Wu, G., Howell, B. J., Renger, J. J., Shughrue, P. J., and McCampbell, A. (2014) A Sensitive Aβ Oligomer Assay Discriminates Alzheimer's and Aged Control Cerebrospinal Fluid. *The Journal of Neuroscience* **34**, 2884-2897
211. Verwey, N. A., van der Flier, W. M., Blennow, K., Clark, C., Sokolow, S., De Deyn, P. P., Galasko, D., Hampel, H., Hartmann, T., Kapaki, E., Lannfelt, L., Mehta, P. D., Parnetti, L., Petzold, A., Pirttila, T., Saleh, L., Skinningsrud, A., Swieten, J. C., Verbeek, M. M., Wiltfang, J., Younkin, S., Scheltens, P., and Blankenstein, M. A. (2009) A worldwide multicentre comparison of assays for cerebrospinal fluid biomarkers in Alzheimer's disease. *Annals of Clinical Biochemistry* **46**, 235-240
212. De, S., Whiten, D. R., Ruggeri, F. S., Hughes, C., Rodrigues, M., Sideris, D. I., Taylor, C. G., Aprile, F. A., Muyldermans, S., Knowles, T. P. J., Vendruscolo, M., Bryant, C., Blennow, K., Skoog, I., Kern, S., Zetterberg, H., and Klenerman, D. (2019) Soluble aggregates present in cerebrospinal fluid change in size and mechanism of toxicity during Alzheimer's disease progression. *Acta Neuropathologica Communications* **7**, 120
213. Noguchi-Shinohara, M., Tokuda, T., Yoshita, M., Kasai, T., Ono, K., Nakagawa, M., El-Agnaf, O. M. A., and Yamada, M. (2009) CSF alpha-synuclein levels in dementia with Lewy bodies and Alzheimer's disease. *Brain Res* **1251**, 1-6
214. Spies, P. E., Melis, R. J., Sjögren, M. J., Rikkert, M. G., and Verbeek, M. M. (2009) Cerebrospinal fluid alpha-synuclein does not discriminate between dementia disorders. *Journal of Alzheimer's Disease* **16**, 363-369
215. Santos, A. N., Torkler, S., Nowak, D., Schlittig, C., Goerdes, M., Lauber, T., Trischmann, L., Schaupp, M., Penz, M., Tiller, F.-W., and Böhm, G. (2007) Detection of Amyloid-β Oligomers in Human Cerebrospinal Fluid by Flow Cytometry and Fluorescence Resonance Energy Transfer. *Journal of Alzheimer's Disease* **11**, 117-125
216. Zetterberg, H., and Burnham, S. C. (2019) Blood-based molecular biomarkers for Alzheimer's disease. *Molecular Brain* **12**, 26
217. Fukumoto, H., Tennis, M., Locascio, J. J., Hyman, B. T., Growdon, J. H., and Irizarry, M. C. (2003) Age but not diagnosis is the main predictor of plasma amyloid beta-protein levels. *Archives of Neurology* **60**, 958-964
218. Janelidze, S., Stomrud, E., Palmqvist, S., Zetterberg, H., van Westen, D., Jeromin, A., Song, L., Hanlon, D., Tan Hehir, C. A., Baker, D., Blennow, K., and Hansson, O. (2016) Plasma β-amyloid in Alzheimer's disease and vascular disease. *Scientific Reports* **6**, 26801
219. Hampel, H., O'Bryant, S. E., Molinuevo, J. L., Zetterberg, H., Masters, C. L., Lista, S., Kiddle, S. J., Batrla, R., and Blennow, K. (2018) Blood-based biomarkers for Alzheimer disease: mapping the road to the clinic. *Nat Rev Neurol* **14**, 639-652
220. Tiiman, A., Jelić, V., Jarvet, J., Järemo, P., Bogdanović, N., Rigler, R., Terenius, L., Gräslund, A., and Vukojević, V. (2019) Amyloidogenic Nanoplaques in Blood Serum of Patients with Alzheimer's Disease Revealed by Time-Resolved Thioflavin T Fluorescence Intensity Fluctuation Analysis. *J Alzheimers Dis* **68**, 571-582
221. Fandos, N., Pérez-Grijalba, V., Pesini, P., Olmos, S., Bossa, M., Villemagne, V. L., Doecke, J., Fowler, C., Masters, C. L., Sarasa, M., and Group, A. R. (2017) Plasma amyloid β 42/40 ratios as biomarkers for amyloid β cerebral deposition in cognitively normal individuals. *Alzheimers Dement (Amst)* **8**, 179-187
222. Shi, M., Zabetian, C. P., Hancock, A. M., Ginghina, C., Hong, Z., Yearout, D., Chung, K. A., Quinn, J. F., Peskind, E. R., Galasko, D., Jankovic, J., Leverenz, J. B., and Zhang, J. (2010) Significance and confounders of peripheral DJ-1 and alpha-synuclein in Parkinson's disease. *Neuroscience Letters* **480**, 78-82
223. Maass, F., Rikker, S., Dambeck, V., Warth, C., Tatenhorst, L., Csoti, I., Schmitz, M., Zerr, I., Leha, A., Bähr, M., and Lingor, P. (2020) Increased alpha-synuclein tear fluid levels in patients with Parkinson's disease. *Scientific Reports* **10**, 8507

224. Devic, I., Hwang, H., Edgar, J. S., Izutsu, K., Presland, R., Pan, C., Goodlett, D. R., Wang, Y., Armaly, J., Tumas, V., Zabetian, C. P., Leverenz, J. B., Shi, M., and Zhang, J. (2011) Salivary α-synuclein and DJ-1: potential biomarkers for Parkinson's disease. *Brain* **134**, e178-e178
225. Knight, J. D., Hebda, J. A., and Miranker, A. D. (2006) Conserved and Cooperative Assembly of Membrane-Bound α-Helical States of Islet Amyloid Polypeptide. *Biochemistry* **45**, 9496-9508

Chapter 3

Cryo-electron microscopy imaging of Alzheimer's amyloid-beta 42 oligomer displayed on a functionally and structurally relevant scaffold

Jinming Wu[1], Thorsten B. Blum[1], Daniel P Farrell[2,3], Frank DiMaio[2,3], Jan Pieter Abrahams[1,4], Jinghui Luo[1,*]

1. Department of Biology and Chemistry, Paul Scherrer Institute, 5232 Villigen, Switzerland
2. Department of Biochemistry, University of Washington, WA 98195 Seattle, US
3. Institute for Protein Design, University of Washington, WA 98195 Seattle, US
4. Biozentrum, Universityof Basel, 4058, Basel, Switzerland

*Corresponding author: Jinghui.luo@psi.ch

Accept by ***Angewandte Chemie International Edition.***

DOI: https://doi.org/10.1002/anie.202104497

3.1 Abstract

Amyloid-β peptide (Aβ) oligomers are pathogenic species of amyloid aggregates in Alzheimer's disease. Like certain protein toxins, Aβ oligomers permeabilize cellular membranes, presumably through a pore formation mechanism. Owing to their structural and stoichiometric heterogeneity, the structure of these pores remains to be characterized. We studied a functional Aβ42-pore equivalent, created by fusing Aβ42 to the oligomerizing, soluble domain of the α-hemolysin (αHL) toxin. Our data reveal Aβ42-αHL oligomers to share major structural, functional, and biological properties with wild-type Aβ42-pores. Single-particle cryo-EM analysis of Aβ42-αHL oligomers (with an overall 3.3 Å resolution) reveals the Aβ42-pore region to be intrinsically flexible. The Aβ42-αHL oligomers will allow many of the features of the wild-type amyloid oligomers to be studied that cannot be otherwise, and maybe a highly specific antigen for the development of immuno-base diagnostics and therapies.

Keywords: Aβ42 oligomer; electron microscopy; protein structures; α-hemolysin

3.2 Introduction

Alzheimer's disease (AD) is characterized by Aβ plaques and tau neurofibrillary tangles (NFTs) deposited in the brains of the patients and stepwise dementia (1). Aβ is a peptide, cleaved from intramembrane proteolytic processing of amyloid precursor protein (APP) by β-/γ-secretase (2). The Aβ peptides aggregate into soluble oligomers, protofibrils, and eventually deposit as insoluble fibrils. Among these aggregates, Aβ oligomers are the most toxic species, responsible for neuronal dysfunction. Like certain protein neuro- and hemolytic toxins, Aβ oligomers are presumed to elicit pore formation in cellular membranes, which may cause local depolarization or other cellular dysfunctions. It has been observed by electron microscopy that the Aβ40 mutant (E22G) forms pore-like structure (3), and that Aβ oligomers display ion-channel activity in lipid membranes with a range of conductances (4-6). The oligomeric Aβ channel activity has been also confirmed in *Xenopus laevis* oocytes by single-channel Ca^{2+} imaging (7). Nuclear magnetic resonance (NMR) and single-channel electrical recordings further revealed that micelle-stabilized Aβ42 oligomers insert as β-barrel pores into lipid membranes with different conductances (8-10). In addition, Aβ oligomers may permeabilize membranes with non-specific pore formation (11-13). These observations indicate the importance of a lipidic environment for the characterization, stabilization and toxicity of Aβ oligomers. Also, the channel conductance discrepancy among the different studies may be caused by their transient nature, structural and stoichiometric heterogeneity (14). So far, stoichiometry-defined and stable Aβ oligomers remain to be explored in a

lipidic environment, as these are potentially valuable for determining the structure and developing conformation-specific antibodies.

In order to stabilize and display Aβ42 oligomers in a membrane environment for structure determination, we designed a α-hemolysin (αHL) scaffold. Secreted by *S.aureus*, αHL can assemble into a lipid-soluble, heptameric toxin, with a transmembrane β-barrel and an outer membrane domain (15). The transmembrane β-barrel structure of the αHL oligomer is reminiscent of the proposed β-barrel-type structure of Aβ42 oligomers in detergent micelles (9). We speculated that the soluble, heptamer-inducing domain of αHL structurally might induce the Aβ42 peptides to adopt a well-defined oligomeric state with enhanced size and symmetry, thus providing a good model system for determining its functional properties and structure by biophysical methods, including single-particle cryo-EM imaging. This idea was inspired by reports that wild-type (WT) αHL shares structural and functional homology with Aβ42 oligomers (16). We hypothesized that WT αHL and WT Aβ oligomers might share similar mechanisms of membrane permeabilization, and that both the β-hairpins in the β-barrel of αHL and Aβ oligomers interact with lipid membranes in a similar manner. To investigate whether αHL might offer a functionally relevant scaffold for oligomerizing and displaying Aβ42 oligomers for structure determination, we replaced the transmembrane beta hairpin of αHL with an Aβ42 sequence (Figure 1). Here, we show that the Aβ sequence is required for oligomerization. A hemolytic assay, single-channel recording, western blot and cell viability assays confirmed that the displayed oligomers are functional and toxicity relevant to the wild type, allowing us to determine the structure of the oligomer by single-particle cryo-EM.

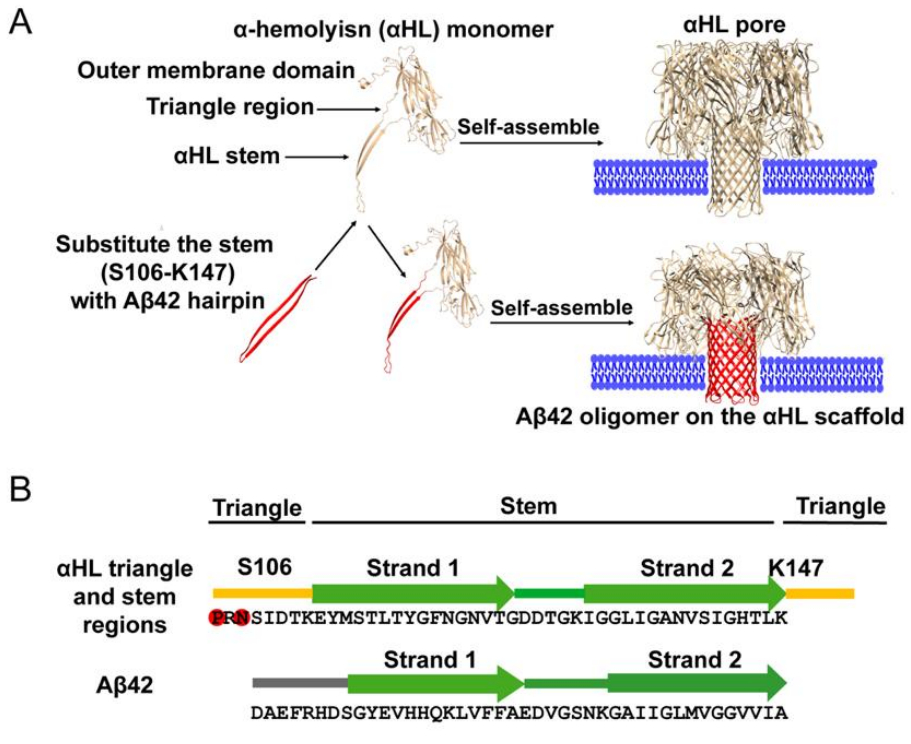

Figure 1. (A) The Aβ42 sequence (red) fused to the soluble domain of α-hemolysin (αHL; yellow) forms a heptameric pore complex that can insert into lipid membranes (blue). (B) Sequence comparison of the triangle and stem regions from WT αHL and Aβ42. The sequences were aligned based on the secondary structure elements from the αHL crystal structure (PDB: 7AHL) and the Aβ hairpin NMR structure (PDB: 2OTK and 2BEG). The stem hairpin is surrounded by two triangle sequences (in yellow) from αHL including the Y102-K110 and Y148-D152 residues (15), that include two residues (P103 and N105; in red) that are important for the assembly of the hairpins (17). The stem is composed of two antiparallel β strands (strand 1, E101-K126 residues and strand 2, I132-K147). In the complex of affibody and Aβ40 (18) or Aβ42 fibril (19), Aβ residues K16-A42 form a β-hairpin, while the structure of the other parts remain to be determined.

3.3 Results

3.3.1 Design rationale

The transmembrane β-barrel of heptameric αHL consists of seven β-hairpins, formed by residues Y110-K147 (15). Like monomeric Aβ42, the region of residues Y110-K147 is flexible in the monomeric state. But it forms a stable hairpin structure in the oligomeric state (20). The oligomerization of αHL may be influenced by the triangle region (residues Y102-K110 and Y148-D152 shown in Figure 1B). For instance, the mutations P103C and N105C can compromise the assembly of αHL (17). The stem residues Y110-K147 are similar to the hairpin structure of Aβ in the presence of affibody or in fibrils, as determined by NMR (18,19), whilst the structure of the N-terminus of Aβ42 remains unclear. To display and oligomerize Aβ42 on the scaffold, we kept residues P103 and N105 in the triangle region and substituted the residues starting from S106, with the Aβ42 residues.

3.3.2 Amyloid oligomerization relevance

In a membrane environment, the β-hairpin sequence (D106-K147) of monomeric WT αHL oligomerizes into heptameric pores. In our study, we substituted the β-hairpin sequence of αHL with an amyloid sequence, Aβ42, Aβ11-42, Aβ1-28, Aβ1-17, Aβ0, or hIAPP (human islet amyloid polypeptide that is associated with type 2 diabetes (21)) (Figure S1). We purified these His-tagged αHL constructs in the presence of 0.38 mM DDM micelles using Co-NTA chromatography and verified them by LC-MS (Figure S2). The Aβ42-αHL, Aβ11-42-αHL, hIAPP-αHL or WT αHL proteins form heptamers but the other constructs migrate as monomers on SDS-PAGE (Figure 2A). Displayed on the same αHL scaffold, the Aβ42 and hIAPP complexes sequences differ in their electrophoretic mobility, where the hlAPP-αHL hybrid complex appears to have a lower molecular weight, presumably forming a water-filled trimeric *β*-sandwich confirmed by molecular dynamics simulation (22). Co-NTA chromatography imidazole

gradient fractionation eluted oligomers and monomers separately from the column (Figure S3). The hybrid Aβ1-28 and Aβ1-17 sequences do not oligomerize even at the highest concentration of imidazole (250 mM). This is consistent with the observation that Aβ1-17 or Aβ1-28 alone cannot form oligomers in lipid membranes (23). The oligomerization requires the presence of Aβ sequences, since upon Aβ42 deletion, (Aβ0, Figure 2A, line 7), the αHL scaffold remains monomeric. We investigated the surface hydrophobic reorganization of these oligomers by 8-anilino-1-naphthalenesulfonic acid (ANS) fluorescence spectroscopy (24). At the same concentration, αHL, Aβ42-αHL, Aβ11-42-αHL and hIAPP-αHL all form oligomers with more hydrophobic surfaces for ANS binding (Figure 2B). These results indicate that the amyloid sequence drives oligomerization whilst the αHL scaffold determines the stoichiometry.

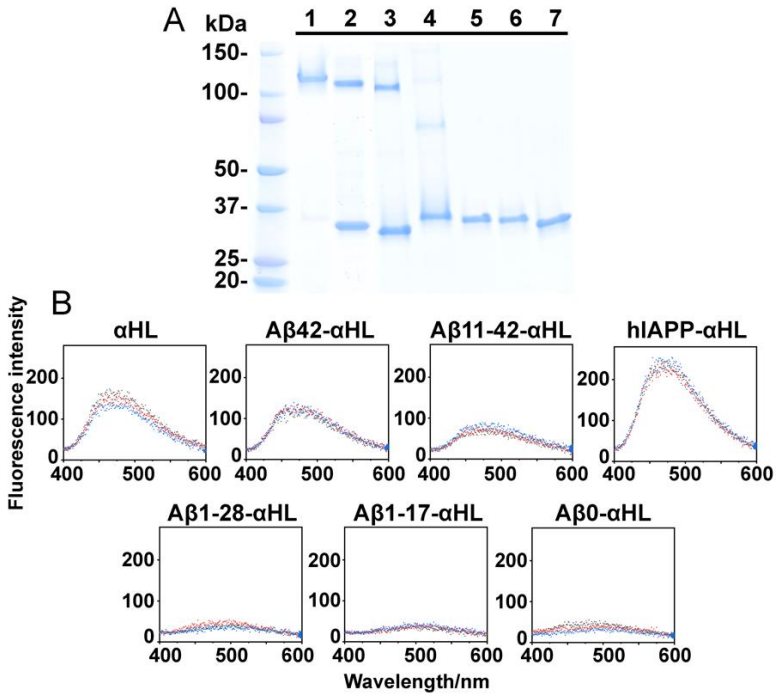

Figure 2. (A) Purification of WT αHL and hybrid amyloid-αHL oligomers with a Co-NTA column in 50 mM Tris-HCl, pH 8.0, 0.5 M NaCl, 250 mM imidazole and 0.38 mM DDM micelles. Lane 1: WT αHL; lane 2-3: hybrid Aβ42-αHL and Aβ11-42-αHL; lane 4: hybrid hIAPP-αHL; Lane 5-7: hybrid Aβ1-28-αHL, Aβ1-17-αHL and Aβ0-αHL respectively. SDS-PAGE electrophoresis was conducted at 200 V for 25 min. (B) Fluorescence emission spectra of 20 μM ANS binding to 10 μM WT αHL and hybrid amyloid-αHL oligomers at excitation wavelength 350 nm. The fluorescence was recorded at wavelengths from 400-600 nm at room temperature in 50 mM Tris-HCl, pH 8.0, 0.5 M NaCl, 250 mM imidazole and 0.38 mM DDM micelles. Each experiment was repeated three times independently.

3.3.3 Stability of Aβ-αHL oligomers

The oligomers of WT αHL remain stable after proteinase K treatment (Figure 3A, lane 3), while αHL monomers begin to degrade (Figure S4), as reported previously (25). This indicates that the assembly state of αHL determines the proteolysis-resistance. However, both the monomeric and heptameric Aβ42 on the αHL scaffold are resistant to proteolysis (Figure 3A, lane 7&8). This is in agreement with previous studies showing that WT Aβ42 monomers and oligomers are resistant to proteolysis (26-28). Apparently, Aβ42 can retain this property on the αHL scaffold. However, hybrid Aβ11-42-αHL and hIAPP-αHL monomers and oligomers can be proteolyzed (Figure S4), suggesting that the Aβ11-42 and hIAPP oligomers are less stable than the Aβ42 oligomers on the scaffold. Aβ1-28-αHL and Aβ1-17-αHL (Figure S5) monomers are also proteolyzed, revealing that the amyloid sequence dominates the stability and protease resistance of the displayed oligomers.

After heat denaturation of αHL (Figure 3A, lane 2&4), we observed more monomeric αHL, indicating dissociation of the oligomers. However, hybrid Aβ42-αHL (Figure 3A, lane 6&8) and Aβ11-42-αHL (Figure S4) are lost upon heat treatment, probably due to aggregation or precipitation. This indicates these constructs can assemble into aggregates larger than heptamers. It has been observed in several studies that, compared to neutrally charged lipids, negatively charged lipid bilayers have stronger interactions with amyloid peptides such as Aβ (29,30), α-synuclein (31-33) and Tau (34). In order to determine the effect of lipid charge on hybrid sequence oligomerization, we incubated these hybrid oligomers with a mixture of DOPC:DOPG (4:1). The Aβ42 sequence exhibits similar oligomerization properties in the presence of neutrally charged DPhPC liposomes (Figure S5), suggesting that the charge of the lipid membranes does not modulate Aβ42-αHL oligomerization. But we cannot exclude that the charge may influence the flexibility of local structure or fibrillation.

ThT fluorescence monitors amyloid formation (35). ThT fluorescence of WT Aβ42 in the presence of 0.38 mM DDM increases much more than that of Aβ42-αHL (Figure 3B), indicating that the Aβ42 fibril formation is inhibited on the αHL. TEM confirmed that hybrid Aβ42-αHL remains present as stable heptameric pores, even after incubation in the ThT assay (Figure 3D&3E). The small increase of the ThT fluorescence signal in the presence of hybrid Aβ42-αHL could have been caused by the formation of the observed oligomers or amorphous aggregates, and not by fibrils, which we did not observe in the TEM images (Figure 3E&S6H). As shown in Figure 3B, WT Aβ42 fibril formation can be observed at around 100 min in the presence of DDM micelles, and is delayed to 500 min without DDM (Figure S6A). Hybrid hIAPP-αHL also gives much less ThT fluorescence than WT hIAPP with or without DDM micelles (Figure S6D-S6F). ThT assays confirmed that WT αHL does not form fibrils (Figure S6C) and remains present as a stable pore, as indicated by TEM imaging (Figure S6G). The slightly different ThT results of WT αHL and the hybrid Aβ42-αHL may reflect a different binding of ThT to the β-barrel, which could

be indicative of the different barrel quaternary structures. The low fluorescence values in the presence of Aβ11-42-αHL, Aβ1-28-αHL, Aβ1-17-αHL or Aβ0-αHL (Figure S6B) reveal that the αHL scaffold does not interfere with the ThT fluorescence assay. These results confirm that the αHL scaffold confines the displayed Aβ42 oligomers and prevents their fibrillation into amyloid.

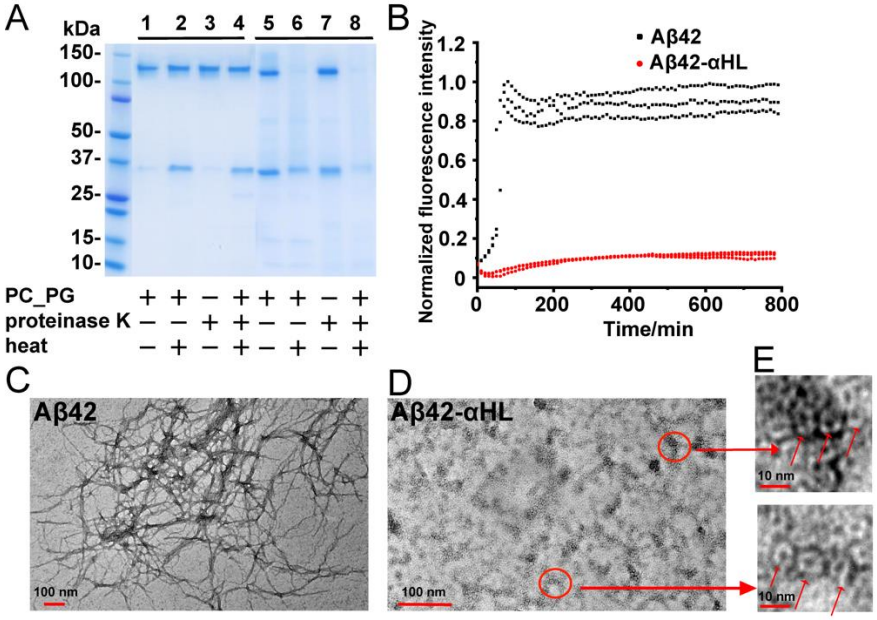

Figure 3. (A) Limited proteolysis with proteinase K of the WT αHL and hybrid Aβ42-αHL oligomers in the presence of DOPC:DOPG (4:1) liposomes (1 mg/mL). Lane 1: αHL treated with DOPC:DOPG liposomes; lane 2: αHL oligomers treated with DOPC:DOPG liposomes and then heat denatured at 95 °C for 15 min; lane 3: αHL oligomers digested with proteinase K; lane 4: αHL oligomers treated with DOPC:DOPG liposomes was further digested by proteinase K and then heat-denatured at 95 °C. Lane 5-8 had the same conditions as 1-4, but hybrid Aβ42-αHL oligomers were used. (B) ThT measurement of fibril formation of WT Aβ42 and hybrid Aβ42-αHL in 50 mM Tris-HCl, pH 8.0, 0.5 M NaCl, 250 mM imidazole and 0.38 mM DDM. The ratio of ThT and the peptides was 4:1 with a ThT final concentration 40 μM. The excitation and emission filters were 430 and 480 nm, respectively. (C-E) TEM images of WT Aβ42 fibrils and hybrid Aβ42-αHL proteins, after the fibrillation kinetics of these samples analyzed by the ThT-assay. Scale bars of Aβ42 fibrils and hybrid Aβ42-αHL oligomers are 100 nm. The zoom-in scale bar is 10 nm.

3.3.4 Pore formation by Aβ-αHL in lipid bilayers

The interaction of WT Aβ42/Aβ42-αHL/αHL oligomers with lipid bilayers was studied using single-channel electrical recordings. WT Aβ42 and Aβ42-αHL oligomers form channels with similar conductance (I/V), which varies from 0.2 to 0.5 nS (Figure 4). The variation and fluctuation of the current

is likely caused by the dynamics and heterogeneity of the oligomers, which was also reported by others (5,6). Aβ42-αHL oligomers apparently retain the characteristic of Aβ42-pores. This indicates that the amyloid sequence is not only required for the oligomerization of Aβ42-αHL sequence but also determines the channel flexibility of the oligomer in the lipid membranes. Both Aβ42-αHL and WT Aβ42 channels appear to be smaller and more dynamic than the WT αHL channel which has a conductance of 0.8 nS. The discrepancy between the WT αHL and Aβ42-αHL channels further confirmed that the transmembrane sequence plays a very important role in determining the size and flexibility of the channels that are formed in lipid membranes. The spread of measured current is higher in the case of pore formation by WT Aβ42 oligomers, compared to Aβ42-αHL oligomers (Figure 4). This could be caused by the non-uniform stoichiometry of the WT pores, compared to the heptameric Aβ42-αHL pores, leading to a predictable increased variability of pore diameters.

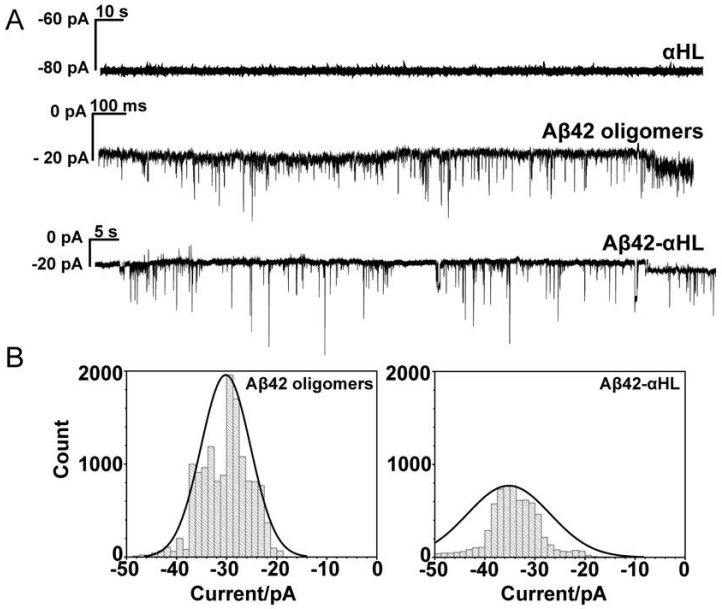

Figure 4. (A) Representative current traces of pore formation by WT αHL, Aβ42 oligomers, and hybrid Aβ42-αHL oligomers in the DOPC:DOPG (4:1) lipid bilayers. Currents were measured in 1 M KCl, 10 mM Hepes (pH 7.4) with the applied voltage -100 mV at room temperature. Aβ42 oligomers were measured in the presence of 0.38 mM DDM micelles. (B) Histograms of the counts generated by the current traces of Aβ42 oligomers and hybrid Aβ42-αHL oligomers. Solid curves were obtained by fitting a Gaussian.

3.3.5 Function and toxicity relevance of Aβ42-αHL oligomers

As the pores formed by WT αHL and Aβ42-αHL show clear differences, they may also differ in cell toxicity. A hemolytic assay (Figure 5A), showed that both Aβ42-αHL and WT Aβ42 oligomers are less hemolytic than WT αHL (which has a HC50 of 24 ng/ml, the concentration of protein giving 50% lysis

at 120 min, n=3). Truncated αHL also has very weak hemolytic activity (36), indicating that Aβ42-αHL and Aβ42 oligomers hardly penetrate erythrocyte membranes. Additionally, we found that WT Aβ42, Aβ42-αHL and Aβ11-42-αHL oligomers behave similarly in the neuronal toxicity assays (Figure 5C). This indicates that the αHL scaffold does not interfere to a major extent with the toxicity of WT Aβ oligomers. WT αHL is most toxic for the neuroblastoma cells, which is in line with the single-channel electrical recordings indicating that WT αHL has much higher conductance (around 0.8 nS) than WT Aβ42 (0.2-0.5 nS).

A conformation-specific amyloid oligomer antibody, A11, was used to confirm the structural similarity between the Aβ42-αH oligomers and WT Aβ42 oligomers (Figure 5B&S7). We observed that αHL (lane 1), Aβ42-αHL (lane 2), Aβ11-42-αHL (lane 3), hIAPP-αHL (lane 4) and WT Aβ42 oligomers (lane 5) can all bind the A11 antibody. Strikingly, the αHL oligomers show the clearest signal, suggesting that the β-barrel moiety of αHL-displayed Aβ oligomers adopts a wider range of conformations and remains more flexible than WT αHL's, which is also suggested by our single particle cryo-EM analysis. These cellular and functional assays suggest that Aβ42-αHL and Aβ42 oligomers share functional and toxicological properties, with a lower toxicity to neuronal and red blood cells compared to αHL.

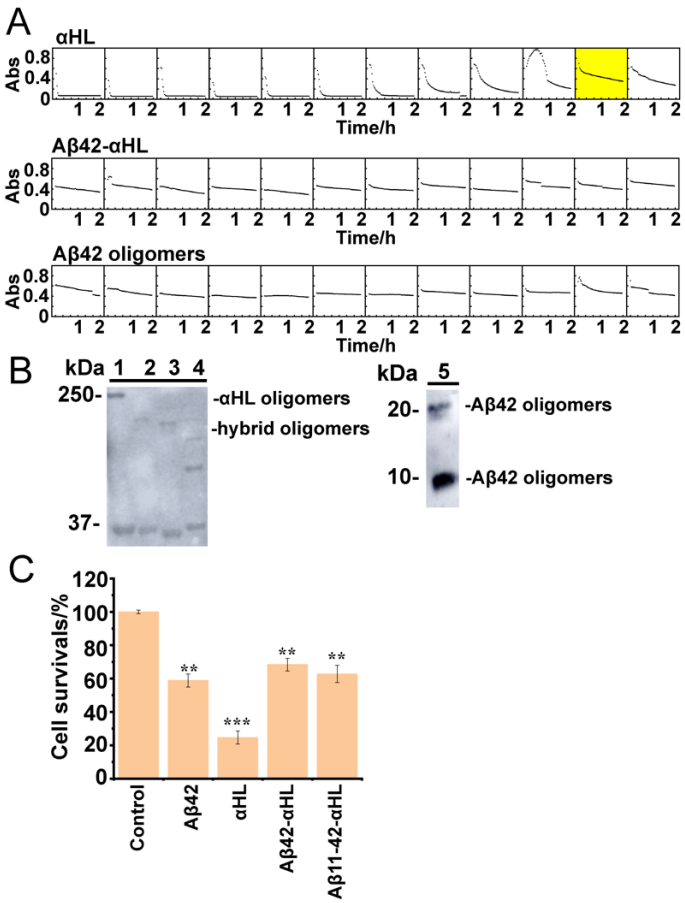

Figure 5. (A) Hemolysis by WT αHL oligomers, hybrid Aβ42-αHL or WT Aβ42 oligomers oligomers. The HC50 of WT αHL (50% cell lysis in 120 min at 37 ℃; yellow box) is 24 ng/mL, indicating specific hemolytic activity. The decrease of absorbance (Abs, y-axis, from 0-1) in light scattering over time (x-axis) was recorded in a microplate reader at 595 nm for 2 h at room temperature. (B) Immunogenic similarity of WT αHL, hybrid Aβ42/11-42-αHL and Aβ42 oligomers by western blot. The anti-Aβ42 oligomer conformation-dependent antibody A11 recognized αHL oligomers (lane 1); hybrid Aβ42-αHL oligomers (lane 2); hybrid Aβ11-42-αHL oligomers (lane 3); hybrid hIAPP-αHL oligomers (lane 4) and Aβ42 oligomers (lane 5). The SDS-PAGE electrophoresis prior to blotting, was conducted at 120 V for 80 min. (C) SH-SY5Y cell viability using a luminescence assay (error bars determined by triplicate experiments). 5 μM WT αHL, Aβ42 and hybrid Aβ42-αHL oligomers were treated with SH-SY5Y cells with 6000 cells/well density after incubating for 48 h at 37°C, 5% CO_2. The results are shown as percentages of control samples. All the Aβ42 oligomers were prepared in the presence of 0.38 mM DDM micelles. Data are represented as the mean S.E.M (standard error of the mean). Two-tailed student's t-test was applied for statistical significance. **P<0.01 (very significant) and ***P<0.001 (highly significant) were compared to the control.

3.3.6 Single-particle cryo-EM analysis

To determine the 3D structure of the Aβ42 oligomer as stabilized by the αHL scaffold, more than 4000 cryo-EM movies of Aβ42-αHL were collected under cryogenic conditions on a Titan Krios. Two representative regions with a high amount of Aβ42-αHL particles are shown in Figure S11. Some particle projection averages (Figure S12, not framed in the red box) are excluded due to noise or contamination. We found the cryo-EM sample to be very homogeneous and no other classes are identified of oligomers other than heptamers. Some 2D classes showing strong features for αHL heptameric core are shown in Figure 6A. 141'366 particles were averaged to a final overall resolution of 3.3 Å (Figure 6B&Table 1). The 3D map shows high-resolution density for the symmetrical core of the αHL scaffold (Figure 6C, EMD-12696). However, the density in the Aβ42 region is weaker and more diffuse, indicative of its flexible nature.

Absence of atomically resolved density for the Aβ42 region prompts us to investigate several possible pairings between adjacent Aβ42 β-hairpins within the membrane-crossing β-barrel. These quaternary structural pairings are compared on the basis of their energies, as calculated by the Rosetta software (Figure S8). On the basis of this analysis, we propose a pairing that also fits best into the density (Figure S8), and the atomic structure (PDB ID: 7O1Q) from the refinement (Table S2) is presented in Figure 6D&6E. A superposition of this most likely model with WT αHL electron density is shown in Figure S9. The apparent dome shape of hybrid Aβ42-αHL barrel is most likely an artifact of the cryo-EM

reconstruction of the flexible Aβ region caused by the application of C7 symmetry. The dynamic conformation of Aβ42 region may explain why Aβ42-αHL forms a fluctuating, transient pore, that we observed by the single-channel electrical recordings. The molecular reconstruction of the Aβ42 oligomer in the electron density map of the hybrid Aβ42-αHL, shows it is a bit shorter (Figure 6E, Figure S8&S9) than that of WT αHL (Figure 6F). The superposition of Aβ42-αHL and WT αHL oligomers shows slightly different β-hairpin topologies in the β-barrels (Figure S10). But the Rosetta energy of WT αHL's β-barrel is much lower than that of Aβ42-αHL in Figure S8. This implies that the β-barrel conformational change is closely associated with its energy, presumably modulating the interaction with lipid membranes. These structure and energy characteristics are in line with the observed functional and electrophysiological behavior of the Aβ42-αHL, compared to WT αHL.

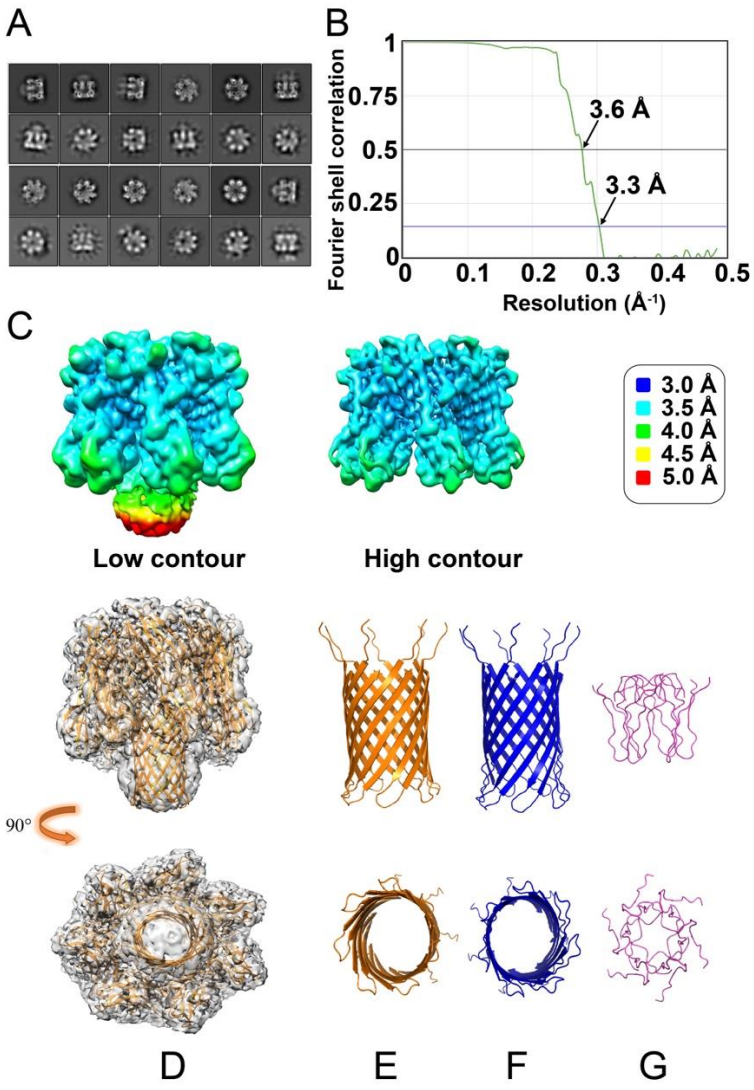

Figure 6. Cryo-EM data of Aβ42-αHL. (A) 2D classes show strong features for the αHL heptameric core, along with clear but more diffuse density for the structure formed by the Aβ42 sequences. (B) The 3D

average after the classification and refinement has an overall resolution of 3.3 Å at FSC=0.143 calculated by the gold-standard Fourier shell correlation (3.6 Å at FSC=0.5). (C) The local resolution density map of hybrid Aβ42-αHL (left) and the αHL scaffold at a higher contour (right). The resolution is color-coded according to the legend on the right. The lower local resolution of the Aβ42 pore region (Low contour, mainly the yellow and red colors), compared to the better local resolution of the αHL part (High contour, mainly the blue and cyan colors) indicates structural flexibility and/or heterogeneity for the pore region. (D) Side (upper image) and top (lower image) views of molecular representation of heptameric Aβ42-αHL in the electron density map (PDB ID: 7O1Q, EMD-12696). (E-G) The comparison of the structures from the side and top views. αHL-displayed Aβ42 pore (yellow, E); WT αHL transmembrane pore (blue, F) and hexameric Aβ42cc (residues 15–42, light purple, G) built by NMR restrained Rosetta simulation with the smallest pore diameter (37).

Table 1. Cryo-EM structure determination

Data collection	
Magnification	48'540x
Pixel size (Å)	1.03
Defocus Range (μm)	-0.9 to -3.0
Voltage (kV)	300
Exposure time (s per frame)	0.2
Number of frames	50
Total dose (e/Å2)	55
Reconstitution	
Box size (pixels)	200
Symmetry	C7
Micrographs	4'284
Automatically picked particles	2'438'446
Particles after 2D classification	204'103
Particles after 3D classification	141'366
Resolution after 3D auto-refine (Å)	3.5
Final overall resolution (Å)	3.3
Estimated map sharpening B-factor (Å2)	-124.06

3.4 Discussion and Conclusion

In the 'toxic Aβ oligomer' hypothesis (38), the Aβ peptides assemble into diverse β-barrel oligomers that breach the integrity of cellular membranes, thus compromising cell viability. The structural and functional characterization of transient and stoichiometric heterogeneous Aβ oligomers is challenging in lipid bilayers, though Aβ oligomers can be stabilized by protein engineering (39) and photo-induced cross-linking (40). By replacing the transmembrane β-hairpin of αHL by Aβ42, we are able to assemble Aβ42 into stable heptamers, structurally and functionally similar to the wild-type oligomers, yielding a single, unique oligomer species for single-particle cryo-EM analysis, biophysical characterization and functional studies.

Our data show that the Aβ sequence is required for oligomerizing the αHL scaffold. Deletion of parts of the Aβ-sequence abrogates oligomerization of the αHL moiety: neither the hybrid Aβ1-17 or 1-28-αHL proteins, nor the control Aβ0-αHL lacking all β-hairpin sequences oligomerizes in a lipid-mimicking environment. This observation is consistent with the principle that the C-terminus of Aβ modulates Aβ oligomerization (41,42). These data also confirm our hypothesis that its amyloid sequence retains its oligomerizing properties when displayed on the αHL scaffold. The resistance to proteolysis and fibrillation confirms the conformational stability of the Aβ42-αHL oligomers. Single-channel electrical recordings reveal that both Aβ42-αHL oligomers and WT Aβ42 oligomers exhibit typical open channel characteristics (approximately 0.2-0.5 nS conductance) with frequent spikes, in line with similar studies on Aβ42 oligomers (43). The 'spiky' behavior of the current is most likely caused by the dynamics of Aβ42 within the negatively charged membranes (44). Single-particle cryo-EM analysis confirms that the conformational flexibility that characterized Aβ42 oligomers is retained within the Aβ42-αHL oligomers too. These results suggest that Aβ42-αHL and the WT oligomers similarly interact with lipid bilayers.
Our cellular assays (Figure 5A&5C) and western blots (Figure 5B) further confirm the structurally similarities between Aβ42-αHL and WT Aβ42 oligomers. Both have negligible hemolytic activity towards rabbit erythrocytes, unlike WT αHL oligomers (hemolytic activity HC50=24 ng/mL), suggesting that the erythrocyte membrane is penetrated by Aβ42 oligomers to a much lesser extent. This is consistent with the weak or lost hemolytic activity of truncated αHL (36). WT αHL oligomers also have the highest toxicity to SH-SY5Y neuroblastoma cells, compared to Aβ42-αHL and WT Aβ42 oligomers, in line with our single-channel electrical recordings and hemolytic assays. These results indicate that the heptamers of WT αHL form larger inner-diameter channels than Aβ42-αHL. Olson *et al.* suggested the pre-stem of αHL converts its conformation, prior to the insertion of the β-strands into the membranes (45). It is highly plausible that Aβ42 oligomerizes on the displayed scaffold followed by the insertion into lipid bilayers. The β-barrel length of WT αHL or Aβ oligomers may play an important role in their toxicity.

The αHL scaffold can also accommodate other amyloid pore-forming sequences, as we demonstrate with the hIAPP-αHL hybrid. The outer-membrane αHL moiety not only increases the size of the pore-forming oligomers, which improves the resolution in cryo-EM imaging, but also prevents fibril formation. Our cryo-EM reconstruction shows the scaffold of αHL at a resolution at ~3 Å, but the resolution of the Aβ42 region is lower (4 to 5 Å). Our best structural model (shown in Figure 6D&6E and Figure S8) suggests that the Aβ42 β-barrel pore has a shorter length (35.5 Å) and a similar inner diameter (27.4 Å) of the largest circular cross-section, compared to the WT αHL barrel (47.8 Å high and 23.8 Å wide (15)). It is longer than a truncated hexameric β-barrel model of Aβ (residues 15–42) built by NMR restrained Rosetta simulation [26]. We compared all these structures in Figure 6E-6G. The observation of a shorter transmembrane length of Aβ42-αHL compared to WT αHL is consistent with our single-channel electrical recordings. We propose that the relatively short transmembrane pore length of the displayed Aβ oligomers affects its interaction with lipid bilayers, which may explain its reduced cell toxicity compared to pores with longer transmembrane domains, like WT αHL.

Stabilizing physiologically relevant, toxic Aβ oligomers allows structure determination and contributes to our understanding of amyloid toxicity in AD. The Nuttall lab determined non-toxic Aβ18-41 dimer/tetramer on an antigen receptor (46). That hybrid Aβ18-41 does not show a β–turn–β hairpin structure as observed in other studies (10,37). In addition, the Aβ18-41 oligomer that is buried in the scaffold, is more difficult to functionally compare with the WT Aβ, as it can't form a pore or be inserted into a lipid membrane. Sandberg *et al.* engineered a double-cysteine Aβ42 mutant to stabilize Aβ oligomers with β-sheet conformation (39). The stabilized Aβ42 oligomers in the absence of lipid membranes, mainly a mixture of dimers and trimers, are prone to form protofibrils.

The WT Aβ42 oligomers likely form heterogeneous structures in the presence of cellular membranes. Our alternative method enables generating functionally and structurally relevant oligomers, displayed as heptameric pores in membrane mimicking DDM micelles. Similar heterogenic pore forming Aβ oligomers were observed in the presence of DDM micelles (8). Österlund *et al.* concluded from native mass spectrometry that the β-barrel pore-forming hexamer might be the biggest Aβ oligomer in the presence of DDM micelles (9). However, hexameric oligomers would result in a significantly narrower pore than we observed for the Aβ42-αHL heptamers (Figure 6G), which would not be in line with the single pore conductance results we report here (Figure 4A). Possibly, the native mass spectroscopy is insensitive to higher molecular-weight oligomers that were reported in other studies (47,48), or DDM micelles preferentially incorporate hexameric oligomers. We point out potential disadvantages of our design: (1) the buried N-terminal or C-terminal Aβ peptides in the scaffold will be not available for

antibody targeting (49); (2) the moiety of αHL only allows Aβ to aggregate into one species of heptameric oligomer for structural and functional characterization, and no other oligomeric states.

In conclusion, we propose a novel protein scaffold for generating a single Aβ42 oligomer species for biochemical characterization and structure determination. We anticipate that the hybrid construct may contribute to improved understanding of the structure and dynamics of amyloid oligomers in lipid membranes, yielding novel insights into the molecular mechanism of oligomer toxicity. Our results also contribute to understanding of membrane protein oligomerization in lipid membranes, especially with regard to the β-sheet-containing proteins that appear to form polymorphic ion channels. The αHL-displayed oligomers, as a mimetic antigen, with a well-defined stoichiometry, may allow developing of novel, conformation-specific antibodies. This would allow alternative approaches for developing immuno-based diagnostics and potentially even therapies for AD and other neurodegenerative diseases.

3.5 Materials and methods

3.5.1 Plasmid preparation for the expression of wild type (WT) αHL oligomers, and αHL-displayed Aβ or hIAPP oligomers

The plasmid encoding Aβ42 sequence was obtained from Sara Linse's group in Lund and the pET20b (+) plasmid for WT αHL with D8H6 tag expression in *E.coli* was commercially constructed by TOP Gene Technologies, Inc. The synthetic genes for Aβ42 sequence and the moiety sequence of αHL with overhangs were produced by using Phusion® High-Fidelity DNA Polymerase with the primers as below. PCR was carried out for Aβ42 in the conditions: 30 s at 98°C, 30 cycles of 98°C for 10 s, 72 °C for 5 s. The similar conditions were used for αHL part, except 30 cycles of 98°C for 10 s, 60°C for 10 s, 72°C for 2 min 15 s, as well as a final elongation at 72°C for 5 min.

According to the manufacturing protocol, NEBuilder® HiFi DNA Assembly Master Mix was used to assemble the DNA fragments of αHL and Aβ42/hIAPP with overhangs, followed by the digestion of template DNA with DpnI enzyme. NEB 5-alpha Competent *E. coli* were transformed with 2 µl of the assembled products for over-night incubation at 37°C, yielding colonies on the plate with ampicillin and then for the sequence validation. The other Aβ fragments and αHL hybrid sequences with overhangs were generated by using Phusion® High-Fidelity DNA Polymerase with the following primers. Following the same procedure of Aβ42-αHL, we fully assembled single linear sequence by using NEBuilder® HiFi DNA Assembly Master Mix for the transformation and yielding colonies. The DNA sequence of hIAPP with overhangs was synthesised by Sigma. The synthetic genes were amplified following by the same procedure as the Aβ42.

WT αHL primers

5' TATGT TCAAC CTGAT TTCAA AACAA TTTTAGAGAGCCCA

3' ATTTCTTGGATAGTAATCAGATATTTGAGCTACTTCATTATCAG

Aβ42-αHL primers

5' TACTATCCAAGAAATGACGCTGAATTCCGTCACGACTCTG

3' ATCAGGTTGAACATAAGCGATCACAACGCCACCAACCATCA

hIAPP-αHL primers

5' ATTGATACAAAAAAATGCAACACTGCCACA

3' ATCAG GTTGA ACATAATATGTATTG

The DNA sequence of hIAPP with overhangs

(AAATTCGATTGATACAAAAAAATGCAACACTGCCACATGTGCAACGCAGCGCCTGGCAAA

TTTTTTAGTTCATTCCAGCAACAACTTTGGTGCCATTCTCTCATCTACCAACGTGGGATCCA

ATACATATTATGT TCAACCTGATTTCAAAACAA)

Aβ0-αHL

5' TCCAAGAAATTATGTTCAACCTGATTTCAAAACA

3' ATCAG GTTGA ACATA ATTTCTTGGATAGTAATCAGATATTTGAG

Aβ1-17-αHL

5' CCAGAAGCTGTATGTTCAACCTGATTTCAAAACAA

3' ATCAGGTTGAACATACAGCTTCTGGTGGTGAAC

Aβ1-28-αHL

3' TCAGGTTGAACATACTTGTTAGAACCCACGTCTTC

5' GTTCTAACAAGTATGTTCAACCTGATTTCAAAACAA

Aβ11-42-αHL

5' TCCAAGAAATGAAGTTCACCACCAGAAGC

3' CTGGTGGTGAACTTCATTTCTTGGATAGTAATCAGATATTTG

3.5.2 Protein expression and purification

The verified αHL plasmids were transformed into competent *E. coli* BL21(DE3) pLysS cells. The cells were incubated on an ampicillin plate (100 μg/mL) overnight at 37 ℃. Then a single colony was picked for incubation with LB medium (200 mL) at 37 ℃, 180 rpm until the OD600 reached around 0.6. The incubation temperature was set to 18 ℃ for the overnight expression induced by IPTG (final conc. 0.5 mM). The cell pellets were harvested and lysed in lysis buffer (50 mM Tris-HCl, pH 8.0, 0.5 M NaCl, 0.38 mM DDM, 10 mM imidazole) on ice with the addition of a final concentration of 5 mM $MgCl_2$, 1 mg/mL lysozyme and 100 units benzonase (Cat. Number: E1014). The lysis was sonicated three times for each 30 seconds, and centrifuged at 24000g for 1 h to remove cell debris. The immobilized metal-

affinity chromatography was used to purify αHL in a high-specificity affinity TALON (Cobalt) column. The supernatant was incubated with the resin for at least 1 h at 4 ℃. To increase the purity of heptameric αHL, Co-NTA chromatography imidazole gradient fractionation (20 mM, 50 mM and 250 mM) was used to elute αHL. SDS-gel (4-20% or 4-12%) electrophoresis was used to determine the elution of monomeric and heptameric αHL. Protein concentration was measured by the Nanodrop Spectrophotometer (ND-2000, Thermos Scientific) at the wavelength of 280 nm. Then the proteins were aliquoted on ice and frozen in liquid N_2 immediately for storage at -80 ℃. For the hybrid Aβ/hIAPP-αHL oligomers, the expression and purification methods were the same with wild type αHL. TCEP was added into the lysis buffer (final conc. 0.5 mM) and elution buffer (final conc. 1 mM) when purifying the hIAPP-αHL oligomer. The procedure was prepared according to the published paper (50).

3.5.3 LC-MS

The purified proteins including wild type αHL and hybrid Aβ/hIAPP-αHL were identified by LC-MS. ESI-TOF MS (LCT Premier Mass Spectrometer, Waters AG, Baden-Dättwil, Switzerland) was combined with the liquid chromatography (LC, Waters 2795). A gradient of ACN/water in the presence of 0.1% formic acid was prepared for the MassPREP Phenyl Guard Column (Waters n°186002785) or the C18 Aeris widepore column (Phenomenex). The obtained MS spectrums for multiply charged protein ions were deconvoluted by using MAxent1 software to obtain the protein mass.

3.5.4 ANS fluorescence assay

The oligomerization of hybrid Aβ/hIAPP-αHL in the solution of 50 mM Tris-HCl, pH 8, 0.5 M NaCl, 0.38 mM DDM, 250 mM imidazole was determined by ANS fluorescence assay on the Synergy™ 4 (BioTek) plate reader. 40 µL solution at the final concentration of 10 µM hybrid Aβ/hIAPP-αHL and 20 µM ANS was prepared on the unsealed OptiPlate™-384 well plate with the material of polystyrene (flat and non-transparent bottom, white, PerkinElmer company, catalogue No.: 6007290). ANS fluorescence was measured with excitation wavelength at 350 nm and emission wavelength at 490 nm. As a control, the buffer was added with 50 mM Tris-HCl, pH 8.0, 0.5 M NaCl, 0.38 mM DDM and 250 mM imidazole. Three independent experiments were conducted.

3.5.5 ThT fluorescence assay and transmission electron microscopy (TEM)

Aβ42 and hIAPP powders were purchased from the rPeptide company (catalogue ID: A-1163-1; Purity >97%) and the AnaSpec company (catalogue ID: AS-60804; Purity>95%) respectively. 1 mg Aβ42 or 1 mg hIAPP was dissolved in 1 mL 10 mM NaOH, followed by the sonication in an ice-water bath for 1 min, as previously described [51,52]. 50 mM Tris-HCl, pH 8.0, 0.5 M NaCl, 250 mM imidazole with or without 0.38 mM DDM was used to dilute the WT Aβ42 and hIAPP peptides. 50 mM Tris-HCl, pH 8.0,

0.5 M NaCl, 250 mM imidazole and 0.38 mM DDM was used to dilute WT αHL and hybrid Aβ/hIAPP-αHL sequences. 40 μL solution was added into a black 384-well, non-treated and flat-bottom microplate with the material of polystyrene (NUNC, Thermo Fisher Scientific, catalogue ID: 24276), which was then sealed with a piece of foil film (Greiner Bio-One GmbH, catalogue No.: 676090). The plate was incubated in a microplate reader (PHERAstar FSX, BMG LABTECH, Germany) at 37 °C without shaking. The final concentration of peptides (WT Aβ42, hIAPP, αHL and a series of hybrid Aβ/hIAPP-αHL sequences) and ThT was 10 μM and 40 μM respectively. The excitation and emission wavelengths for ThT assay were set up 430 nm and 480 nm respectively. Buffer with 50 mM Tris-HCl, pH 8.0, 0.5 M NaCl, 0.38 mM DDM and 250 mM imidazole was added as a control. Three independent experiments were conducted.

The end points of ThT assay of WT Aβ42, αHL and hybrid Aβ42-αHL were taken to prepare the TEM samples. Negative-staining method was used to prepare the samples. First, 6 μL each sample was dipped on a freshly glow-charged 400-mesh Formvar-carbon coated copper grid and absorbed for 2 min. The excess solution was then removed by a piece of filter paper, and the grids were washed by 20 μL ddH_2O for 30 s. Next, the grids were stained with 6 μL 2 % uranyl acetate for 60 s and washed by the 20 μL ddH_2O for 15 s twice. Images were taken with a TEM (JEOL 2010) at an voltage of 200 KV.

3.5.6 Limited proteolysis of wild type αHL and hybrid Aβ/hIAPP-αHL oligomers

20 mg/mL, 50 μL Dioleoylphosphatidylcholine (DOPC, Avanti polar lipids), dioleoylphosphatidyglycerol (DOPG, Avanti polar lipids) mixture at a ratio of 4:1 in pentane was dried by N_2 gas and then put in a desiccator overnight under high vacuum to totally get dried. 1 mL, 10 mM Tris-HCl buffer, pH 8.0 containing 1 mM EDTA was added to suspend the lipid film. To get unilamellar liposomes, the solution was extruded through two 0.1 μm polycarbonate membranes (Whatman™). 1,2-diphytanoyl phosphophatidycholine (DPhPC, Avanti polar lipids) liposomes were prepared using the same method.

10 μL, 1 mg/mL DOPC:DOPG liposomes were incubated with 50 μL, 0.2 mg/mL wild type αHL (50 mM Tris-HCl, pH 8, 0.5 M NaCl, 0.38 mM DDM, 20 mM imidazole) or hybrid Aβ/hIAPP-αHL with the same buffer for 2 h at room temperature. 0.1 mg/mL, 2 μL proteinase K (Sigma Aldrich) in water solution was added to 20 μL of incubating solution at room temperature. After 10 min, 1 μL, 40 mM phenylmethanesulfonyl fluoride (PMSF in ethanol, Thermo Scientific) was added to inactivate the proteinase K. Then the solution was heated for 15 min at 95 ℃ for denaturation. 15 μL solution was added into 5 μL sample loading buffer (5x) and was run the SDS-gel (4%-20%).

3.5.7 Hemolysis assays

MBSA buffer (150 mM NaCl and 10 mM MOPS, pH7.4, containing 0.1% BSA) was prepared to wash rabbit blood cells (rRBC) repeatedly on ice and then centrifuged at 1200 rpm for 2 min until the supernatant becomes clear. 1% rRBC solution was freshly prepared before the experiment. The recombinant wild type αHL and hybrid Aβ42-αHL oligomers in the solution of 50 mM Tris-HCl, pH 8.0, 0.5 M NaCl, 250 mM imidazole and 0.38 mM DDM were used for the hemolysis assay. 2 μL of 1.24 mg/mL wild type αHL or hybrid Aβ42-αHL oligomers were mixed with MBSA (98 μL) in the first well. Then 50 μL was transferred to the second well for the dilution with 50 μL MBSA buffer. Repeat this step to the 12th well. Then, each well had a volume of 50 μL and serially two-fold diluted. To keep the same concentration, 2 μL, 35 μM Aβ42 oligomer was added into the first well instead. Then, 50 μL fresh 1% rRBC was added into each well. The hemolytic activities of wild type αHL oligomers, hybrid Aβ42-αHL oligomers and wild type Aβ42 oligomers were determined in the non-treated, unsealed and flat-bottom 96-well plate (Greiner Bio-One^{TM}, catalogue No.: 655101) with the material of polystyrene on the Synergy™ 4 (BioTek) plate reader. The decrease of absorbance in light scattering at 595 nm was recorded for 2 h at room temperature. The concentration of 50 % lysis to show the specific hemolytic activity (HC50) was calculated. Three independent experiments were conducted.

3.5.8 Single-channel electrical recording

Single-channel electrical recordings were performed in an apparatus with two Delrin compartments at room temperature. The compartments consist of two sides, cis- (connected with ground electrode) and trans- (connected with voltage electrode) sides, separated by a 25 μm thick polytetrafluoroethylene (PTFE) film with a 100 μm aperture (Good Fellow Inc., #FP301200). After the painting of the film with 2 μl 2% (v/v) hexadecane in pentane, 10 μL of DOPC:DOPG mixture (4:1) dissolved in pentane at a concentration of 20 mg/mL was added into the cis and trans parts of the home-made chamber which was filled with 500 μL of 10 mM Hepes buffer, pH 7.4 with 1 mM EDTA and 1 M KCl. The black lipid membrane was formed by slowly pipetting the solution. 0.1 mg/mL wild type αHL or hybrid Aβ42-αHL oligomers were diluted 100 times in 50 mM Tris-HCl buffer, pH 8, 0.5 M NaCl, 250 mM imidazole and 0.38 mM DDM detergent. Then 5 μL diluted samples were added into the grounded cis compartment of the chamber for the recordings which were connected by Ag/AgCl electrodes and amplified by the patch-clamp amplifier (Axopatch 200B, Axon instrument). A lowpass-filter at 5 kHz and a sampling frequency at 10 kHz were applied for the data collection at room temperature by a Digidata 1440A digitizer (Axon instrument). Clampfit software was used for the data analysis.

3.5.9 Western blot

To obtain the oligomer-enriched Aβ42, 100 μM Aβ42 was incubated at 37 °C under quiescent conditions for 2 h (53). 15 μL of 1 mg/mL, wild type αHL or hybrid Aβ/hIAPP-αHL in 50 mM Tris-HCl buffer, pH 8, 0.5 M NaCl, 250 mM imidazole, 0.38 mM DDM were boiled for 5 min at 95 ℃. 5 μL, 4x sample loading buffer was mixed and 7 μL was loaded into the SDS-gel (Bio-Rad 4–20% Mini-PROTEAN® TGX™ Precast Protein Gels). The SDS-PAGE Electrophoresis was conducted at 120 V for 80 min. The whole page was then transferred using trans-blot turbo mini 0.2 μm PVDF transfer pack (Bio-Rad, #1704156) on the transfer apparatus. After blocking the membrane with 3% nonfat milk in TBST (10 mM Tris-HCl, pH 8.0, 150 mM NaCl, 0.5% Tween 20) for 1 h, the membrane was incubated with anti-oligomer A11 antibody (1:500) for 2 h. The membrane was washed 3 times for 10 min by TBST buffer. Then the membrane was incubated with a 1:1500 dilution of goat anti-rabbit HRP-conjugated secondary antibody for 1 h. Blots were washed with TBST three times and developed with the chemiluminescent reagent (LumiGLO, Chemiluminescent Substrate Kit).

3.5.10 Cell viability assay

Neuroblastoma SH-SY5Y cells were cultured in EMEM medium supplemented with 15 % (v/v) fetal bovine serum, 2 mM Glutamine (final concentration), and 1% (v/v) penicillin/streptomycin. Cells were kept at 37°C, 5 % CO_2 in a petri dish. The maximum passage number is 15 times. 50 μL resuspended cells with 6000 cells/well density were dispensed to a tissue culture treated, flat-bottom 96-well plate (Biofil^R, Item No.: 011096) with the material of polystyrene. The plated cells were incubated for 24 h at 37°C, 5 % CO_2. Aβ42 oligomers were prepared by dissolving the powder in PBS (53) or the buffer with DDM (50 mM Tris-HCl, pH 8.0, 0.5 M NaCl, 250 mM imidazole and 0.38 mM DDM) at a concentration of 1 mg/ml followed by the incubation at 37°C for 2 h. 2 μL of Aβ42 oligomers, wild type αHL, hybrid Aβ42-αHL or Aβ11-42-αHL oligomers at a final concentration of 5 μM was added to each well. PBS and buffer (50 mM Tris-HCl, pH 8.0, 0.5 M NaCl, 250 mM imidazole and 0.38 mM DDM) were used as the control. Afterwards, the wells were incubated with the serum-free medium for 48 h, and then the plate was equilibrated at room temperature for 30 min. A volume of CellTiter-Glo luminescent reagent (Promega, cat. G7571) was equally added to the cell culture medium present in each well. This assay has been applied to study the toxicity of Aβ aggregates on SH-SY5Y cells (54). To induce cell lysis, the plate was put on an orbital shaker for 2 min and incubated at room temperature for 10 min to stabilize the luminescent signal. The luminescent intensity was measured on the PHERAstar 96-well plate reader and performed three independent experiments. Data are represented as the mean S.E.M (standard error of the mean). Two-tailed student's t-test was applied for statistical significance. **P<0.01 (very significant) and ***P<0.01 (highly significant) were compared to the control.

3.5.11 Single-particle Cryo-EM

3 µl of the protein solution (4.83 mg/ml protein, 50 mM Tris-HCl, pH 8.0, 0.5 M NaCl, 250 mM imidazole and 0.38 mM DDM) was pipetted onto a glow-discharged UltrAuFoil grid (R 1.2/1.3, Au 300). Grids were blotted for 1 s with blot force 2 and plunge-frozen in liquid ethane using a Vitrobot Mark IV (ThermoFisher Scientific) with 100% humidity at 7 ˚C. Data were acquired on a Titan Krios electron microscope at 300 keV (Thermo Fisher), with a GIF Quantum LS Imaging filter (20 eV slit width), a K2 Summit electron counting direct detection camera (Gatan), using a magnification of 48'540x, resulting in a calibrated pixel size of 1.03Å. The defocus varied between –0.9 and –3.0 µm using SerialEM (55). For helical reconstruction, 4'284 movies were recorded with a total dose of 55 e^-/Å2 per movie (10 sec exposure in total, 0.2 sec per frame, 50 frames in total). The dose rate was ~5.5 e^-/Å2 per second (~1.1 e^-/$Å^2$ per frame). The Focus software (56) was used to drift-correct and dose-weight using MotionCor2 (57). The reconstruction was done with RELION 3.0 (58). We automatically picked 2'438'446 particles from 4'284 micrographs, using RELION 3.0. The particles were extracted using a box size of 200 pixels (~206Å, Table 1). Several rounds of 2D and 3D classification were executed to remove bad particles resulting in 141'366 particles. The particles were used for 3D auto-refine and the beam tilt values for the entire data set and the defocus for each segment was estimated. Afterwards another run of 3D auto-refine was executed followed by Post Process, using a soft-edge mask and an estimated map sharpening B-factor of −124.06 $Å^2$, was performed resulting in a map with a resolution of 3.6 Å and 3.3 Å (by the FSC 0.5 and 0.143 criterion; Figure 6B).

3.5.12 Structure modelling

Three initial models were built by using Modeller 9.24 (59). The first model was built using the standard protocols using only the αHL heptameric structure (PDB ID: 7AHL). In order to build the second and third models, the hairpin structure of Aβ42 hairpin NMR (PDB ID: 6RHY) was grafted onto the β-barrel region of 7AHL using two separate methods. In the first method, the symmetry of 7AHL was used in order to graft the structure of 6RHY based on the threading of αHL's β-barrel. For the second method, we performed grafting similar to the first method, but did so without the use of the threading information. The Aβ42-αHL protein chimera was modeled into the cryo-EM density with homology modeling using Rosetta (60). First, the chimeric sequence was aligned to the 7AHL sequence with hhalign (61) and the alignment was used to thread the chimeric sequence onto the previously described models. These threaded models were unambiguously docked into the cryo-EM density using UCSF chimera (62) and, using the 7AHL pdb as a reference for symmetry, these models were used as templates for symmetric refinement into the density using RosettaCM (63). 5,000 trajectories of RosettaCM were run (command line and input files described at 10.5281/zenodo.3967686) and the model with the lowest energy was the

final model. The same methodology was applied to the manual threading model except for substituting the manual alignment in the initial sequence threading step.

In order to generate the shortened beta barrel models, atom pair distance and angle constraints were applied to shift the hydrogen bonding backbone N and O atoms of the adjacent subunits by 2 residues. These models were coarsely minimized using a custom-made set of constraints and the rosetta scripts Rosetta application. The command lines and example constraint files are also described in further detail at: 10.5281/zenodo.3967686. Finally, these coarse models were refined into the cryo-EM density as templates to RosettaCM with the same methodology as described previously. The score of the 5 top scoring models from all 4 conformations are plotted in Figure S8.

3.6 Acknowledgments

We thank Alain Blanc (Paul Scherrer Institute) for the experiments of LC-MS, Urmi Sengupta and Rakez Kayed (University of Texas Medical Branch) for providing the A11 antibody. We thank Prof. Dr. Henning Stahlberg for the usage of the electron microscope, and Ricardo Adaixo for discussing. The calculations were performed at sciCORE (http://scicore.unibas.ch/) scientific computing core facility at University of Basel.

3.7 Author Contributions

Jinming Wu: Investigation, validation, project administration. Thorsten B. Blum: Investigation, validation. Daniel P Farrell and Frank DiMaio: Investigation, validation. Jan Pieter Abrahams: data analysis, validation. Jinghui Luo: Conceptualization, validation, the project administration and funding acquisition.

3.8 References

1. Ross, C. A., and Poirier, M. A. (2004) Protein aggregation and neurodegenerative disease. *Nat Med* **10 Suppl**, S10-17
2. Hardy, J., and Selkoe, D. J. (2002) The amyloid hypothesis of Alzheimer's disease: progress and problems on the road to therapeutics. *Science* **297**, 353-356
3. Lashuel, H. A., Hartley, D., Petre, B. M., Walz, T., and Lansbury, P. T. (2002) Amyloid pores from pathogenic mutations. *Nature* **418**, 291-291
4. Arispe, N., Pollard, H. B., and Rojas, E. (1993) Giant multilevel cation channels formed by Alzheimer disease amyloid beta-protein [A beta P-(1-40)] in bilayer membranes. *Proceedings of the National Academy of Sciences of the United States of America* **90**, 10573-10577
5. Quist, A., Doudevski, I., Lin, H., Azimova, R., Ng, D., Frangione, B., Kagan, B., Ghiso, J., and Lal, R. (2005) Amyloid ion channels: a common structural link for protein-misfolding disease. *Proceedings of the National Academy of Sciences* **102**, 10427-10432

6. Jang, H., Arce, F. T., Ramachandran, S., Capone, R., Azimova, R., Kagan, B. L., Nussinov, R., and Lal, R. (2010) Truncated beta-amyloid peptide channels provide an alternative mechanism for Alzheimer's Disease and Down syndrome. *Proc Natl Acad Sci U S A* **107**, 6538-6543
7. Demuro, A., Smith, M., and Parker, I. (2011) Single-channel Ca2+ imaging implicates Aβ1–42 amyloid pores in Alzheimer's disease pathology. *Journal of Cell Biology* **195**, 515-524
8. Serra-Batiste, M., Ninot-Pedrosa, M., Bayoumi, M., Gairí, M., Maglia, G., and Carulla, N. (2016) Aβ42 assembles into specific β-barrel pore-forming oligomers in membrane-mimicking environments. *Proc Natl Acad Sci U S A* **113**, 10866-10871
9. Österlund, N., Moons, R., Ilag, L. L., Sobott, F., and Gräslund, A. (2019) Native Ion Mobility-Mass Spectrometry Reveals the Formation of β-Barrel Shaped Amyloid-β Hexamers in a Membrane-Mimicking Environment. *J Am Chem Soc* **141**, 10440-10450
10. Ciudad, S., Puig, E., Botzanowski, T., Meigooni, M., Arango, A. S., Do, J., Mayzel, M., Bayoumi, M., Chaignepain, S., Maglia, G., Cianferani, S., Orekhov, V., Tajkhorshid, E., Bardiaux, B., and Carulla, N. (2020) Aβ(1-42) tetramer and octamer structures reveal edge conductivity pores as a mechanism for membrane damage. *Nature Communications* **11**, 3014
11. Butterfield, S. M., and Lashuel, H. A. (2010) Amyloidogenic Protein–Membrane Interactions: Mechanistic Insight from Model Systems. *Angewandte Chemie International Edition* **49**, 5628-5654
12. Wu, J., Cao, C., Loch, R. A., Tiiman, A., and Luo, J. (2020) Single-molecule studies of amyloid proteins: from biophysical properties to diagnostic perspectives. *Quarterly Reviews of Biophysics* **53**, e12
13. Kayed, R., Sokolov, Y., Edmonds, B., McIntire, T. M., Milton, S. C., Hall, J. E., and Glabe, C. G. (2004) Permeabilization of Lipid Bilayers Is a Common Conformation-dependent Activity of Soluble Amyloid Oligomers in Protein Misfolding Diseases *. *Journal of Biological Chemistry* **279**, 46363-46366
14. Henderson, R. (1995) The potential and limitations of neutrons, electrons and X-rays for atomic resolution microscopy of unstained biological molecules. *Q Rev Biophys* **28**, 171-193
15. Song, L., Hobaugh, M. R., Shustak, C., Cheley, S., Bayley, H., and Gouaux, J. E. (1996) Structure of staphylococcal alpha-hemolysin, a heptameric transmembrane pore. *Science* **274**, 1859-1866
16. Yoshiike, Y., Kayed, R., Milton, S. C., Takashima, A., and Glabe, C. G. (2007) Pore-forming proteins share structural and functional homology with amyloid oligomers. *Neuromolecular Med* **9**, 270-275
17. Du, Y., Liu, L., Zhang, C., and Zhang, Y. (2018) Two residues in Staphylococcus aureus α-hemolysin related to hemolysis and self-assembly. *Infect Drug Resist* **11**, 1271-1274
18. Hoyer, W., Grönwall, C., Jonsson, A., Ståhl, S., and Härd, T. (2008) Stabilization of a β-hairpin in monomeric Alzheimer's amyloid-β peptide inhibits amyloid formation. *Proceedings of the National Academy of Sciences* **105**, 5099-5104
19. Lührs, T., Ritter, C., Adrian, M., Riek-Loher, D., Bohrmann, B., Döbeli, H., Schubert, D., and Riek, R. (2005) 3D structure of Alzheimer's amyloid-β(1–42) fibrils. *Proceedings of the National Academy of Sciences of the United States of America* **102**, 17342-17347
20. Kawate, T., and Gouaux, E. (2003) Arresting and releasing Staphylococcal alpha-hemolysin at intermediate stages of pore formation by engineered disulfide bonds. *Protein science : a publication of the Protein Society* **12**, 997-1006
21. Jaikaran, E. T. A. S., and Clark, A. (2001) Islet amyloid and type 2 diabetes: from molecular misfolding to islet pathophysiology. *Biochimica et Biophysica Acta (BBA) - Molecular Basis of Disease* **1537**, 179-203
22. Poojari, C., Xiao, D., Batista, V. S., and Strodel, B. (2013) Membrane permeation induced by aggregates of human islet amyloid polypeptides. *Biophys J* **105**, 2323-2332

23. Peters, C., Bascuñán, D., Opazo, C., and Aguayo, L. G. (2016) Differential Membrane Toxicity of Amyloid-β Fragments by Pore Forming Mechanisms. *J Alzheimers Dis* **51**, 689-699
24. Bolognesi, B., Kumita, J. R., Barros, T. P., Esbjorner, E. K., Luheshi, L. M., Crowther, D. C., Wilson, M. R., Dobson, C. M., Favrin, G., and Yerbury, J. J. (2010) ANS binding reveals common features of cytotoxic amyloid species. *ACS Chem Biol* **5**, 735-740
25. Jayasinghe, L., Miles, G., and Bayley, H. (2006) Role of the amino latch of staphylococcal alpha-hemolysin in pore formation: a co-operative interaction between the N terminus and position 217. *J Biol Chem* **281**, 2195-2204
26. Tjernberg, L. O., Näslund, J., Thyberg, J., Gandy, S. E., Terenius, L., and Nordstedt, C. (1996) Generation of Alzheimer Amyloid β Peptide through Nonspecific Proteolysis*. *Journal of Biological Chemistry* **272**, 1870-1875
27. Langer, F., Eisele, Y. S., Fritschi, S. K., Staufenbiel, M., Walker, L. C., and Jucker, M. (2011) Soluble Aβ seeds are potent inducers of cerebral β-amyloid deposition. *J Neurosci* **31**, 14488-14495
28. Ruiz-Riquelme, A., Lau, H. H. C., Stuart, E., Goczi, A. N., Wang, Z., Schmitt-Ulms, G., and Watts, J. C. (2018) Prion-like propagation of β-amyloid aggregates in the absence of APP overexpression. *Acta Neuropathologica Communications* **6**, 26
29. Yu, X., Wang, Q., Pan, Q., Zhou, F., and Zheng, J. (2013) Molecular interactions of Alzheimer amyloid-β oligomers with neutral and negatively charged lipid bilayers. *Physical Chemistry Chemical Physics* **15**, 8878-8889
30. Ahyayauch, H., Raab, M., Busto, J. V., Andraka, N., Arrondo, J.-L. R., Masserini, M., Tvaroska, I., and Goñi, F. M. (2012) Binding of β-amyloid (1-42) peptide to negatively charged phospholipid membranes in the liquid-ordered state: modeling and experimental studies. *Biophysical journal* **103**, 453-463
31. Davidson, W. S., Jonas, A., Clayton, D. F., and George, J. M. (1998) Stabilization of α-Synuclein Secondary Structure upon Binding to Synthetic Membranes*. *Journal of Biological Chemistry* **273**, 9443-9449
32. Pirc, K., and Ulrih, N. P. (2015) α-Synuclein interactions with phospholipid model membranes: Key roles for electrostatic interactions and lipid-bilayer structure. *Biochimica et Biophysica Acta (BBA) - Biomembranes* **1848**, 2002-2012
33. van Rooijen, B. D., Claessens, M. M. A. E., and Subramaniam, V. (2009) Lipid bilayer disruption by oligomeric α-synuclein depends on bilayer charge and accessibility of the hydrophobic core. *Biochimica et Biophysica Acta (BBA) - Biomembranes* **1788**, 1271-1278
34. Jones, E. M., Dubey, M., Camp, P. J., Vernon, B. C., Biernat, J., Mandelkow, E., Majewski, J., and Chi, E. Y. (2012) Interaction of tau protein with model lipid membranes induces tau structural compaction and membrane disruption. *Biochemistry* **51**, 2539-2550
35. Khurana, R., Coleman, C., Ionescu-Zanetti, C., Carter, S. A., Krishna, V., Grover, R. K., Roy, R., and Singh, S. (2005) Mechanism of thioflavin T binding to amyloid fibrils. *J Struct Biol* **151**, 229-238
36. Stoddart, D., Ayub, M., Höfler, L., Raychaudhuri, P., Klingelhoefer, J. W., Maglia, G., Heron, A., and Bayley, H. (2014) Functional truncated membrane pores. *Proceedings of the National Academy of Sciences of the United States of America* **111**, 2425-2430
37. Lendel, C., Bjerring, M., Dubnovitsky, A., Kelly, R. T., Filippov, A., Antzutkin, O. N., Nielsen, N. C., and Härd, T. (2014) A Hexameric Peptide Barrel as Building Block of Amyloid-β Protofibrils. *Angewandte Chemie International Edition* **53**, 12756-12760
38. Cline, E. N., Bicca, M. A., Viola, K. L., and Klein, W. L. (2018) The Amyloid-β Oligomer Hypothesis: Beginning of the Third Decade. *Journal of Alzheimer's disease : JAD* **64**, S567-S610
39. Sandberg, A., Luheshi, L. M., Söllvander, S., Pereira de Barros, T., Macao, B., Knowles, T. P., Biverstål, H., Lendel, C., Ekholm-Petterson, F., Dubnovitsky, A., Lannfelt, L., Dobson, C. M.,

and Härd, T. (2010) Stabilization of neurotoxic Alzheimer amyloid-beta oligomers by protein engineering. *Proc Natl Acad Sci U S A* **107**, 15595-15600
40. Bitan, G., Kirkitadze, M. D., Lomakin, A., Vollers, S. S., Benedek, G. B., and Teplow, D. B. (2003) Amyloid beta -protein (Abeta) assembly: Abeta 40 and Abeta 42 oligomerize through distinct pathways. *Proceedings of the National Academy of Sciences* **100**, 330-335
41. Fradinger, E. A., Monien, B. H., Urbanc, B., Lomakin, A., Tan, M., Li, H., Spring, S. M., Condron, M. M., Cruz, L., Xie, C. W., Benedek, G. B., and Bitan, G. (2008) C-terminal peptides coassemble into Abeta42 oligomers and protect neurons against Abeta42-induced neurotoxicity. *Proc Natl Acad Sci U S A* **105**, 14175-14180
42. Gordon, L. M., Nisthal, A., Lee, A. B., Eskandari, S., Ruchala, P., Jung, C. L., Waring, A. J., and Mobley, P. W. (2008) Structural and functional properties of peptides based on the N-terminus of HIV-1 gp41 and the C-terminus of the amyloid-beta protein. *Biochim Biophys Acta* **1778**, 2127-2137
43. Arispe, N., Pollard, H. B., and Rojas, E. (1996) Zn2+ interaction with Alzheimer amyloid beta protein calcium channels. *Proc Natl Acad Sci U S A* **93**, 1710-1715
44. Grimaldi, M., Scrima, M., Esposito, C., Vitiello, G., Ramunno, A., Limongelli, V., D'Errico, G., Novellino, E., and D'Ursi, A. M. (2010) Membrane charge dependent states of the beta-amyloid fragment Abeta (16-35) with differently charged micelle aggregates. *Biochim Biophys Acta* **1798**, 660-671
45. Olson, R., Nariya, H., Yokota, K., Kamio, Y., and Gouaux, E. (1999) Crystal structure of staphylococcal LukF delineates conformational changes accompanying formation of a transmembrane channel. *Nat Struct Biol* **6**, 134-140
46. Streltsov, V. A., Varghese, J. N., Masters, C. L., and Nuttall, S. D. (2011) Crystal Structure of the Amyloid-β p3 Fragment Provides a Model for Oligomer Formation in Alzheimer's Disease. *The Journal of Neuroscience* **31**, 1419-1426
47. Kandel, N., Zheng, T., Huo, Q., and Tatulian, S. A. (2017) Membrane Binding and Pore Formation by a Cytotoxic Fragment of Amyloid β Peptide. *The Journal of Physical Chemistry B* **121**, 10293-10305
48. Kandel, N., Matos, J. O., and Tatulian, S. A. (2019) Structure of amyloid β(25-35) in lipid environment and cholesterol-dependent membrane pore formation. *Sci Rep* **9**, 2689
49. Frenkel, D., Balass, M., Katchalski-Katzir, E., and Solomon, B. (1999) High affinity binding of monoclonal antibodies to the sequential epitope EFRH of beta-amyloid peptide is essential for modulation of fibrillar aggregation. *J Neuroimmunol* **95**, 136-142
50. Castell, O. K., Berridge, J., and Wallace, M. I. (2012) Quantification of membrane protein inhibition by optical ion flux in a droplet interface bilayer array. *Angew Chem Int Ed Engl* **51**, 3134-3138
51. Wallin, C., Hiruma, Y., Wärmländer, S. K. T. S., Huvent, I., Jarvet, J., Abrahams, J. P., Gräslund, A., Lippens, G., and Luo, J. (2018) The Neuronal Tau Protein Blocks in Vitro Fibrillation of the Amyloid-β (Aβ) Peptide at the Oligomeric Stage. *Journal of the American Chemical Society* **140**, 8138-8146
52. Wang, H., Lallemang, M., Hermann, B., Wallin, C., Loch, R., Blanc, A., Balzer, B. N., Hugel, T., and Luo, J. (2021) ATP Impedes the Inhibitory Effect of Hsp90 on Aβ40 Fibrillation. *Journal of Molecular Biology* **433**, 166717
53. Broersen, K., Jonckheere, W., Rozenski, J., Vandersteen, A., Pauwels, K., Pastore, A., Rousseau, F., and Schymkowitz, J. (2011) A standardized and biocompatible preparation of aggregate-free amyloid beta peptide for biophysical and biological studies of Alzheimer's disease. *Protein Eng Des Sel* **24**, 743-750
54. Luo, J., Mohammed, I., Wärmländer, S. K. T. S., Hiruma, Y., Gräslund, A., and Abrahams, J. P. (2014) Endogenous Polyamines Reduce the Toxicity of Soluble Aβ Peptide Aggregates Associated with Alzheimer's Disease. *Biomacromolecules* **15**, 1985-1991

55. Zivanov, J., Nakane, T., Forsberg, B. O., Kimanius, D., Hagen, W. J., Lindahl, E., and Scheres, S. H. (2018) New tools for automated high-resolution cryo-EM structure determination in RELION-3. *Elife* **7**
56. Biyani, N., Righetto, R. D., McLeod, R., Caujolle-Bert, D., Castano-Diez, D., Goldie, K. N., and Stahlberg, H. (2017) Focus: The interface between data collection and data processing in cryo-EM. *J Struct Biol* **198**, 124-133
57. Li, X., Mooney, P., Zheng, S., Booth, C. R., Braunfeld, M. B., Gubbens, S., Agard, D. A., and Cheng, Y. (2013) Electron counting and beam-induced motion correction enable near-atomic-resolution single-particle cryo-EM. *Nature methods* **10**, 584-590
58. Scheres, S. H. (2012) RELION: implementation of a Bayesian approach to cryo-EM structure determination. *J Struct Biol* **180**, 519-530
59. Webb, B., and Sali, A. (2016) Comparative Protein Structure Modeling Using MODELLER. *Curr Protoc Bioinformatics* **54**, 5.6.1-5.6.37
60. Fleishman, S. J., Leaver-Fay, A., Corn, J. E., Strauch, E.-M., Khare, S. D., Koga, N., Ashworth, J., Murphy, P., Richter, F., Lemmon, G., Meiler, J., and Baker, D. (2011) RosettaScripts: A Scripting Language Interface to the Rosetta Macromolecular Modeling Suite. *PLOS ONE* **6**, e20161
61. Steinegger, M., Meier, M., Mirdita, M., Vöhringer, H., Haunsberger, S. J., and Söding, J. (2019) HH-suite3 for fast remote homology detection and deep protein annotation. *BMC Bioinformatics* **20**, 473
62. Pettersen, E. F., Goddard, T. D., Huang, C. C., Couch, G. S., Greenblatt, D. M., Meng, E. C., and Ferrin, T. E. (2004) UCSF Chimera--a visualization system for exploratory research and analysis. *J Comput Chem* **25**, 1605-1612
63. Song, Y., DiMaio, F., Wang, R. Y., Kim, D., Miles, C., Brunette, T., Thompson, J., and Baker, D. (2013) High-resolution comparative modeling with RosettaCM. *Structure* **21**, 1735-1742

3.9 Supporting information

Wild-type αHL

ADSD INIKT G TTD I GSNTT V KTGDLVTYDK ENGMHKKVFY SFIDDKNHN K K LLV I RTKG T

IAGQYRVYS E EGANKSGLAW PS AFKVQLQL PDN E VAQ I SD YYPRN SIDT K EYM STLTY G F

NGNVTGDDTG K IGGLIGAN V S IGHT LKYVQ PDF K T I L ESP TDKKVGWKVI FNNMVNQNWG

PYDRD SWNPV YGNQLFMKT R NGSMKAADNF LDPNK A SSL L SSGF S P DFA T V IT MD RK AS K

QQTNI DVIYE RVRDDYQLHW TSTNW KGTNT KDKWT DRSSE RYKID WEKEE MTNDD DDDDD

DHHHHHH

Wild-type Aβ42 DAEFRHDSGY EVHHQKLVFF AEDVGSNKGA I IGLMVGGVV IA

Hybrid Aβ42-αHL

ADSD INIKT G TTD I GSNTT V KTGDLVTYDK ENGMHKKVFY SFIDDKNHN K K LLV I RTKG T

IAGQYRVYS E EGANKSGLAW PS AFKVQLQL PDN E VAQ I SD YYPRN DAEFR HDSG Y EVHHQ

KLVFFAEDVG SNKGAI IGLM VGGVVIAYVQ PDF K T I L ESP TDKKVGWKVI FNNMVNQNWG

PYDRD SWNPV YGNQLFMKT R NGSMKAADNF LDPNK A SSL L SSGF S P DFA T V IT MD RKASK

QQTNI DVIYE RVRDDYQLHW TSTNW KGTNT KDKWT DRSSE RYKID WEKEE MTNDD DDDDD

DHHHHHH

Hybrid Aβ11-42-αHL

ADSD INIKT G TTD I GSNTT V KTGDLVTYDK ENGMHKKVFY SFIDDKNHN K K LLV I RTKG T

IAGQYRVYS E EGANKSGLAW PS AFKVQLQL PDN E VAQ I SD YYPRN EVHHQ K LVF F AEDVG

SNKGAI IGLM VGGVV IAYVQ PDF K T I L ESP TDKKVGWKVI FNNMVNQNWG PYDRD SWNPV

YGNQLFMKT R NGSMKAADNF LDPNK A SSL L SSGF S P DFA T V IT MD RKASK QQTNI DVIYE

RVRDDYQLHW TSTNW KGTNT KDKWT DRSSE RYKID WEKEE MTNDD DDDDD DHHHHHH

Hybrid Aβ1-28-αHL

ADSD INIKT G TTD I GSNTT V KTGDLVTYDK ENGMHKKVFY SFIDDKNHN K K LLV I RTKG T

IAGQYRVYS E EGANKSGLAW PS AFKVQLQL PDN E VAQ I SD YYPRN DAEFR HDSGY EVHHQ

KLVFF AEDVG SNKYV Q PDFK T IL ESP TDKK VGWKV I FNNM VNQNW GPYDR DSWNP VYGNQ

LFMKTRNGSM KAADN FLDPN KA SSL L SSGF S P DFA T V IT M D RKAS KQQTN I DVI Y ERVRD

DYQLH WTSTN WKGTN TKDKW TDRSS ERYKI DWEKE EMTND D DDDDD DHHHHHH

Hybrid Aβ1-17-αHL

ADSD INIKT G TTD I GSNTT V KTGDLVTYDK ENGMHKKVFY SFIDDKNHN K K LLV I RTKG T

IAGQYRVYS E EGANKSGLAW PS AFKVQLQL PDN E VAQ I SD YYPRN DAEFR HDSGY EVHHQ

KLYVQ PDFKT ILESP TDKKV GWKVIFNNMV NQNWG PYDRD SWNPV YGNQL FMKTR NGSMK

AADNF LDPNK A SSL L SSGFS P DFA T V IT MD RKASK QQTNI DVI YE RVRDD YQLHW TSTNW

KGTNT KDKWT DRSSE RYKID WEKEE MTNDD DDDDD DHHHHHH

Hybrid Aβ0-αHL

ADSD I NIKT G TTD I GSNTT V KTGDLVTYD K ENGMHKKVFY SFIDDKNHN K K LLV I RTKG T

IAGQY RVYS E EGANKSGLAW PS AFKVQLQ L PDN E VAQ I SD YYPRNYVQPD F KTI L ES P TD

KKVGW KVIFN NMVNQ NWGPY DRDSW NPVYG NQLFM KT RNG SMKAA DNFLD P N KAS SL LSS

GFSPD FATV I TMDRK ASKQ Q TNIDV IYE R V RDDYQ LHWTS TNWKG TNTKD KWTDR S SERY

KIDWE KEEMT NDDDD DDDDH HHHHH

Wild-type hIAPP **KCNTA TCATQ RLANF LVHSS NNFGA ILSST NVGSN TY**

10 20 30 37

Hybrid hIAPP-αHL

ADSD INIKT G TTD I GSNTT V KTGDLVTYDK ENGMHKKVFY SFIDDKNHN K K LLV I RTKG T

IAGQYRVYS E EGANKSGLAW PS AFKVQLQL PDN E VAQ I SD YYPRN SIDTK KCNTA T CA T Q

RLANF LVHSS NNFGA ILSST NVGSN TYYVQ PDF K T I L ESP TDKKVGWKVI FNNMVNQNWG

PYDRD SWNPV YGNQLFMKT R NGSMKAADNF LDPNK A SSL L SSGF S P DFA T V IT MD RKASK

QQTNI DVIYE RVRDDYQLHW TSTNW KGTNT KDKWT DRSSE RYKID WEKEE MTNDD DDDDD

DHHHHHH

Figure S1. The full sequences of wild type (WT) αHL, WT Aβ42, a series of hybrid Aβ-αHL peptides, WT hIAPP and hybrid hIAPP- αHL. Aβ amino acids substituted the transmembrane β-hairpin part of αHL (red). The substituted Aβ or hIAPP sequences were shown in blue.

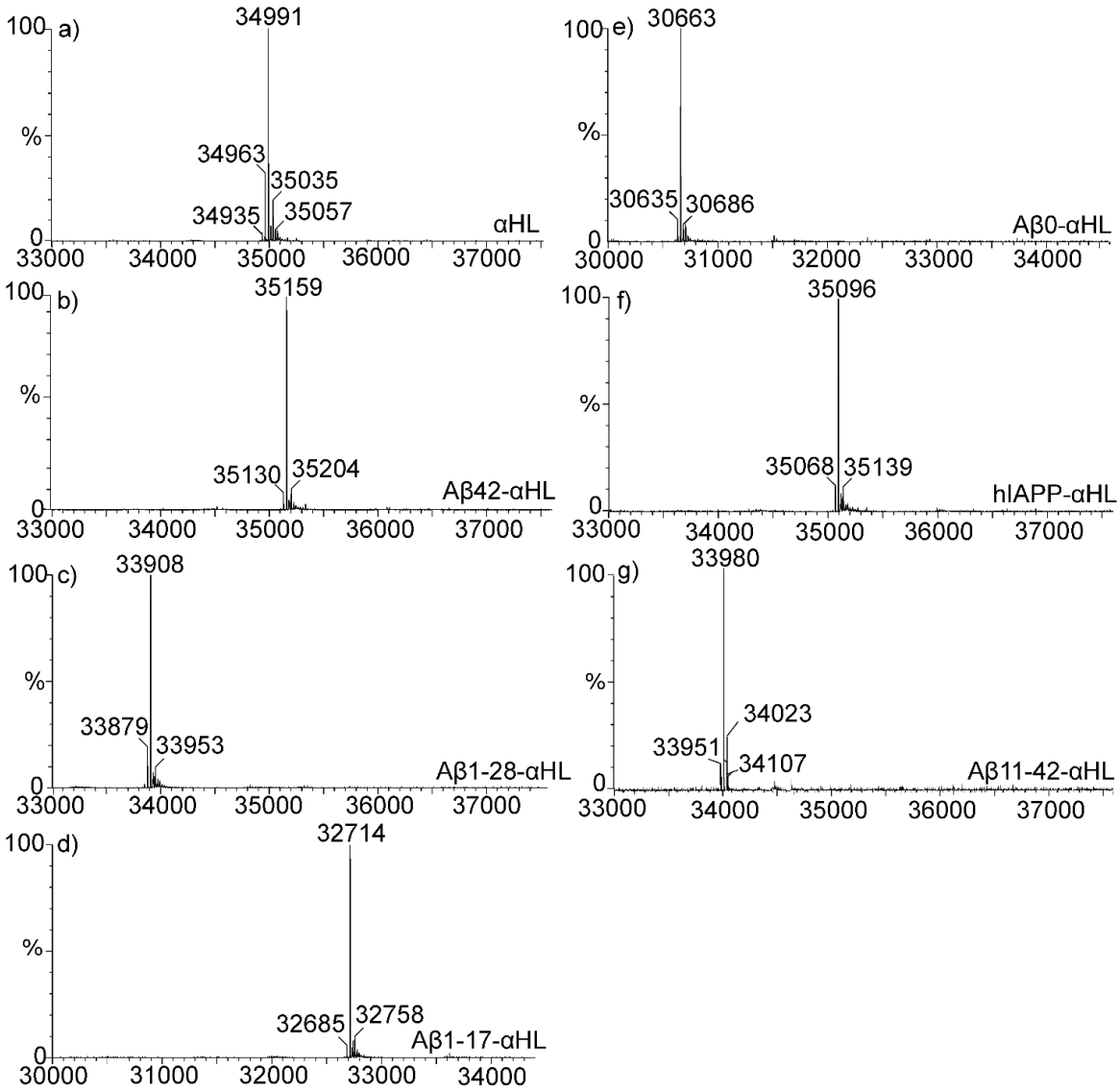

Figure S2. Deconvoluted mass spectrum of the purified WT αHL and a series of hybrid Aβ/hIAPP–αHL peptides. LC-MS experiments were conducted to confirm the molecule weight of a series of hybrid Aβ/hIAPP-αHL proteins including WT αHL. Results are compared to the calculated weight, which have been listed in Table S1.

Table S1. The theoretical molecule weight of WT αHL and a series of hybrid Aβ/hIAPP-αHL.

Peptide	Calculated weight (MW)/Da	Observed $[M+H]^+$/Da
Wild type αHL	34991	34991
Hybrid Aβ42-αHL	35158	35159
Hybrid Aβ11-42-αHL	33980	33980
Hybrid Aβ1-28-αHL	33907	33908
Hybrid Aβ1-17-αHL	32712	32714
Hybrid Aβ0-αHL	30662	30663
Hybrid hIAPP-αHL	35095	35096

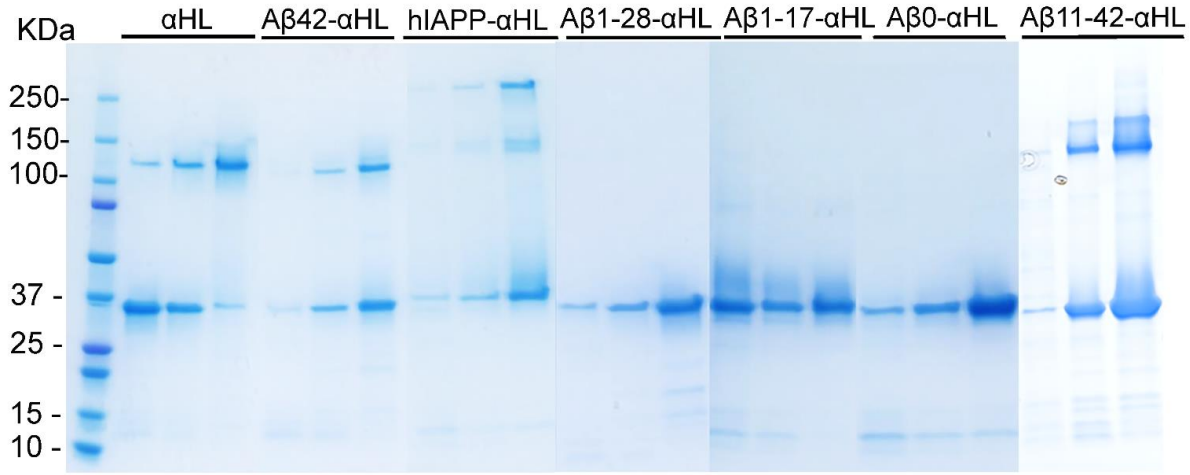

Figure S3. Purification of WT αHL and a series of hybrid Aβ/hIAPP–αHL proteins. All the proteins were expressed in *E. coli* and purified on the Co-NTA affinity column by using the His-tag at the C-terminus. SDS-PAGE Electrophoresis (Bio-Rad, 4-20 %) was conducted at 200 mV to monitor the protein quality. There was an imidazole concentration gradient (20 mM, 50 mM and 250 mM respectively) in the elution buffer (50 mM Tris-HCl, pH 8.0, 500 mM NaCl and 0.38 mM DDM) to separate the monomer and oligomer. The SDS-PAGE Electrophoresis was conducted at 200 V for 25 min.

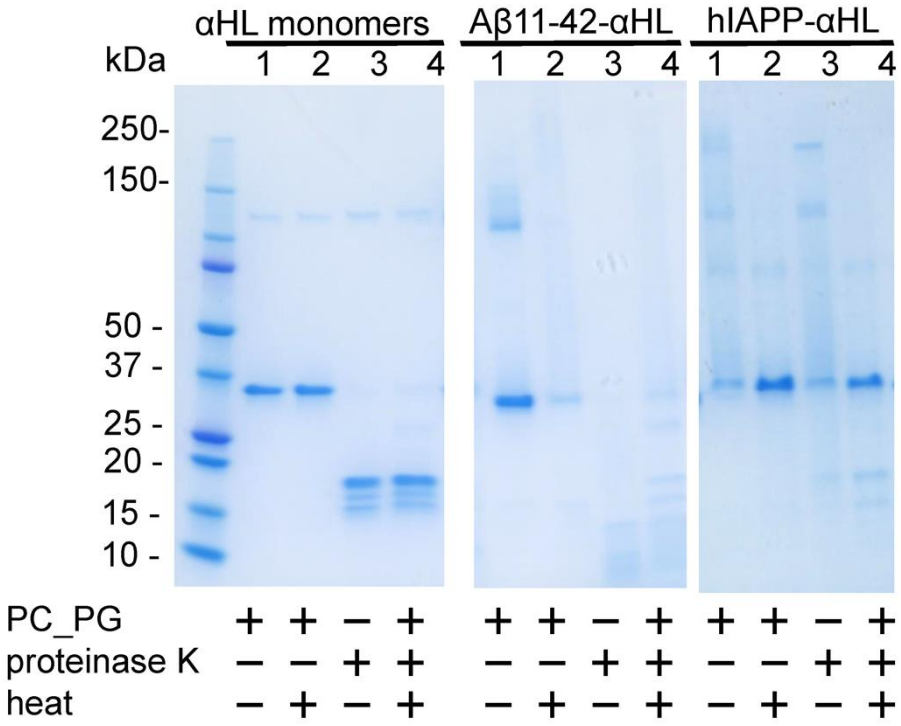

Figure S4. Limited proteolysis with proteinase K of the WT αHL monomers, hybrid Aβ11-42-αHL and hybrid hIAPP-αHL oligomers in the presence of DOPC:DOPG (4:1) liposomes (1 mg/ mL). For WT αHL monomers, Lane 1: αHL monomers were treated with DOPC:DOPG liposomes; lane 2: αHL monomers were treated with DOPC:DOPG liposomes and then got heat denatured at 95 °C for 15 min; lane 3: αHL monomers were digested with proteinase K; lane 4: αHL monomers treated with DOPC:DOPG liposomes were further digested by proteinase K and then heat-denatured at 95 °C. There were the same conditions for hybrid Aβ11-42-αHL and hybrid hIAPP-αHL oligomers. Monomeric WT αHL in the presence of proteinase K is taken as a control and shows more prone to breakdown, as reported previously [14]. Hybrid Aβ11-42-αHL and hybrid hIAPP-αHL oligomers exhibit the obvious proteolysis and heat denaturation.

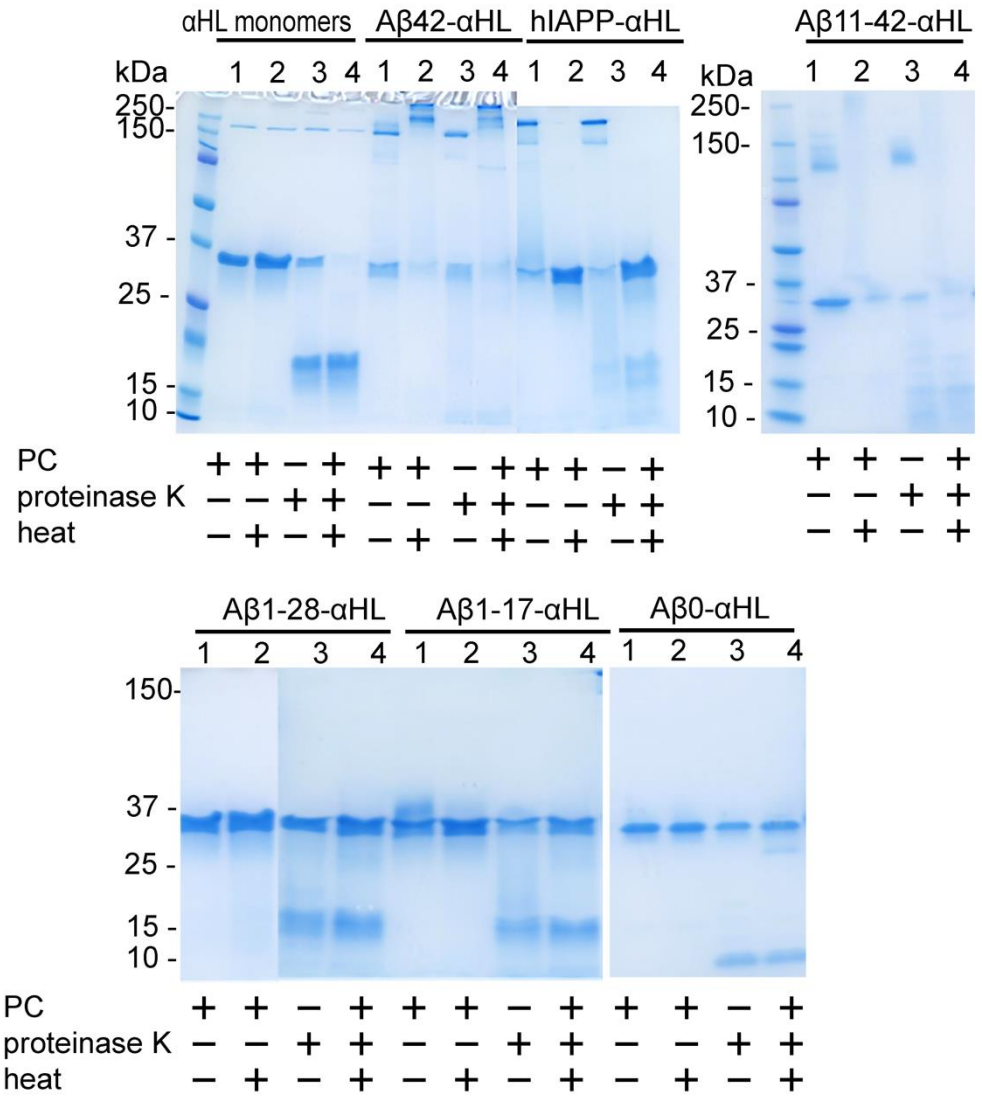

Figure S5. Limited proteolysis with proteinase K of WT αHL monomers and hybrid Aβ/hIAPP-αHL oligomers in the presence of DPhPC liposomes (1 mg/ mL). For αHL, Lane 1: αHL monomers were treated with DPhPC liposomes; lane 2: αHL monomers were treated with DPhPC liposomes and then got heat denatured at 95 °C for 15 min; lane 3: αHL monomers were digested with proteinase K; lane 4: αHL monomers treated with DPhPC liposomes were further digested by proteinase K and then heat-denatured at 95 °C. There were the same conditions for hybrid Aβ/hIAPP-αHL proteins.

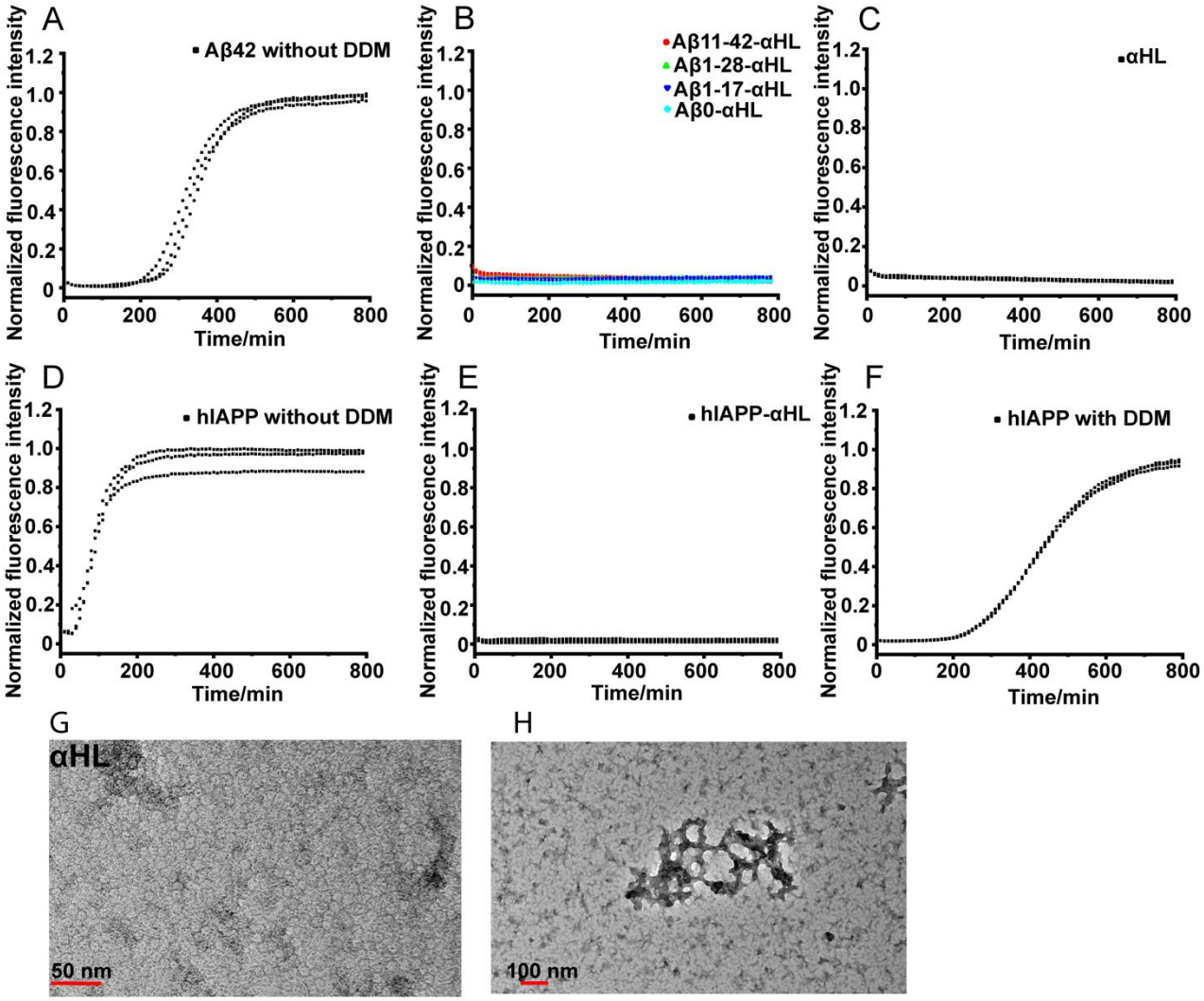

Figure S6. ThT fibrillation kinetics of the WT amyloid peptides, αHL displayed Aβ, or WT αHL proteins (A-F) and TEM images of WT αHL oligomers (G) as well as the amorphous aggregates of hybrid Aβ42-αHL (H). Higher ThT fluorescence intensity indicates more fibril formation. (A) WT Aβ42 in the buffer of 50 mM Tris-HCl, pH 8.0, 0.5 M NaCl and 250 mM imidazole. (B) A series of hybrid Aβ-αHL oligomers including Aβ11-42-αHL, Aβ1-28-αHL, Aβ1-17-αHL or Aβ0-αHL, prepared in the same condition as Aβ42-αHL in Figure 3B (50 mM Tris-HCl, pH 8.0, 500 mM NaCl, 250 mM imidazole and 0.38 mM DDM). (C) WT αHL in the buffer of 50 mM Tris-HCl, pH 8.0, 0.5 M NaCl, 250 mM imidazole and 0.38 mM DDM. (D) WT hIAPP amyloid aggregation assay in the buffer of 50 mM Tris-HCl, pH 8.0, 0.5 M NaCl, 250 mM imidazole. (E) Hybrid hIAPP-αHL or (F) WT hIAPP was used for the kinetic assay in the buffer of 50 mM Tris-HCl, pH 8.0, 0.5 M NaCl, 250 mM imidazole and 0.38 mM DDM. The ratio of ThT and proteins was 4:1 with a ThT final concentration at 40 μM. The excitation and emission filters were 430 and 480 nm, respectively. (G-H) The samples were obtained

from the end of ThT kinetics for TEM imaging. Scale bars of WT αHL oligomers (G) and the amorphous aggregates of hybrid Aβ42-αHL (H) are 50 nm and 100 nm respectively.

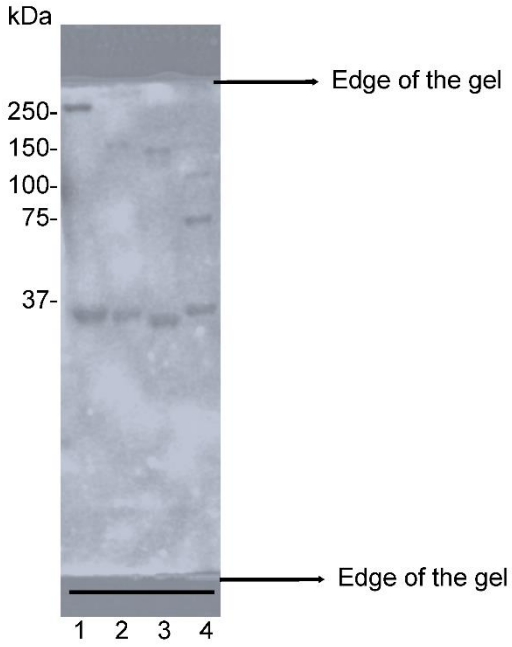

Figure S7. Immunogenic similarity of WT αHL, hybrid Aβ42/11-42-αHL and hybrid hIAPP-αHL by western blot. The anti-Aβ42 oligomer conformation-dependent antibody A11 recognized αHL oligomers (lane 1); hybrid Aβ42-αHL oligomers (lane 2); hybrid Aβ11-42-αHL oligomers (lane 3); hybrid hIAPP-αHL oligomers (lane 4). The SDS-PAGE electrophoresis prior to blotting, was conducted at 120 V for 80 min. No bands with molecule weight lower than the monomer bands (around 30-35 kDa) were found on the gel.

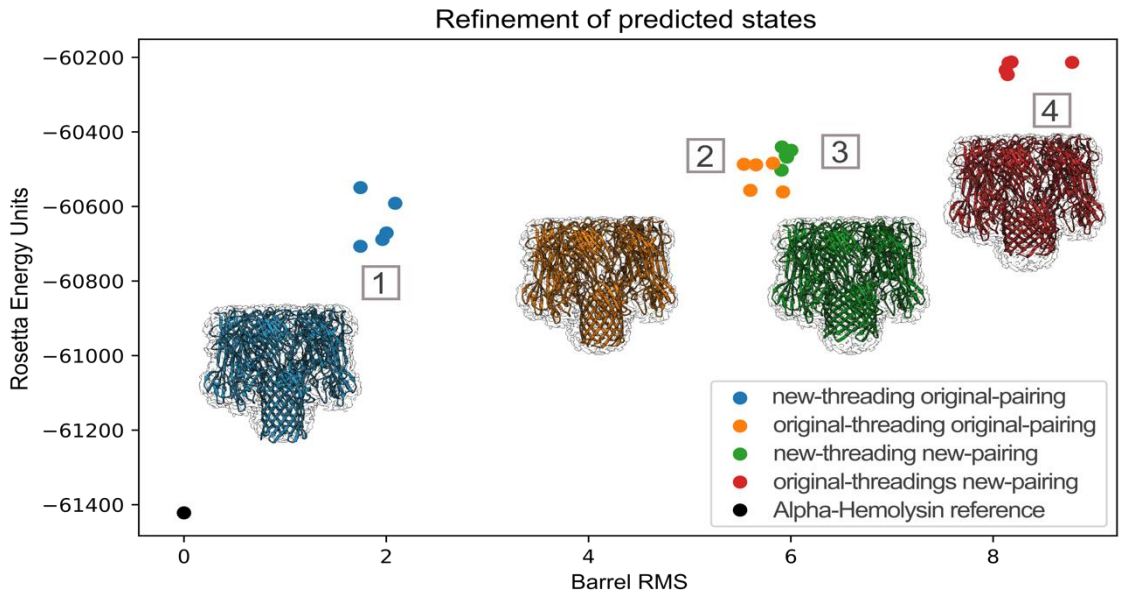

Figure S8. Total score comparison between the four assessed states of the Aβ-αHL chimera as evaluated by the Rosetta full atom score function (lower score is better/more stable). The x-axis is the RMS (Root Mean Square) deviation of our models to the αHL (PDB: 7AHL) scaffold, and each of the clusters of points represent a particular modeled conformation of our Aβ42-αHL. The y-axis represents the energy landscape of the possible conformations of Aβ42 region on the αHL scaffold, given the low-resolution electron density. We found the models to be ranked as follows: 1. original β-barrel strand pairing with custom alignment (blue), 2. original β-barrel strand pairing with hhpred alignment (orange), 3. shifted β-barrel strand pairing with custom alignment (green), 4. shifted β-barrel strand pairing with hhpred alignment (red).

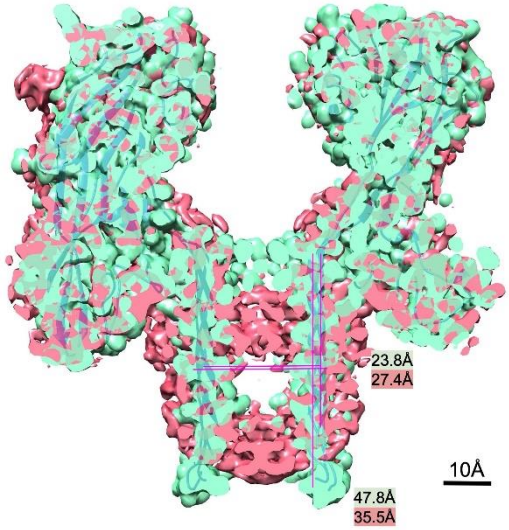

Figure S9. Map superposition of WT αHL (green) and the hybrid Aβ42-αHL (red). The hybrid Aβ42-αHL β-barrel pore has a shorter length (35.5 Å) and a similar inner diameter (27.4 Å) of the largest circular cross-section, compared to the WT αHL barrel (47.8 Å high and 23.8 Å wide).

Table S2. Structure refinement by Phenix software

Model	
Composition (#)	
Chains	7
Atoms	32434 (Hydrogens: 15921)
Residues	Protein: 2051 Nucleotide: 0
Water	0
Ligands	0
Bonds (RMSD)	
Length (Å) (# > 4σ)	0.007 (0)
Angles (°) (# > 4σ)	0.560 (0)
MolProbity score	1.35
Clash score	4.28
Ramachandran plot (%)	
Outliers	0
Allowed	2.75
Favored	97.25
Rama-Z (Ramachandran plot Z-score, RMSD)	
Whole (N = 2037)	0.21 (0.18)
Helix (N = 42)	4.43 (0.08)
Sheet (N = 1057)	0.32 (0.16)
Loop (N = 938)	0.35 (0.20)
Rotamer outliers (%)	0.39
Cβ outliers (%)	0
Peptide plane (%)	
Cis proline/general	11.1/0.0
Twisted proline/general	0.0/0.0
CaBLAM outliers (%)	0.69
ADP (B-factors)	
Iso/Aniso (#)	16513/0
min/max/mean	
Protein	28.63/173.52/59.28
Nucleotide	---
Ligand	---
Water	---
Occupancy	
Mean	1
occ = 1 (%)	100
0 < occ < 1 (%)	0
occ > 1 (%)	0
Data	
Box	
Lengths (Å)	112.27, 112.27, 111.24
Angles (°)	90.00, 90.00, 90.00

Supplied Resolution (Å)	3.3	
Resolution Estimates (Å)	Masked Unmasked	
d FSC (half maps; 0.143)	---	---
d 99 (full/half1/half2)	3.4/---/---	3.4/---/---
d model	3.3	3.3
d FSC model (0/0.143/0.5)	2.7/3.1/3.3 2.7/3.1/3.3	
Map min/max/mean	-0.08/0.14/0.00	
Model vs. Data		
CC (mask)	0.8	
CC (box)	0.73	
CC (peaks)	0.74	
CC (volume)	0.79	

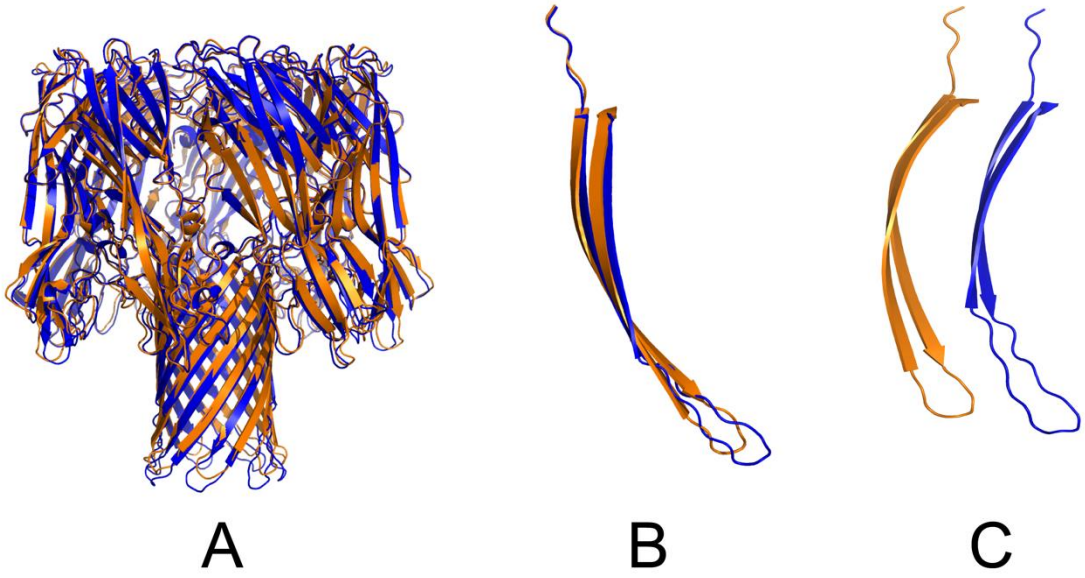

Figure S10. A: Superposition of heptameric Aβ42 displayed on the αHL scaffold (in orange) and WT αHL (in blue). B-C: Comparison of the displayed Aβ42 sequence (in orange) and αHL pre-stem domain (residues 106-147 in blue).

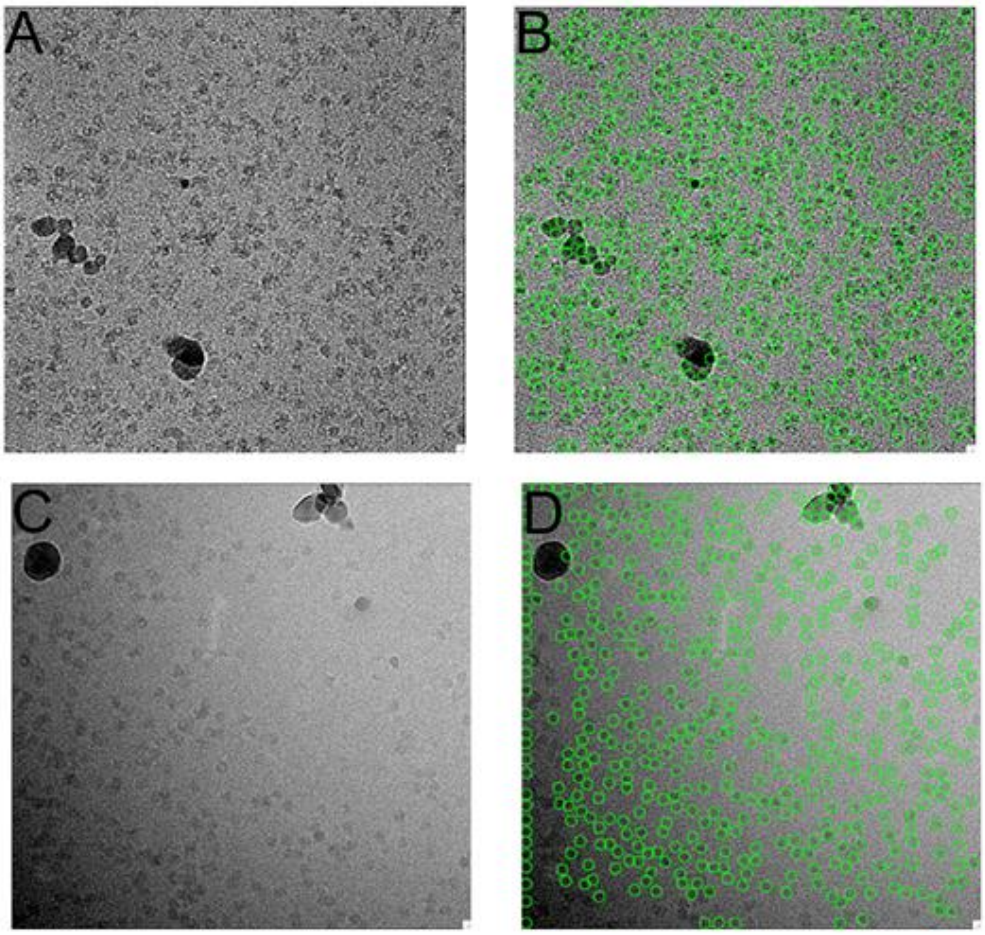

Figure S11. The visualization of hybrid Aβ42-αHL particles in two regions by cryo-EM. 2'438'446 particles (green box) from 4'284 micrographs were automatically picked by RELION 3.0.

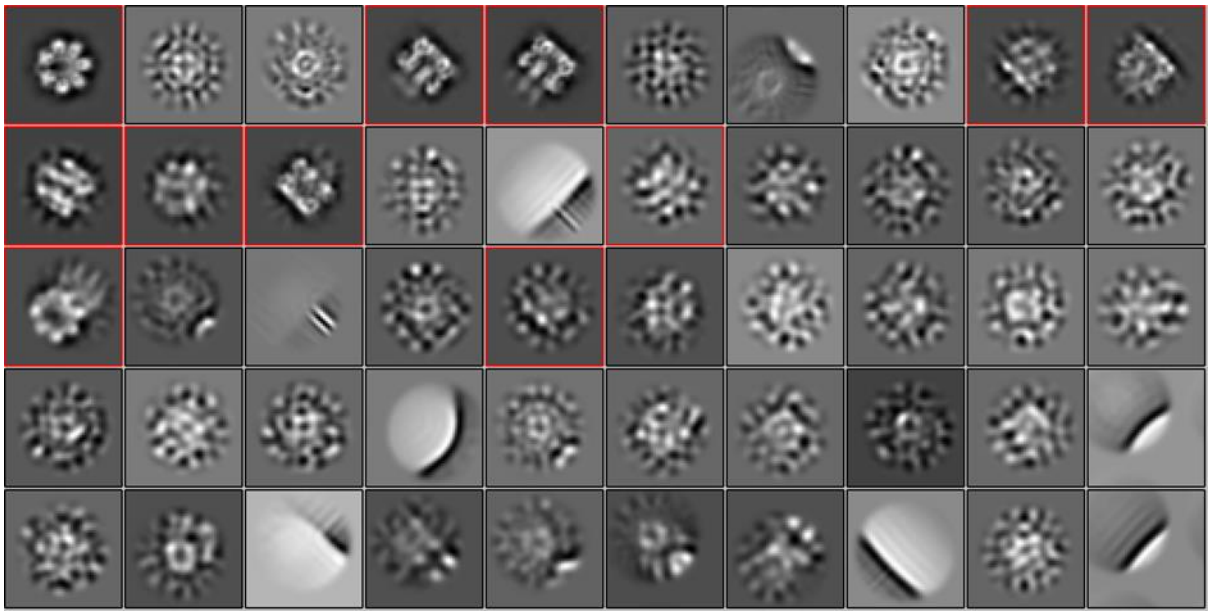

Figure S12. The primary 2D classification of hybrid Aβ42-αHL particles. Some classes that are not framed in red boxes contained noise or contamination and thus were dropped before proceeding on the density map. The particles being framed in the red box were used for 3D auto-refine and the beam tilt values for the entire data set.

Chapter 4

The channel activities of the full-length prion and truncated proteins

Jinming Wu[1], Xue Wang[1], Asvin Lakkaraju[2], Rebecca Sternke-Hoffmann[1], Bilal M. Qureshi[3], Adriano Aguzzi[2], Jinghui Luo[1,*]

1. Department of Biology and Chemistry, Paul Scherrer Institute, 5232 Villigen, Switzerland.
2. Institute of Neuropathology, University of Zurich and University Hospital Zurich, Zurich 8091, Switzerland.
3. Scientific Center for Optical and Electron Microscopy (ScopeM), ETH Zurich, Zurich, Switzerland

[*]Email: Jinghui.luo@psi.ch

Accepted by ***ACS Chemical Neuroscience***.

DOI：https://doi.org/10.1021/acschemneuro.3c00412

4.1 Abstract

Prion disease is a fatal neurodegenerative disorder characterized by the conversion of the cellular prion protein (PrPC) into a misfolded prion form, which is believed to disrupt cellular membranes. However, the exact mechanisms underlying prion toxicity, including the formation of membrane pores, are not fully understood. Prion protein consists of two domains: a globular domain (GD) and a flexible N-terminus (FT) domain. Although a proximal polybasic amino acid (FT(23-31)) sequence of FT is a prerequisite for cellular membrane permeabilization, other functional domain regions may modulate its effects. Through single-channel electrical recordings and cryo-electron microscopy (cryo-EM), we discovered that the FT(23-50) fragment forms pore-shaped oligomers and plays a dominant role in membrane permeabilization within the full-length mouse prion protein (mPrP(23-230)). In contrast, the FT(51-110) domain or the C-terminal domain down-regulate the channel activity of FT(23-50) and mPrP(23-230). The addition of prion mimetic antibody, POM1 significantly amplifies mPrP(23-230) membrane permeabilization, whereas POM1_Y104A, a mutant that binds to PrP but cannot elicit toxicity, has a negligible effect on membrane permeabilization. Additionally, anti-N-terminal antibody POM2 or Cu^{2+} binds to the FT domain, subsequently enhancing FT(23-110) channel activity. Importantly, our setup provides a novel approach without an external fused protein to examine the channel activity of truncated PrP in the lipid membranes. We therefore propose that the primary N-terminal residues are essential for membrane permeabilization, while other functional segments of PrP play a vital role in modulating the pathological effects of PrP-mediated neurotoxicity.

Keywords: Prion disease, channel activity, membrane permeabilization, antibody, neurotoxicity

4.2 Introduction

Prion diseases comprise a range of fatal neurodegenerative disorders characterized by the progressive loss of neurons. Notable examples include human Creutzfeldt-Jakob disease (CJD), scrapie in sheep, and mad cow disease. Central to the pathology of these diseases are two prion isoforms, each consisting of 209 amino acids: the physiological/cellular prion proteins (PrPC), which predominantly has an α-helical structure, and the insoluble scrapie isoform (PrPSc) characterized by a β-sheet rich structure [1]. The conformational transition from soluble PrPC to

infectious PrPSc, characterized by structural misfolding, is believed to underline prion propagation. However, the exact toxic pathogenic mechanism remains elusive. While aggregated PrPsc fibril alone is not considered the primary agent of pathogenesis [2, 3], membrane-bound PrPC plays a crucial role in prion-mediated neurodegeneration [3, 4]. Interestingly, soluble low-molecular-weight PrP oligomers display significantly higher infectivity and neurotoxicity than insoluble PrPSc fibrils, both in vitro and in vivo [5, 6]. This observation aligns with the 'toxic oligomer hypothesis' [7] prevalent in neurodegeneration where the oligomers emerge as the most neurotoxic species [8] through permeabilizing cellular membranes and leading to cellular dysfunction [9, 10].

Extensive research has indicated that amyloid oligomers can adopt ring-like structures, forming pores within lipid membranes [6-8]. Investigation using techniques such as Atomic Force Microscopy (AFM) and Electron Microscopy (EM) has uncovered pore-like morphologies in a range of amyloid proteins, including Aβ (1–40), α-synuclein, ABri, ADan, serum amyloid A, and IAPP [6-8]. These findings provide insights into their interactions with lipid vesicles and planar bilayers, as observed through single-channel electrical recordings, demonstrating diverse channel behaviors ranging from transient states to high conductance states and fluctuations [6-8]. Notably, other freshly prepared amyloid proteins, including IAPP, β2-microglobulin, and a prion protein fragment, exhibit activities akin to Aβ pores in planar bilayers [7,8]. Furthermore, amyloid proteins can induce lipid membrane permeability through additional mechanisms such as carpeting and detergent effects [8]. This increased permeability leads to the influx of calcium ions into neurons, triggering a cascade of downstream effects that contribute to neurotoxicity, neuronal cell death, and the progression of prion diseases and other neurodegenerative disorders. Therefore, comprehending the molecular relationship between protein sequence and channel permeabilization holds paramount importance in the development of potential therapeutic strategies aimed at targeting these processes, potentially slowing or halting the advancement of neurodegenerative diseases.

Single-channel electrical recordings have revealed that membrane poration could be a mechanism underlying the neurotoxic effects of prions [11-14]. The prion protein is composed of two domains: a flexible N-terminal domain (FT) and a globular C-terminal domain (GD), as illustrated in Fig. 1. The FT region is intrinsically disordered and plays a crucial role in the pathogenesis of prion diseases 15. Notably, a specific segment of polybasic amino acids (23-31) has been identified as a prerequisite for channel activity of a truncated PrP protein, where

105-125 amino acids are deleted (ΔCR PrP) [11, 12]. However, the influence of the GD and other sections of the FT domain on the primary N-terminal region's channel activity remains a topic of investigation. An intriguing feature of the FT domain is the octa-repeats (OR) region (residues 51-90), which has an affinity for metal ions such as Cu^{2+} or Zn^{2+} [16, 17]. This region plays a role in mediating the interactions between FT and GD domains [18-20]. Antibodies have been utilized to modulate the neurotoxic effects of PrP [16]. Among these antibodies, POM1, which specifically targets the GD region of PrP, has demonstrated a potent capacity to enhance neurotoxicity. However, its mutant variant, POM1_Y104A, shares the same epitope of mPrP(23-230) with the POM1 but could mitigate its impact on the neurotoxicity of PrP [21]. Conversely, POM2, which targets the N-terminal region's octapeptide repeat segment, has been shown to exert a lesser impact on the neurotoxicity of PrP compared to POM1 [22-24]. Other functional segments within the FT, such as two charged clusters (CC1 and CC2), and a hydrophobic domain (HD), may also regulate channel activity of the primary N-terminal residues. Delving into how these various segments within FT and GD influence channel activity could shed light on the toxic mechanism of prions.

In this study, we utilized single-channel electrical recordings to explore the potential of the prion protein to induce pore formation, as well as how the different functional segments of FT and GD change the channel activity of the primary N-terminus region. Combined with cryo-electron microscopy (cryo-EM), we found that the primary N-terminal domain FT(23-50) can form sizeable pores in lipid membranes. Moreover, extending the sequence from the primary N-terminal domain results in diminished channel activity. Additionally, Cu^{2+} and anti-prion antibodies (POM1 or POM2) that can bind to the GD or FT domains subsequently enhance membrane permeabilization. We therefore reveal that the primary N-terminal domain (FT(23-50)) is essential for permeabilizing cell membranes but other functional segments within the full-length mouse PrP (mPrP(23-230)) appear to down-regulate the activity or other fragments, suggesting they might modulate the pathological effects associated with PrP-medicated neurotoxicity.

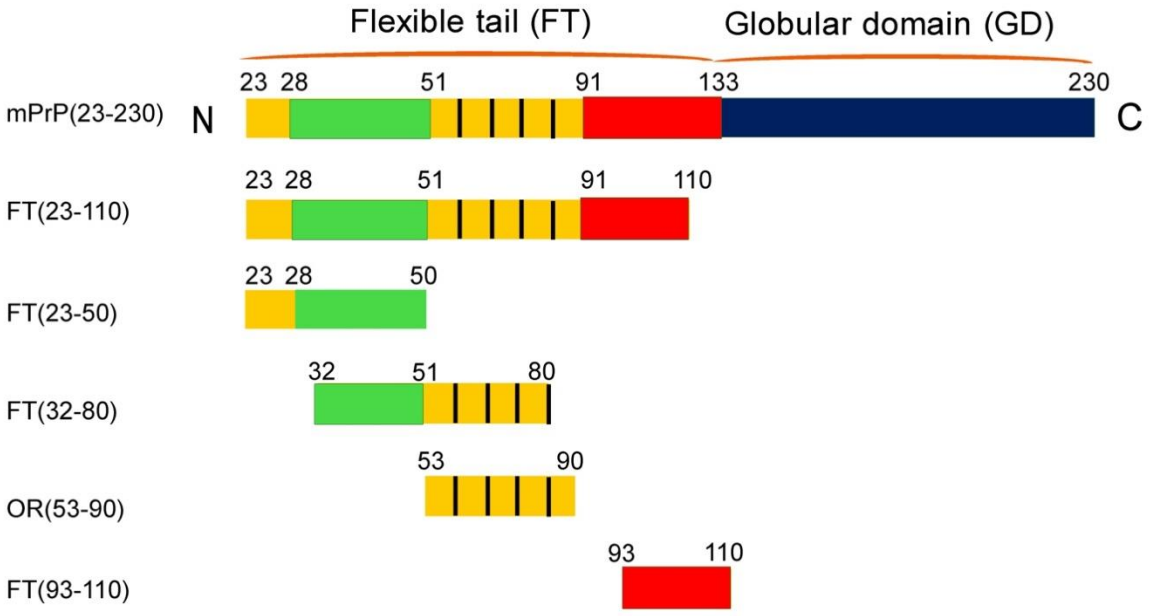

Figure 1. Schematic representation of recombinant mouse full-length mPrP(23-230), consisting of a flexible tail (FT) and a globular domain (GD). The FT domain of the prion protein contains several distinct regions, including the charged clusters CC1 (residues 23-28), CC2 (residues 100-109), the octa-repeat region (OR, residues 51-91), and a hydrophobic domain (HD, residues 112-133). In order to study their influence on mPrP ion channel formation in lipid bilayers, specific PrP fragments corresponding to these regions were selected for investigation.

4.3 Results

4.3.1 PrP sequence with more amino acids remaining in the primary N-terminal domain shows less channel-forming activity in lipid membranes

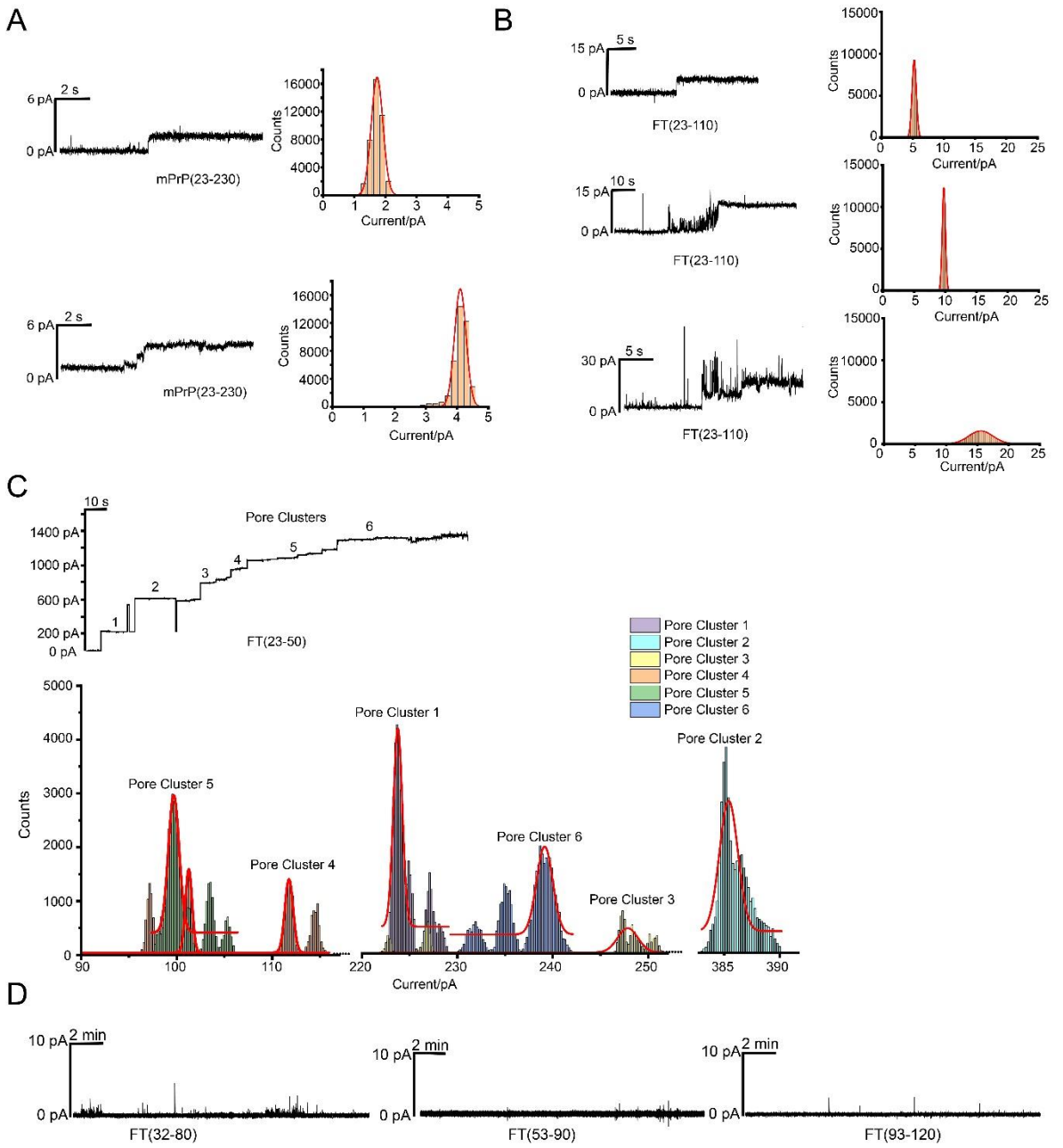

Figure 2. The representative current traces from single-channel electrical recordings. (A) The trace corresponds to the full-length recombinant mPrP(23-230) protein, while traces (B-D) depict the truncated N-terminal domains of PrP. Within the current trace of truncated FT(23-50) (C), six pore clusters were identified, suggesting the presence of different oligomeric states in the lipid membranes. The heterogeneous channels exhibit subtle variations in currents. Histograms of the counts, generated from the induced current traces, are displayed alongside the current trace. The difference between two currents is represented as ΔCurrent. The distribution of these counts was fitted using the Gaussian distribution function method, where the area under the curve indicates the number of observations. Utilizing the Gaussian function

allows for analysis of raw data without biased processing, minimizing the influence of performer or operator prejudices. The peptides were present at a final concentration of 0.4 μM in 10 mM Hepes buffer (pH 7.4) with 1 M KCl in the trans side of the chamber. Lipid bilayers were prepared using a lipid mixture comprising 10 mg/mL DOPC:DOPG at a ratio of 4:1.

Table 1 presents the probabilities of membrane permeabilization induced by truncated prion proteins, denoted as n/N, where n represents the observed ion-channel formation events and N represents the total number of experiments conducted.

Fragment	n/N (n is the observed ion-channel formation events, N is the total performed times)
mPrP(23-230)	3/5
FT(23-110)	4/7
FT(23-50)	3/7
FT(23-110) with POM2 antibody	4/5
FT(23-110) with Cu^{2+}	3/5
mPrP(23-230) with POM1 antibody	3/6
mPrP(23-230) with POM1_Y104A antibody	5/6
mPrP(23-230) with POM2 antibody	4/7

To investigate the channel activity of different PrP segments, single-channel electrical recordings were first carried out across physiologically relevant and negatively charged membranes comprised of DOPC and DOPG at a ratio of 4:1, suspended in 10 mM Hepes buffer (pH 7.4) with 1 M KCl [25]. The two sides separated by the lipid bilayer are cis or trans side, in which the cis part is defined as the grounded side. When a positive potential is applied, the positively charged analytes, like full-length mPrP(23-230) and other functional fragments, translocate from trans to cis through the bilayer. We added the recombinant PrP into the trans part of the chamber and monitored channel formation under 100 mV. Shown in Fig.2A-C, the near-zero currents indicated the low baseline permeability of the lipid membranes. The abrupt jumps in the recordings were attributed to channel formation, signifying the onset of individual ion channels facilitating ion diffusion across the membranes. A higher amplitude in these recordings suggests more ion permeation through the membranes induced by prion proteins. Fig. 2A represents the amplitude histograms, which display the number of observations that fall within a specific amplitude distribution. This figure has the upper and lower two plots, both showing unique observations of the full-length prion, mPrP(23-230) in single-channel electrical recording. The first plot indicates a single channel formation, while the second showcases a step-wise channel formation. mPrP(23-230) displayed two similar channels with distinct conductance (0.02 and 0.04 nS (Nanosiemens)), presumably caused by the conformational transition of heterogeneous PrP in lipid bilayers [26]. The conductance was

calculated through a formula: conduction=current/voltage. Interestingly, the multilevel conductance is very similar to the Alzheimer-associated Aβ pores [27] but differs from the typical folded, functional ion channels, which usually have two steady-state current levels (open and closed states) for controlling the ion flux [28-30]. This specific current pattern was seen in 60% of our experiments (n/N=3/5, where n represents the ion-channel formation events and N denotes the total experimental iterations), as detailed in Table 1.

We next aim to discern whether the N-terminus of prion protein (FT) could alone induce channel formation. Our observations revealed that both the FT(23-110), which spans the entire FT region (Fig. 2B), and FT(23-50) (Fig. 2C) sequences formed channels in the lipid bilayers. In contrast, other FT segments (residues 32-80, 53-90, and 93-120 in Fig. 2D) failed to induce pores formation in the lipid bilayers, This underscores the pivotal role of the proximal N-terminal amino acids (23-50) in the formation of PrP channel. These findings are consistent with previous research showing that mice expressing the initial nine amino acids (23–31) manifest spontaneous neurodegenerative phenotypes [31]. Additionally, this segment is identified as a transduction domain crucial for lipid membrane insertion [11, 12]. Our results further support the significance of FT (23–31) in PrP-related neurotoxicity. Interestingly, among all the mPrP segments and the full-length mPrP, the shortest fragment FT(23-50) exhibited the most pronounced channel formation. We identified six distinct pore clusters within the current trace of FT(23-50), varying the conductance from 2.25 to 11 nS. This stands in contrast to the FT(23-110) which only showed a conductance between 0.05-0.15 nS (Fig. 2C). Our data suggests that the FT(23-50) segment of the PrP protein is primarily responsible for membrane permeabilization, while the C-terminal domain and other FT sequences appear to down-regulate the channel formation of FT(23-50), especially within the context of the full-length mPrP(23-230) protein.

To validate that membrane permeabilization results from pore formation in the lipid bilayer, we employed cryo-electron microscopy (cryo-EM). Given its pronounced channel activity, the FT(23-50) fragment was selected for study, as we postulated that it could form oligomers of a size suitable for visualization under cryo-EM. Indeed, our cryo-EM observations identified pore-shaped oligomers with an average size of approximately 8-9 nm (Fig. 3). However, due to the inherent heterogeneity of these structures, it remains challenging to pinpoint the precise structure and determine the number of subunits constituting each pore. Nevertheless, the identification of pore formation in the FT(23-50) fragment lends weight to the toxic oligomer

hypothesis that the prion oligomers induce cellular membrane permeabilization, leading to the formation of pores or channels, thereby culminating in cellular dysfunction [14, 32, 33]. For comparison, we assessed the FT(23-100) pore formation using cryo-EM (Fig. S2) and found an absence of pore formation. This observation aligns with our expectation, given that FT(23-100) displays a significantly lower conductance, compared to FT(23-50). Such diminished conductance implies minimal channel activity, suggesting the formation of pores so minuscule that they elude detection via cryo-EM. Furthermore, the full-length mPrP(23-230) exhibited an even reduced conductance than FT(23-110), leading us to infer the absence of pore formation in the full-length mPrP(23-220).

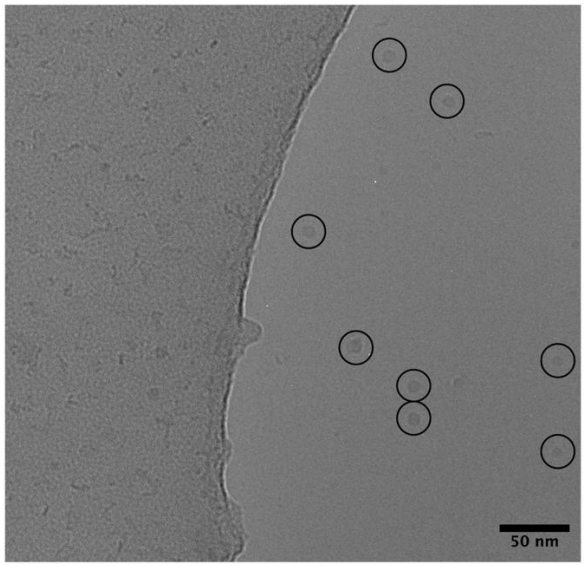

Figure 3. Cryo-EM image of prion fragment FT(23-50) (2 mg/mL). The sample was prepared at a concentration of 2 mg/mL. The image reveals the presence of pore formation in the FT(23-50) fragment, which is indicated by black circles. The average size of these pores is estimated to be approximately 8-9 nm.

4.3.2 Globular domain modulates the full-length mPrP(23-230) channel-forming activity in lipid membranes

To validate that the globular domain (GD) down-regulates the full-length mPrP(23-230) channel activity, we introduced the GD binding antibody, POM1. Our single-channel electrical recording data revealed a marked enhancement in the channel-forming activity of mPrP(23-230) (Fig. 4B). Given that POM1 alone does not induce the channel activity (Fig. S1), this suggests that upon binding to GD, POM1 augments the N-terminus interaction with lipid

membranes. This implies a possible conformational change of mPrP(23-230), driven by POM1 binding, that promotes the N-terminus interaction with the lipid bilayer, thus facilitating pore formation.

To substantiate our findings on the effect of POM1, we examined its mutant variant, POM1_Y104A antibody [21]. Though targeting the same epitope as POM1 on mPrP(23-230), the variant doesn't change the toxicity of mPrP (23-230) [21]. Notably, POM1_Y104A almost abolishes the channel-forming activity of mPrP(23-230) in the lipid bilayers (Fig. 4D). This points to the inability of POM1_Y104A to induce the toxic conformation that facilitates the FT's interaction with lipid membranes. Thus, it's inferred that POM1_Y104A alters the GD segment's conformation, allowing the C-terminus to inhibit the FT segment's interaction with lipid membranes. Our study is in agreement with the previous work by Frontzek et al., who demonstrated the neuroprotective effect of POM1_Y104A on neuronal cells expressing the prion proteins [34]. In essence, the antibodies modulate the prion protein neurotoxicity by interacting with the GD domain, thereby influencing the FT(23-50) channel-forming activity in lipid membranes.

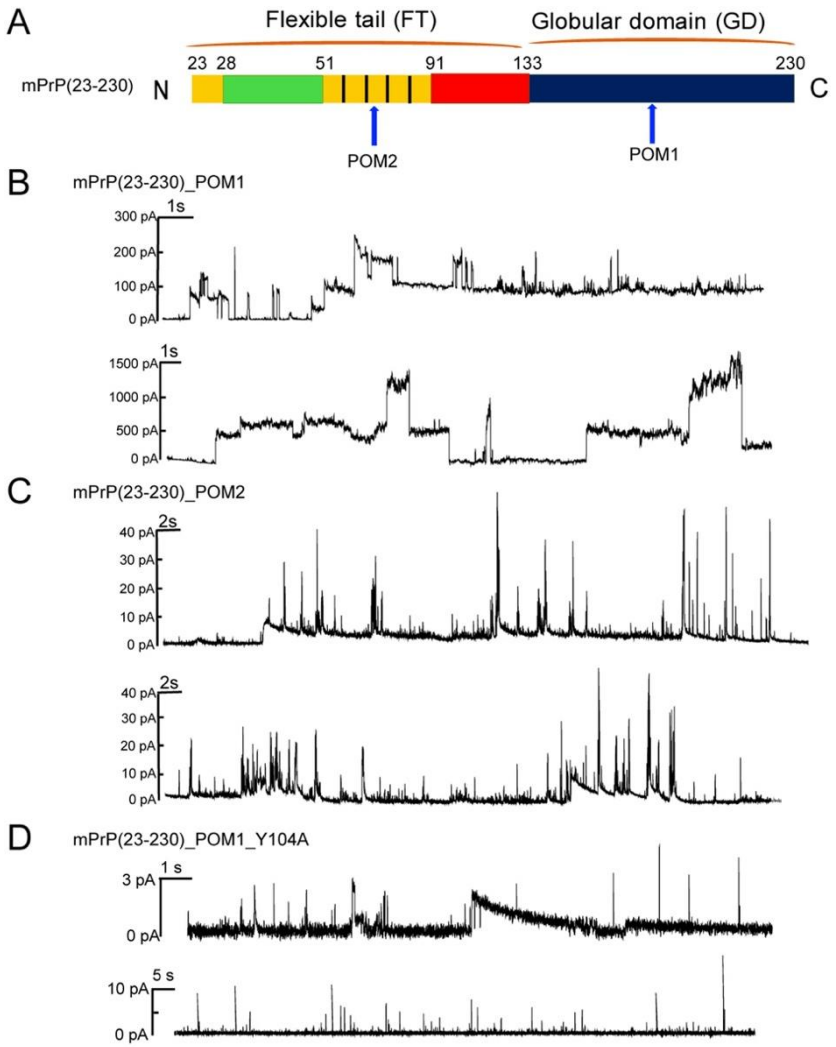

Figure 4. Schematic representative of single-channel electrical recordings with the full-length recombinant mPrP(23-230) protein in the presence of antibodies. (A) The binding of POM1 and POM2 antibodies to the GD domain and the octarepeats of the FT region, respectively, is depicted. (B) Representative traces of spontaneous currents recorded from mPrP(23-230) in the presence of POM1 (B), POM2 (C), and POM1_Y104A (D) are shown. It can be observed that POM1 significantly enhances the channel-forming activity of mPrP(23-230), while POM2 has a negligible effect on channel formation. POM1_Y104A retains the channel-forming activity. The proteins were added to the trans side at a final concentration of 0.4 μM.

4.3.3 The role of octarepeats (OR) stabilization and external agents on PrP channel-forming activity

So far, our data have highlighted that the primary N-terminus of the prion protein, particularly the FT(23-50), plays a pivotal role in channel formation. Based on this result, we sought to discern if the stabilization of other FT domains could modulate this activity. To this end, we introduced POM2, an antibody specifically targeting the octarepeat (OR) region, which spans residues 51-90. Upon the addition of POM2 to mPrP(23-230), we observed a pronounced surge in transient spike events, as depicted in Fig. 4C. These transient spikes are often indicative of impending prion ion channel formation and are emblematic of membrane destabilization [35]. Consequently, this increase suggests that the antibody-bound N-terminus might promote the interaction of mPrP(23-230) with lipid membranes. Such interactions would, in turn, increase the propensity for membrane destabilization. However, despite this interaction, POM2 didn't notably enhance the overall channel-forming activity of mPrP(23-230). From this observation, we hypothesize that the stabilization of the OR domain doesn't seem to counteract the inhibitory effects exerted by the GD domain on mPrP(23-230) channel activity.

To validate this hypothesis, we conducted further experiments with the FT(23-110) in the presence of the POM2 antibody, as presented in Fig. 5A. Given the absence of the GD domain, we anticipated that stabilizing OR might induce conformational changes in the FT fragment, thereby influencing prion channel activity. We indeed observed a marked increase in conductance, approximately 0.1-0.3 nS (Fig. 5B), compared to FT(23-110) alone. Surprisingly, we also detected an exceptionally high and diverse channel current, with conductance soaring to 30 nS. This conductance even surpassed that of FT(23-50), which implies that POM2 might render the FT(23-110) conformation more unstable and heterogeneous, yet more adept at permeabilizing lipid membranes. This outcome further underscores the repressive influence of the GD domain on the channel-forming capability of the N-terminus in full-length prion proteins within lipid membranes. Hence, we deduce that while the OR domain binding might exert a minimal effect on the channel-forming activity of the full-length mPrP(23-230), its stabilization in the absence of the GD domain significantly boosts the channel-forming prowess of the FT domain.

In addition to POM2, Cu^{2+} ions are also known to associate with the OR region, modulating PrP toxicity under physiological conditions [36]. Thus, we assessed whether Cu^{2+} ions would either enhance or diminish the channel-forming capacity of FT(23-110). Mirroring the effects observed with POM2, Cu^{2+} ions augmented the channel-forming activity of FT(23-110), as evidenced in Fig. 5C. These results further reinforce our understanding that conformational

changes in the OR segment, induced by Cu^{2+}, can amplify the neurotoxic properties of the FT(23-110) segment.

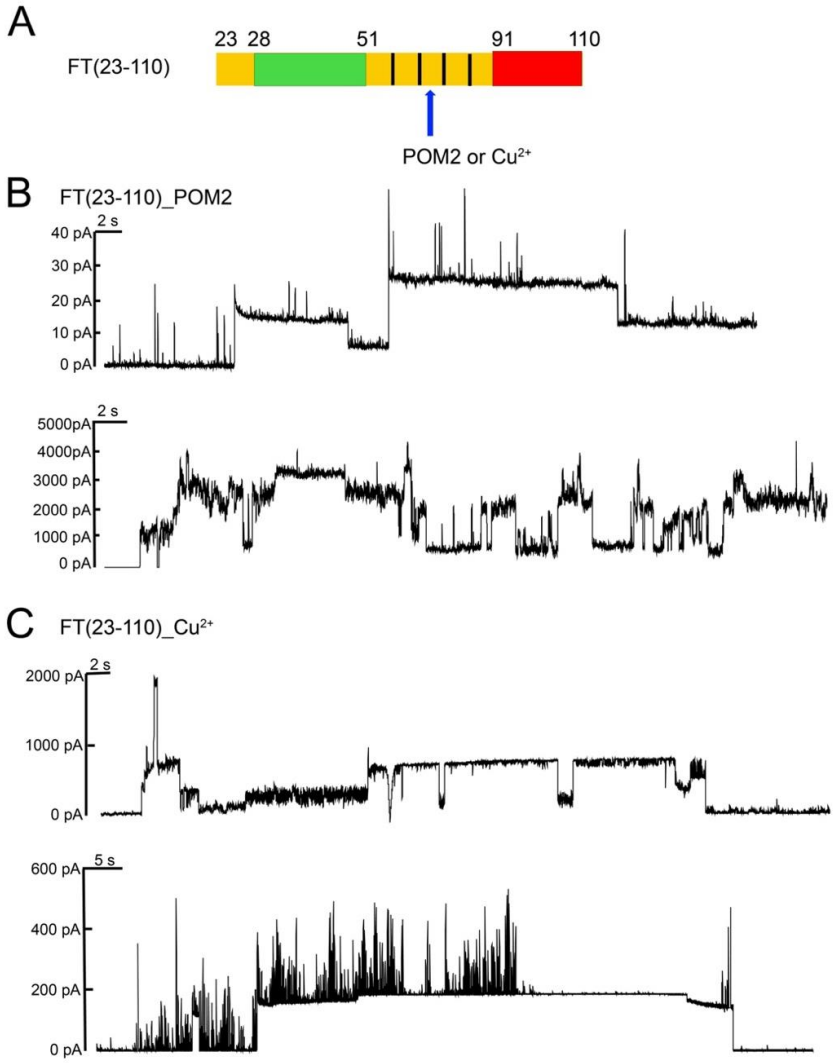

Figure 5 Representative single-channel electrical current traces of FT(23-110) in the presence of Cu^{2+} or antibodies. (A) The binding sites of the POM2 antibody and Cu2+ ions on the FT(23-110) sequence are depicted. (B-C) The representative traces of spontaneous currents were recorded from mPrP(23-230) in the presence of POM2 or Cu^{2+}. It is evident that both POM2 and Cu^{2+} significantly enhance the channel-forming activity of FT(23-110).

4.4 Discussion

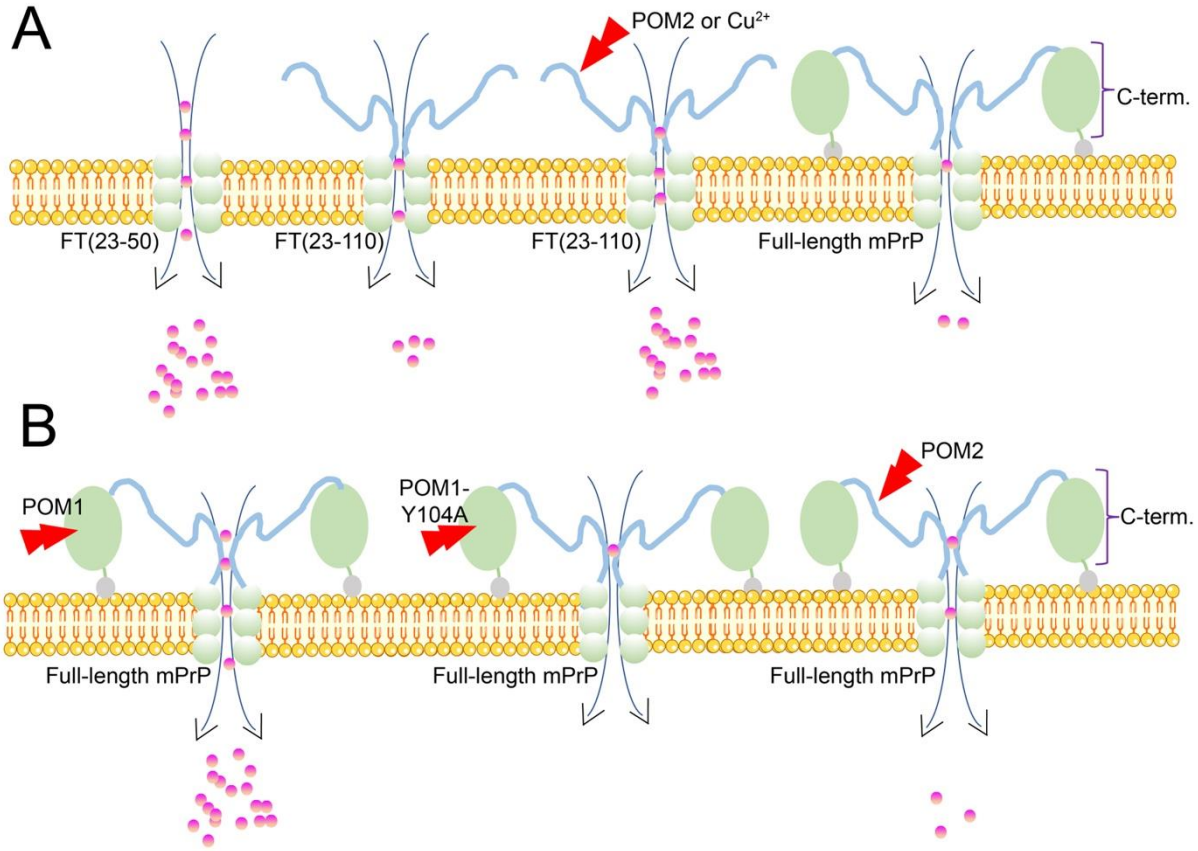

Figure 6. Ion channel formation model of prion fragments in the presence or absence of antibodies or Cu^{2+}. (A) Ion channel formation of N-terminal regions of FT(23-50), FT(23-110), FT(23-110) with POM2 antibody or Cu^{2+} and full-length mPrP. FT(23-50) (represented by green round balls) exhibits the highest channel-forming activity, indicating that FT(23-50) potential drives pore formation, enabling the permeation of cations (represented by pink round balls) through the lipid bilayer. POM2 antibody or Cu^{2+} binding to the OR segment of FT(23-110) enhances its channel-forming activity. (B) Ion channel formation of full-length mPrP with the antibody POM1, POM1_Y104A or POM2. POM1 antibody, which targets the C-terminus (GD domain represented by a green elliptical ball) of mPrP, significantly enhances channel-forming activity. POM1_Y104A antibody nearly abolishes the channel-forming activity of mPrP in lipid bilayers. POM2, on the other hand, does not enhance the channel-forming activity of mPrP, suggesting that the GD domain down-regulates N-terminus channel formation in full-length prion protein.

Neurodegenerative disorders, such as Alzheimer's, Parkinson's, and prion diseases, are thought to share a common neurotoxic mechanism involving the interaction of the misfolded amyloid proteins with cellular membranes, leading to the generation of pores or membrane

permeabilization and subsequent cell dysfunction [14, 27]. It has been shown that membrane poration could be a mechanism underlying the neurotoxic effects of prions [11-14]. The FT region, an intrinsically disordered domain, has been identified as playing a critical role in the pathogenesis of prion diseases [15]. Elucidating the contribution of different fragments of the prion protein to channel formation activity provides insights into the mechanism underlying prion-induced neurodegeneration. Recently, the Harris group demonstrated the primary polybasic amino acids (23-31) of the prion sequence as a prerequisite for the channel-forming activity of the truncated PrP protein (ΔCR PrP with 105-125 amino acids deleted) [11, 12]. However, the way in which GD and other FT regions modulate the primary N-terminal's channel-forming activity remains unclear. Here, several truncated fragments of prion proteins including different N-terminal functional regions were chosen to determine their roles in channel-forming activity. Utilizing the sensitive and dynamic single-channel electrical technique, our investigation revealed the prominent influence of the FT region and the inhibitory role of GD in modulating prion channel-forming activity, especially within the primary region.

Our results shed light on the intricate interplay between prion domains and lipid membranes in channel formation. We show that the full-length recombinant mPrP(23-230) is less active in channel formation than the N-terminal fragment FT(23-110). Interestingly, as we extend the amino acid sequence from FT(23-31), the channel-forming activity in the lipid bilayer diminishes. The fragment FT(23-50) stands out with the largest conductance within all the chosen prion fragments, ranging from 2.25-11 nS, indicating the highest channel activity. Our cryo-EM observations of this fragment revealed pore-like structures (Fig. 3), lending credence to the toxic oligomer hypothesis. Although we discerned six distinct pore clusters of FT(23-50) oligomers (Fig. 2C), the heterogeneity and insufficient particle numbers make it arduous to make a 2D classification of the particles and characterize the number of subunits in each pore.

Both FT(23-110) and full-length mPrP(23-230) display a reduced conductance, down to 0.2 nS. This data implies that GD or added FT sequence might be obstructing the channel-forming activity. Previous research reported that truncated PrP(1-109) induces higher ionic currents on N2a cells than that of truncated PrP segment FT(1-90), followed by FT(1-58) [12]. We postulate that the discrepancies from their findings arise due to the potential artifacts from the EGFP (enhanced green fluorescence protein) molecule equipped with a GPI (glycosylphosphatidylinositol) anchor linked to N-terminal PrP [12]. Similar to other FT

functional segments, we think the fused EGFP sequence presumably modulates the interaction of the primary N-terminal FT(23-50) with lipid membranes. Our setup provides a straightforward method without involving any external fused proteins to examine the channel-forming activity of truncated PrP in the lipid membranes.

The enhanced full-length mPrP(23-230) channel-forming activity with a C-terminal binding antibody POM1 rather than the N-terminal binding antibody POM2 reinforces the conclusion that the GD domain down-regulates the full-length mPrP channel-forming activity in the lipid membranes. Moreover, the binding of FT(23-110) to POM2 or Cu^{2+} increases the channel-forming activity. The provoked spontaneous ionic currents agree with the previous observation where the toxic POM1 antibody acted as a prion mimetic inducing neuronal death [37].

The detection of pore formations in FT(23-50) lends further support to the idea that these formations are responsible for the channel permeabilization in the lipid bilayer (Fig. 3). Although we noted the small current conductance (0.02-0.04 nS) of full-length mPrP(23-230), such subtle changes could be negligible in a complicated environment of cellular studies [11, 13]. In the presence of POM1,the conductance of mPrP(23-230) varied (approximately from 1-11 nS), with the peak levels closely mirroring those of FT(23-50). It is plausible that the POM1 binding stabilizes the C-terminus of mPrP(23-230), triggering a conformational shift that promotes mPrP(23-230) oligomerization and its N-terminal interaction with the lipid bilayer. However, there is a marked difference in the persistence of high conductance between mPrP(23-230) within POM1 and FT(23-50), in which the former lasts as short as only 1-2 seconds, indicative of being more transient and unstable, and the latter retains stable at around 11 nS for extended periods. Such heterogeneity in channel activity of mPrP(23-230) within POM1 complicates the direct confirmation of pore formation by Cryo-EM, even though this technique offers robust evidence for pore formations. To further validate mPrP(23-230) pore formations induced by antibodies, we suggest exploring other imaging methods capable of characterizing dynamic systems, though such investigations are beyond the current scope. However, it is imperative to acknowledge the limitations if our study. The truncated fragments are synthetic and do not naturally exist in human neurons. While the lipid we chose is physiologically relevant, it remains a simplified model lipid that lacks the intricate nuances of cellular environment.

In summary, our findings highlight the significant channel-forming activity and membrane permeabilization attributes of the primary N-terminal FT(23-50) fragment, as demonstrated in Fig 6. This observation aligns with the critical role of the primary nine amino acids (23-31) in driving channel formation (11). Additionally, we observed a negative correlation between membrane permeabilization and the presence of the C-terminal extended segment of the prion protein. The stabilization of this functional C-terminal segment appears to positively influence membrane permeabilization, shedding light on the molecular mechanism underlying prion neurotoxicity. These insights provide a basis for potential treatments or drug screening strategies targeting the toxic N-terminal FT(23-50) fragment while sparing other fragments. Moreover, our in-bulk approach, using single-channel electrical recordings combined with $_{cryo}$-EM imaging, provides an innovative and straightforward method to delineate the membrane permeabilization of the PrP pore-shaped oligomers, which can reveal the molecular and structural intricacies driving prion-mediated neurotoxicity. Understanding these processes can be helpful, not only for crafting tailored therapeutic strategies but also for screening inhibitors that can negate channel activity, especially in mitigating the oligomer-induced toxicity in other neurodegenerative diseases.

4.5 Materials and methods

4.5.1 Protein expression and purification

The recombinant full-length mouse mPrP(21-230), FT(23-119) and GD(111-231) have been previously described [38]. A series of fragmented PrP sequences, including the N-terminal flexible tail FT peptides (FT(23-50), FT(32-80), FT(53-90), FT(93-110)) were all purchased from EZ Biosciences.

4.5.2 Preparation of black bilayer lipid membrane

First, a mixture of DOPC (1,2-Dioleoyl-sn-glycero-3-phosphocholine): DOPG (1,2-Dioleoyl-sn-glycero-3-phospho-rac-(1-glycerol)) (20 mg/mL) at a ratio of 4:1 (w/w) which was dissolved in chloroform was prepared in a glass vial and then dried by N2 in a fume hood. To thoroughly eliminate the chloroform, a vacuum desiccator was further used overnight. The thin lipid film was added pentane (99%, Sigma-Aldrich, Cat number: 236705) to a final concentration of 10 mg/mL. The lipid bilayer was formed followed by the “Montal-Muller” technique [39]. Briefly, a home-made chamber separated by a 25 μm thick Teflon film (Good Fellow Inc., #FP301200) with a 150 μm aperture was prepared. The aperture was pretreated by

0.5 µL, 10 % (v/v) hexadecane/pentane mixture and was dried immediately by N2. Then 500 µL, 10 mM Hepes buffer (pH 7.4, with 1 M KCl) and 5 uL DOPC:DOPG (4:1, 10 mg/mL) was added into the two compartments (cis and trans) of the home-made chamber. The single-channel electrical recording was carried out at room temperature through a pair of Ag/AgCl electrodes. The cis side was defined as the grounded side and a voltage potential was applied to the trans side, which means that the positively charged analytes translocate from trans to cis through the bilayer.

4.5.3 Single-channel electrical recordings and data analysis

Single-channel electrical recordings were conducted in a whole cell mode with a patch clamp amplifier (Axopatch 200 B, Axon instrument, Molecular Devices, CA). The purified recombinant full-length mPrP(23-230) or the fragmented PrP (FT(23-110), FT(23-50), FT(32-80), OR(53-90) or FT(93-110)) in the presence of 0.1 % DDM, was added to the trans part of the chamber with the final concentration 0.4 µM. 100 mV voltage was applied during all the experiments. For data acquisition, a DigiData 1440 A/D converter (Axon) was equipped with a PC, where the pClamp and Clampfit were installed for data process. Ion channel permeabilization experiments with each prion fragment were performed at least three times, more typically 5-7 times.

4.5.4 Prion protein pore image by cryo-electron microscopy (cryo-EM)

3.5 µl of the FT(23-50) (2 mg/ml protein in PBS buffer) was pipetted onto a glow-discharged Quantifoil grid (R 1.2/1.3, Cu 200). Grids were blotted for 3.5 s with blot force 15 and plunge-frozen in liquid ethane using a Vitrobot Mark IV (ThermoFisher Scientific) with 100% humidity at 4 ˚C. Images were acquired on a Titan Krios electron microscope at 300 keV (Thermo Fisher), with a GIF Quantum LS Imaging filter (20 eV slit width), a K2 Summit electron counting direct detection camera (Gatan), using a magnification of 130000, resulting in a calibrated pixel size of 1.07Å.

4.5.5 Data availability

All data generated or analyzed during this study are included in this manuscript.

4.6 Funding and additional information

This work was supported by the Swiss National Science Foundation project grants (310030 197626 (J.L), the Brightfocus foundation (A20201759S (J.L.)), and China scholarship council (CSC).

4.7 Conflict interest

The authors declare that they have no conflicts of interest with the contents of this article.

4.8 References

(1) Prusiner, S. B. Prions. *Proceedings of the National Academy of Sciences* **1998**, *95* (23), 13363-13383. DOI: 10.1073/pnas.95.23.13363.
(2) Chiesa, R.; Harris, D. A. Prion Diseases: What Is the Neurotoxic Molecule? *Neurobiology of Disease* **2001**, *8* (5), 743-763. DOI: https://doi.org/10.1006/nbdi.2001.0433.
(3) Harris, D. A.; True, H. L. New Insights into Prion Structure and Toxicity. *Neuron* **2006**, *50* (3), 353-357. DOI: https://doi.org/10.1016/j.neuron.2006.04.020.
(4) Biasini, E.; Turnbaugh, J. A.; Unterberger, U.; Harris, D. A. Prion protein at the crossroads of physiology and disease. *Trends in Neurosciences* **2012**, *35* (2), 92-103. DOI: https://doi.org/10.1016/j.tins.2011.10.002.
(5) Silveira, J. R.; Raymond, G. J.; Hughson, A. G.; Race, R. E.; Sim, V. L.; Hayes, S. F.; Caughey, B. The most infectious prion protein particles. *Nature* **2005**, *437* (7056), 257-261. DOI: 10.1038/nature03989 PubMed.
(6) Simoneau, S.; Rezaei, H.; Salès, N.; Kaiser-Schulz, G.; Lefebvre-Roque, M.; Vidal, C.; Fournier, J.-G.; Comte, J.; Wopfner, F.; Grosclaude, J.; et al. In Vitro and In Vivo Neurotoxicity of Prion Protein Oligomers. *PLOS Pathogens* **2007**, *3* (8), e125. DOI: 10.1371/journal.ppat.0030125.
(7) Kayed, R.; Sokolov, Y.; Edmonds, B.; McIntire, T. M.; Milton, S. C.; Hall, J. E.; Glabe, C. G. Permeabilization of lipid bilayers is a common conformation-dependent activity of soluble amyloid oligomers in protein misfolding diseases. *J Biol Chem* **2004**, *279* (45), 46363-46366. DOI: 10.1074/jbc.C400260200 From NLM.
(8) Wu, J.; Cao, C.; Loch, R. A.; Tiiman, A.; Luo, J. Single-molecule studies of amyloid proteins: from biophysical properties to diagnostic perspectives. *Quarterly Reviews of Biophysics* **2020**, *53*, e12. DOI: 10.1017/S0033583520000086 From Cambridge University Press Cambridge Core.
(9) Wang, X.; Wang, F.; Arterburn, L.; Wollmann, R.; Ma, J. The interaction between cytoplasmic prion protein and the hydrophobic lipid core of membrane correlates with neurotoxicity. *J Biol Chem* **2006**, *281* (19), 13559-13565. DOI: 10.1074/jbc.M512306200 From NLM.
(10) Caughey, B.; Baron, G. S.; Chesebro, B.; Jeffrey, M. Getting a grip on prions: oligomers, amyloids, and pathological membrane interactions. *Annu Rev Biochem* **2009**, *78*, 177-204. DOI: 10.1146/annurev.biochem.78.082907.145410 PubMed.
(11) Solomon, I. H.; Biasini, E.; Harris, D. A. Ion channels induced by the prion protein: mediators of neurotoxicity. *Prion* **2012**, *6* (1), 40-45. DOI: 10.4161/pri.6.1.18627 PubMed.
(12) Wu, B.; McDonald, A. J.; Markham, K.; Rich, C. B.; McHugh, K. P.; Tatzelt, J.; Colby, D. W.; Millhauser, G. L.; Harris, D. A. The N-terminus of the prion protein is a toxic effector regulated by the C-terminus. *eLife* **2017**, *6*, e23473. DOI: 10.7554/eLife.23473.

(13) Solomon, I. H.; Huettner, J. E.; Harris, D. A. Neurotoxic mutants of the prion protein induce spontaneous ionic currents in cultured cells. *The Journal of biological chemistry* **2010**, *285* (34), 26719-26726. DOI: 10.1074/jbc.M110.134619 PubMed.
(14) Ambadi Thody, S.; Mathew, M. K.; Udgaonkar, J. B. Mechanism of aggregation and membrane interactions of mammalian prion protein. *Biochimica et Biophysica Acta (BBA) - Biomembranes* **2018**, *1860* (9), 1927-1935. DOI: https://doi.org/10.1016/j.bbamem.2018.02.031.
(15) Hara, H.; Sakaguchi, S. N-Terminal Regions of Prion Protein: Functions and Roles in Prion Diseases. *International journal of molecular sciences* **2020**, *21* (17), 6233. DOI: 10.3390/ijms21176233 PubMed.
(16) Chattopadhyay, M.; Walter, E. D.; Newell, D. J.; Jackson, P. J.; Aronoff-Spencer, E.; Peisach, J.; Gerfen, G. J.; Bennett, B.; Antholine, W. E.; Millhauser, G. L. The Octarepeat Domain of the Prion Protein Binds Cu(II) with Three Distinct Coordination Modes at pH 7.4. *Journal of the American Chemical Society* **2005**, *127* (36), 12647-12656. DOI: 10.1021/ja053254z.
(17) Watt, N. T.; Taylor, D. R.; Kerrigan, T. L.; Griffiths, H. H.; Rushworth, J. V.; Whitehouse, I. J.; Hooper, N. M. Prion protein facilitates uptake of zinc into neuronal cells. *Nature Communications* **2012**, *3* (1), 1134. DOI: 10.1038/ncomms2135.
(18) Evans, E. G. B.; Millhauser, G. L. Chapter Two - Copper- and Zinc-Promoted Interdomain Structure in the Prion Protein: A Mechanism for Autoinhibition of the Neurotoxic N-Terminus. In *Progress in Molecular Biology and Translational Science*, Legname, G., Vanni, S. Eds.; Vol. 150; Academic Press, 2017; pp 35-56.
(19) Evans, Eric G. B.; Pushie, M. J.; Markham, Kate A.; Lee, H.-W.; Millhauser, Glenn L. Interaction between Prion Protein's Copper-Bound Octarepeat Domain and a Charged C-Terminal Pocket Suggests a Mechanism for N-Terminal Regulation. *Structure* **2016**, *24* (7), 1057-1067. DOI: https://doi.org/10.1016/j.str.2016.04.017.
(20) Thakur, A. K.; Srivastava, A. K.; Srinivas, V.; Chary, K. V. R.; Rao, C. M. Copper Alters Aggregation Behavior of Prion Protein and Induces Novel Interactions between Its N- and C-terminal Regions. *Journal of Biological Chemistry* **2011**, *286* (44), 38533-38545. DOI: https://doi.org/10.1074/jbc.M111.265645.
(21) Frontzek, K.; Bardelli, M.; Senatore, A.; Henzi, A.; Reimann, R. R.; Bedir, S.; Marino, M.; Hussain, R.; Jurt, S.; Meisl, G.; et al. A conformational switch controlling the toxicity of the prion protein. *Nature Structural & Molecular Biology* **2022**, *29* (8), 831-840. DOI: 10.1038/s41594-022-00814-7.
(22) Polymenidou, M.; Moos, R.; Scott, M.; Sigurdson, C.; Shi, Y.-z.; Yajima, B.; Hafner-Bratkovič, I.; Jerala, R.; Hornemann, S.; Wuthrich, K.; et al. The POM Monoclonals: A Comprehensive Set of Antibodies to Non-Overlapping Prion Protein Epitopes. *PLOS ONE* **2008**, *3* (12), e3872. DOI: 10.1371/journal.pone.0003872.
(23) Frontzek, K.; Pfammatter, M.; Sorce, S.; Senatore, A.; Schwarz, P.; Moos, R.; Frauenknecht, K.; Hornemann, S.; Aguzzi, A. Neurotoxic Antibodies against the Prion Protein Do Not Trigger Prion Replication. *PLoS One* **2016**, *11* (9), e0163601. DOI: 10.1371/journal.pone.0163601 From NLM.
(24) Herrmann, U. S.; Sonati, T.; Falsig, J.; Reimann, R. R.; Dametto, P.; O'Connor, T.; Li, B.; Lau, A.; Hornemann, S.; Sorce, S.; et al. Prion Infections and Anti-PrP Antibodies Trigger Converging Neurotoxic Pathways. *PLOS Pathogens* **2015**, *11* (2), e1004662. DOI: 10.1371/journal.ppat.1004662.
(25) Wu, J.; Blum, T. B.; Farrell, D. P.; DiMaio, F.; Abrahams, J. P.; Luo, J. Cryo-electron microscopy imaging of Alzheimer's amyloid-beta 42 oligomer displayed on a functionally and structurally relevant scaffold. *Angewandte Chemie International Edition n/a* (n/a). DOI: https://doi.org/10.1002/anie.202104497.

(26) Kourie, J. I.; Culverson, A. L.; Farrelly, P. V.; Henry, C. L.; Laohachai, K. N. Heterogeneous amyloid-formed ion channels as a common cytotoxic mechanism. *Cell Biochemistry and Biophysics* **2002**, *36* (2), 191-207. DOI: 10.1385/CBB:36:2-3:191.
(27) Quist, A.; Doudevski, I.; Lin, H.; Azimova, R.; Ng, D.; Frangione, B.; Kagan, B.; Ghiso, J.; Lal, R. Amyloid ion channels: A common structural link for protein-misfolding disease. *Proceedings of the National Academy of Sciences* **2005**, *102* (30), 10427-10432. DOI: doi:10.1073/pnas.0502066102.
(28) Wu, J.; Blum, T. B.; Farrell, D. P.; DiMaio, F.; Abrahams, J. P.; Luo, J. Cryo-electron Microscopy Imaging of Alzheimer's Amyloid-beta 42 Oligomer Displayed on a Functionally and Structurally Relevant Scaffold. *Angewandte Chemie International Edition* **2021**, *n/a* (n/a), https://doi.org/10.1002/anie.202104497. DOI: https://doi.org/10.1002/anie.202104497 (acccessed 2021/07/29).
(29) Tombola, F.; Pathak, M. M.; Isacoff, E. Y. How Does Voltage Open an Ion Channel? *Annual Review of Cell and Developmental Biology* **2006**, *22* (1), 23-52. DOI: 10.1146/annurev.cellbio.21.020404.145837.
(30) Jang, H.; Arce, F. T.; Capone, R.; Ramachandran, S.; Lal, R.; Nussinov, R. Misfolded Amyloid Ion Channels Present Mobile β-Sheet Subunits in Contrast to Conventional Ion Channels. *Biophys J* **2009**, *97* (11), 3029-3037. DOI: https://doi.org/10.1016/j.bpj.2009.09.014.
(31) Westergard, L.; Turnbaugh, J. A.; Harris, D. A. A Nine Amino Acid Domain Is Essential for Mutant Prion Protein Toxicity. *The Journal of Neuroscience* **2011**, *31* (39), 14005-14017. DOI: 10.1523/jneurosci.1243-11.2011.
(32) Hu, P. P.; Huang, C. Z. Prion protein: structural features and related toxicity. *Acta Biochimica et Biophysica Sinica* **2013**, *45* (6), 435-441. DOI: 10.1093/abbs/gmt035 (acccessed 5/28/2022).
(33) Legname, G.; Scialò, C. On the role of the cellular prion protein in the uptake and signaling of pathological aggregates in neurodegenerative diseases. *Prion* **2020**, *14* (1), 257-270. DOI: 10.1080/19336896.2020.1854034.
(34) Frontzek, K.; Bardelli, M.; Senatore, A.; Henzi, A.; Reimann, R. R.; Bedir, S.; Marino, M.; Hussain, R.; Jurt, S.; Meisl, G.; et al. A conformational switch controlling the toxicity of the prion protein. *bioRxiv* **2021**, 2021.2009.2020.460912. DOI: 10.1101/2021.09.20.460912.
(35) Bode, D. C.; Baker, M. D.; Viles, J. H. Ion channel formation by amyloid-β42 oligomers but not amyloid-β40 in cellular membranes. *Journal of Biological Chemistry* **2017**, *292* (4), 1404-1413.
(36) Evans, E. G. B.; Pushie, M. J.; Markham, K. A.; Lee, H.-W.; Millhauser, G. L. Interaction between Prion Protein's Copper-Bound Octarepeat Domain and a Charged C-Terminal Pocket Suggests a Mechanism for N-Terminal Regulation. *Structure* **2016**, *24* (7), 1057-1067. DOI: 10.1016/j.str.2016.04.017 PubMed.
(37) Sonati, T.; Reimann, R. R.; Falsig, J.; Baral, P. K.; O'Connor, T.; Hornemann, S.; Yaganoglu, S.; Li, B.; Herrmann, U. S.; Wieland, B.; et al. The toxicity of antiprion antibodies is mediated by the flexible tail of the prion protein. *Nature* **2013**, *501* (7465), 102-106. DOI: 10.1038/nature12402.
(38) Küffer, A.; Lakkaraju, A. K. K.; Mogha, A.; Petersen, S. C.; Airich, K.; Doucerain, C.; Marpakwar, R.; Bakirci, P.; Senatore, A.; Monnard, A.; et al. The prion protein is an agonistic ligand of the G protein-coupled receptor Adgrg6. *Nature* **2016**, *536* (7617), 464-468. DOI: 10.1038/nature19312.
(39) Montal, M.; Mueller, P. Formation of bimolecular membranes from lipid monolayers and a study of their electrical properties. *Proceedings of the National Academy of Sciences of the United States of America* **1972**, *69* (12), 3561-3566. DOI: 10.1073/pnas.69.12.3561 PubMed.

4.9 Abbreviations

DOPC: 1,2-Dioleoyl-sn-glycero-3-phosphocholine

DOPG: 1,2-Dioleoyl-sn-glycero-3-phospho-rac-(1-glycerol)

FT: flexible tail

GD: globular domain

4.10 Supporting information

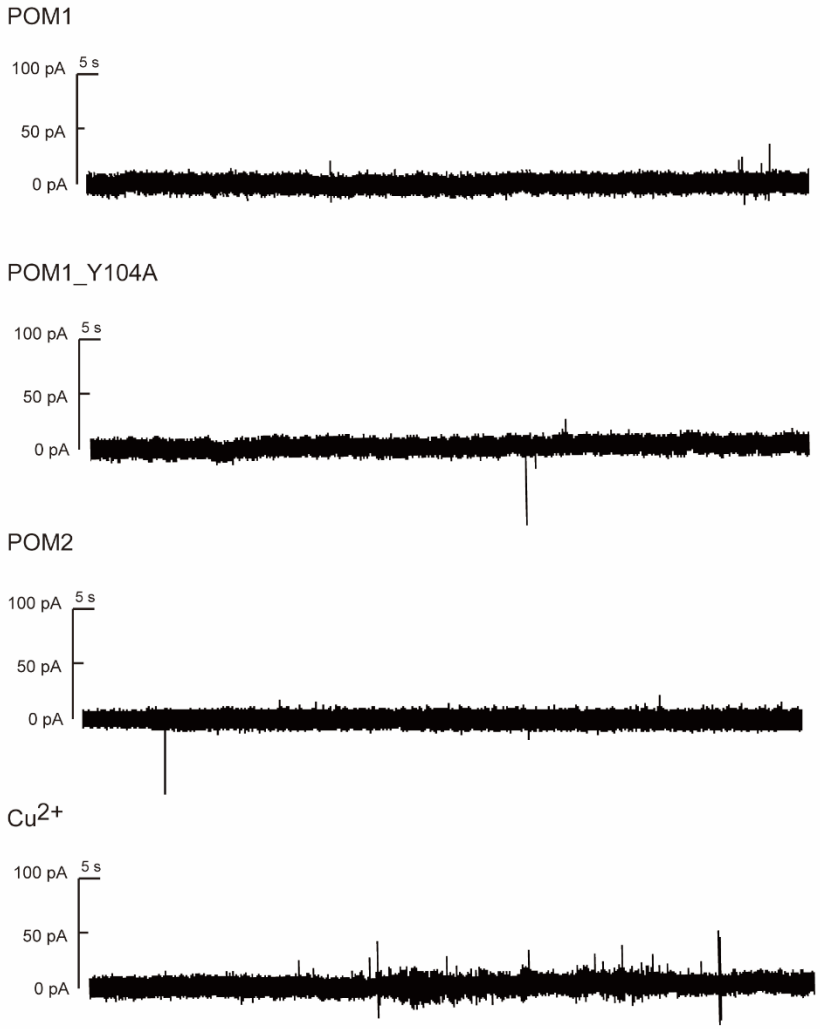

Figure S1. Representative single-channel electrical current traces of 0.4 μM POM1, 0.4 μM POM1_Y104A, 0.4 μM POM2 or 5 μM Cu^{2+} ions. The experiments were conducted under 100 mV.

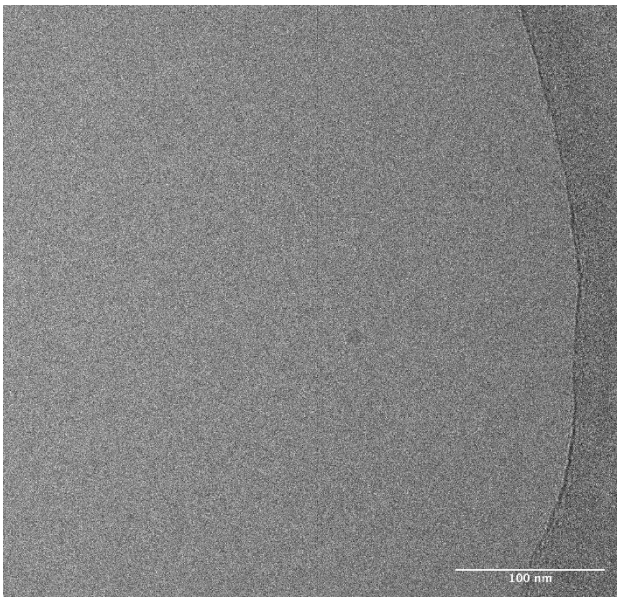

Figure S2. Example of a cryo-electron microscopy (Cryo-EM) micrograph of the prion fragment FT(23-110). The sample was prepared at a concentration of 2 mg/ml. No stable oligomeric species/pore by the FT(23-110) fragment could be visualized by cryo-EM imaging.

Chapter 5

Identifying the role of co-aggregation of Alzheimer's amyloid-β with amorphous protein aggregates of non-amyloid proteins

Jinming Wu[1], Nicklas Österlund[2,3], Hongzhi Wang[1], Rebecca Sternke-Hoffmann[1], Hegne Pupart[1], Leopold L. Ilag[3], Astrid Gräslund[2], Jinghui Luo[1,*]

1. Department of Biology and Chemistry, Paul Scherrer Institute, 5232 Villigen, Switzerland
2. Department of Biochemistry and Biophysics, Stockholm University, Stockholm 106 91, Sweden
3. Department of Materials and Environmental Chemistry, Stockholm University, Stockholm 106 91, Sweden

*Corresponding author: Jinghui.luo@psi.ch

Accepted by ***Cell Reports Physical Science***.

DOI：https://doi.org/10.1016/j.xcrp.2022.101028

5.1 Abstract

Protein homeostasis collapse typically leads to protein aggregation into amyloid fibrils and diffuse amorphous aggregates, which both occur in Alzheimer's and other neurodegenerative diseases, but their relationship remains to be clarified. Here we examine the interactions between the amorphously aggregated non-chaperone proteins (albumin, β-lactoglobulin, and superoxide dismutase 1) and Alzheimer's amyloid-β (Aβ) peptides. Amorphous aggregates suppress the primary nucleation and elongation of Aβ fibrillation and modulate Aβ toxicity. The higher inhibitory efficiency of intermediately sized molten globular aggregates (20-300 nm) on Aβ fibrillation is hypothesized to be due to the higher amount of exposed hydrophobic residues and higher free energy. The formed co-aggregates are off-pathway species that favor formation of the amorphous end-state instead of fibrillar amyloid structures normally formed by Aβ. Our findings expand our knowledge of how the native and aggregated cellular proteins modulate Aβ aggregation at the molecular and mesoscopic level and point out the major conclusions.

Keywords: amorphous aggregates; neurodegenerative diseases; globular proteins; aggregation; toxicity

5.2 Introduction

In a balanced proteome, protein homeostasis (proteostasis) maintains the protein quality-control systems [1] through molecular chaperones, proteolytic systems, and other molecular regulators [2]. For instance, molecular chaperones control the folding status of the native protein state from the intermediates. Proteostasis collapse occurs when these protein systems and processes do not function properly and are out of balance. Such collapse thus results in increased protein misfolding, new types of intra- and intermolecular interactions, and subsequent protein aggregation [2]. Aggregation can in turn lead to the accumulation of a series of different non-native species, including transient or metastable oligomers, amorphous aggregates without defined structure, or highly ordered amyloid fibrils [3-6]. As two common end deposits, amorphous aggregates, and amyloid fibrils are thermodynamically more stable than other aggregated species [7].

Aging is a predominant risk factor for proteostasis collapse, which contributes to the development of neurodegenerative and other disorders related to protein aggregation, such as Alzheimer's (AD) and Parkinson's diseases (PD) [8,9]. Over 35 peptides/proteins have been

reported to deposit as amyloid fibrils in human pathologies [8,9], including the amyloid-β (Aβ) peptide in AD and the α-synuclein protein in PD. Amorphous aggregates (e.g., from protein p53 and superoxide dismutase 1 (SOD1)), are furthermore associated with about 20 human diseases including cancer and amyotrophic lateral sclerosis [8]. Amorphous protein aggregates as diffuse deposits are also known to co-exist with more compact fibrillar amyloid aggregates in human AD brains [10]. In both cases, the Aβ peptide is a major component of the deposits [11,12]. It has been suggested that amorphous protein aggregates can interconvert to the fibrillar ones [7,13-15]. However, the more detailed molecular understanding about the interaction between different types of amorphous protein aggregates, fibrillar aggregates and disease mechanisms remains unclear.

Aggregation is greatly affected by other proteins in the cellular context. For example, it has been shown that amyloid fibril formation can be modulated by chaperone proteins [16], non-chaperone proteins [17-19], and other amyloidogenic proteins [20-23]. Prevalent molecular chaperones, e.g., Bri2 [24-26], Brichos [27,28], αB-crystallin [29], and DNAJB6 [30], show potent anti-amyloid activity and also decrease oligomer-related neurotoxicity [31]. Some globular non-chaperone proteins, like lysozyme and human serum albumin (HSA) [32,33], can inhibit Aβ fibril formation, although the molecular interaction mechanisms remain to be explored [17,18]. In such studies, the fibrillation kinetic assays are typically carried out at 37°C in bulk solution, where these chaperone and globular proteins themselves are prone to the formation of mesoscopic amorphous aggregates [34]. It is possible or even likely that aggregates of chaperone and globular protein may influence amyloid protein fibrillation during fibrillation assays where monomeric proteins are added at the starting point. Furthermore, amorphous aggregates have been observed in the presence of amyloid protein with chaperone or non-chaperone proteins [35]. It has recently been suggested that intrinsic aggregation propensity is an important and general property of ATP-independent chaperones [35], as such chaperones are often polydisperse and exchange rapidly between different aggregation states [36,37]. It is therefore of great interest to investigate further how aggregated species of common non-chaperone proteins affect amyloid formation.

Here we have investigated the molecular interactions between amorphous protein aggregates, formed from common globular proteins, and the Aβ peptide undergoing fibrillation in vitro. Amorphous aggregates have been prepared from human serum albumin (HSA), β-lactoglobulin (BLG), and superoxidase dismutase 1 (SOD1). All these proteins are common model proteins for simple small soluble proteins. HSA is the most abundant protein in the human plasma [38], and is regarded as one of the most potent Aβ sequestering systems in that it binds 90% to

95% of the Aβ in the blood plasma [39]. SOD1 is a key antioxidant enzyme, and is also one of the major targets for oxidative damage in the brains of patients suffering from Alzheimer's disease (AD) [40,41]. BLG is the major protein of milk at an approximate concentration of 3 g/l [42]. Although not being a human protein, BLG is assumed to form amorphous aggregates that may affect human proteins within a digestive system. We observed that all of these proteins, and amorphous aggregates formed from them, can suppress Aβ fibrillation and regulate the toxicity in neuronal cells. The fibrillation inhibition efficiency can be regulated by the size of the amorphous aggregates. By using native ion mobility-mass spectrometry (MS), we revealed that partially unfolded BLG can form co-complexes with Aβ. Our study provides new insights into amyloid protein interaction with chaperone and non-chaperone proteins and delivers a possible molecular relationship between diffuse deposits and Aβ fibrils in AD.

5.3 Results

5.3.1 HSA, BLG, and SOD1 form amorphous aggregates in vitro after heat treatment

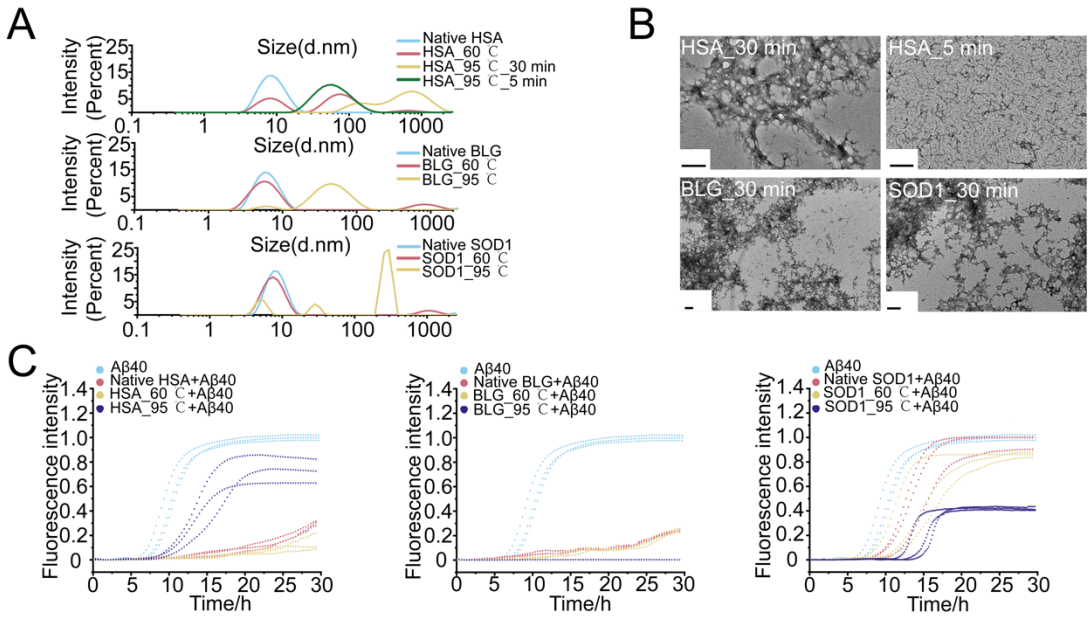

Figure 1. Preparation of amorphous aggregates and their inhibitory effects on Aβ40 aggregation. (A) Scattering intensity of size distribution (diameter, d.nm) of non-chaperone proteins (HSA, BLG and SOD1) under the native and amorphous states. The final concentration of proteins is 7.5 μM. The amorphous aggregates were prepared by denaturing at 60 (red line) or 95 °C (yellow line) for 30 min respectively. HSA was optimized by decreasing the denaturation time to 5 min at 95 °C (green line). The native proteins were freshly prepared on ice as a control (blue line). **(B)** TEM images of 5 μM amorphous aggregates

of HSA, BLG, and SOD1. HSA was denatured at 95 °C for 30 min or 5 min. BLG or SOD1 was denatured at 95 °C for 30 min. The scale bar is 200 nm. **(C)** ThT (20 μM) measurement of Aβ40 aggregation kinetics in the presence of native or amorphous states of non-chaperone proteins. The measurement was conducted at 37 ℃ without agitation. The final concentration of Aβ40 is 10 μM with 0.5 μM non-chaperone proteins in 20 mM PB buffer (pH 7.4).

Protein aggregates were prepared by denaturing the freshly prepared non-chaperone proteins (HSA, BLG, and SOD1, each at 50 μM) at 95 °C for 30 min. Denaturation at 60 °C for 30 min was also performed as a comparison. The size distribution of the denatured proteins was then analyzed using dynamic light scattering (DLS) experiments (Figure 1A). DLS analysis of HSA revealed a broad size distribution with two populations, ranging from 150 nm to 700 nm after incubation at 95°C for 30 min (Figure 1A, yellow trace). No peak for a native species expected to be located at around 7 nm (blue trace) was detected, which is in accordance with a previous study [43]. This indicates substantial conversion from monomers to higher-order aggregates. The denaturation of HSA at 60°C for 30 min, led to aggregation into particles with smaller diameters (red trace). A relatively high amount of the native species was also retained after incubation at this lower temperature. Similar sized HSA aggregates as were obtained at 60°C could also be obtained by a short incubation at 95°C for only 5 min (green trace). Incubation of BLG and SOD1 (Figure 1A) at 95°C for 30 min led to the formation of aggregates with diameters of 50 nm or 300 nm. Compared to the size distribution of these samples incubated at 60 °C, the aggregates were predominant in the solution and the relative number of native species was small.

Native MS (mass spectrometry) analysis of samples similarly incubated at 95°C for 30 min revealed that SOD1 convert into a state with large unresolved peaks indicative of large aggregates, in addition to more clearly distinguishable monomeric and dimeric states (Figure S1A) typically detected for native wild-type SOD1 [44]. All signals for incubated SOD1 are however low in intensity, indicating that most of the protein population has converted into a state not observable by native MS. BLG on the other hand was observed as a wide distribution of charge states, corresponding to unfolded monomers, dimers, and trimers, after incubation at the same conditions (Figure S1B). The signal intensity was in this case high and all signals could be nicely resolved. It has been observed from the DLS result (Figure 1A) that a higher amount of BLG monomers formed the amorphous aggregates compared to the SOD1 monomers, but a well-resolved charge state distribution including the monomers was only observed for BLG, but not SOD1. We assume the reason mainly attributed to the different

stabilities and equilibrium to the monomer or other low molecular oligomers of BLG and SOD1 aggregates in the gas phase via the process of electrospray ionization in the native MS measurement. HSA could on the other hand not be sprayed and analyzed in native MS at all after incubation at 95°C for 30 min. These observations are in agreement with the DLS results (Figure 1A), as BLG is converted into smaller aggregates compared to SOD1 and HSA after the incubation. Further native MS experiments were thus focused on BLG.

BLG incubation over time induced a shift from a native folded state in which monomers and dimers are in low charged states below, to a state where dimers dissociate into unfolded monomers with higher electrospray charge. Electrospray charging is dependent on solvent accessible surface area (SASA) and a shift from low charge states to higher charge states is associated with unfolding, as the detected SASA is increasing [45]. The so-called Rayleigh limit (zR) is the highest electrospray charge state that can theoretically originate from ionization of a folded protein of a particular size, and charge states of higher charge than this indicates a shift towards more extended states (Figure S2A). Such unfolding over time was also confirmed using circular dichroism (CD) spectroscopy and ion-mobility (IM) spectrometry. The melting of the protein could be seen in CD spectroscopy as a shift from the native β-sheet structure of BLG into a more helical structure (Figure S2B). Unfolding of BLG with increased temperature was furthermore observed in IM as the drift time of ions increased (Figure S2C). Taken together this seems to indicate that heating of BLG results in the formation of a soluble molten globular state which then aggregates to form non-native oligomers and aggregates.

The amorphous morphology of aggregates formed from these globular proteins at 95 °C was confirmed by transmission electron microscopy (TEM) imaging (Figure 1B). BLG and SOD1 aggregate homogeneously after 30 min incubation at 95 °C. HSA heated at 95 °C for 30 min and 5 min shows different morphologies, in which the latter displays smaller aggregates in agreement with the DLS data. HSA incubated at 60 °C for 30 min displayed incomplete denaturation (Figure S3). To further demonstrate how different denaturation conditions induce the partially or fully denatured HSA, circular dichroism (CD) spectroscopy measurements were further applied. The results shown in Figure S3B exhibited the characteristic CD spectra of native HSA measured in the far-UV region with two negative signals at ~208 nm and ~222 nm and one positive signal at ~ 193 nm, attributions to the typical α-helical conformation of HSA [46]. The CD signal gradually decreased as the denaturation temperature increased from 60 °C to 95 °C both for 30 min, indicative of the loss of the α-helix content caused by the formation of large aggregates over denaturation. Though the shape of CD curves remained very similar

between denatured HSA at 60 °C and at 95 °C for 30 min, the TEM observation (Figure 1B & S3) provided complementary information to show the structural difference of the denatured aggregates. HSA denatured at 95 °C for 5 min showed a lower diminished CD intensity than the denaturation at 95 °C for 30 min, suggesting the less aggregated states of HSA at a shorter time. This is consistent with the TEM results in figure 1B that HSA formed a bigger size of aggregates when denatured at 95 °C for 30 min. These results confirm that HSA forms homogeneous-size amorphous aggregates after 5min incubation at 95 °C.

5.3.2 Amorphous aggregates show better Aβ40 fibril inhibition than natively folded proteins

To monitor the effects of amorphous aggregates on Aβ40 peptide fibrillation, Thioflavin T (ThT) aggregation kinetics assays were carried out at 37 ℃. ThT is a common fluorescence probe for binding amyloid fibrils with an increased emitted fluorescence. Here, Aβ40 was used instead of Aβ42, which was mainly due to the longer primary nucleation of Aβ40 than that of Aβ42 under the same fibrillation conditions. The longer nucleation process would allow us to better determine how the amorphous aggregates affect Aβ monomeric or oligomeric species during the primary nucleation. Additionally, we have established a highly reproducible kinetic protocol for Aβ40 fibrillation based on our previous publication [16,22] but not for Aβ42 peptides, due to the Aβ42's fast accumulation kinetics. On the other hand, though Aβ42 is more toxic than Aβ40, Aβ40 can be substantially deposited in AD's brain as well. Therefore, we chose Aβ40 peptides to understand the interactions with amorphously aggregated globular proteins (HSA, BLG, and SOD1).

In agreement with previous studies [5], Aβ40 fibrillation kinetics in figure 1C can be fitted with a sigmoidal kinetic curve. The presence of 0.5 μM of any of the three studied globular native proteins led to a decrease in aggregation rate. Native HSA and BLG were particularly effective at decreasing the aggregation rate. The result is consistent with previous reports that the monomeric HSA [32,33] and BLG [17] inhibit Aβ40 fibrillation kinetics, and significantly prolong the lag time. The inhibitory effect on Aβ40 fibrillation increased further when SOD1 and BLG were pre-incubated at 95°C for 30 min before mixing with Aβ40, while proteins pre-incubated at 60°C had similar inhibitory effects as native proteins. This can be explained by the fact that DLS measurements revealed a high fraction of native species in these samples. The ratio of globular proteins to Aβ40 (0.5 μM:10 μM) was chosen based on our previous report that a series of native globular proteins can prevent Aβ40 fibrillation at a substoichiometric ratio [17]. On the other hand, a higher concentration of globular proteins can completely suppress Aβ40

at both monomeric and amorphously aggregated states, in which the different effects of different states of globular proteins on Aβ fibrillation cannot be distinguished. The ThT results (Figure 1C) show that denatured and aggregated states of non-chaperone proteins show stronger inhibitory efficiency on Aβ40 peptides aggregation than their natively folded states.

It was noted that the concentration of globular proteins via DLS measurements is 7.5 μM, which is higher than the concentration (0.5 μM) to interact with Aβ40 in the ThT assay. The reason we chose a higher concentration in DLS measurements is due to the low DLS signal-to-noise ratio when the protein concentration is in the range of 0.01-0.4 μM. To further demonstrate the concentration variation will not change the distribution percentage of globular proteins in an aqueous solution, here we applied CD spectroscopy to compare the secondary structure of BLG between a higher and a lower concentration. The result in figure S3C showed that the higher concentration of BLG has a bigger CD signal intensity, but the CD signal shape curve was retained at the same position under these two different concentrations. This suggested that concentration dilution would not affect the secondary structure of the denatured proteins, which will not influence the proportion of aggregates in the solution.

Aggregates of HSA prepared at 95 ℃ for 30 min, which were larger than aggregates formed by BLG and SOD1, did only display a marginal retardation of Aβ40 aggregation compared to HSA monomers. The smaller aggregates formed after incubation at 60 ℃ for 30 min did however prolong Aβ40 fibrillation times more than monomeric HSA. This indicates that not all protein aggregates are capable of suppressing fibrillation, and that the smaller amorphous HSA aggregates formed at 60 ℃ suppress Aβ40 aggregation more effectively compared to monomers, or the bigger aggregates formed at 95 ℃. We therefore further optimized the preparation method of HSA aggregates by reducing the denaturation time at 95 ℃ for 30 min to 5 min. Under these conditions, we observed formation of smaller (40 nm diameter) amorphous HSA aggregates with a single peak from the DLS result (Figure 1A), which indeed also displayed a stronger inhibitory effect on Aβ40 aggregation from ThT fluorescence assay (Figure S4). These results indicate an important correlation between formation of intermediate sized amorphous protein aggregates and Aβ40 fibrillation inhibition, that has not been studied before.

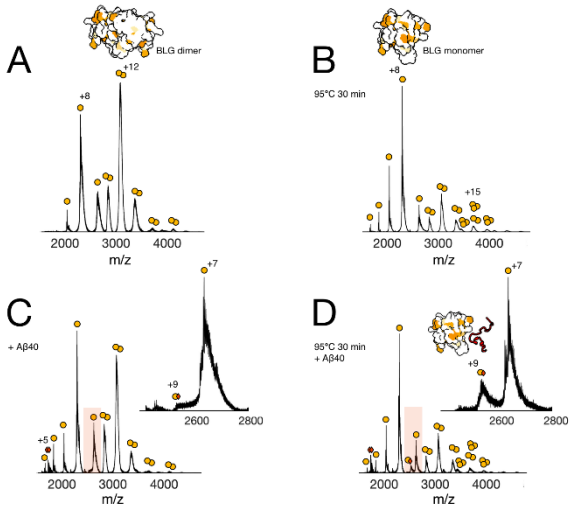

Figure 2. Native MS (mass spectrometry) spectra of BLG. Orange circles indicate BLG signals. Dimers are marked by double circles, trimers by triple circles. The major electrospray charge states are also indicated with numbers. A native BLG crystal structure [47] is shown, with hydrophobic residues colored orange. **(A)** BLG under native conditions, after 30 minutes incubation at 37 °C. **(B)** BLG under denatured conditions, after 30 minutes incubation at 95 °C followed by 30 minutes incubation at 37 °C. **(C)** BLG + Aβ40 (1:1 ratio) under native conditions, after 30 minutes of co-incubation at 37 °C after the addition of Aβ40. Aβ40 signals are indicated by red diamonds. An insert of the $(BLG + Aβ40)^{+9}$ signal is shown (orange circle + red diamond). **(D)** BLG + Aβ40 (1:1 ratio) under denatured conditions, after 30 minutes pre-incubation of BLG at 95 °C followed by 30 minutes co-incubation at 37 °C after addition of Aβ40.

Native MS was further used to probe if an increase in Aβ40 binding to BLG was indeed observed upon partial denaturation of BLG. This was done by adding Aβ40 at a 1:1 ratio to samples of native or partially denatured BLG, followed by incubation of the sample for 30 minutes at 37 °C prior to MS analysis. BLG pre-incubated at 37 °C for 30 minutes (Figure 2A) was shown to retain the native fold. This native state includes a solution state equilibrium between folded dimers and monomers. Pre-incubation first at 95°C for 30 minutes and then at 37°C for 30 minutes (Figure 2B) showed that also the denatured state of BLG with unfolded monomers and non-native trimers could still be observed. Addition of Aβ40 to the native BLG sample followed by pre-incubation (Figure 2C) resulted in a slight shift in the BLG dimer-monomer equilibrium, towards the monomeric state. A small signal for a BLG-Aβ40 complex with charge of +9 could also be observed. The identity of this complex was confirmed using MS/MS (Figure S5). The shift in dimer-monomer equilibrium points towards an effect on the

native BLG structure upon Aβ binding. This is also further exemplified by the fact that higher charge states above the Rayleigh limit (zR) of the BLG monomer appear upon Aβ binding. Aβ binding would probably take place preferentially to hydrophobic surfaces on the globular protein, which would be buried in the native state. One example of such a hydrophobic binding site would be the dimer-dimer interface. Binding of Aβ at the hydrophobic dimer interface could therefore explain the relative decrease in the dimer signals.

The formation of the BLG-Aβ40 complex was further increased if Aβ was instead pre-incubated with the partially denatured BLG sample (Figure 2D). Binding of Aβ to BLG was also under these conditions detected as a +9 complex, indicating a similar binding mode. A plausible mechanism is thus that Aβ40 binds to hydrophobic sites which are partially buried in the native state, these sites become increasingly exposed upon denaturation and the amount of Aβ binding is consequently increased. This off-pathway binding of Aβ to BLG competes with Aβ-Aβ association events which are on-pathway for fibril formation.

5.3.3 Amorphous protein aggregates delay the elongation of Aβ fibrillation

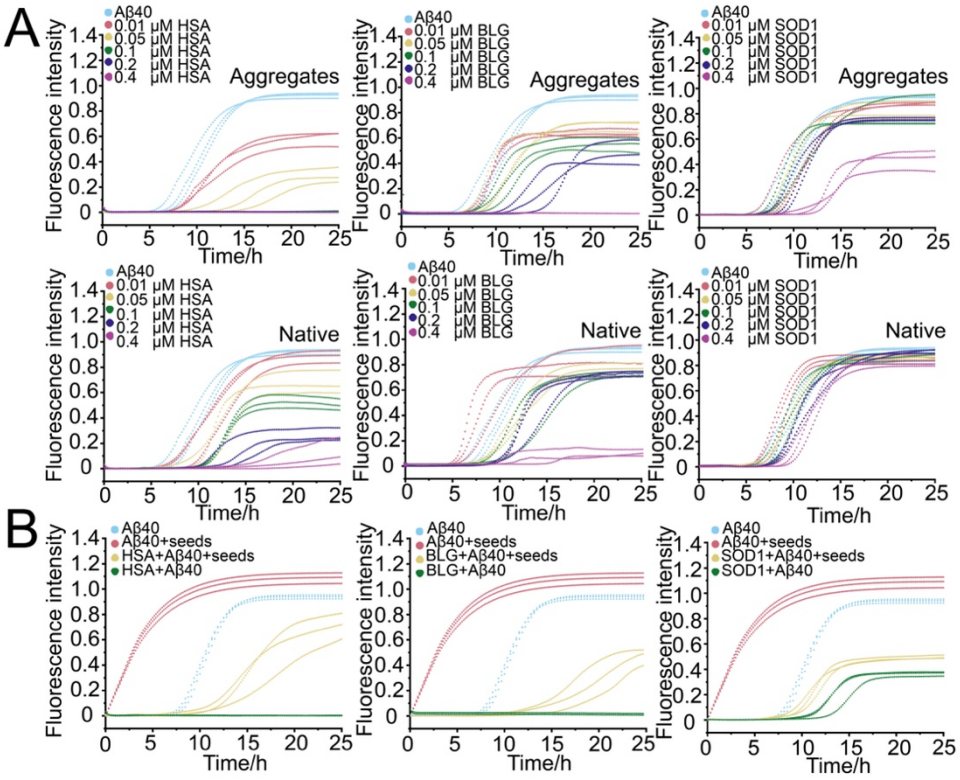

Figure 3. Amorphous protein aggregates delay the elongation of Aβ fibrillation. (A) 10 μM Aβ40 aggregation kinetics in the presence of monomeric and amorphous states of non-chaperone proteins (HSA, BLG, and SOD1) with a concentration gradient (0.01 μM to 0.4 μM). **(B)** The seeding kinetics of 10 μM Aβ40 in the presence of 1 μM Aβ40 seeds or/and 0.5 μM amorphous aggregates. The seeds were prepared by taking the beginning point of the plateau

phase of Aβ40 fibrillation. Both measurements were conducted with 20 μM ThT in 20 mM PB buffer (pH 7.4) at 37 °C.

To further test our hypothesis of how Aβ interact with partially denatured proteins and their amorphous aggregates, we evaluated the ThT fluorescence data further to gain insights into how the microscopic rate constants for Aβ40 fibrillation are modulated. This was done by varying the concentrations of amorphous aggregates during the ThT kinetics assay (Figure 3A) and then performing the global fitting of the data, as has been described earlier [48].

Sigmoidal curve fitting was first applied to analyze the aggregation curves, yielding the Aβ40 aggregation lag-time (t_{lag}) and half-time ($t_{1/2}$) shown in table 1 and table S1, respectively. In the absence of the globular proteins, 10 μM Aβ40 peptides formed amyloid fibrils with t_{lag} and $t_{1/2}$ 7.3±0.5 h and 10.4±0.5 h, respectively. Both the native and aggregated globular proteins lead to a prolonged t_{lag} and $t_{1/2}$ of Aβ40 fibrillation with increasing concentrations (Figure S6). The amorphous aggregates increased t_{lag} and t1/2 of Aβ40 fibrillation compared to the corresponding native proteins. The ThT-fluorescence endpoints (Table S2 and Figure S6) for Aβ40 aggregation was reduced more in the presence of amorphous aggregates, compared to the native proteins, for HSA and BLG. In the presence of 0.1 μM HSA or 0.4 μM BLG amorphous aggregates, the Aβ40 peptides did not form any ThT-active material over the experimental time of 25 h (Table 1). All these results demonstrate that compared to the native proteins, the amorphous aggregates have a stronger inhibitory activity against Aβ40 amyloid aggregation.

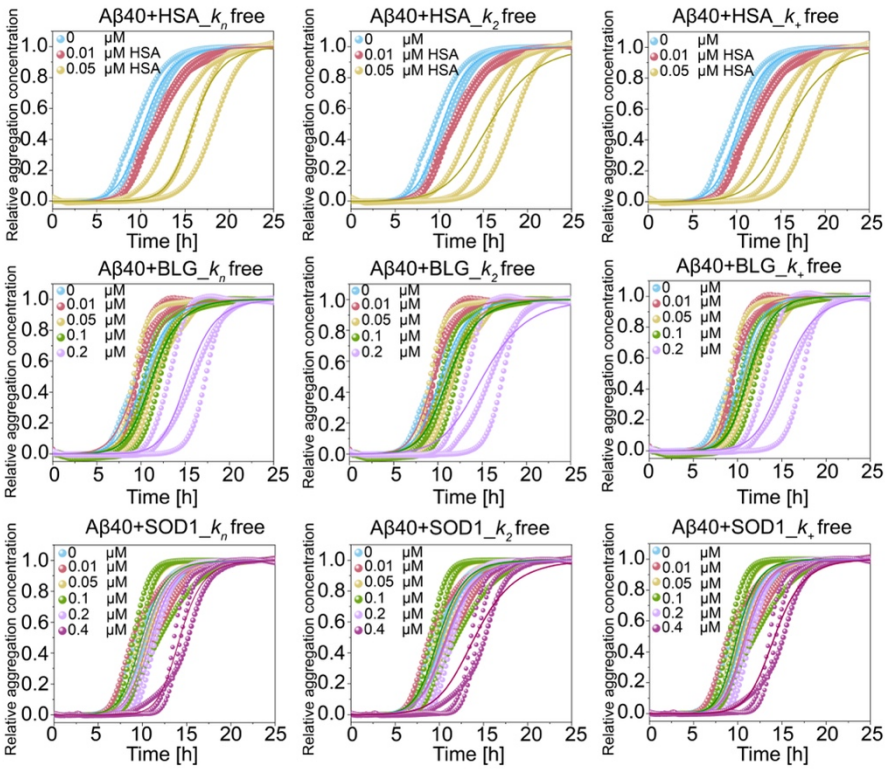

Figure 4. The influence of amorphous aggregates of globular proteins (HSA, BLG and SOD1) on secondary processes of Aβ40 fibrillation. ThT fluorescence over time was performed to monitor the aggregation kinetics of 10 μM Aβ40 in the absence or presence of amorphous aggregates (the raw data was derived from figure 3A and then global fitting was used on the *AmyloFit* online software server [48]). Aβ40 alone was first fitted with a secondary nucleation-dominated model, from which a set of parameters including k_n, k_2, and k_+ of Aβ40 fibrillation were obtained and used as the initial guess values for the following global fit. The kinetic data was then globally analyzed using an integrated rate law [49] by the AmyloFit online software server [48]. Amyloid aggregates have been widely demonstrated to nucleate through primary (fibril independent) or secondary (fibril dependent) nucleation events, aggregation then proceeds by elongation of the formed nuclei [50,51]. The rate of Aβ40 peptide aggregation is dominated by the secondary nucleation processes [16,22,51]. Thus, three parameters, the primary nucleation rate constant (k_n), the secondary nucleation rate constant (k_2) and the elongation rate constant (k_+), were obtained based on the secondary nucleation model in *AmyloFit.* The results in figure 4 show that k_n and k_+, rather than k_2, can be freely fitted to explain the effects of the amorphous protein aggregates on Aβ40 aggregation. Analysis of the samples with the native protein species show that these also similarly affect k_n and k_+ (Figure S7). Our data, therefore, suggest that the tested non-chaperone proteins interfere with the elongation process or primary nucleation of Aβ40 aggregation rather than the secondary

nucleation. Both the monomeric proteins and the aggregated proteins have this effect. The absolute effect is however larger for the aggregated species than it is for the monomeric proteins. To characterize which microscopic rate constant, k_n or k_+, is mostly influenced by these amorphous aggregates, seeding kinetic experiments of Aβ40 fibrillation in the presence of amorphous aggregates were performed. The main role of pre-formed seed fibrils is to act as templates for elongation. As shown in figure 3B, Aβ40 alone with the addition of seeds (red line) presents a concave kinetic curve as well as significantly accelerated fibrillation, indicative of the elongation-dominated process. This result is consistent with the previous publication [16]. Notably, the amorphous aggregates supplemented with the seeds, especially HSA and BLG, prolonged the lag time of Aβ40 fibrillation than Aβ40 alone with seeds, as well as dimmed the lag time of Aβ40 fibrillation, compared to the unseeded samples (green line). These results suggest that the amorphous aggregates significantly influence the elongation process (k_+) of Aβ40 fibrillation with seeds, due to the fact that the addition of the seeds has negligible influence on Aβ40 primary aggregation [52].

Briefly, our sigmoidal curve fitting reveals that both the native species and amorphous aggregates prolonged the lag time (t_{lag}, Table 1) and half time ($t_{1/2}$, Table S1) of Aβ40 aggregation within the concentration increasing. Combined with the end-point fluorescence intensity (Table S2), the amorphous protein aggregates have a stronger inhibitory efficiency than the corresponding monomers. Global data analysis of these kinetic curves (Figure 4) suggests that amorphous protein aggregates influence both the primary nucleation and elongation processes. The seeding assay confirms the finding that the elongation process of Aβ40 is significantly modulated by the amorphous protein aggregates.

Table 1. Phenomenological parameters for Aβ40 aggregation (t_{lag}, h), calculated from the sigmoidal curve fitting of the ThT fluorescence kinetic assay.

	Concentration	t_{lag}(h)	
		Amorphous aggregates	Native proteins
Aβ40	10 μM	7.3±0.5	
HSA+ Aβ40	0.01 μM	7.9±0.1	8.2±0.8
	0.05 μM	12.7±1.5	10.3±0.6
	0.1 μM	>25 h	11.1±0.1

	0.2 μM	>25 h	11.9±1.0
	0.4 μM	>25 h	16.3±1.5
BLG+ Aβ40	0.01 μM	7.9±0.2	6.5±0.9
	0.05 μM	8.5±0.5	8.6±0.3
	0.1 μM	8.9±0.6	10.2±0.8
	0.2 μM	13.1±1.2	10.7±0.3
	0.4 μM	>25 h	11.5±1.8
SOD1+ Aβ40	0.01 μM	7.6±0.8	6.8±0.4
	0.05 μM	8.0±0.4	7.7±0.3
	0.1 μM	7.7±0.2	7.6±0.4
	0.2 μM	8.8±0.5	8.2±0.07
	0.4 μM	11.2±0.2	9.7±0.5

5.3.4 Amorphous aggregates redirect Aβ40 aggregation towards a non-fibrillar end-state, but do not disaggregate mature Aβ40 fibrils

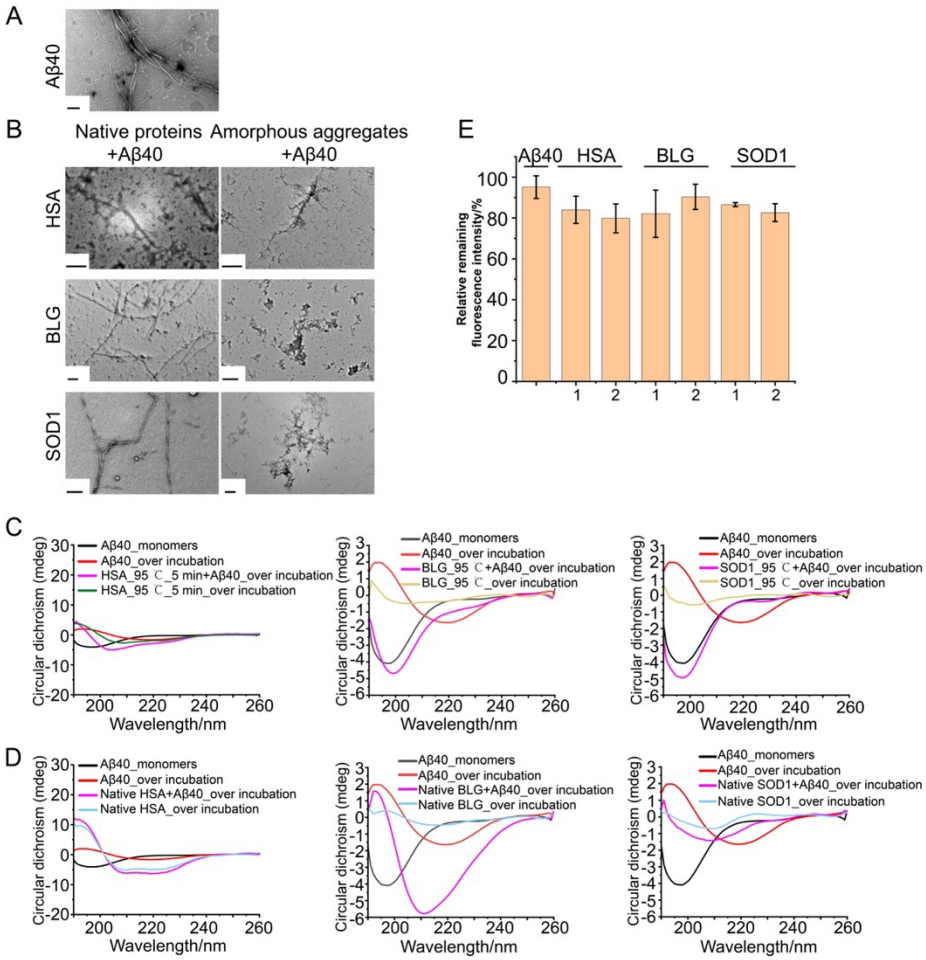

Figure 5. The non-fibrillar end-state of Aβ40 aggregation and the disassembility of mature Aβ40 fibrils by the amorphously aggregated or natively folded proteins. TEM images of 10 μM Aβ40 alone **(A)**, or **(B)** incubating with 0.5 μM monomeric or amorphous non-chaperone proteins (HSA, BLG, and SOD1). The amorphous aggregates of HSA, BLG, and SOD1 were denatured at 95 °C for 5, 30, and 30 min, respectively. The samples are collected at the end-point of ThT measurement in figure 1C&S2. The scale bar is 200 nm. **(C)** The effect of amorphously aggregated or natively folded proteins **(D)** (HSA, BLG and SOD1) on the secondary structure transition of Aβ40 by the far-UV CD spectroscopy. 0.5 μM native or amorphous aggregated proteins (HSA, BLG and SOD1) with or without 10 μM Aβ40 were prepared in PB buffer (20 mM, no NaCl) after incubation at 37°C for 30 h without any shaking. 10 μM Aβ40 monomers without incubation were taken as a control. The amorphous aggregates of HSA, BLG, and SOD1 were denatured at 95 °C for 5, 30, and 30 min, respectively. **(E)** Disaggregation of 10 μM Aβ40 pre-formed fibrils by adding 2 μM HSA, BLG, or SOD1 (amorphous aggregates and monomers). Line 1 and line 2 represent the monomers and amorphous aggregates, respectively. The end-point ThT fluorescence intensity was presented

after incubating at 37 °C for 24 h. Higher fluorescence intensity indicates more fibrils in the solution, suggesting a lower disassembling mature fibril ability of non-chaperone proteins.

TEM imaging was further conducted to verify Aβ40 fibril formation (Figure 5A) in the presence and absence of the native or amorphously aggregated proteins after 30 h aggregation, at 37 °C. Amyloid fibrils were observed in the presence of 10 μM Aβ40 (Figure 5A), with or without 0.5 μM monomeric HSA, BLG, or SOD1 (Figure 5B). In contrast, the presence of 0.5 μM amorphous aggregates of HSA, BLG, or SOD1 only generated an end-state with amorphous aggregates, which is consistent with the ThT fluorescence assays that show a decrease in ThT active material. This shows that the observed interactions between Aβ40 and the amorphous protein aggregates modulate the Aβ aggregation rate and also redirect Aβ40 aggregation into a non-fibrillar state. To further support TEM observations in figure 5B, the far-UV CD spectroscopy measurements were carried out by monitoring the effects of the amorphously aggregated proteins on the secondary structure change of Aβ40. It is known that under the incubation environment, Aβ monomers undergo a conformational transition from the random coil structure to α-helical intermediates, and gradually convert to the predominate β-sheet-rich fibrils. We observed the structural transformation of Aβ40 alone (10 μM) after incubation at 37 °C for 30 h from a negative minima at ~ 198 nm (Figure 5C, black line), which represents the random coil structure, to a negative signal at ~ 220 nm (Figure 5C, red line), indicative of the formation of β-sheet fibrils. In the presence of 0.5 μM amorphous aggregates (HSA, BLG, or SOD1), no negative CD signal at ~ 220 nm was observed, which is in agreement with the TEM results in figure 5B that there were no Aβ40 fibrils observed in the presence of the amorphous aggregates. Instead, we observed the CD signal of HSA aggregates with Aβ40 at ~ 203 nm after incubation, which was located between monomeric Aβ40 (~ 198 nm) and HSA aggregates (~ 205 nm) alone. We assume the signal at ~ 203 nm results from the mixture of HSA aggregates and monomeric or oligomeric Aβ40 species, but not from the specific single species. BLG and SOD1 aggregates also shifted the negative signal of Aβ40 fibrils from 220 nm to ~ 200 nm, in which the solution is hypothesized to be monomeric Aβ40 predominate. BLG aggregates slightly shifted the minima peak from Aβ40 monomers, which is ascribed to the structure of BLG aggregates alone. For the native globular proteins, HSA monomers with Aβ40 after incubation (Figure 5D) do not show the typical fibril CD signal at ~ 220 nm, but have a very similar curve to native HSA alone, suggesting the significant structural overlap from native HSA. But we cannot conclude there is no β-sheet fibril in the

presence of native HSA proteins. The native BLG retained the Aβ40 fibril peak at ~220 nm and SOD1 monomers exhibited a mixture signal at ~ 205 nm. In total, the addition of natively folded proteins to Aβ40 induced a less shift of Aβ40 fibril signal from ~220 nm compared to the amorphous aggregates, representing the formation of β-sheet contents in the aqueous solution within the native proteins. We noticed that the intensity of CD signals in the presence of non-chaperone proteins both in native and aggregated states is stronger than the monomeric Aβ40 alone. The main reason lies in the fact that the secondary structures of non-chaperone proteins would overlap CD signals of Aβ40 peptides, making a higher signal than Aβ40 proteins alone. The CD results support the conclusion that the amorphous aggregates show a higher inhibitory efficiency of Aβ40 fibrillation than the native ones.

Apart from the inhibitory effect on Aβ aggregation, the disaggregating effect on the existing plaques is also of importance. It has been demonstrated that reversing existing plaques is less effective than preventing new plaque formation when it comes to potential AD treatments [53]. Therefore, it is necessary to investigate whether amorphous protein aggregates can solubilize pre-formed Aβ40 fibrillar assemblies. 10 μM Aβ40 peptides were incubated until a fibrillation plateau was reached. 2 μM amorphous aggregates or monomeric test proteins (HSA, BLG, or SOD1) were added to the pre-formed mature fibrils for an additional incubation of 24 h. As shown in figure 5E, the remaining fluorescence intensity of Aβ40 treated with amorphous aggregates (Line 2) did not show a dramatic decrease, compared to Aβ40 fibrils alone. This indicates that the disaggregation of Aβ40 fibrils is negligible in the presence of the amorphous aggregates. The monomeric non-chaperone proteins (Line 1) also showed an insignificant effect on disaggregation against the pre-formed Aβ40 fibrils. We increased the concentration of these non-chaperone proteins to 10 μM with a final ratio of 1:1 to Aβ40 fibrils, however, no higher disassembling abilities than these of 2 μM non-chaperone proteins were observed (data not shown). The result indicates though the amorphous aggregates are able to disrupt Aβ40 aggregation, their solubilization of Aβ40 fibrils is very weak.

5.3.5 Amorphous protein aggregates retain Aβ toxicity

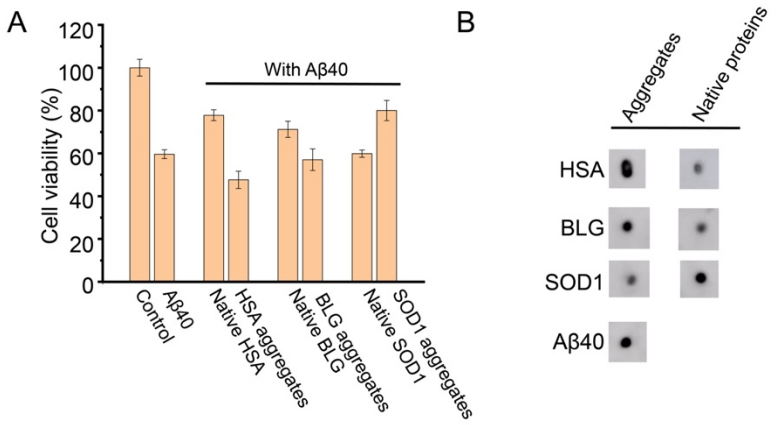

Figure 6. The toxicity of Aβ40 in the presence of amorphous protein aggregates. (A) The cytotoxic effect of the amorphous aggregates (HSA, BLG, and SOD1) on Aβ40-induced toxicity. The final concentration of Aβ40 and amorphous aggregates were 10 and 1 μM, respectively. All the SH-SY5Y cells were incubated in EMEM medium at 37 °C for 48 h. **(B)** Dot blot analysis of Aβ40 oligomer formation in the presence of amorphous aggregates or monomers. The final concentration of the globular proteins and Aβ40 was 10 and 25 μM, respectively. The anti-amyloid oligomer antibody A11 was used as the primary antibody. At least three times were repeated for the dot blot experiment.

We have so far shown that amorphous aggregates interact with soluble Aβ40 peptides, inhibit their amyloid aggregation, and re-direct them towards non-fibrillar aggregates. In order to investigate whether these amorphous aggregates could alleviate the toxicity induced by the Aβ40 peptides, cell viability assays were carried out in human neuroblastoma cells (SH-S5Y5) as described previously [5]. To rule out the assumption whether these globular proteins alone (native species or amorphous aggregates) could be toxic to the cells, we first treated SH-S5Y5 cells with 1 μM globular proteins alone for 48 h and found no effects on cell viability at this concentration (Figure S5A). Afterwards, these amorphous aggregates were mixed with Aβ40 at a molar ratio of 1:10 and incubated for 48 h in the presence of SH-S5Y5 cells. Though all of these amorphous aggregates show similar inhibitory effects on Aβ40 fibrillation, their cytotoxic effects are different. The result (Figure 6A) showed that Aβ40 peptides induce higher cytotoxicity after the addition of HSA aggregates, while BLG aggregates almost retain and SOD1 aggregates alleviate Aβ40 cytotoxicity. Based on the "toxic Aβ oligomer" hypothesis [5], we assume there are different amounts of Aβ40 oligomers induced in the presence of these amorphous aggregates, and the higher cytotoxicity (or lower cell viability) indicates more Aβ40 oligomers. To support our hypothesis, a dot blot assay by using the A11 antibody, which only characterizes Aβ oligomers but not monomers or fibrils, was further applied. As shown in figure

6B, in the presence of aggregates, HSA displayed the biggest oligomer stain, indicating the highest generation of Aβ40 oligomers, followed by BLG, and then SOD1. Aβ40 alone has a similar stain as BLG aggregates, suggesting the comparable oligomers between them. This result is in total agreement with the cytotoxic effects shown in figure 6A, showing that the lower cell viability in vivo correlates well with the higher Aβ40 oligomer concentrations detected in vitro.

Native globular proteins, especially HSA and BLG, can also suppress Aβ40 fibrillation, however, their cytotoxic effects are different from the corresponding amorphous states. For HSA, the aggregates increase Aβ40 cytotoxicity while native proteins decrease it. BLG monomers are more efficient than the aggregates to decrease Aβ40 cytotoxicity, while SOD1 has a reversal effect. We assume metal ions including Cu^{2+} and Zn^{2+} inside SOD1 themselves or the formation of the complex with Aβ40 are also involved in the regulation of cellular toxicity [54]. The correlation of SOD1 with Aβ40 differs from HSA or BLG due to the metal ions, which may, at least partially, render the reversal effect of the cytotoxicity of SOD1 amorphous aggregates. As evidenced by the dot blot result, the main reason could be attributed to the production of different yields of Aβ40 oligomers induced by the different states of the globular proteins.

5.4 Discussion

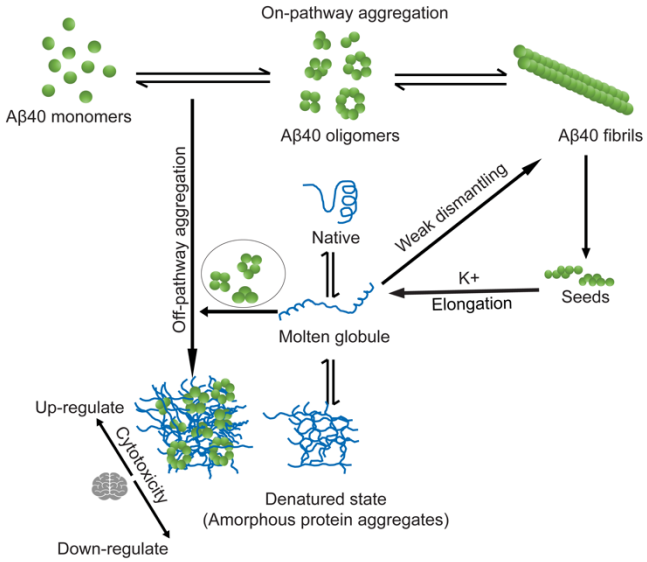

Figure 7. A schematic illustration of the molecular pathway of Aβ40 aggregation modulated by the globular protein amorphous aggregates. On the contrary to the Aβ on-pathway aggregation, the Aβ off-pathway aggregation has been observed in the presence of the protein amorphous aggregates. These aggregates have a size distribution from 20 nm to 300

nm. From the amorphous aggregates, the protein molten globule is proposed to form hetero-oligomers with Aβ40 aggregates, leading to amorphous hetero-aggregation, inhibiting Aβ40 primary nucleation and elongation processes, and modulating Aβ40 cytotoxicity.

Using a range of different biophysical techniques, we have here presented an investigation on the effects of three selected globular non-chaperone proteins (HSA, BLG, and SOD1) on Aβ aggregation, both in their native state and in a denatured state where they form amorphous aggregates. Our results have shown that the proteins in their denatured states were generally observed to be more efficient at reducing Aβ40 aggregation compared to in their native states. Amorphous protein aggregates ranging from 20 nm to 300 nm exhibited the optimal inhibition of Aβ40 fibrillation at a sub-stoichiometric ratio. Native MS and TEM imaging revealed that the denatured proteins can form the heterocomplexes with Aβ40 both at the microscopic protein-protein scale and at the mesoscopic aggregate scale. These complexes lead to the off-pathway aggregation of Aβ40 into a non-fibrillar end-state, which is structurally distinct from the amyloid fibrils which are typically the end-state when Aβ40 aggregates by itself in vitro.

Binding between Aβ and the non-chaperone proteins is increased in the denatured state, which could partially be due to an increase in hydrophobic surfaces in the non-chaperone proteins upon unfolding. From the perspective of Aβ40 peptides, the size of monomeric Aβ40 peptides is smaller than the native or aggregated non-chaperone proteins, thus monomeric Aβ40 would have a higher collision frequency with other Aβ40 proteins than with the non-chaperone proteins. However, the fact that non-chaperone proteins showing the effective inhibition of Aβ40 aggregation even with the lower frequencies of collisions implies these non-chaperone proteins might interact with specific oligomeric Aβ40, which have a similar size to the non-chaperone proteins. This assumption is consistent with the previous report that HSA monomers have a significantly higher affinity for Aβ42 aggregates than for Aβ42 monomers [33]. When these non-chaperone proteins become partially folded, their hydrophobic surfaces can favorably interact with the hydrophobic Aβ aggregates, prevent their self-association, but remain oligomeric Aβ42 cytotoxicity, as well as increase their solubility [55]. Co-association between Aβ and a non-chaperone protein might however also be greatly favored by increasing the free energy of the non-chaperone protein by denaturation. Perturbing the protein structure results in a loss of favorable native interactions, which makes the system energetically frustrated. This is experimentally seen by the increase of BLG polydispersity as detected by native MS. Not only is the partially unfolded protein populating several conformational states, but it also populates several oligomeric states, including a non-native trimeric state (Figure

2B&2C). The system tries to decrease the energy of the partially unfolded protein by populating different non-native structures, none of which represent a particularly energetically favorable state [56]. The binding of Aβ to the partially unfolded protein leads to a larger decrease in the free energy of the system compared to Aβ binding to the native protein, as the native protein is in itself lower in energy compared to the denatured protein. This is similar to how some polydisperse "holdase"-type chaperones such as DNAJB6 and crystallins have been suggested to suppress aggregation [35]. This type of reasoning could also explain why the large HSA aggregates were poorer at suppressing Aβ fibrillation. Larger and more mature aggregates are probably more stable in themselves compared to the partially unfolded monomers and intermediate protein aggregates, which occur earlier in the aggregation pathway. Such "high-energy" intermediate states of the non-chaperone proteins are thus more prone to co-aggregate with Aβ compared to both their native states, and their mature aggregates.

We observed that the denatured proteins significantly reduce the rate of primary nucleation and elongation in the Aβ40 fibrillation process. Binding of soluble Aβ40 monomers and oligomers to the denatured proteins to form off-pathway states are in agreement with inhibition of primary nucleation. Primary nucleation can be envisioned as interactions between individual soluble Aβ species. Such binding to early Aβ oligomers has previously been detected for the DNAJB6 chaperone, which specifically modulates the primary nucleation rate of Aβ [57]. Inhibition of elongation could instead be interpreted as an interaction between the proteins and/or their amorphous aggregates and the Aβ fibril ends [58]. It is however observed in figure 5E that the amorphous aggregates cannot solubilize pre-formed Aβ40 fibrils. This points towards the fact that the effect on aggregation does indeed originate from the earlier phases of aggregation where off-pathway species are generated, leading to formation of co-aggregated amorphous structures. This co-aggregate is probable a state where both the aggregation prone species, the intrinsically unstable Aβ monomer and the destabilized denatured protein, have together reached an energetically stable state. The mature fibrillar Aβ aggregates are on the other hand already in a stable state and are therefore less prone to mix with the proteins and their amorphous aggregates.

Toxicity of the formed off-pathway aggregates does however differ, with hetero-aggregates of Aβ40 and HSA showing higher cytotoxicity to the neuronal cells than these of SOD1 and BLG. This illustrates that the effect on toxicity is more complex than simply redirecting Aβ aggregation from the fibrillar state. The dot blot assay further supports this idea, by showing that the effect on the formation of oligomers is different after co-incubation with different

proteins. The different cytotoxicities are presumably caused by different global structures of oligomeric complexes, responsible for lipid membrane permeabilization and other oligomer toxicity pathways. This could be related to various variables of the Aβ-binding protein, such as size, charge, hydrophobicity, or aggregate morphology. This might lead to the stabilization of Aβ at different aggregation states. Our work highlights that those denatured proteins and their amorphous aggregates can play an important role in the modulation of amyloid protein toxicity and aggregation.

Our work further illustrates how amyloid aggregation and co-aggregation are in general affected by the folding/unfolding and aggregation of proteins that could exist in the cellular environment. This would include chaperones [16,27,59,60], globular proteins[17], and some amyloidogenic proteins [21,22]. The activity of the Brichos domain, a human chaperone, has for example been shown to depend on its aggregation state, with the dimeric form inhibiting amyloid aggregation and the oligomeric form inhibiting amorphous protein aggregation [25]. The Brichos domain does, however, unlike the proteins studied in here, inhibit surface-catalyzed secondary nucleation of Aβ aggregates [28]. Also, the ATP-dependent chaperone Hsp70 has been shown to have a reversible dynamic equilibrium between monomeric, dimeric, trimeric, and higher-order oligomeric species in vitro [61]. The small heat-shock proteins, including αA or αB-crystallin [62-64], also form globular assemblies including some large, aggregated clusters. It has been demonstrated that aggregated state of molecular chaperones shows different binding to the substrates and exhibits the maximum activity [65-68]. Additionally, many globular proteins, for example, the bovine or human serum albumin [69,70], lysozyme [70], SOD1 [71], and BLG [72] grow supramolecular amorphous aggregates under some experimental conditions.

Co-aggregation is also known to take place between different disease-related aggregation-prone proteins. We have for example previously studied the co-aggregation of Aβ with tau protein and with insulin [20,22]. Co-aggregation with tau protein can similarly redirect Aβ aggregation from fibrillar aggregates to amorphous aggregates. Tau also displays different binding affinities to different aggregated species from on-pathway fibrillation of Aβ [22]. It is possible that Aβ and tau aggregate into hetero-oligomers or hetero-aggregates. Hetero-assemblies with aggregation-prone protein species have also been observed for the interactions of human prion protein (PrP) with Aβ as well as with the human islet amyloid polypeptide (hIAPP). Upon binding to Aβ oligomer, the human prion protein changes its structure and co-aggregates into large hetero-assemblies where the N-terminal of PrP is immobilized [73]. Also, the prion fragment (PrP106–126) forms hetero-oligomeric aggregates with hIAPP in which

hIAPP converts into an amyloidogenic β-hairpin conformation [74]. This comparison suggests that the partially unfolded high-energy molten globule state of globular proteins may display similarities with amyloidogenic proteins, which are also intrinsically unstable due to a high free energy. The molten globule state can just as amyloidogenic proteins either self-interact and form homo-aggregates or interact with other proteins and form hetero-aggregates.

Both diffuse deposits of amorphous aggregates and plaque deposits of amyloid fibril have been observed in AD and represent two states that could form in cells due to proteostasis collapse. Our study demonstrates how amorphous aggregates from other proteins may interact with Aβ and lead to inhibition of fibrillation in favor of non-fibrillar aggregation. Aggregates observed in AD patients are indeed known to contain many other proteins [75], illustrating that co-aggregation is important to consider in the real disease mechanism. Further studies of co-aggregation with cellular proteins and how this affects the Aβ aggregation process will probably be of importance for understanding the molecular pathogenesis in AD.

5.5 Supplemental information

The experimental section (Materials and methods) and Figures S1-8 and Tables S1-S2 are available in supporting information.

5.6 Acknowledgements

We thank Prof. Roland Riek (ETH Zurich) for invaluable insights as well as critical advice on our work. We acknowledge funding from the Swedish Research Council (L.L.I.), the Olle Engkvist Foundation (L.L.I.), Swiss National Science Foundation project 310030_197626 (J.L), the Brightfocus foundation A20201759S (J.L.) and the PSI CROSS initiative. The Native IM-MS infrastructure was supported by a SciLifeLab Technology Development Grant from the Faculty of Science at Stockholm University (to L.L.I.).

5.7 Author contributions

J.W., J.L.: designed research; J.W., N.Ö., H.P.: performed research; J.W. N.Ö., H.W., R.S.H.: analyzed data; L.I.; A.G.: contributed new analytical tools; J.W., J.L.: wrote the paper; J.W., N.Ö., A.G., J.L.: revised the paper.

5.8 Declaration of Interests

The authors declare no competing interests.

5.9 References

1. Balch, W.E., Morimoto, R.I., Dillin, A., and Kelly, J.W. (2008). Adapting Proteostasis for Disease Intervention. Science *319*, 916-919. doi:10.1126/science.1141448.
2. Hipp, M.S., Kasturi, P., and Hartl, F.U. (2019). The proteostasis network and its decline in ageing. Nature Reviews Molecular Cell Biology *20*, 421-435. 10.1038/s41580-019-0101-y.
3. Adamcik, J., and Mezzenga, R. (2018). Amyloid Polymorphism in the Protein Folding and Aggregation Energy Landscape. Angewandte Chemie International Edition *57*, 8370-8382. https://doi.org/10.1002/anie.201713416.
4. Wu, J., Cao, C., Loch, R.A., Tiiman, A., and Luo, J. (2020). Single-molecule studies of amyloid proteins: from biophysical properties to diagnostic perspectives. Quarterly Reviews of Biophysics *53*, e12, e12. 10.1017/S0033583520000086.
5. Wu, J., Blum, T.B., Farrell, D.P., DiMaio, F., Abrahams, J.P., and Luo, J. (2021). Cryo-electron Microscopy Imaging of Alzheimer's Amyloid-beta 42 Oligomer Displayed on a Functionally and Structurally Relevant Scaffold. Angewandte Chemie International Edition *60*, 18680-18687. https://doi.org/10.1002/anie.202104497.
6. Luo, J., Wärmländer, S.K.T.S., Gräslund, A., and Abrahams, J.P. (2014). Alzheimer Peptides Aggregate into Transient Nanoglobules That Nucleate Fibrils. Biochemistry *53*, 6302-6308. 10.1021/bi5003579.
7. Nishikawa, N., Sakae, Y., Gouda, T., Tsujimura, Y., and Okamoto, Y. (2017). Two major stable structures of amyloid-forming peptides: amorphous aggregates and amyloid fibrils. Molecular Simulation *43*, 1370-1376. 10.1080/08927022.2017.1359746.
8. Chiti, F., and Dobson, C.M. (2017). Protein Misfolding, Amyloid Formation, and Human Disease: A Summary of Progress Over the Last Decade. Annual Review of Biochemistry *86*, 27-68. 10.1146/annurev-biochem-061516-045115.
9. Eisenberg, D., and Jucker, M. (2012). The amyloid state of proteins in human diseases. Cell *148*, 1188-1203. 10.1016/j.cell.2012.02.022.
10. Lau, H.H.C., Ingelsson, M., and Watts, J.C. (2021). The existence of Aβ strains and their potential for driving phenotypic heterogeneity in Alzheimer's disease. Acta Neuropathologica *142*, 17-39. 10.1007/s00401-020-02201-2.
11. Miller, D.L., Papayannopoulos, I.A., Styles, J., Bobin, S.A., Lin, Y.Y., Biemann, K., and Iqbal, K. (1993). Peptide compositions of the cerebrovascular and senile plaque core amyloid deposits of Alzheimer's disease. Arch Biochem Biophys *301*, 41-52. 10.1006/abbi.1993.1112.
12. Güntert, A., Döbeli, H., and Bohrmann, B. (2006). High sensitivity analysis of amyloid-beta peptide composition in amyloid deposits from human and PS2APP mouse brain. Neuroscience *143*, 461-475. 10.1016/j.neuroscience.2006.08.027.
13. Yoshimura, Y., Lin, Y., Yagi, H., Lee, Y.-H., Kitayama, H., Sakurai, K., So, M., Ogi, H., Naiki, H., and Goto, Y. (2012). Distinguishing crystal-like amyloid fibrils and glass-like amorphous aggregates from their kinetics of formation. Proceedings of the National Academy of Sciences *109*, 14446-14451. 10.1073/pnas.1208228109.
14. Gorman, P.M., Yip, C.M., Fraser, P.E., and Chakrabartty, A. (2003). Alternate Aggregation Pathways of the Alzheimer β-Amyloid Peptide: Aβ Association Kinetics at Endosomal pH. Journal of Molecular Biology *325*, 743-757. https://doi.org/10.1016/S0022-2836(02)01279-2.
15. Sandberg, A., Luheshi, L.M., Söllvander, S., Pereira de Barros, T., Macao, B., Knowles, T.P.J., Biverstål, H., Lendel, C., Ekholm-Petterson, F., Dubnovitsky, A., et

al. (2010). Stabilization of neurotoxic Alzheimer amyloid-β oligomers by protein engineering. Proceedings of the National Academy of Sciences *107*, 15595-15600. 10.1073/pnas.1001740107.

16. Wang, H., Lallemang, M., Hermann, B., Wallin, C., Loch, R., Blanc, A., Balzer, B.N., Hugel, T., and Luo, J. (2021). ATP Impedes the Inhibitory Effect of Hsp90 on Aβ40 Fibrillation. Journal of Molecular Biology *433*, 166717. https://doi.org/10.1016/j.jmb.2020.11.016.
17. Luo, J., Wärmländer, S.K.T.S., Gräslund, A., and Abrahams, J.P. (2014). Non-chaperone proteins can inhibit aggregation and cytotoxicity of Alzheimer amyloid β peptide. The Journal of biological chemistry *289*, 27766-27775. 10.1074/jbc.M114.574947.
18. Luo, J., Wärmländer, S.K.T.S., Gräslund, A., and Abrahams, J.P. (2013). Human lysozyme inhibits the in vitro aggregation of Aβ peptides, which in vivo are associated with Alzheimer's disease. Chemical Communications *49*, 6507-6509. 10.1039/C3CC42325E.
19. Assarsson, A., Hellstrand, E., Cabaleiro-Lago, C., and Linse, S. (2014). Charge Dependent Retardation of Amyloid β Aggregation by Hydrophilic Proteins. ACS Chemical Neuroscience *5*, 266-274. 10.1021/cn400124r.
20. Luo, J., Wärmländer, S.K.T.S., Gräslund, A., and Abrahams, J.P. (2016). Reciprocal Molecular Interactions between the Aβ Peptide Linked to Alzheimer's Disease and Insulin Linked to Diabetes Mellitus Type II. ACS Chemical Neuroscience *7*, 269-274. 10.1021/acschemneuro.5b00325.
21. Luo, J., Wärmländer, S.K.T.S., Gräslund, A., and Abrahams, J.P. (2016). Cross-interactions between the Alzheimer Disease Amyloid-β Peptide and Other Amyloid Proteins: A Further Aspect of the Amyloid Cascade Hypothesis. The Journal of biological chemistry *291*, 16485-16493. 10.1074/jbc.R116.714576.
22. Wallin, C., Hiruma, Y., Wärmländer, S.K.T.S., Huvent, I., Jarvet, J., Abrahams, J.P., Gräslund, A., Lippens, G., and Luo, J. (2018). The Neuronal Tau Protein Blocks in Vitro Fibrillation of the Amyloid-β (Aβ) Peptide at the Oligomeric Stage. Journal of the American Chemical Society *140*, 8138-8146. 10.1021/jacs.7b13623.
23. Braun, G.A., Dear, A.J., Sanagavarapu, K., Zetterberg, H., and Linse, S. (2022). Amyloid-β peptide 37, 38 and 40 individually and cooperatively inhibit amyloid-β 42 aggregation. Chemical Science *13*, 2423-2439. 10.1039/D1SC02990H.
24. Willander, H., Askarieh, G., Landreh, M., Westermark, P., Nordling, K., Keränen, H., Hermansson, E., Hamvas, A., Nogee, L.M., Bergman, T., et al. (2012). High-resolution structure of a BRICHOS domain and its implications for anti-amyloid chaperone activity on lung surfactant protein C. Proceedings of the National Academy of Sciences *109*, 2325-2329. 10.1073/pnas.1114740109.
25. Chen, G., Abelein, A., Nilsson, H.E., Leppert, A., Andrade-Talavera, Y., Tambaro, S., Hemmingsson, L., Roshan, F., Landreh, M., Biverstål, H., et al. (2017). Bri2 BRICHOS client specificity and chaperone activity are governed by assembly state. Nature Communications *8*, 2081. 10.1038/s41467-017-02056-4.
26. Chen, G., Andrade-Talavera, Y., Tambaro, S., Leppert, A., Nilsson, H.E., Zhong, X., Landreh, M., Nilsson, P., Hebert, H., Biverstål, H., et al. (2020). Augmentation of Bri2 molecular chaperone activity against amyloid-β reduces neurotoxicity in mouse hippocampus in vitro. Communications Biology *3*, 32. 10.1038/s42003-020-0757-z.
27. Willander, H., Presto, J., Askarieh, G., Biverstål, H., Frohm, B., Knight, S.D., Johansson, J., and Linse, S. (2012). BRICHOS Domains Efficiently Delay Fibrillation of Amyloid beta-peptide. Journal of Biological Chemistry *287*, 31608-31617. 10.1074/jbc.M112.393157.

28. Cohen, S.I.A., Arosio, P., Presto, J., Kurudenkandy, F.R., Biverstål, H., Dolfe, L., Dunning, C., Yang, X., Frohm, B., Vendruscolo, M., et al. (2015). A molecular chaperone breaks the catalytic cycle that generates toxic Aβ oligomers. Nature Structural & Molecular Biology *22*, 207-213. 10.1038/nsmb.2971.
29. Scheidt, T., Carozza, J.A., Kolbe, C.C., Aprile, F.A., Tkachenko, O., Bellaiche, M.M.J., Meisl, G., Peter, Q.A.E., Herling, T.W., Ness, S., et al. (2021). The binding of the small heat-shock protein αB-crystallin to fibrils of α-synuclein is driven by entropic forces. Proceedings of the National Academy of Sciences *118*, e2108790118. 10.1073/pnas.2108790118.
30. Månsson, C., Arosio, P., Hussein, R., Kampinga, H.H., Hashem, R.M., Boelens, W.C., Dobson, C.M., Knowles, T.P.J., Linse, S., and Emanuelsson, C. (2014). Interaction of the Molecular Chaperone DNAJB6 with Growing Amyloid-beta 42 (Aβ42) Aggregates Leads to Sub-stoichiometric Inhibition of Amyloid Formation*. Journal of Biological Chemistry *289*, 31066-31076. https://doi.org/10.1074/jbc.M114.595124.
31. Flagmeier, P., De, S., Michaels, T.C.T., Yang, X., Dear, A.J., Emanuelsson, C., Vendruscolo, M., Linse, S., Klenerman, D., Knowles, T.P.J., and Dobson, C.M. (2020). Direct measurement of lipid membrane disruption connects kinetics and toxicity of Aβ42 aggregation. Nature Structural & Molecular Biology *27*, 886-891. 10.1038/s41594-020-0471-z.
32. Stanyon, H.F., and Viles, J.H. (2012). Human Serum Albumin Can Regulate Amyloid-β Peptide Fiber Growth in the Brain Interstitium: IMPLICATIONS FOR ALZHEIMER DISEASE*. Journal of Biological Chemistry *287*, 28163-28168. https://doi.org/10.1074/jbc.C112.360800.
33. Wang, C., Cheng, F., Xu, L., and Jia, L. (2016). HSA targets multiple Aβ42 species and inhibits the seeding-mediated aggregation and cytotoxicity of Aβ42 aggregates. RSC advances *6*, 71165-71175.
34. Zapadka, K.L., Becher, F.J., Gomes dos Santos, A.L., and Jackson, S.E. (2017). Factors affecting the physical stability (aggregation) of peptide therapeutics. Interface Focus *7*, 20170030. doi:10.1098/rsfs.2017.0030.
35. Linse, S., Thalberg, K., and Knowles, T.P.J. (2021). The unhappy chaperone. QRB Discovery *2*, e7, e7. 10.1017/qrd.2021.5.
36. Baldwin, Andrew J., Lioe, H., Hilton, Gillian R., Baker, Lindsay A., Rubinstein, John L., Kay, Lewis E., and Benesch, Justin L.P. (2011). The Polydispersity of αB-Crystallin Is Rationalized by an Interconverting Polyhedral Architecture. Structure *19*, 1855-1863. https://doi.org/10.1016/j.str.2011.09.015.
37. Karamanos, T.K., Tugarinov, V., and Clore, G.M. (2019). Unraveling the structure and dynamics of the human DNAJB6b chaperone by NMR reveals insights into Hsp40-mediated proteostasis. Proceedings of the National Academy of Sciences *116*, 21529-21538. doi:10.1073/pnas.1914999116.
38. Peters Jr, T. (1995). All about albumin: biochemistry, genetics, and medical applications (Academic press).
39. Kuo, Y.-M., Kokjohn, T.A., Kalback, W., Luehrs, D., Galasko, D.R., Chevallier, N., Koo, E.H., Emmerling, M.R., and Roher, A.E. (2000). Amyloid-β Peptides Interact with Plasma Proteins and Erythrocytes: Implications for Their Quantitation in Plasma. Biochemical and Biophysical Research Communications *268*, 750-756. https://doi.org/10.1006/bbrc.2000.2222.
40. Murakami, K., Murata, N., Noda, Y., Tahara, S., Kaneko, T., Kinoshita, N., Hatsuta, H., Murayama, S., Barnham, K.J., Irie, K., et al. (2011). SOD1 (Copper/Zinc Superoxide Dismutase) Deficiency Drives Amyloid β Protein Oligomerization

and Memory Loss in Mouse Model of Alzheimer Disease *. Journal of Biological Chemistry *286*, 44557-44568. 10.1074/jbc.M111.279208.
41. Gella, A., and Durany, N. (2009). Oxidative stress in Alzheimer disease. Cell adhesion & migration *3*, 88-93. 10.4161/cam.3.1.7402.
42. Kontopidis, G., Holt, C., and Sawyer, L. (2004). Invited Review: β-Lactoglobulin: Binding Properties, Structure, and Function. Journal of Dairy Science *87*, 785-796. https://doi.org/10.3168/jds.S0022-0302(04)73222-1.
43. Zhou, C., Qi, W., Neil Lewis, E., and Carpenter, J.F. (2015). Concomitant Raman spectroscopy and dynamic light scattering for characterization of therapeutic proteins at high concentrations. Analytical Biochemistry *472*, 7-20. https://doi.org/10.1016/j.ab.2014.11.016.
44. McAlary, L., Aquilina, J.A., and Yerbury, J.J. (2016). Susceptibility of Mutant SOD1 to Form a Destabilized Monomer Predicts Cellular Aggregation and Toxicity but Not In vitro Aggregation Propensity. Front Neurosci *10*, 499. 10.3389/fnins.2016.00499.
45. Li, J., Santambrogio, C., Brocca, S., Rossetti, G., Carloni, P., and Grandori, R. (2016). Conformational effects in protein electrospray-ionization mass spectrometry. Mass Spectrometry Reviews *35*, 111-122. https://doi.org/10.1002/mas.21465.
46. Narazaki, R., Maruyama, T., and Otagiri, M. (1997). Probing the cysteine 34 residue in human serum albumin using fluorescence techniques. Biochimica et Biophysica Acta (BBA)-Protein Structure and Molecular Enzymology *1338*, 275-281.
47. Vijayalakshmi, L., Krishna, R., Sankaranarayanan, R., and Vijayan, M. (2008). An asymmetric dimer of β-lactoglobulin in a low humidity crystal form—Structural changes that accompany partial dehydration and protein action. Proteins: Structure, Function, and Bioinformatics *71*, 241-249. https://doi.org/10.1002/prot.21695.
48. Meisl, G., Kirkegaard, J.B., Arosio, P., Michaels, T.C.T., Vendruscolo, M., Dobson, C.M., Linse, S., and Knowles, T.P.J. (2016). Molecular mechanisms of protein aggregation from global fitting of kinetic models. Nature Protocols *11*, 252-272. 10.1038/nprot.2016.010.
49. Cohen, S.I.A., Vendruscolo, M., Dobson, C.M., and Knowles, T.P.J. (2011). Nucleated polymerization with secondary pathways. II. Determination of self-consistent solutions to growth processes described by non-linear master equations. The Journal of Chemical Physics *135*, 065106. 10.1063/1.3608917.
50. Cohen, S.I.A., Vendruscolo, M., Dobson, C.M., and Knowles, T.P.J. (2012). From Macroscopic Measurements to Microscopic Mechanisms of Protein Aggregation. Journal of Molecular Biology *421*, 160-171. https://doi.org/10.1016/j.jmb.2012.02.031.
51. Meisl, G., Yang, X., Hellstrand, E., Frohm, B., Kirkegaard, J.B., Cohen, S.I.A., Dobson, C.M., Linse, S., and Knowles, T.P.J. (2014). Differences in nucleation behavior underlie the contrasting aggregation kinetics of the Aβ40 and Aβ42 peptides. Proceedings of the National Academy of Sciences *111*, 9384. 10.1073/pnas.1401564111.
52. Linse, S. (2019). Mechanism of amyloid protein aggregation and the role of inhibitors. Pure and Applied Chemistry *91*, 211 - 229.
53. Garcia-Alloza, M., Subramanian, M., Thyssen, D., Borrelli, L.A., Fauq, A., Das, P., Golde, T.E., Hyman, B.T., and Bacskai, B.J. (2009). Existing plaques and neuritic abnormalities in APP:PS1 mice are not affected by administration of the gamma-secretase inhibitor LY-411575. Molecular Neurodegeneration *4*, 19. 10.1186/1750-1326-4-19.

54. Valentine, J.S., Doucette, P.A., and Zittin Potter, S. (2005). Copper-zinc superoxide dismutase and amyotrophic lateral sclerosis. Annu Rev Biochem *74*, 563-593. 10.1146/annurev.biochem.72.121801.161647.
55. Österlund, N., Kulkarni, Y.S., Misiaszek, A.D., Wallin, C., Krüger, D.M., Liao, Q., Mashayekhy Rad, F., Jarvet, J., Strodel, B., Wärmländer, S.K.T.S., et al. (2018). Amyloid-β Peptide Interactions with Amphiphilic Surfactants: Electrostatic and Hydrophobic Effects. ACS Chemical Neuroscience *9*, 1680-1692. 10.1021/acschemneuro.8b00065.
56. Strodel, B. (2021). Energy Landscapes of Protein Aggregation and Conformation Switching in Intrinsically Disordered Proteins. Journal of Molecular Biology *433*, 167182. https://doi.org/10.1016/j.jmb.2021.167182.
57. Österlund, N., Lundqvist, M., Ilag, L.L., Gräslund, A., and Emanuelsson, C. (2020). Amyloid-β oligomers are captured by the DNAJB6 chaperone: Direct detection of interactions that can prevent primary nucleation. Journal of Biological Chemistry *295*, 8135-8144. https://doi.org/10.1074/jbc.RA120.013459.
58. Scheidt, T., Łapińska, U., Kumita, J., Whiten, D., Klenerman, D., Wilson, M., Cohen, S., Linse, S., Vendruscolo, M., Dobson, C., et al. (2019). Secondary nucleation and elongation occur at different sites on Alzheimer's amyloid-β aggregates. Science Advances *5*, eaau3112. 10.1126/sciadv.aau3112.
59. Månsson, C., Arosio, P., Hussein, R., Kampinga, H.H., Hashem, R.M., Boelens, W.C., Dobson, C.M., Knowles, T.P., Linse, S., and Emanuelsson, C. (2014). Interaction of the molecular chaperone DNAJB6 with growing amyloid-beta 42 (Aβ42) aggregates leads to sub-stoichiometric inhibition of amyloid formation. Journal of Biological Chemistry *289*, 31066-31076.
60. Arosio, P., Michaels, T.C.T., Linse, S., Månsson, C., Emanuelsson, C., Presto, J., Johansson, J., Vendruscolo, M., Dobson, C.M., and Knowles, T.P.J. (2016). Kinetic analysis reveals the diversity of microscopic mechanisms through which molecular chaperones suppress amyloid formation. Nature Communications *7*, 10948. 10.1038/ncomms10948.
61. Aprile, F.A., Dhulesia, A., Stengel, F., Roodveldt, C., Benesch, J.L.P., Tortora, P., Robinson, C.V., Salvatella, X., Dobson, C.M., and Cremades, N. (2013). Hsp70 Oligomerization Is Mediated by an Interaction between the Interdomain Linker and the Substrate-Binding Domain. PLOS ONE *8*, e67961. 10.1371/journal.pone.0067961.
62. Aquilina, J.A., Benesch, J.L.P., Bateman, O.A., Slingsby, C., and Robinson, C.V. (2003). Polydispersity of a mammalian chaperone: Mass spectrometry reveals the population of oligomers in αB-crystallin. Proceedings of the National Academy of Sciences *100*, 10611-10616. 10.1073/pnas.1932958100.
63. Peschek, J., Braun, N., Franzmann, T.M., Georgalis, Y., Haslbeck, M., Weinkauf, S., and Buchner, J. (2009). The eye lens chaperone alpha-crystallin forms defined globular assemblies. Proc Natl Acad Sci U S A *106*, 13272-13277. 10.1073/pnas.0902651106.
64. Stengel, F., Baldwin, A.J., Painter, A.J., Jaya, N., Basha, E., Kay, L.E., Vierling, E., Robinson, C.V., and Benesch, J.L.P. (2010). Quaternary dynamics and plasticity underlie small heat shock protein chaperone function. Proceedings of the National Academy of Sciences *107*, 2007-2012. 10.1073/pnas.0910126107.
65. Feil, I.K., Malfois, M., Hendle, J., van der Zandt, H., and Svergun, D.I. (2001). A Novel Quaternary Structure of the Dimeric α-Crystallin Domain with Chaperone-like Activity*. Journal of Biological Chemistry *276*, 12024-12029. https://doi.org/10.1074/jbc.M010856200.

66. Smirnova, E., Chebotareva, N., and Gurvits, B. (2013). Transient transformation of oligomeric structure of alpha-crystallin during its chaperone action. Int J Biol Macromol *55*, 62-68. 10.1016/j.ijbiomac.2012.12.013.
67. Hochberg, G.K.A., Ecroyd, H., Liu, C., Cox, D., Cascio, D., Sawaya, M.R., Collier, M.P., Stroud, J., Carver, J.A., Baldwin, A.J., et al. (2014). The structured core domain of αB-crystallin can prevent amyloid fibrillation and associated toxicity. Proceedings of the National Academy of Sciences *111*, E1562-E1570. 10.1073/pnas.1322673111.
68. Wright, M.A., Aprile, F.A., Arosio, P., Vendruscolo, M., Dobson, C.M., and Knowles, T.P. (2015). Biophysical approaches for the study of interactions between molecular chaperones and protein aggregates. Chem Commun (Camb) *51*, 14425-14434. 10.1039/c5cc03689e.
69. Ishtikhar, M., Ali, M.S., Atta, A.M., Al-Lohedan, H., Badr, G., and Khan, R.H. (2016). Temperature dependent rapid annealing effect induces amorphous aggregation of human serum albumin. International Journal of Biological Macromolecules *82*, 844-855. https://doi.org/10.1016/j.ijbiomac.2015.10.071.
70. Yang, M., Dutta, C., and Tiwari, A. (2015). Disulfide-Bond Scrambling Promotes Amorphous Aggregates in Lysozyme and Bovine Serum Albumin. The Journal of Physical Chemistry B *119*, 3969-3981. 10.1021/acs.jpcb.5b00144.
71. McAlary, L., Aquilina, J.A., and Yerbury, J.J. (2016). Susceptibility of Mutant SOD1 to Form a Destabilized Monomer Predicts Cellular Aggregation and Toxicity but Not In vitro Aggregation Propensity. Frontiers in Neuroscience *10*. 10.3389/fnins.2016.00499.
72. Hamada, D., and Dobson, C.M. (2002). A kinetic study of beta-lactoglobulin amyloid fibril formation promoted by urea. Protein science : a publication of the Protein Society *11*, 2417-2426. 10.1110/ps.0217702.
73. König, A.S., Rösener, N.S., Gremer, L., Tusche, M., Flender, D., Reinartz, E., Hoyer, W., Neudecker, P., Willbold, D., and Heise, H. (2021). Structural details of amyloid β oligomers in complex with human prion protein as revealed by solid-state MAS NMR spectroscopy. J Biol Chem *296*, 100499. 10.1016/j.jbc.2021.100499.
74. Ilitchev, A.I., Giammona, M.J., Olivas, C., Claud, S.L., Lazar Cantrell, K.L., Wu, C., Buratto, S.K., and Bowers, M.T. (2018). Hetero-oligomeric Amyloid Assembly and Mechanism: Prion Fragment PrP(106-126) Catalyzes the Islet Amyloid Polypeptide β-Hairpin. J Am Chem Soc *140*, 9685-9695. 10.1021/jacs.8b05925.
75. Liao, L., Cheng, D., Wang, J., Duong, D.M., Losik, T.G., Gearing, M., Rees, H.D., Lah, J.J., Levey, A.I., and Peng, J. (2004). Proteomic characterization of postmortem amyloid plaques isolated by laser capture microdissection. J Biol Chem *279*, 37061-37068. 10.1074/jbc.M403672200.

5.10 Supporting information

5.10.1 Materials and methods

Aβ40 and amorphous aggregates preparation

Recombinant Aβ40 was purchased from Alexotech (purity>95 %, Umeå, Sweden). Albumin human (HSA, purity>96%, Cat No. A9731), β-lactoglobulin (BLG) (purity>90%, Cat No. L3908). Thioflavin T (ThT, Cat No. T3516) were obtained from Sigma-Aldrich (St. Louis MO, USA). Superoxide dismutase 1 (SOD1) was produced as described below. 1x PBS saline without Ca2+ and Mg2+ (Cat No. 14190144) was obtained from Gibco. All solvents and other

reagents were obtained from Sigma-Aldrich unless otherwise stated. All the buffers were filtered by 0.22 μm filter prior to use.

1 mg Aβ40 powder was dissolved in 1 mL 10 mM NaOH and sonicated on ice-water bath for 1 min, like the previously reported preparations [1]. Then the solution was aliquoted on ice and stored at −80 °C.

Recombinant full-length SOD1 was expressed and purified following an established protocol [2]. Briefly, the SOD1 protein was expressed in E-coli BL21(DE3)plysS and induced by 0.5 mM IPTG when an OD600 of 0.5-0.6 was reached. The cells were incubated for 4 h at 37℃, 180 rpm and then harvested by centrifuging at 8000 g for 15 min at 4 ℃ and ultra-sonicated with the bigger horn on ice (1 min with three times, each 1 s sonication and 0.5 s pause). Solid ammonium sulphate was added into the lysate supernatant to a final concentration of 50% and mixed at 4 ℃ for 2 h. The supernatant was collected and solid ammonium sulphate was added to a final concentration of 60% and mixed at 4 ℃ for 2 h. Afterwards, the supernatant was collected again and solid ammonium sulphate was added to a final concentration of 90 % and mixed at 4 ℃ for 2 h. The precipitated proteins were later collected by centrifuging and dissolved in 50 mM Tris-HCl, pH 7.5, before loading on a size-exclusion chromatography column HiLoad Superdex 75, 16-60 column. The SOD1 containing fractions were further loaded onto a 5 mL HiTrap Q FF column for further purification. The fractions with SOD1 were verified by SDS-PAGE. In order to lyophilize SOD1, the protein was dialyzed against 20 mM ammonium acetate solution.

The amorphous aggregates were freshly prepared by dissolving the powders of HSA, BLG and SOD1 in 1x PBS buffer on ice. The solutions were then filtered by a 0.22 μm filter. The concentrations were determined by measuring the UV-absorption at 280 nm using Nanodrop. 50 μM proteins were denatured at different temperatures 60 and 95 ℃ for 30 min respectively. The optimized HSA amorphous aggregates were prepared by denaturing at 95 ℃ for 5 min. To check the size of aggregates of these denatured proteins, DLS (dynamic light scattering) was further used.

Dynamic light scattering (DLS)

To characterize the sizes of the amorphous aggregates, Malvern Zetasizer Nano S (Malvern Instruments Ltd., UK) with a detection angle of 173° was applied. The intensity size distributions of 7.5 μM denatured globular proteins of HSA, BLG and SOD1 were obtained.

Each sample has at least 3 repeat measurements to check the result repeatability. All measurements were taken at room temperature.

ThT fluorescence assay

To investigate the inhibitory effect of the denatured proteins (HSA, BLG and SOD1) on the kinetics of Aβ40 aggregation, 10 μM Aβ40 was incubated with 0.5 μM of the above globular proteins in 20 mM PB buffer (pH 7.4) with 20 μM ThT fluorescence dye. 45 μL of each sample was transferred to a 384-well black plate with a transparent bottom (NUNC, Cat No. 242764, Thermo Fisher). The plate was then sealed and the ThT fluorescence intensity was measured using a PHERAstar FSX (BMG LABTECH, Germany) microplate reader (excitation: 430 nm, emission: 480 nm) at 37 °C under quiescent conditions.

To get further insight into the microscopic mechanism, another set of ThT fluorescence assays was prepared by using a concentration gradient (0.01, 0.05, 0.1, 0.2 and 0.4 μM) of aggregated HSA (95 ℃, 5 min), BLG (95 ℃, 30 min) and SOD1 (95 ℃, 30 min) incubating with 10 μM Aβ40 at 37 °C under quiescent conditions. The final concentration of ThT was 20 μM. The averaged data were normalized and then globally fitted, based on the published protocol [3].

In the seeding assay, Aβ40 seeds were prepared by monitoring the ThT (20 μM) fluorescence intensity of 10 μM Aβ40 until the beginning of final phase of Aβ40 fibril formation. Then, the seeds were sonicated in an ice-water bath for 2 min. The final concentration of Aβ40 seeds and Aβ40 in the presence of 0.5 μM amorphous aggregates was 1 and 10 μM, respectively.

To investigate the potential disaggregating effect of amorphously aggregated globular proteins, Aβ40 fibrils were prepared by incubating 10 μM Aβ40 with 20 μM ThT in a 384-well plate at 37 ℃. When the fluorescence intensity of Aβ40 reached the plateau phase, the freshly prepared monomeric and denatured globular proteins (HSA, BLG and SOD1) were added to the mature fibrils. The final concentration of the globular proteins and Aβ40 were 4.5 and 9 μM respectively. The decreased fluorescence was monitored by the plate-reader (PHERAstar FSX, BMG LABTECH, Germany) at 37 °C without shaking.

Transmission electron microscopy imaging (TEM)

To confirm the morphology of the amorphous aggregates, 50 μM aggregated proteins of HSA, BLG and SOD1 were diluted to 5 μM by PBS buffer. 6 μL of the above proteins without Aβ40 were absorbed on a freshly glow-charged 400-mesh Formvar-carbon coated copper grid for 2 min. The grids were then washed by 20 μL ddH2O for 30 s. 6 μL 2 % uranyl acetate were

stained onto the grids for 30 s twice and 20 μL ddH2O was applied to wash the grid for 15 s twice. Images were taken with a TEM (JEOL 2010) at an accelerating voltage of 200 KV.

For the inhibitory effect of the amorphous aggregates on Aβ40 fibrillation, TEM samples were all taken from the ThT ending point and prepared as the above procedures.

Circular dichroism (CD) spectroscopy

The far-UV region of CD spectra was recorded from 190-260 nm on a Chirascan plus CD spectropolarimeter (Applied Photophysics Limited, U.K.) under constant N2 flow. The samples were measured in a quartz cuvette with a path length of 1 mm, using a bandwidth of 1 nm, step size of 1nm, and 1 s response time. The final concentration of native or amorphous aggregated proteins (HSA, BLG, and SOD1) was 0.5 μM in 20 mM PB buffer (pH 7.4) without NaCl.

The samples of Aβ40 with or without native or amorphous aggregated proteins (HSA, BLG, and SOD1) were prepared by incubating 10 μM Aβ40 in or out of the presence of 0.5 μM native or amorphous aggregated proteins (HSA, BLG, and SOD1) at 37 °C without shaking for 30 h. The incubation buffer is 20 mM PB buffer (pH 7.4) without NaCl. Each spectrum represents the average of three accumulated scans. The relevant baseline was subtracted by PB (20 mM, pH 7.4) alone as a blank.

Dot blot

To determine the oligomer formation of Aβ40 with or without the presence of the amorphous aggregates, 25 μM Aβ40 (final concentration) was incubated with 10 μM (final concentration) freshly-prepared aggregated or monomeric states of HSA, BLG, or SOD1 at 37 °C for 2 h under quiescent conditions. A 96-well dot blot plate system (GE Whatman) with a piece of dry nitrocellulose (Amersham, Catalogue No 10600124) membrane was applied and each well was added into 50 uL of 10 times-diluted above described Aβ40 oligomer with or without the presence of the amorphous aggregates. A vacuum pump was used to dry the membrane for 30 min. The blot was blocked with 5 % non-fat milk in TBS-T (20 mM Tris-HCl, pH 7.5, 0.8 % (w/v) NaCl, 0.1 % (v/v) Tween-20) for 1 h at room temperature. The membrane was then incubated with the primary antibody A11, which was diluted 1:1000 and kept in 1 % non-fat milk in TBS-T buffer overnight at 4 ℃. Blots were later washed 3 x 10 min with TBS-T. The goat anti-Rabbit IgG H&L (HRP) secondary antibody (Abcam) was diluted 1:4000 in 1 % non-fat milk TBS-T and incubated for 1 h at room temperature. It was then washed 3x 10 min with

TBS-T buffer. Blots were later developed with the chemiluminescent reagent (LumiGLO, Chemiluminescent Substrate Kit).

Cell toxicity

Neuroblastoma SH-SY5Y cells were cultured in EMEM medium supplemented with 15 % (v/v) fetal bovine serum, 2 mM glutamine (final concentration), and 1% (v/v) penicillin/streptomycin. Cells were kept at 37 °C, 5 % CO2 in a petri dish. The maximum passage number was 15 times. 50 µL of the resuspended cells with 6000 cells/well density was dispensed to a 96-well plate. The plated cells were incubated for 24 h at 37 °C, 5 % CO2. The amorphous aggregates and monomers of HSA, BLG and SOD1 (final concentration 1 µM) in the presence or absence of Aβ40 (final concentration 10 µM) were added into the cells. PBS buffer was used as the control. Afterwards, the wells were incubated with the serum-free medium for 48 h. Before adding an equal volume of CellTiter-Glo luminescent reagent (Promega, cat. G7571) to the cell culture, the plate was equilibrated at room temperature for 30 min. Afterwards, the plate was put on an orbital shaker for 2 min and waited for 10 min to stabilize the luminescent signal. The luminescent intensity was measured on the PHERAstar 96-well plate reader. Three independent experiments were performed.

Native ion mobility-mass spectrometry

Samples of denatured globular proteins (50 µM) were buffer exchanged into 200 mM ammonium acetate pH 7.0 using Micro Bio-Spin 6 columns (Bio-Rad) for native IM-MS analysis. Denatured BLG was also mixed with Aβ40, to final concentrations of 10 µM BLG and 10 µM Aβ40 in 200 mM ammonium acetate pH 7.0. Samples were then left to equilibrate for 15 minutes before IM-MS analysis.

Samples were introduced into a Waters Synapt G2S IM-MS instrument via nESI ionization using borosilicate emitters (Thermo Scientific). Instrument parameters were tuned to retain native protein behavior in the gas phase. Protein structure was monitored by IM drift time to ensure that instrument settings did not cause gas phase unfolding. Parameters were as follows: Capillary voltage 1.5 kV, Sampling cone 20 V, Source temperature 20 °C, Trap energy 5 V, Transfer energy 2 V, Trap Gas 10 mL/min, Helium Gas 100 mL/min, IMS Gas 50 mL/min, IMS Wave Velocity 900 m/s, IMS Wave Height 40 V.

5.10.2 Results

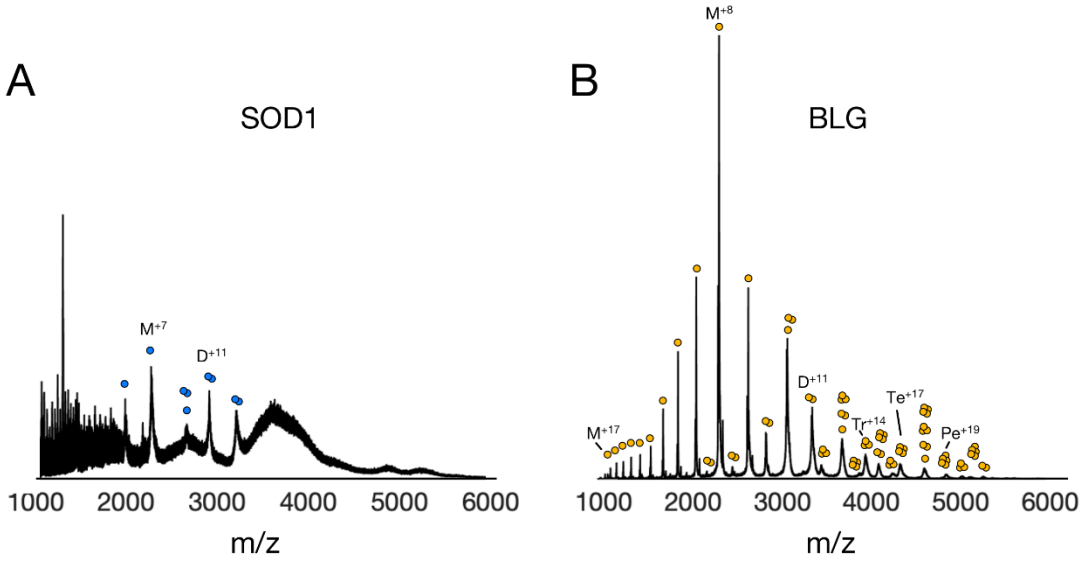

Fig. S1. Mass spectra of SOD1 (A) and BLG (B) after incubation in PBS at 95 °C for 30 minutes and then buffer exchanged into 200 mM ammonium acetate pH 7.0. Species are annotated as Oligomeric state+charge state, M = monomer, D = dimer, Tr = trimer, Te = tetramer, Pe = pentamer. The mass spectrum for SOD1 has additional broad peaks that could not be annotated.

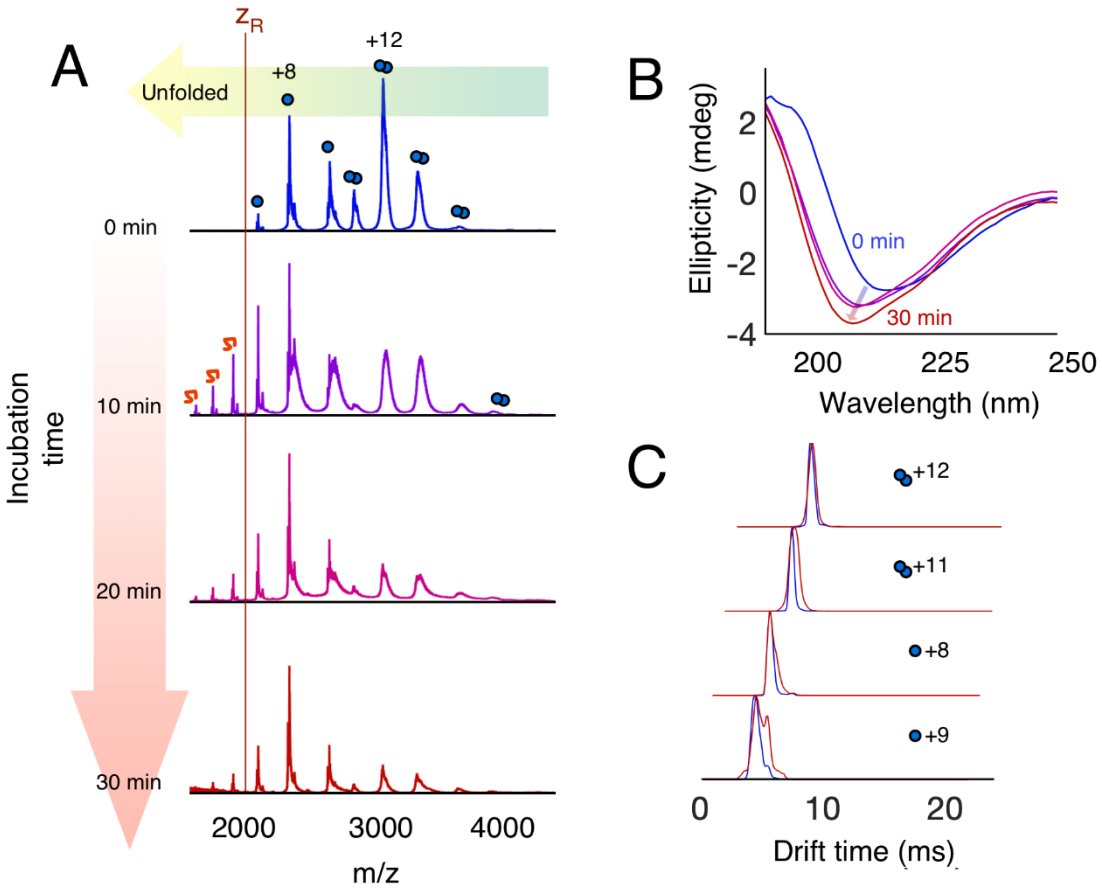

Fig. S2. Samples of 50 μM BLG were incubated in PBS at 95 °C for 0-30 minutes and then buffer exchanged into 200 mM ammonium acetate pH 7.0 (for IM-MS) or 20 mM sodium phosphate buffer pH 7.3 (for CD spectroscopy) using micro Bio-Spin P6 columns (Bio-Rad).MS analysis of the non-heated sample show a dimer-monomer equilibrium with low-charged ions detected (**A, top panel**), indicative of folded structures. The theoretical Rayleigh limit (z_R) was calculated to be +9 for monomeric BLG, and +13 for the dimer. z_R is the highest theoretical electrospray charge that a folded protein of a certain mass can acquire. Charges higher than z_R are thus likely to arise from more unstructured species. z_R for the monomer is indicated in the figure with a red line. +9 was the highest monomeric charge state and +13 was the highest dimeric charge state experimentally detected for the non-heated sample. This is in excellent agreement with the theoretical predication. Upon heating the mass spectrum notably shifts towards both smaller m and higher z **(A)**. The monomer-dimer equilibrium shifts towards the monomeric states, and monomeric charge states +10 to +12 appear. These higher charge states indicate a shift towards more unstructured monomeric species becoming populated. Also the dimeric species display a wider distribution of charges upon heating, indicating a wider ensemble of structures being populated. The signal to noise for the MS peaks become increasingly worse with increased incubation time, perhaps indicating a loss of protein to a state that can not be detected by MS. The shift in structure that is indicated in MS could also be detected using CD spectroscopy **(B)** and ion mobility (IM) spectrometry **(C)**. CD shows a shift from the native β-sheet structure with a minimum around 215 nm towards a more unstructured/helical structure with a spectral minimum at slightly lower wavelength upon heat treatment. IM similarly detects a slight extension of the structure, as seen by an increased drift time. This is most noticeable at charges close to z_R.

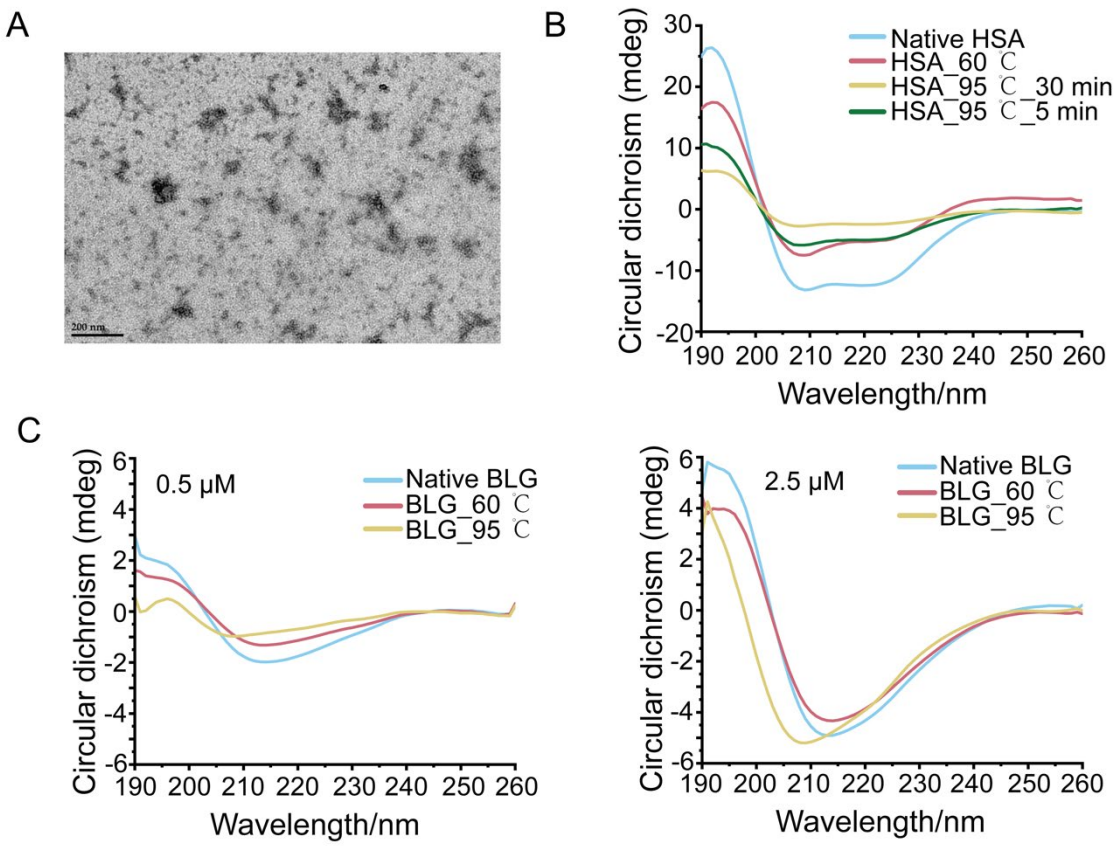

Fig. S3. (A) TEM images of 5 μM HSA denatured at 60 °C for 30 min. The scale bar is 200 nm. (B) Far-UV CD spectroscopy of 0.5 μM HSA in the native and denatured states. Denatured HSA was prepared by heating at 60 °C for 30 min, or 95 °C for 30 min and 5 min respectively. (C) Far-UV CD spectroscopy of BLG in the native and denatured states. Two different concentrations of BLG (0.5 μM and 2.5 μM) were applied. Denatured BLG was prepared by heating at 60 °C for 30 min, or 95 °C for 30 min.

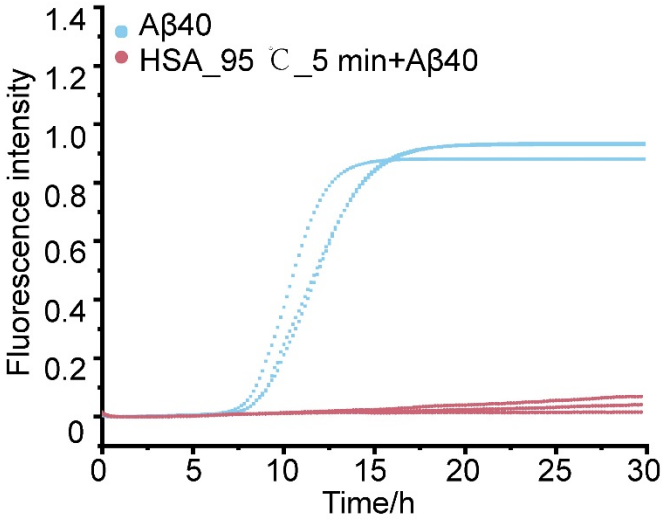

Fig. S4. ThT measurement of Aβ40 aggregation kinetics in the presence of HSA amorphous states. HSA was denatured at 95 ℃ for 5 mins. The measurement was conducted at 37 ℃ without agitation. The final concentration of Aβ40 is 10 μM with 0.5 μM HSA in 20 mM PB buffer (pH 7.4).

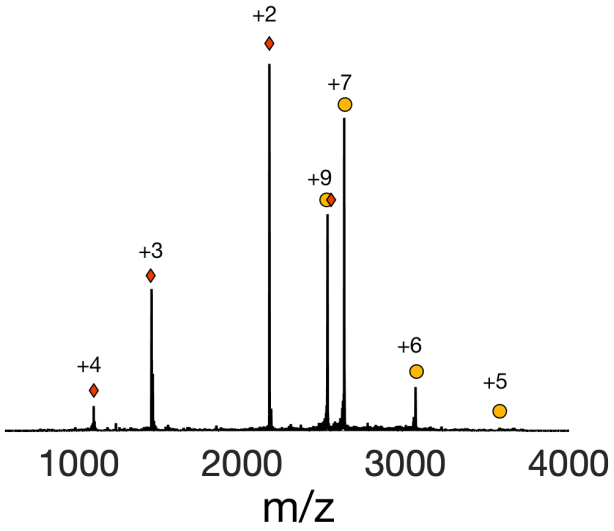

Fig. S5. MS/MS spectrum for the peak at m/z = 2522 after collisional activation in the trap cell of the MS instrument, confirming the identity of a BLG-Aβ40 heterodimer (+9). BLG monomers are annotated as yellow circles, while Aβ40 monomers are annotated as red diamonds.

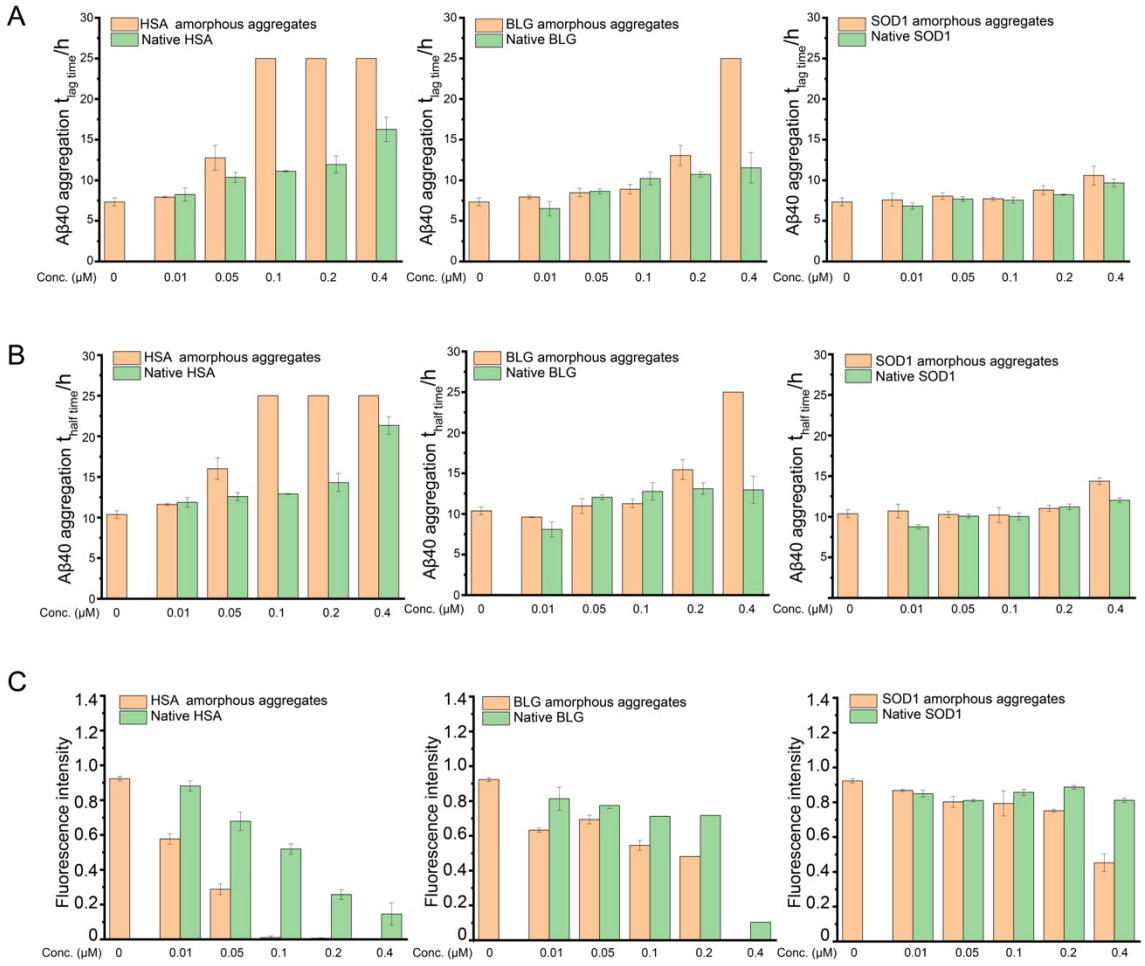

Fig. S6. The lag time (tlag time, h) (A), half time (t1/2, h) (B) and the end point (C) of fluorescence intensity of Aβ40 aggregation kinetics in the presence of native or amorphous states of HSA, BLG or SOD1. The final concentration of Aβ40 is 10 μM with a varying concentration 0-0.4 μM above non-chaperone proteins in 20 mM PB buffer (pH 7.4).

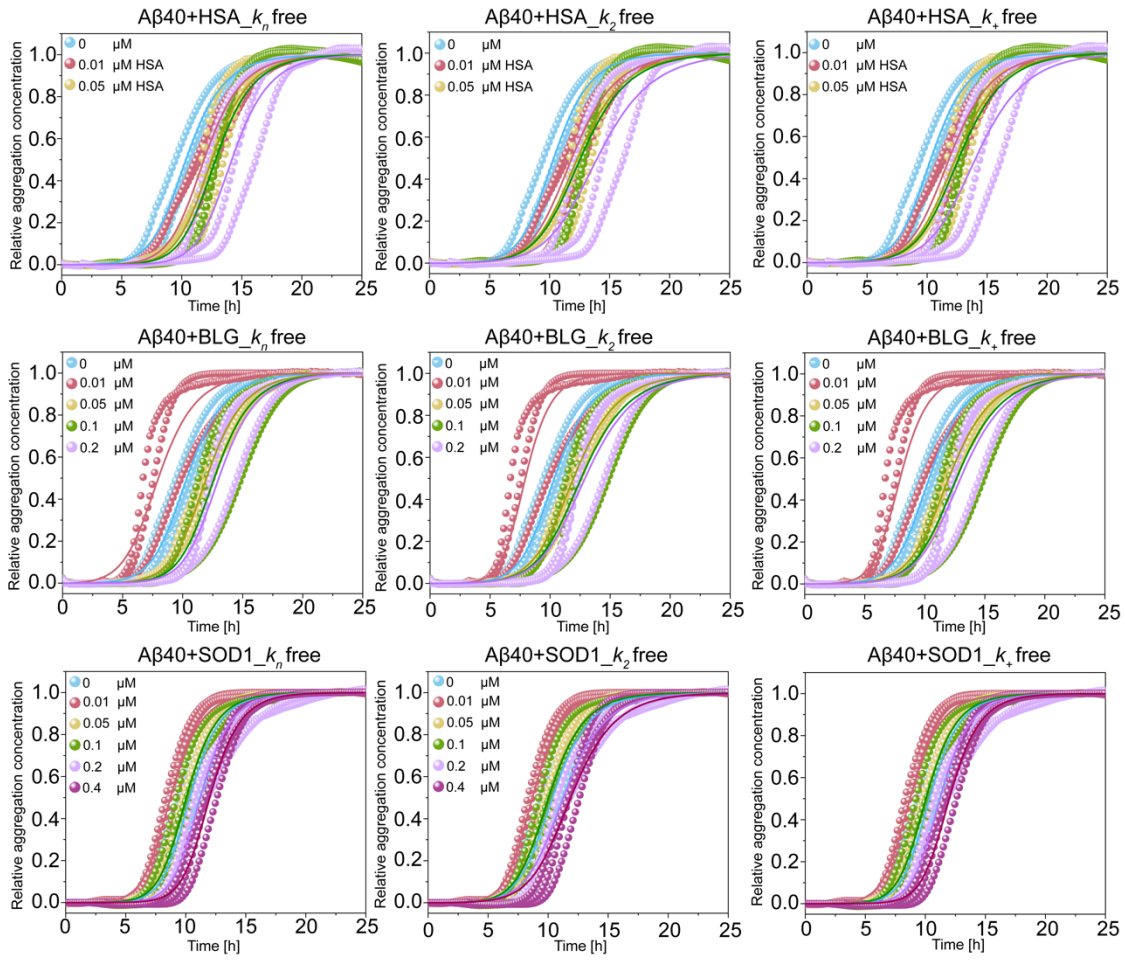

Fig. S7. The influence of native folded non-chaperone proteins (HSA, BLG and SOD1) on secondary processes of Aβ40 fibrillation. ThT fluorescence over time was performed to monitor the aggregation kinetics of 10 μM Aβ40 in the absence or presence of the native proteins (the raw data was derived from figure 6 and then globally fitting was used on the *AmyloFit* online software server [3]). Aβ40 alone were first fitted with a secondary nucleation dominated model, from which a set of parameters including k_n, k_2, and k_+ of Aβ40 fibrillation were obtained and used as the initial guess values for the following global fit.

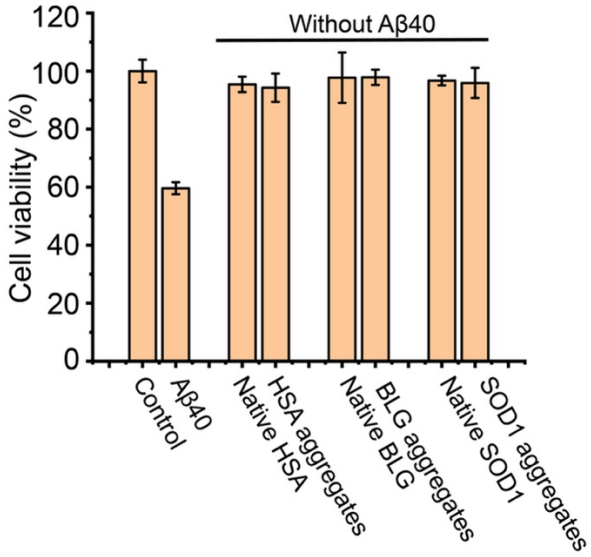

Fig. S8. The cytotoxic effects of the native and amorphous aggregates (HSA, BLG and SOD1) alone on SH-SY5Y cells. The final concentration these non-chaperone proteins was 1 μM. All the SH-SY5Y cells were incubation in EMEM medium at 37 °C for 48 h.

Table S1. Phenomenological parameters for Aβ40 aggregation (t1/2, h), calculated from sigmoidal curve fitting to Thioflavin T (ThT) fluorescence kinetic data.

t1/2(thalf time, h)			
	Conc. (μM)	Amorphous aggregates	Natively folded proteins
Aβ40		10.4±0.5	
HSA	0.01	11.6±0.1	11.8±0.5
	0.05	16±1.3	12.6±0.5
	0.1	>25 h	12.9±0.03
	0.2	>25 h	14.3±1.1
	0.4	>25 h	21.3±1.1
BLG	0.01	9.6±0.04	8.1±0.9
	0.05	10.9±0.9	12±0.3
	0.1	11.3±0.5	12.8±1.0
	0.2	15.4±1.2	13.0±0.7
	0.4	>25 h	13.0±1.6
SOD1	0.01	10.7±0.8	8.8±0.3
	0.05	10.2±0.4	10.0±0.2
	0.1	10.2±0.9	10.0±0.4
	0.2	11±0.4	11.2±0.4
	0.4	14.4±0.4	12±0.3

Table S2. Phenomenological parameter of end fluorescence point of Aβ40 aggregation in the presence of non-chaperone proteins, calculated from sigmoidal curve fitting to Thioflavin T (ThT) fluorescence kinetic data.

End fluorescence point			
	Conc. (μM)	Amorphous aggregates	Natively folded proteins
Aβ40	10	0.92±0.01	
HSA	0.01	0.58±0.03	0.88±0.03
	0.05	0.29±0.03	0.68±0.05
	0.1	0.01±0.009	0.52±0.03
	0.2	0.006±0.002	0.26±0.03
	0.4	0.0007±0.0003	0.15±0.06
BLG	0.01	0.63±0.01	0.81±0.07
	0.05	0.69±0.02	0.77±0.02
	0.1	0.55±0.03	0.71±0.01
	0.2	0.48±0.05	0.71±0.02
	0.4	0.03±0.00	0.1±0.02
SOD1	0.01	0.86±0.01	0.85±0.02
	0.05	0.8±0.03	0.86±0.01
	0.1	0.79±0.07	0.86±0.01
	0.2	0.75±0.01	0.88±0.01

	0.4	0.45±0.05	0.81±0.01

5.10.3 SI References

1. Wu, J., Blum, T.B., Farrell, D.P., DiMaio, F., Abrahams, J.P., and Luo, J. (2021). Cryo-electron Microscopy Imaging of Alzheimer's Amyloid-beta 42 Oligomer Displayed on a Functionally and Structurally Relevant Scaffold. Angewandte Chemie International Edition *60*, 18680-18687. https://doi.org/10.1002/anie.202104497.
2. Ahl, I.-M., Lindberg, M.J., and Tibell, L.A.E. (2004). Coexpression of yeast copper chaperone (yCCS) and CuZn-superoxide dismutases in Escherichia coli yields protein with high copper contents. Protein Expression and Purification *37*, 311-319. https://doi.org/10.1016/j.pep.2004.06.006.
3. Meisl, G., Kirkegaard, J.B., Arosio, P., Michaels, T.C.T., Vendruscolo, M., Dobson, C.M., Linse, S., and Knowles, T.P.J. (2016). Molecular mechanisms of protein aggregation from global fitting of kinetic models. Nature Protocols *11*, 252-272. 10.1038/nprot.2016.010.

Chapter 6

Single-molecule nanopore dielectrophoretic trapping of α-Synuclein with lipid membranes

Jinming Wu[1], Tohru Yamashita[2], Andrew D. Hamilton[2,3], and Sam Thompson[2,4], Jinghui Luo[1,*]

1. Department of Biology and Chemistry, Paul Scherrer Institute, 5232 Villigen, Switzerland
2. Department of Chemistry, University of Oxford, Oxford, OX1 3TA, UK
3. Department of Chemistry, New York University, NY 10003, USA
4. Department of Chemistry, University of Southampton, Southampton, SO17 1BJ, UK

*Corresponding author: Jinghui.luo@psi.ch

Accepted by ***Cell Reports Physical Science****.*

DOI: https://doi.org/10.1016/j.xcrp.2022.101243

6.1 Abstract

The lipid-α-Synuclein (α-Syn) interaction plays a crucial role in the pathogenesis of Parkinson's disease. Here, we trap α-Syn in conjunction with an α-hemolysin (αHL) single nanopore-lipid to investigate the lipid binding and unbinding kinetics of α-Syn in a lipidic environment. The hybridized α-Syn is generated through a reaction between a 5'-thiol-modified nucleotide oligo (dC30) and the α-Syn mutant (A140C). Owing to an applied voltage, single-molecule hybridized α-Syn can be trapped at the single nanopore. The trapping events are associated with dielectrophoretic force. The conformational switch events of α-Syn can be observed at the pore-membrane junction through the interpretation of blockade current amplitudes and dwell time. This can be related to the protein quaternary structure influenced by the α-Syn-membrane interaction, allowing further analysis of α-Syn conformational dynamics. We studied how disease-associated metal ions (Cu^{2+}, Zn^{2+}) modulate the dynamics of α-Syn at the interface of the membranes and pore, and how α-helical peptidomimetics stabilize the helical conformation of α-Syn in the presence of a membrane. These studies aid our understanding of the complexity of the interaction of α-Syn, lipid membranes, and metal ions, and in using peptidomimetics, a new strategy against α-Syn toxicity and aggregation is advanced.

Keywords: α-Synuclein; single-nanopore; lipid bilayer; peptidomimetic; neurodegeneration

6.2 Introduction

Contributing to the pathogenesis of Parkinson's disease (PD), intrinsically disordered α-Synuclein (α-Syn), a 140-residue protein, is extensively expressed in neurons and enriched in the synaptic cleft [1]. α-Syn consists of 3 domains: a membrane binding region with positively charged N-terminal residues from 1-60 [2, 3], an aggregation associated central hydrophobic domain (NAC: from residues 61-95) and a disordered acidic C-terminal residues from 96-140 [4, 5]. During aging, the protein deposits as β-sheet rich amyloid fibrils [6], with contemporaneous neuronal dysfunction and degeneration in the brain of PD. Although the biological role of α-Syn remains elusive, a number of studies suggest that it interacts with phospholipid membranes in physiology and pathology, such as synaptic regulation and neuronal death [6, 7]. In an effort to reveal the molecular basis of α-Syn toxicity and aggregation, the interaction of α-Syn with membranes has been widely explored [8-10]. Several models have been presented to explain the α-Syn induced toxicity to lipid membranes: (1) membrane-permeabilizing toroidal or barrel

pores [11]; (2) carpet model of disrupting and thinning membrane [12, 13]; and (3) lipid extraction model [14]. Reciprocally, the nature of the lipid membrane affects the binding, misfolding, and aggregation of α-Syn [15]. For instance, α-Syn preferentially binds to membranes with negative charges and high curvatures [16]. α-Syn is also reported to induce lipid expansion and lead to membrane remodeling [17]. Additionally, the decreased α-Syn/membrane interaction can facilitate α-Syn aggregation and enhance the neurotoxicity [18]. Folding and unfolding of α-Syn in a lipid membrane environment has been reported to play a vital role in toxicity yet the kinetics remain to be fully explored [19]. It is known that the level of metal ions varies in PD patients and healthy brains [20, 21]. For example, the cerebrospinal fluid of the substantia nigra from PD patients has abnormally high concentrations of Cu^{2+}, $Fe^{3+,}$ and Zn^{2+} [22-24]. In addition, metal chelators were able to inhibit the production of α-Syn oligomer-induced reactive oxygen species and meanwhile prevent oligomer-induced neuronal death [25]. It suggests that metal ions also act as an important factor to modulate α-Syn folding, aggregation, and neurotoxicity [26]. Overall, both the metal ions and lipid membrane interaction with α-Syn are two main factors that are involved in the pathogenesis of PD, either in a direct causal manner or as a consequence of misfolding. Thus, it would be important to investigate how metal ions modulate the α-Syn binding and unbinding to the lipid membranes for further understanding of the molecular mechanisms of α-Syn in the pathology of PD.

Single-nanopore technologies have been used to record the interaction or aggregation among amyloid proteins with or without metal ions or small molecules at the single-molecule level [27-30]. The recording is on the basis of individual amyloid proteins blocking or translocating through a single nanopore. The dwell time and residual current of single-nanopore transient blockade by individual amyloid proteins can be extracted to gain an understanding of protein folding, topology, and noncovalent interactions of the lumen in the nanopore [31, 32]. A biological nanopore, such as an α-hemolysin (αHL) nanopore, is an assembly of pore-forming toxins in reconstituted lipid membranes across *cis* (ground side) and *trans* sides (**Fig. 1**). Secreted by Staphylococcus aureus, αHL oligomerizes and self-assembles into a heptameric mushroom-shaped β-barrel pore [33]. By adding the amyloid peptides into the *cis*-side of wild-type αHL, Wang *et al*. investigated how amyloid proteins block or translocate the single nanopore for the characterization of amyloid aggregation or interaction [28, 29]. As αHL pore entry (which is *cis*-side in our convention) is elevated ~5 nm above the bilayer, the *trans*-entrance (αHL exit) of the channel lies close to the bilayer surface. When the peptides are added to the *trans*-side, the molecules, especially those preferring to interact with membranes like α-Syn [34], will easily

enter the channel. After the addition of α-Syn into the *trans*-side, Gurnev *et al*. observed the membrane-binding α-Syn, of which the C-terminal tail entered the pore and the N and NAC domains partitioned on the surface of the lipid membrane [10]. Tavassoly *et al.* used the same setup and found that Cu^{2+} ions induce large conformational changes of α-Syn [35]. However, in these cases, it is unclear how the whole sequence of α-Syn interacts with the lipid membranes and how metal ions regulate the entire α-Syn binding and unbinding to lipid membranes. Recently, Rodriguez-Larrea *et al.* studied the unfolding kinetics of thioredoxin (Trx) in a conjunction with a DNA oligonucleotide leader oligo(dC30) through a nanopore [36, 37]. The oligo(dC30) linked Trx was added to the *cis* part of the chamber, where the unfolding of Trx only occurs without interacting with lipid membranes. Their work provides an insight into the unfolding kinetics of Trx without interacting with lipid membranes. The dynamics of α-Syn in a lipid membrane environment play a vital role in toxicity yet the kinetics remain to be fully explored.

Using single-nanopore analysis, we investigated how Cu^{2+} modulates α-Syn dynamic lipid binding and unbinding states on the *trans* side that has a lipidic environment shown in **Fig.1** at the single-molecular level. By conjunction α-Syn mutant (A140C) with oligo(dC30), we observed two step-wise blockades of single-nanopore by the oligo-linked α-Syn, which may be explained by single-nanopore dielectrophoresis (DEP) force model [38]. In this model, the observed two blockade levels were caused by its interaction with the lipid membrane and trapped by a strong DEP force at the pore-membrane junction. We further studied two metal ions, Cu^{2+}, $Zn^{2+,}$ and a helix mimetic compound that modulates α-Syn dynamics in a lipidic environment. These studies seek insights into the complexity of α-Syn interactions with lipid membranes in the presence of metal ions and small molecule modulators of misfolding, thus allowing the development of new strategies against α-Syn toxicity and aggregation.

6.3 Results and discussion

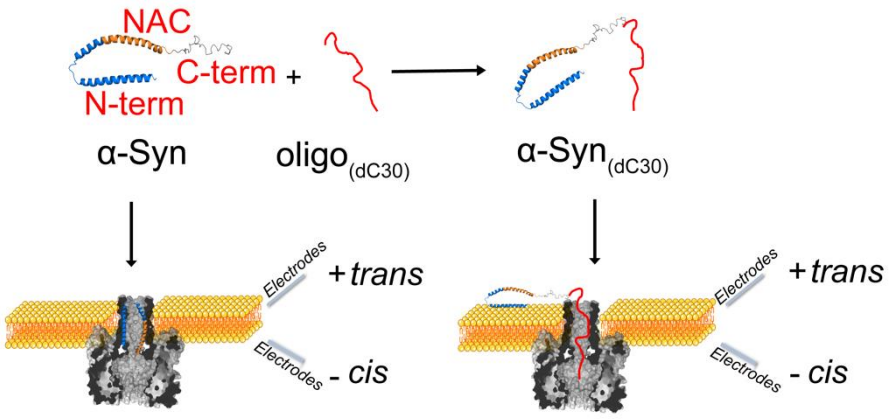

Figure 1. Illustration of α-Syn-membrane interactions studied by single-molecule nanopore analysis. Wild-type (WT) α-Syn was added to the *trans* side of a single α-hemolysin (αHL) nanopore and induced the blockage of the αHL channel in a lipid bilayer. To study the interaction of full-length α-Syn with the lipid membrane, α-Syn mutant (A140C) was linked to oligonucleotide dC30. The conjunction α-Syn$_{(dC30)}$ was then added to the *trans* side of the αHL nanopore and induced the dielectrophoresis trapping of α-Syn$_{(dC30)}$ in lipid membranes.

To investigate whether PD-associated Cu^{2+} ions modulate the binding between the lipid bilayer and α-Syn, we conducted a single-molecule αHL nanopore electrical recording in the presence of α-Syn with or without Cu^{2+} ions, shown in **Fig. 1**. The αHL nanopore was reconstituted in a planar lipid bilayer, composed of a mixture of neutrally charged DOPC (1,2-dioleoyl-sn-glycero-3-phosphocholine) and negatively charged DOPG (1,2-dioleoyl-sn-glycero-3-phospho-(1′-rac-glycerol)) with a ratio of 4:1. Though α-Syn is negatively charged (+3 net charge of N-terminus and -8 net charge of C-terminus), it is generally accepted that it is the N-terminus that modulates α-Syn interaction with membranes, while the C-terminus remains unbound [39]. Additionally, α-Syn preferentially binds to more physiologically relevant lipids (bilayer or small unilamellar vesicles) with anionic headgroups like PG [40], which typically takes up less than 30 % of lipids and has been used as a model lipid in the study of peptides with membrane-driven association [41, 42], cell-penetrating [43-45], and the channel activities [46]. Thus, the mixture of DOPC: DOPG (4:1) is chosen in our setup to study the interaction of α-Syn with lipid membranes.

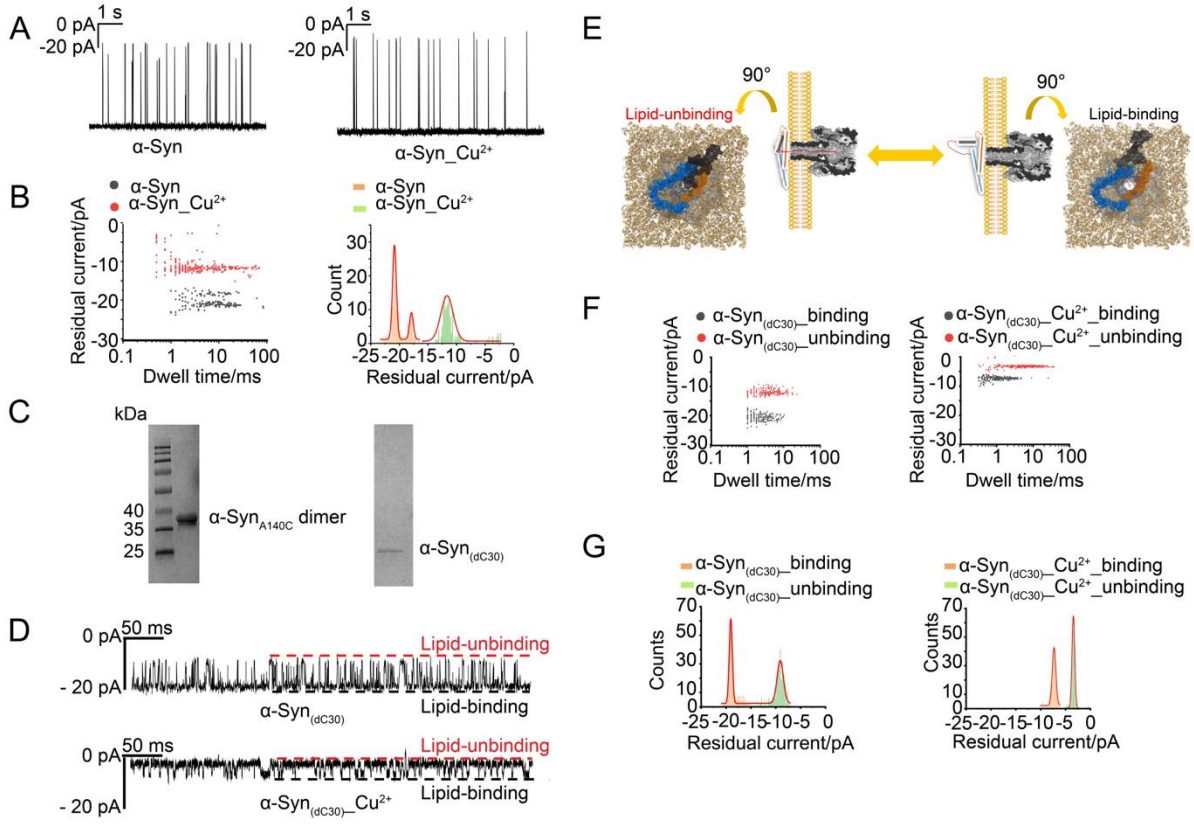

Figure 2. (A) Representative current traces reveal the translocation of wild-type (WT) α-Syn through a single αHL nanopore in the presence or absence of Cu^{2+} ions with the applied voltage -100 mV. The samples were added to the *trans* side of the lipid bilayer, composed of DOPC and DOPG (4:1). (B) Left: scatter distribution of the event dwell time plotted against the residue current in the presence of WT α-Syn with or without Cu^{2+} ions. Right: residue current histogram in the presence of WT α-Syn with or without Cu^{2+} ions. (C) The conjunction α-Syn (A140C) with single-strand DNA oligos (dC30) through pyridyl disulfide reaction (Left) and α-Syn (A140C) dimer. (D) Representative current recording of a single αHL nanopore across a planar lipid bilayer composed of DOPC and DOPG (4:1) in the presence of α-Syn$_{(dC30)}$ with or without Cu^{2+} at -100 mV (Upper). (E) Illustration of α-Syn conformational switch in lipid membranes. α-Syn binding to lipid membranes accompanies the higher residual current. (F) Scatter distribution of the event dwell time plotted against the residual current in the presence of α-Syn$_{(dC30)}$ with or without Cu^{2+} ions. Due to the nanopore dielectrophoresis trapping, α-Syn$_{(dC30)}$ binding to lipid bilayer generated a higher residual current than the unbinding state. Two distinct events were classified, the lipid-unbinding (red scatters) and lipid-binding events (black scatters) of α-Syn$_{(dC30)}$. (G) Residual current histogram in the presence of α-Syn$_{(dC30)}$ with or without Cu^{2+} ions. Similar to the presence of WT α-Syn, the addition of Cu^{2+} ions to

the hybrid α-Syn reduced the residual current of electrical recording, suggesting the different α-Syn conformations in the presence of Cu^{2+} ions. For all the nanopore experiments, the two sides of the chamber (*cis* and *trans*) are filled with 10 mM HEPES buffer, pH 7.4, with 1 M KCl. The final concentration of WT or hybridized α-Syn$_{(dC30)}$ and Cu^{2+} is 0.2 μM and 5 μM respectively.

It has been reported that no blockage event for WT α-Syn in the αHL nanopore is observed [10, 29] when the voltage is lower than 40 mV. Here, we applied the potential between the lipid bilayer -100 mV due to the easy observation of the full blocked capture of WT α-Syn in the αHL nanopore [29]. Additionally, higher voltage makes current interruptions easily discernible. α-Syn binding to channels has also been demonstrated to vary with the bulk salt concentration 10. The higher salt concentration makes the capture by the channel easier, due to the decreased Coulomb and/or solvation barriers by high salt concentrations, in which these barriers are suggested to control the rate of α-Syn binding to channels. We fixed the salt concentration at 1 M, which is a standard salt concentration that has been applied in several publications [47-51]. Fig. 2A shows transient blockade events of the α-Syn without and with Cu2+ from the trans side, which is consistent with the previous observation that α-Syn causes transient nanopore blockage [29]. The final concentration of Cu2+ is 5 μM, which is far from the concentration (0.3 mM) that Cu2+ would change the architecture of αHL nanopore and keep the current unstable [52]. The stoichiometry of WT α-Syn to Cu2+ is 1:25, which is based on the previous publication that this ratio would induce α-Syn to a more folding and compact structure [35]. In the presence of Cu2+, α-Syn induces a lower residual current, which is shown as the red scatter distribution in Fig. 2B. The histogram analysis of the residual current amplitudes estimates α-Syn with and without Cu2+ ions to be -21 pA and -11.5 pA respectively. The lower nanopore blockage induced by the addition of Cu2+ ions revealed a more folded structure of α-Syn. This result is consistent with the previous publication that Cu2+ can induce the more α-helical signal of α-Syn in the presence of lipid vesicles [53]. The transient nanopore blockage may be caused by the translocation of α-Syn to the cis side 10. The charged C-terminus of α-Syn presumably leads the translocation of the full-length protein into the lumen of the nanopore. When the C-terminus enters the lumen, the current changes can be mainly attributed to the bilayer interaction with the N-terminus rather than the full-length protein. However, the transient current signal does not provide informative biophysical characterization for single-molecule α-Syn interaction with a lipid membrane.

To gain insights into the interaction of full-length α-Syn with lipid membranes, we linked the mutated α-Syn(A140C) to a single-strand 5′-thiol-modified DNA oligonucleotide dC30 with a hexamethylene linker which was activated with 2,2'-dipyridyl disulfide to yield 5′-S-thiopyridyl oligonucleotides for coupling to α-Syn(A140C) (**Fig. S3B**) [36]. Since α-Syn(A140C) only has one cysteine residue on the 140th amino acid alanine (A), dC30 will be coupled to the terminal cysteine residue (C). In this reaction, α-Syn(A140C) can be dimerized through cysteine-cysteine (that is S-S) linkage. We fractionated hybrid α-Syn(A140C)-dC30 (abbreviation α-Syn$_{(dC30)}$) and α-Syn dimer by ionic exchange column and confirmed α-Syn$_{(dC30)}$ and αSyn dimer bands on the SDS-gel page (**Fig. 2C**). The purpose of oligo(dC30) is used as a leading to thread into the αHL pore [36, 47, 54]. When applying a negative potential at the *trans* side, the negative-charged oligonucleotides dC30 in the *trans* part will facilitate the C-terminal end of α-Syn into the channel. Also, the N-terminal and NAC domains of α-Syn interact with membranes [39]. In this scenario, the dC30 will get trapped in the nanopore under applied voltage due to α-Syn N-terminal interaction with the lipids and highly negative charges of dC30. The trapped dC30 does not affect α-Syn conformation and interaction, especially the interaction with lipids. The interaction can remain the protein away from the translocation into the nanopore and trap the single protein for understanding their interaction kinetics with lipids. The shorter oligo-nucleotides will be more difficult to control their passing through the nanopore due to the high-speed translocation and insufficient dwell time to reach analytic resolution [55]. The oligonucleotide dC30 was chosen instead of dA30 or dT30, mainly due to poly(dC) giving a better discernible signal than poly(dA) [55] and a longer duration times of dC than that of dT [56]. The purification of hybrid α-Syn$_{(dC30)}$ was shown on SDS-PAGE in **Fig. 2C**. The addition of α-Syn$_{(dC30)}$ to the *trans* side caused the trapping of αHL nanopore in **Fig. 2D**. This may be attributed to two factors: (1) α-Syn$_{(dC30)}$ released the full-length α-Syn for the interaction with the head group of lipid membranes; (2) with its longer sequence, α-Syn$_{(dC30)}$ had a stronger dielectrophoretic force (DEP) at the nanopore conjunction than the WT. DEP trapping was observed in a previous study where α-Syn could be trapped in the constriction of a nanopore and was considered as a reservoir−microchannel junction [29]. Here, we observed two distinguished trapping levels in **Fig. 2D-G**, with approximately 10 pA current difference in the presence of α-Syn$_{(dC30)}$ but not WT α-Syn. At nanopore conjunction, a DEP of the opposite electric field induces particle deflection, focusing, and trapping [38]. Large complexes, like α-Syn$_{(dC30)}$, can be trapped in the conjunction but the smaller WT α-Syn translocates through the nanopore. Two different trapping events can be induced by the α-Syn interaction with the lipid

surface and a DEP that contributed to the binding and unbinding of α-Syn to the lipid membranes (**Fig. 2E**). The lower residue current we observed is assumed to be due to the folding of α-Syn. After applying the voltage, the single-strand oligo(dC30) would drag the folded α-Syn away from the lipid membrane, unbind to the lipid membrane and block the nanopore. The dwell time that α-Syn trapped in the pore is the *t*m_unbinding in our study. Thus, the higher residue current indicates the oligo(dC30)-linked-α-Syn, that is α-Syn$_{(dC30)}$, would block the nanopore less. We assume that α-Syn would not keep this folded state but unfold or change conformation and further get released from the nanopore, thus inducing the higher residue current. The time that α-Syn remains as the unfolding state is the *t*m_binding, which was calculated from the interevent interval of two lipid-unbinding levels, that is the time between two times of folded α-Syn trapped in the pore. The longer *t*m_binding indicates the more time that α-Syn would take to recover from the unfolding state to the folding state. In this case, the unfolded α-Syn would preferably bind to the lipid membrane, which is shown as the lipid-binding level in **Fig.2E**. The repeated two levels (lipid-unbinding and lipid-binding) suggest that α-Syn may display dynamics and kinetics with two conformational states while trapped at the lipid and nanopore conjunction. The dynamics and kinetics could be modulated by metal ions or small molecule ligands. For instance, shown in **Fig. 2D**, the inverted signal in the presence of Cu^{2+} ions represents more blockage by an α-Syn complex with Cu^{2+}. Cu^{2+} ions refolded α-Syn in a more compacted structure with the reduced residue current and longer dwell time in the electrical recording in **Fig. 2F-G**. Analysis of these trapping events offers insights into the conformational dynamics and kinetics of α-Syn in the presence of lipid membranes, metal ions, and aggregation inhibitors.

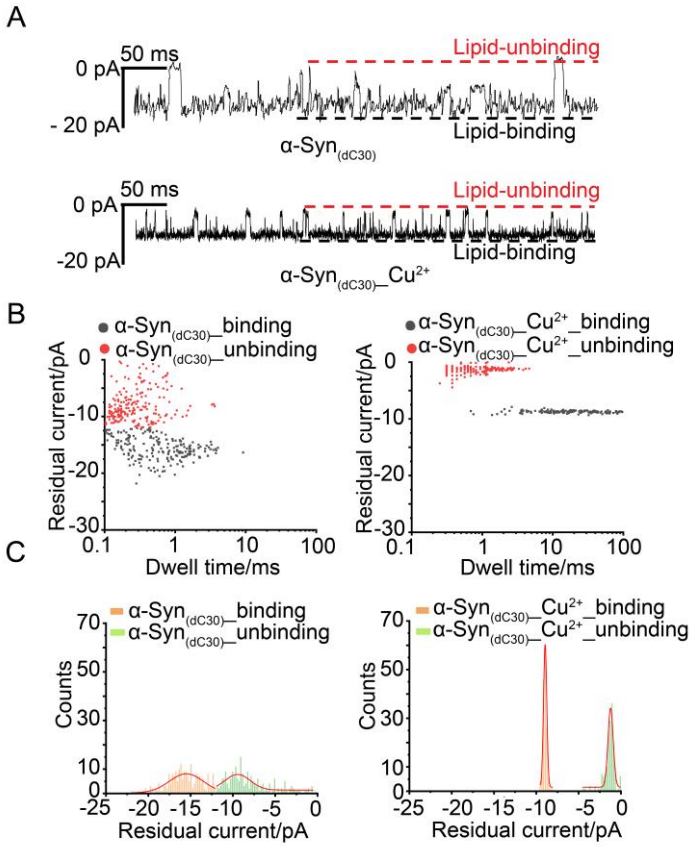

Figure 3. (A) Representative current recording of hybridized α-Syn$_{(dC30)}$ with or without Cu^{2+} translocating a single αHL nanopore on the neutrally charged DPhPC lipid bilayer at -100 mV. Two distinct conformational switch events of α-Syn$_{(dC30)}$ were classified. The unbinding α-Syn$_{(dC30)}$ to lipid membranes induced a smaller residual current than the binding conformation. The final concentration of hybridized α-Syn$_{(dC30)}$ and Cu^{2+} is 0.2 μM and 5 μM respectively. 10 mM HEPES buffer, pH 7.4, with 1 M KCl was used to fill the two sides of the chambers (*cis* and *trans*). (B) Scatter distribution of the dwell time plotted against the residue current of α-Syn$_{(dC30)}$ with or without Cu^{2+}. The red and black scatters represent the unbinding and binding events respectively. (C) The distributions of residue current of α-Syn$_{(dC30)}$ with or without Cu^{2+} are plotted as histograms, fitting with the multiple-peak Gaussian function.

As a control, we investigated the conformational dynamics of α-Syn$_{(dC30)}$ in the presence of a neutrally charged lipid membrane, composed of DPhPC (1,2-diphytanoyl-sn-glycero-3-phosphocholine). **Fig. 3A** shows that α-Syn displays fewer binding and unbinding events in DPhPC lipids than that in negatively charged DOPC: DOPG (4:1) lipid membranes (**Fig. 2D**), suggesting less completely α-Syn trapping into the nanopore. This may be explained by the greater association of α-Syn with a negatively charged lipid membrane, in agreement with

previous studies [57-59]. Similar to the presence of a negatively charged lipid membrane, the addition of Cu^{2+} ions and the hybridized α-Syn to the neutrally charged lipid membrane gave reduced residue current in the electrical recording. This reveals both Cu^{2+} ions and the nature of the lipid determine the conformation of α-Syn.

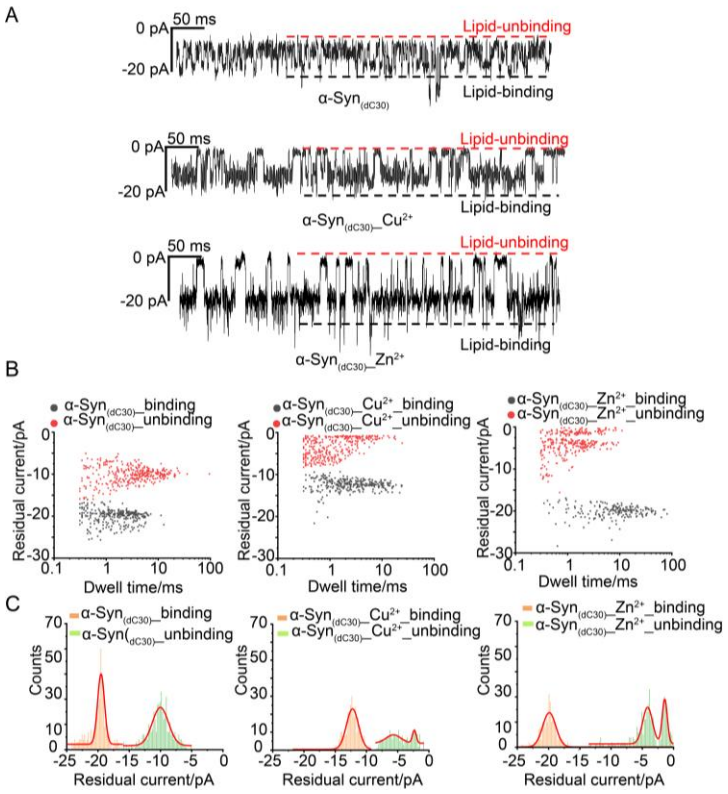

Figure 4. (A) Representative current recording of hybridized α-Syn(dC30) with or without Cu^{2+} or Zn^{2+} translocating a single αHL nanopore on the negatively charged DOPC: DOPG (4:1) lipid bilayer at -200 mV. Two distinct conformational switch events of α-Syn(dC30) were classified. The unbinding α-Syn(dC30) to lipid bilayers induced less blocked current than the binding structure. The final concentration of hybridized α-Syn(dC30) and Cu^{2+} or Zn^{2+} is 0.2 μM and 5 μM respectively. The two sides of the chamber (*cis* and *trans*) are filled with 10 mM HEPES buffer, pH 7.4, with 1 M KCl. (B) Scatter distribution of the dwell time plotted against the residue current of α-Syn(dC30) with or without Cu^{2+} or Zn^{2+}. The red and black scatters represent the unbinding and binding events respectively. (C) The distributions of residue current of α-Syn(dC30) with or without Cu^{2+} or Zn^{2+} are plotted as histograms, fitting with the multiple-peak Gaussian function. The metal ions Cu^{2+} and Zn^{2+} are obtained from $CuCl_2$ and $ZnSO_4$, respectively.

An increased dielectrophoretic force was carried out for studying different trapping events. We increased the voltage to -200 mV and observed in **Fig. 4A** that the trapping events are similar

to the recording at -100 mV in **Fig. 2D**. However, the presence of Cu^{2+} ions slightly changes the effect of trapping at -200 mV in **Fig. 4A**, in comparison to the trapping at -100 mV. It suggests a higher voltage may give a stronger dielectrophoretic force for the trapping and interaction of the α-Syn moiety with the lipid membranes in the presence of Cu^{2+} ions. A plausible explanation is that α-Syn forms a folded complex with Cu^{2+} ions, taking a stronger dielectrophoretic force at a higher voltage. We compared the modulation of the α-Syn interaction with lipid membranes in the presence of Cu^{2+} and Zn^{2+} at -200 mV. Since the lowest blockade current is observed with Cu^{2+} this suggests a more compacted α-Syn conformation. Likewise, the lipid-unbinding time constant (τ_1) is higher with Cu^{2+} than Zn^{2+} (**Table 1**), suggesting Cu^{2+} forms a more stable complex with α-Syn in the lipid membrane. This result is consistent with the outcome from nESI-IM-MS method that Cu^{2+} induced a more compact α-Syn conformation when Cu^{2+} binds to α-Syn *in vitro* [60].

Additionally, we found the addition of Cu^{2+} to α-Syn induced the longer *t*m_binding than that of α-Syn alone, which means Cu^{2+} induced the longer time for unfolded or conformation switched α-Syn to fold again. The main reason was assumed to be the formation of a more compact folded structure of α-Syn in the presence of Cu^{2+}, based on the observation of the lower residue current of α-Syn compared to α-Syn alone at the lipid-unbinding level. Such compact α-Syn conformation would take more time from unfolding to folding to bind to Cu^{2+}. Though Zn^{2+} induced an even longer *t*m_binding compared to Cu^{2+}, Zn^{2+} did not show a lower residue current at the lipid-unbinding level, suggesting Zn^{2+}-α-Syn forms a less compact conformation than that of Cu^{2+}-α-Syn. A plausible explanation is that Zn^{2+} induced different α-Syn conformation changes from Cu^{2+}. This conformation with Zn^{2+} would take more time for unfolded α-Syn to fold again compared to Cu^{2+}. Our trapping method as a complementary technique observed the dynamics of α-Syn within Cu^{2+} binding to lipid membranes. The residue current and time constant provide insight into the folding and complex stability information of metal ions, α-Syn, and lipid membranes.

Table 1. The conformational switch events of α-Syn$_{(dC30)}$ with or without Cu^{2+} at -100 mV on DPhPC and DOPC:DOPG (4:1) lipid bilayer. The time constant τ_1_lipid-unbinding and τ_2_lipid-binding are calculated from the scatter distribution of the dwell time against the residue current, which was fitted by the double-exponential decay function. The rate constant is $K_{on}=1/[\tau_{on}\times C_{peptide}]$. t_m represents the mean value of the dwell time [29]. $C_{peptide}$ represents the final concentration of the testing peptide in the aqueous phase.

	α-Syn$_{(dC30)}$	α-Syn$_{(dC30)}$ Cu^{2+}	α-Syn$_{(dC30)}$ Zn^{2+}
τ_1_unbinding (ms)	0.623±0.266	1.29±0.201	0.68±0.025
τ_2 binding (ms)	0.515±0.097	1.80±0.119	4.537±0.134
K_{on} unbinding ($L \cdot ms^{-1} \cdot g^{-1}$)	1.60×10^6	1.94×10^6	1.47×10^6
K_{on} binding ($L \cdot ms^{-1} \cdot g^{-1}$)	7.750×10^5	5.56×10^5	2.20×10^5
t_m unbinding (ms)	6.047±0.866	2.12±0.158	1.85±0.10
t_m binding (ms)	2.108±0.100	4.106±0.25	12.82±0.87

The single-nanopore trapping technique was further applied to investigate how small molecules, which can disrupt amyloid protein fibrillization kinetics, modulate α-Syn conformation in the presence of a lipid membrane (**Fig. 5**). Compound **3**, an α-helical mimetic compound that can imitate the topography of an α-helix, is functionalized with, at physiological pH, cationic NH_3^+, anionic COO^-, and branched alkyl groups in the *i*, *i+4* and *i+7* positions respectively (**Fig. 5B**) [61]. Mimetic **3** is designed to target the helical surface of α-Syn comprising three amino acids (negatively charged Glu^{46}, positively charged His^{50} and hydrophobic Ala^{53}) that occupy the *i*, *i + 4* and *i + 7* positions (**Fig. 5A**), by forming complementary contacts. We have previously successfully demonstrated such an approach with islet amyloid polypeptide [62]. As shown in **Fig. 5C**, compared to α-Syn$_{(dC30)}$ alone, the conformational switch events of α-Syn in the presence of mimetic **3** in lipid membranes are significantly reduced, consistent with the stabilization of the helical protein. Besides peptidomimetic **3**, dopamine, another compound that kinetically stabilizes α-Syn oligomers [63-66], also reduces the binding and unbinding events of α-Syn to lipid membranes, but with more spikes and greater residual current, indicative of the weaker binding of dopamine to α-Syn than that of mimetic **3**. These results suggest single-nanopore trapping is a suitable method to characterize the effect small molecules exert on α-Syn conformational dynamics in the presence of lipid membranes. Moreover, it may find use as a primary tool for the screening and optimization of aggregation inhibitors.

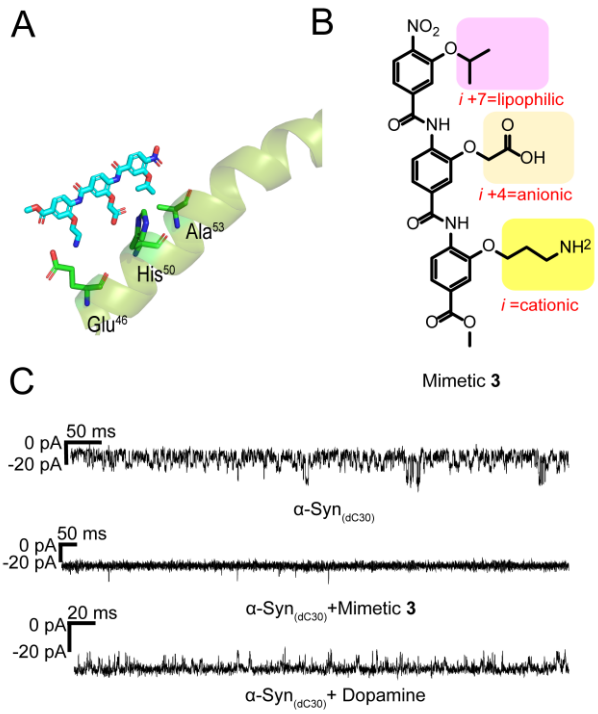

Figure 5. (A) Schematic representation of an α-helix mimetic compound interacting with three residues (Glu^{46}, His^{50}, and Ala^{53}) located in the α-helical region of membrane-bound α-Syn. (B) Structure of α-helix mimetic compound 3 with three side chains (yellow, orange and pink highlights) designed to form complementary contacts with residues Glu^{46}, His^{50} and Ala^{53} through salt bridges at *i* and *i+4*, and hydrophobic interactions at *i+7*. (C) Representative current recordings of hybridized α-Syn$_{(dC30)}$ in the presence of mimetic 3 or dopamine. Negatively charged DOPC: DOPG (4:1) lipid bilayer was formed under the voltage of -200 mV.

6.4 Conclusions

Previously, single-nanopore studies characterized the conformation and dynamics of amyloid proteins using several heterogeneous events rather than the kinetics of a single-molecule amyloid protein. Here we observed the α-Syn interaction with lipids at a single-molecule level by trapping the molecule under externally applied dielectrophoretic force. We show that the conformational switch kinetics of α-Syn in the presence of lipid membranes can be extracted from single-molecule nanopore dielectrophoretic trapping. The binding and unbinding of α-Syn are modulated by the charged nature of the lipids constituting the membranes and the metal ions. Therefore, the nanopore trapping method offers a single-molecule detection for understanding the kinetic conformation switch of intrinsically disordered proteins in a lipidic environment.

The limitations of our study are that binding and unbinding characteristics of trapping for hybridized α-Syn are under externally applied dielectrophoretic force. The external force and hybridization may influence the intrinsic structural properties of α-Syn in a lipidic environment. To address these issues future work in our laboratory will explore the use of electrode-free nanopore sensing [67]. Additionally, the single-nanopore technique in our study still remains challenging to visualize the dynamics and kinetics of α-Syn, in which direct imaging would be more straightforward to validate these two conformational states at a single-molecule level. The combination of fluorescence-based diffusion method would be one potential method to observe the different status of molecules through the fluorescence signal changes [67], though it is beyond the scope of our work.

Last, we found that disease-associated metal ions and peptidomimetic compounds modulate the conformational dynamics of α-Syn in lipid membranes. In principle, the method can be used for screening inhibitors suppressing the interaction between lipid and α-Syn, which will be the subject of further study. The development of microelectrode-cavity arrays, such as the commercial Orbit 16 TC equipped with the dedicated low-noise 16-channel amplifier, allows the formation of 16 selected ion-conducting channels or pores parallelly [68]. We believe that further parallelization of single-molecule nanopore trapping has the potential to enable high-throughput screening of potential therapeutics against intrinsically disordered proteins in lipidic environments.

6.5 Materials and methods

6.5.1 Protein expression of wild-type (WT) αHL and WT α-Syn

WT αHL was expressed based on the previous reports [68]. In brief, αHL plasmid was transformed into competent E.*coil* BL21(DE3)pLysS cells. A single colony was cultured in 100 mL LB medium with 100 μg/mL ampicillin at 37 ℃, 180 rpm. Once the E.*coli* reached an OD600 of 0.6, IPTG was added up to a concentration of 1 mM and the culture was incubated at 18 ℃, 180 rpm overnight. The cell pellet was further lysed in 50 mM Tris (pH 8.0), 500 mM NaCl, 10 mM imidazole and 3.8 mM DDM (n-Dodecyl β-D-maltoside, Cat.ID D310S, Anatrace (Ohio, USA)) on ice. For His-tagged αHL purification, immobilized metal-affinity chromatography (IMAC) was used in a high-affinity TALON (Cobalt) resin (Sigma-Aldrich). The imidazole gradient elution with concentrations of 20 mM, 50 mM and 500 mM was applied for purifying αHL monomers from heptamers in 50 mM Tris buffer (pH 8.0), with 500 mM NaCl and 3.8 mM DDM. The purified proteins were aliquoted and stored at -80 °C. SDS-PAGE gel electrophoresis (Bio-rad, 4-20 % Mini-PROTEAN® TGX™ Precast Protein Gels) at 200

mV was implemented to verify the protein purification. The protein concentration was determined by Nanodrop at 280 nm.

The primary procedure of WT α-Syn plasmid transformation is similar with αHL. IPTG (final concentration 1 mM) was added into the overnight culture of transformed BL21(DE3)pLysS, after the E.*coli* reached an OD600 of 1.04. After 4 h incubation at 37 °C, 180 rpm, the cell pellet was harvested at 4°C. Osmotic shock purification was carried out. 1L cell pellet was suspended in 100 ml, 40% sucrose osmotic shock buffer with 30 mM Tris, pH 7.2, and 2 mM EDTA disodium. After the incubation for 10 min at room temperature, centrifugation at 12,000 rpm for 20 min was applied for recollecting the pellet, then subjected to 90 ml cold water with 37.5 µl of saturated MgCl2. After 3 min incubation on ice, the periplasm α-Syn proteins were collected in the supernatant by centrifugation at 12,000 rpm for 20 min. After dialyzed in 20 mM Tris buffer, pH 8 overnight, α-Syn was eluted in a 0-0.5 M NaCl gradient in 20 mM Tris, pH 8.0 by ion-exchange chromatography (IEX) on a 5 mL HiTrap Q-Sepharose Fast Flow column (GE Healthcare). Fractions containing a large amount of α-Syn were collected and precipitated by adding the saturated ammonium sulfate solution (4.3 M at room temperature) until 50% saturation (1:1) was reached. The precipitated α-Syn was dissolved in 20 mM Tris (pH 7.2) and subjected to size exclusion chromatography (SEC) on a GF Hiload Superdex 75 16/60 column (GE Healthcare), and eluted with 20 mM Tris, pH7.2. After the SDS-PAGE gel electrophoresis (4–20% Mini-PROTEAN® TGX™ Precast Protein Gels), fractions containing α-Syn were aliquoted and stored at -80 °C.

6.5.2 The purification of α-Syn conjugated with nucleotide oligo (dC30)

The residue Ala^{140} of α-Syn was mutated to Cysteine by using a Quick Change II XL site-directed mutagenesis kit (Stratagene) and confirmed by the sequencing. The plasmid containing α-Syn A140C was expressed and purified as WT α-Syn protein production mentioned above. Prior to the conjunction, α-Syn A140C protein was reduced in the presence of DDT and purified by using size exclusion chromatography (Superdex 75 Increase 10/300 GL, GE Healthcare). Oligo(dC)30 was reacted with α-Syn A140C by using established protocol reported previously [69]. Briefly, 2,2'-Dipyridyldisulfide (Sigma-Cat.ID: 8411090005) was used to activate 5'-thiol (hexamethylene linker)-modified oligo(dC)30 (Integrated DNA Technologies) and 10 mM DTT was subsequently applied for the reduction of the activated oligos for 1 hour. The oligos were separated from DTT by size-exclusion chromatography (Superdex 75 Increase 10/300 GL, GE Healthcare) and reacted with purified α-Syn A140C for

16 h at room temperature. The final product was purified by 0-1 M KCl gradient elution with HiTrap Q FF ion exchange column, GE Healthcare) in 10 mM Tris pH 8.0 with 1 mM EDTA and verified by SDS-Page gel and LC-MS.

6.5.3 Preparation of lipid bilayer

A mixture of 20 mg/mL DOPC (1,2-dioleoyl-sn-glycero-3-phosphocholine, Cat.ID 850375P, Avanti Polar Lipids (Alabaster, AL)):DOPG (1,2-dioleoyl-sn-glycero-3-phospho-(1′-rac-glycerol), Cat.ID 840475C, Avanti Polar Lipids (Alabaster, AL)) (in a ratio of 4:1) in chloroform was prepared in a glass vial, and dried by the N_2 gas. To completely remove the chloroform, the glass vial was transferred to a vacuum desiccator for 4 h. Pentane (99%, Sigma-Aldrich,) was added to dissolve the dried lipid film of DOPC:DOPG mixture or DPhPC lipid powder at a concentration of 10 mg/mL. The black lipid bilayer was formed by using Montal and Mueller method [70] with 5 μL DOPC:DOPG (4:1) or DPhPC in two compartments (*cis* or *trans*) of the home-made chamber. The chamber was separated by a 25 μm thick Teflon film (Good Fellow Inc., #FP301200) with a 100 μm aperture. The single-channel electrical recording was carried out in 500 μL, 10 mM Hepes buffer, pH 7.4, with 1 mM KCl. The aperture was pretreated with 0.5 μL, 2 % (v/v) hexadecane/pentane mixture and was dried immediately by N_2. The electrical signals were collected through a pair of Ag/AgCl electrodes separately into the *cis*- and *trans*-compartments. The *cis* side was defined as the grounded side and a voltage potential was applied to the *trans* side. It means that the positively charged analytes can translocate from *trans* to *cis* through the bilayer.

6.5.4 Single-channel recording and data analysis

The single-channel recordings were conducted in a whole-cell mode with a patch-clamp amplifier (Axopatch 200 B, Axon instrument, Molecular Devices, CA). For data acquisition, a DigiData 1440 A/D converter (Axon) was equipped with a PC, where the pClamp and Clampfit were installed for the data process. The purified αHL in 50 mM Tris buffer, pH 8.0, with 500 mM NaCl, 500 mM imidazole, and 3.8 mM DDM, was diluted to 1 μg/mL. 2 μL αHL proteins were added to the *cis* part of the chamber for a single nanopore formation. The purified protein was added into the *trans* part of the chamber with a final concentration 0.2 μM. The ratio of protein and metal ions is 1:25. All the experiments were carried out at room temperature.

6.5.5 LC-MS (Liquid chromatography–mass spectrometry)

The molecule weight of purified proteins including WT αHL, α-Syn and nucleotide oligo (dC30) conjuncted α-Syn were identified by LC-MS. ESI-TOF MS (LCT Premier Mass Spectrometer, Waters AG, Baden-Dättwil, Switzerland) was combined with the LC (Waters 2795). A gradient of ACN/water in the presence of 0.1% formic acid was prepared for the MassPREP Phenyl Guard Column (Waters n°186002785) or the C18 Aeris widepore column (Phenomenex). The obtained MS spectrums for multiply charged protein ions were deconvoluted by using MAxent1 software to obtain the protein mass. The LC-MS results were shown in the supporting information Fig.S3.

6.5.6 Synthesis of helix mimic compound 3

The synthesis procedure is followed by the previous publication [71].

6.6 Author Contributions

J.W., J.L. designed research; J.W.: performed research and analyzed data; T.Y., S.T.: provided mimetic compound 3; A.D.H., J.W., J.L.: revised the paper.

6.7 Acknowledgements

We acknowledge financial support from The Universities of Oxford and Southampton, the Paul Scherrer Insitute, the EPSRC (EP/S028722/1, S.T.), the Swiss National Scientific Foundation ((310030_197626, J.L.), the Brightfocus foundation (A20201759S, J.L.) and Takeda Pharmaceutical Company Limited for their generosity in providing financial and logistical support during a sabbatical position for T.Y. as a visiting Scientist in The University of Oxford.

6.8 References

(1) Jakes, R.; Spillantini, M. G.; Goedert, M. Identification of two distinct synucleins from human brain. *FEBS letters* **1994**, *345* (1), 27-32.
(2) Davidson, W. S.; Jonas, A.; Clayton, D. F.; George, J. M. Stabilization of α-synuclein secondary structure upon binding to synthetic membranes. *Journal of Biological Chemistry* **1998**, *273* (16), 9443-9449.
(3) Rovere, M.; Sanderson, J. B.; Fonseca‐Ornelas, L.; Patel, D. S.; Bartels, T. Refolding of helical soluble α‐synuclein through transient interaction with lipid interfaces. *FEBS letters* **2018**, *592* (9), 1464-1472.
(4) Eliezer, D.; Kutluay, E.; Bussell Jr, R.; Browne, G. Conformational properties of α-synuclein in its free and lipid-associated states. *Journal of molecular biology* **2001**, *307* (4), 1061-1073.
(5) Chen, M.; Margittai, M.; Chen, J.; Langen, R. Investigation of α-synuclein fibril structure by site-directed spin labeling. *Journal of Biological Chemistry* **2007**, *282* (34), 24970-24979.

(6) Comellas, G.; Lemkau, L. R.; Zhou, D. H.; George, J. M.; Rienstra, C. M. Structural intermediates during α-synuclein fibrillogenesis on phospholipid vesicles. *Journal of the American Chemical Society* **2012**, *134* (11), 5090-5099.
(7) Perrin, R. J.; Woods, W. S.; Clayton, D. F.; George, J. M. Interaction of human α-synuclein and Parkinson's disease variants with phospholipids: structural analysis using site-directed mutagenesis. *Journal of Biological Chemistry* **2000**, *275* (44), 34393-34398.
(8) van Rooijen, B. D.; Claessens, M. M.; Subramaniam, V. Membrane binding of oligomeric α-synuclein depends on bilayer charge and packing. *FEBS letters* **2008**, *582* (27), 3788-3792.
(9) Ghio, S.; Kamp, F.; Cauchi, R.; Giese, A.; Vassallo, N. Interaction of α-synuclein with biomembranes in Parkinson's disease—role of cardiolipin. *Progress in lipid research* **2016**, *61*, 73-82.
(10) Gurnev, P. A.; Yap, T. L.; Pfefferkorn, C. M.; Rostovtseva, T. K.; Berezhkovskii, A. M.; Lee, J. C.; Parsegian, V. A.; Bezrukov, S. M. Alpha-synuclein lipid-dependent membrane binding and translocation through the α-hemolysin channel. *Biophys J* **2014**, *106* (3), 556-565. DOI: 10.1016/j.bpj.2013.12.028 PubMed.
(11) Pacheco, C.; Aguayo, L. G.; Opazo, C. An extracellular mechanism that can explain the neurotoxic effects of α-synuclein aggregates in the brain. *Frontiers in physiology* **2012**, *3*, 297.
(12) Wu, J.; Blum, T. B.; Farrell, D. P.; DiMaio, F.; Abrahams, J. P.; Luo, J. Cryo‐electron Microscopy Imaging of Alzheimer's Amyloid‐beta 42 Oligomer Displayed on a Functionally and Structurally Relevant Scaffold. *Angewandte Chemie International Edition* **2021**, *60* (34), 18680-18687.
(13) Wu, J.; Cao, C.; Loch, R. A.; Tiiman, A.; Luo, J. Single-molecule studies of amyloid proteins: from biophysical properties to diagnostic perspectives. *Quarterly Reviews of Biophysics* **2020**, *53*.
(14) Pandey, A. P.; Haque, F.; Rochet, J.-C.; Hovis, J. S. Clustering of α-synuclein on supported lipid bilayers: role of anionic lipid, protein, and divalent ion concentration. *Biophys J* **2009**, *96* (2), 540-551.
(15) Ugalde, C. L.; Lawson, V. A.; Finkelstein, D. I.; Hill, A. F. The role of lipids in α-synuclein misfolding and neurotoxicity. *Journal of Biological Chemistry* **2019**, *294* (23), 9016-9028. DOI: https://doi.org/10.1074/jbc.REV119.007500.
(16) Middleton, E. R.; Rhoades, E. Effects of Curvature and Composition on α-Synuclein Binding to Lipid Vesicles. *Biophys J* **2010**, *99* (7), 2279-2288. DOI: https://doi.org/10.1016/j.bpj.2010.07.056.
(17) Ouberai, M. M.; Wang, J.; Swann, M. J.; Galvagnion, C.; Guilliams, T.; Dobson, C. M.; Welland, M. E. α-Synuclein senses lipid packing defects and induces lateral expansion of lipids leading to membrane remodeling. *Journal of Biological Chemistry* **2013**, *288* (29), 20883-20895.
(18) Burré, J.; Sharma, M.; Südhof, T. C. Definition of a Molecular Pathway Mediating α-Synuclein Neurotoxicity. *The Journal of Neuroscience* **2015**, *35* (13), 5221-5232. DOI: 10.1523/jneurosci.4650-14.2015.
(19) Ugalde, C. L.; Finkelstein, D. I.; Lawson, V. A.; Hill, A. F. Pathogenic mechanisms of prion protein, amyloid-β and α-synuclein misfolding: the prion concept and neurotoxicity of protein oligomers. *Journal of Neurochemistry* **2016**, *139* (2), 162-180. DOI: https://doi.org/10.1111/jnc.13772.
(20) Hozumi, I.; Hasegawa, T.; Honda, A.; Ozawa, K.; Hayashi, Y.; Hashimoto, K.; Yamada, M.; Koumura, A.; Sakurai, T.; Kimura, A. Patterns of levels of biological metals in CSF differ among neurodegenerative diseases. *Journal of the neurological sciences* **2011**, *303* (1-2), 95-99.

(21) Dexter, D.; Wells, F.; Lee, A.; Agid, F.; Agid, Y.; Jenner, P.; Marsden, C. Increased nigral iron content and alterations in other metal ions occurring in brain in Parkinson's disease. *Journal of neurochemistry* **1989**, *52* (6), 1830-1836.
(22) Barnham, K. J.; Bush, A. I. Metals in Alzheimer's and Parkinson's diseases. *Current opinion in chemical biology* **2008**, *12* (2), 222-228.
(23) Deas, E.; Cremades, N.; Angelova, P. R.; Ludtmann, M. H.; Yao, Z.; Chen, S.; Horrocks, M. H.; Banushi, B.; Little, D.; Devine, M. J. Alpha-synuclein oligomers interact with metal ions to induce oxidative stress and neuronal death in Parkinson's disease. *Antioxidants & redox signaling* **2016**, *24* (7), 376-391.
(24) Binolfi, A.; Rasia, R. M.; Bertoncini, C. W.; Ceolin, M.; Zweckstetter, M.; Griesinger, C.; Jovin, T. M.; Fernández, C. O. Interaction of α-synuclein with divalent metal ions reveals key differences: A link between structure, binding specificity and fibrillation enhancement. *Journal of the American Chemical Society* **2006**, *128* (30), 9893-9901.
(25) Alpha-Synuclein Oligomers Interact with Metal Ions to Induce Oxidative Stress and Neuronal Death in Parkinson's Disease. *Antioxidants & Redox Signaling* **2016**, *24* (7), 376-391. DOI: 10.1089/ars.2015.6343.
(26) Rasia, R. M.; Bertoncini, C. W.; Marsh, D.; Hoyer, W.; Cherny, D.; Zweckstetter, M.; Griesinger, C.; Jovin, T. M.; Fernández, C. O. Structural characterization of copper (II) binding to α-synuclein: Insights into the bioinorganic chemistry of Parkinson's disease. *Proceedings of the National Academy of Sciences* **2005**, *102* (12), 4294-4299.
(27) Houghtaling, J.; List, J.; Mayer, M. Nanopore‐Based, Rapid Characterization of Individual Amyloid Particles in Solution: Concepts, Challenges, and Prospects. *Small* **2018**, *14* (46), 1802412.
(28) Wang, H.-Y.; Ying, Y.-L.; Li, Y.; Kraatz, H.-B.; Long, Y.-T. Nanopore analysis of β-amyloid peptide aggregation transition induced by small molecules. *Analytical chemistry* **2011**, *83* (5), 1746-1752.
(29) Wang, H.-Y.; Gu, Z.; Cao, C.; Wang, J.; Long, Y.-T. Analysis of a single α-synuclein fibrillation by the interaction with a protein nanopore. *Analytical chemistry* **2013**, *85* (17), 8254-8261.
(30) Asandei, A.; Iftemi, S.; Mereuta, L.; Schiopu, I.; Luchian, T. Probing of various physiologically relevant metals: Amyloid-β peptide interactions with a lipid membrane-immobilized protein nanopore. *The Journal of Membrane Biology* **2014**, *247* (6), 523-530.
(31) Movileanu, L.; Schmittschmitt, J. P.; Scholtz, J. M.; Bayley, H. Interactions of peptides with a protein pore. *Biophys J* **2005**, *89* (2), 1030-1045.
(32) Mereuta, L.; Schiopu, I.; Asandei, A.; Park, Y.; Hahm, K.-S.; Luchian, T. Protein nanopore-based, single-molecule exploration of copper binding to an antimicrobial-derived, histidine-containing chimera peptide. *Langmuir* **2012**, *28* (49), 17079-17091.
(33) Song, L.; Hobaugh, M. R.; Shustak, C.; Cheley, S.; Bayley, H.; Gouaux, J. E. Structure of Staphylococcal alpha-Hemolysin, a Heptameric Transmembrane Pore. *Science* **1996**, *274* (5294), 1859-1865. DOI: doi:10.1126/science.274.5294.1859.
(34) Ferreon, A. C. M.; Gambin, Y.; Lemke, E. A.; Deniz, A. A. Interplay of α-synuclein binding and conformational switching probed by single-molecule fluorescence. *Proceedings of the National Academy of Sciences* **2009**, *106* (14), 5645-5650. DOI: doi:10.1073/pnas.0809232106.
(35) Tavassoly, O.; Nokhrin, S.; Dmitriev, O. Y.; Lee, J. S. Cu(II) and dopamine bind to α-synuclein and cause large conformational changes. *Febs j* **2014**, *281* (12), 2738-2753. DOI: 10.1111/febs.12817 From NLM.
(36) Rodriguez-Larrea, D.; Bayley, H. Protein co-translocational unfolding depends on the direction of pulling. *Nature Communications* **2014**, *5* (1), 4841. DOI: 10.1038/ncomms5841.

(37) Rodriguez-Larrea, D.; Bayley, H. Multistep protein unfolding during nanopore translocation. *Nature Nanotechnology* **2013**, *8* (4), 288-295. DOI: 10.1038/nnano.2013.22.
(38) Zhu, J.; Hu, G.; Xuan, X. Electrokinetic particle entry into microchannels. *Electrophoresis* **2012**, *33* (6), 916-922.
(39) Lashuel, H. A.; Overk, C. R.; Oueslati, A.; Masliah, E. The many faces of α-synuclein: from structure and toxicity to therapeutic target. *Nat Rev Neurosci* **2013**, *14* (1), 38-48. DOI: 10.1038/nrn3406 From NLM.
(40) Davidson, W. S.; Jonas, A.; Clayton, D. F.; George, J. M. Stabilization of alpha-synuclein secondary structure upon binding to synthetic membranes. *J Biol Chem* **1998**, *273* (16), 9443-9449. DOI: 10.1074/jbc.273.16.9443 From NLM.
(41) Epand, R. F.; Maloy, L.; Ramamoorthy, A.; Epand, R. M. Amphipathic helical cationic antimicrobial peptides promote rapid formation of crystalline states in the presence of phosphatidylglycerol: lipid clustering in anionic membranes. *Biophys J* **2010**, *98* (11), 2564-2573.
(42) Paterson, D. J.; Tassieri, M.; Reboud, J.; Wilson, R.; Cooper, J. M. Lipid topology and electrostatic interactions underpin lytic activity of linear cationic antimicrobial peptides in membranes. *Proceedings of the National Academy of Sciences* **2017**, *114* (40), E8324-E8332.
(43) Magzoub, M.; Kilk, K.; Eriksson, L. G.; Langel, Ü.; Gräslund, A. Interaction and structure induction of cell-penetrating peptides in the presence of phospholipid vesicles. *Biochimica et Biophysica Acta (BBA)-Biomembranes* **2001**, *1512* (1), 77-89.
(44) Jobin, M.-L.; Bonnafous, P.; Temsamani, H.; Dole, F.; Grélard, A.; Dufourc, E. J.; Alves, I. D. The enhanced membrane interaction and perturbation of a cell penetrating peptide in the presence of anionic lipids: toward an understanding of its selectivity for cancer cells. *Biochimica et Biophysica Acta (BBA)-Biomembranes* **2013**, *1828* (6), 1457-1470.
(45) Binder, H.; Lindblom, G. A molecular view on the interaction of the trojan peptide penetratin with the polar interface of lipid bilayers. *Biophys J* **2004**, *87* (1), 332-343.
(46) Deol, S. S.; Domene, C.; Bond, P. J.; Sansom, M. S. Anionic phospholipid interactions with the potassium channel KcsA: simulation studies. *Biophys J* **2006**, *90* (3), 822-830.
(47) Rosen, C. B.; Rodriguez-Larrea, D.; Bayley, H. Single-molecule site-specific detection of protein phosphorylation with a nanopore. *Nature Biotechnology* **2014**, *32* (2), 179-181. DOI: 10.1038/nbt.2799.
(48) Maglia, G.; Restrepo, M. R.; Mikhailova, E.; Bayley, H. Enhanced translocation of single DNA molecules through alpha-hemolysin nanopores by manipulation of internal charge. *Proc Natl Acad Sci U S A* **2008**, *105* (50), 19720-19725. DOI: 10.1073/pnas.0808296105 From NLM.
(49) Hu, R.; Diao, J.; Li, J.; Tang, Z.; Li, X.; Leitz, J.; Long, J.; Liu, J.; Yu, D.; Zhao, Q. Intrinsic and membrane-facilitated α-synuclein oligomerization revealed by label-free detection through solid-state nanopores. *Sci Rep* **2016**, *6*, 20776. DOI: 10.1038/srep20776 From NLM.
(50) Wang, H. Y.; Ying, Y. L.; Li, Y.; Kraatz, H. B.; Long, Y. T. Nanopore analysis of β-amyloid peptide aggregation transition induced by small molecules. *Anal Chem* **2011**, *83* (5), 1746-1752. DOI: 10.1021/ac1029874 From NLM.
(51) Meyer, N.; Arroyo, N.; Janot, J. M.; Lepoitevin, M.; Stevenson, A.; Nemeir, I. A.; Perrier, V.; Bougard, D.; Belondrade, M.; Cot, D.; et al. Detection of Amyloid-β Fibrils Using Track-Etched Nanopores: Effect of Geometry and Crowding. *ACS Sens* **2021**, *6* (10), 3733-3743. DOI: 10.1021/acssensors.1c01523 From NLM.
(52) Stefureac, R. I.; Madampage, C. A.; Andrievskaia, O.; Lee, J. S. Nanopore analysis of the interaction of metal ions with prion proteins and peptidesThis paper is one of a selection of papers published in this special issue entitled "Canadian Society of Biochemistry, Molecular & Cellular Biology 52nd Annual Meeting — Protein Folding: Principles and

Diseases" and has undergone the Journal's usual peer review process. *Biochemistry and Cell Biology* **2010**, *88* (2), 347-358. DOI: 10.1139/O09-176 (acccessed 2022/03/11).
(53) Wang, H.; Mörman, C.; Sternke-Hoffmann, R.; Huang, C.-Y.; Prota, A.; Ma, P.; Luo, J. Cu2+ ions modulate the interaction between α-synuclein and lipid membranes. *Journal of Inorganic Biochemistry* **2022**, *236*, 111945. DOI: https://doi.org/10.1016/j.jinorgbio.2022.111945.
(54) Feng, J.; Martin-Baniandres, P.; Booth, M. J.; Veggiani, G.; Howarth, M.; Bayley, H.; Rodriguez-Larrea, D. Transmembrane protein rotaxanes reveal kinetic traps in the refolding of translocated substrates. *Communications Biology* **2020**, *3* (1), 159. DOI: 10.1038/s42003-020-0840-5.
(55) Stoddart, D.; Heron, A. J.; Mikhailova, E.; Maglia, G.; Bayley, H. Single-nucleotide discrimination in immobilized DNA oligonucleotides with a biological nanopore. *Proceedings of the National Academy of Sciences* **2009**, *106* (19), 7702-7707. DOI: doi:10.1073/pnas.0901054106.
(56) Ding, Y.; Kanavarioti, A. Single pyrimidine discrimination during voltage-driven translocation of osmylated oligodeoxynucleotides via the α-hemolysin nanopore. *Beilstein J Nanotechnol* **2016**, *7*, 91-101. DOI: 10.3762/bjnano.7.11 PubMed.
(57) van Rooijen, B. D.; Claessens, M. M.; Subramaniam, V. Lipid bilayer disruption by oligomeric alpha-synuclein depends on bilayer charge and accessibility of the hydrophobic core. *Biochim Biophys Acta* **2009**, *1788* (6), 1271-1278. DOI: 10.1016/j.bbamem.2009.03.010 From NLM.
(58) Kjaer, L.; Giehm, L.; Heimburg, T.; Otzen, D. The influence of vesicle size and composition on alpha-synuclein structure and stability. *Biophys J* **2009**, *96* (7), 2857-2870. DOI: 10.1016/j.bpj.2008.12.3940 PubMed.
(59) Stöckl, M.; Fischer, P.; Wanker, E.; Herrmann, A. α-Synuclein Selectively Binds to Anionic Phospholipids Embedded in Liquid-Disordered Domains. *Journal of Molecular Biology* **2008**, *375* (5), 1394-1404. DOI: https://doi.org/10.1016/j.jmb.2007.11.051.
(60) Moons, R.; Konijnenberg, A.; Mensch, C.; Van Elzen, R.; Johannessen, C.; Maudsley, S.; Lambeir, A.-M.; Sobott, F. Metal ions shape α-synuclein. *Scientific Reports* **2020**, *10* (1), 16293. DOI: 10.1038/s41598-020-73207-9.
(61) Bavinton, C. E.; Sternke-Hoffmann, R.; Knipe, P. C.; Yamashita, T.; Hamilton, A. D.; Luo, J.; Thompson, S. Rationally Designed Helical Peptidomimetics Disrupt alpha–Synuclein Fibrillation. *Chemical Communications* **2022**.
(62) Peacock, H.; Luo, J.; Yamashita, T.; Luccarelli, J.; Thompson, S.; Hamilton, A. D. Non-covalent S⋯ O interactions control conformation in a scaffold that disrupts islet amyloid polypeptide fibrillation. *Chemical science* **2016**, *7* (10), 6435-6439.
(63) Cappai, R.; Leck, S.-L.; Tew, D. J.; Williamson, N. A.; Smith, D. P.; Galatis, D.; Sharpies, R. A.; Curtain, C. C.; Ali, F. E.; Cherny, R. A.; et al. Dopamine promotes α-synuclein aggregation into SDS-resistant soluble oligomers via a distinct folding pathway. *The FASEB Journal* **2005**, *19* (10), 1377-1379. DOI: https://doi.org/10.1096/fj.04-3437fje.
(64) Planchard, M. S.; Exley, S. E.; Morgan, S. E.; Rangachari, V. Dopamine‐induced α‐synuclein oligomers show self‐and cross‐propagation properties. *Protein Science* **2014**, *23* (10), 1369-1379.
(65) Fischer, A. F.; Matera, K. M. Stabilization of alpha-synuclein oligomers in vitro by the neurotransmitters, dopamine and norepinephrine: the effect of oxidized catecholamines. *Neurochemical research* **2015**, *40* (7), 1341-1349.
(66) Mor, D. E.; Tsika, E.; Mazzulli, J. R.; Gould, N. S.; Kim, H.; Daniels, M. J.; Doshi, S.; Gupta, P.; Grossman, J. L.; Tan, V. X. Dopamine induces soluble α-synuclein oligomers and nigrostriatal degeneration. *Nature neuroscience* **2017**, *20* (11), 1560-1568.

(67) Wang, Y.; Wang, Y.; Du, X.; Yan, S.; Zhang, P.; Chen, H.-Y.; Huang, S. Electrode-free nanopore sensing by DiffusiOptoPhysiology. *Science advances* **2019**, *5* (9), eaar3309.
(68) Wu, J.; Blum, T. B.; Farrell, D. P.; DiMaio, F.; Abrahams, J. P.; Luo, J. Cryo-electron Microscopy Imaging of Alzheimer's Amyloid-beta 42 Oligomer Displayed on a Functionally and Structurally Relevant Scaffold. *Angewandte Chemie International Edition* **2021**, *60* (34), 18680-18687. DOI: https://doi.org/10.1002/anie.202104497.
(69) Rodriguez-Larrea, D.; Bayley, H. Protein co-translocational unfolding depends on the direction of pulling. *Nat Commun* **2014**, *5*, 4841. DOI: 10.1038/ncomms5841 From NLM.
(70) Montal, M.; Mueller, P. Formation of bimolecular membranes from lipid monolayers and a study of their electrical properties. *Proceedings of the National Academy of Sciences of the United States of America* **1972**, *69* (12), 3561-3566. DOI: 10.1073/pnas.69.12.3561 PubMed.
(71) Bavinton, C. E.; Sternke-Hoffmann, R.; Yamashita, T.; Knipe, P. C.; Hamilton, A. D.; Luo, J.; Thompson, S. Rationally designed helical peptidomimetics disrupt α-synuclein fibrillation. *Chemical Communications* **2022**, *58* (33), 5132-5135, 10.1039/D2CC00212D. DOI: 10.1039/D2CC00212D.

6.9 Supporting information

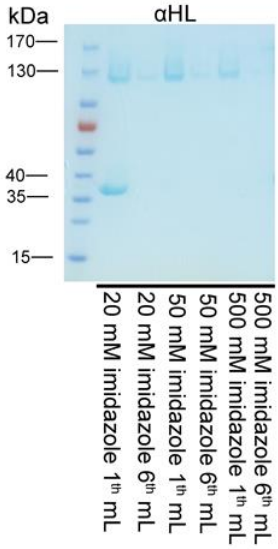

Figure S1. The purification of His-tagged WT αHL. Imidazole concentration gradient (20, 50 and 500 mM) was applied to elute αHL monomers and heptamers in the buffer of 50 mM Tris (pH 8.0), 500 mM NaCl and 3.8 mM DDM. Total 6 mL elution buffer was used to elute the supernatant from 100 mL culture for each imidazole concentration. The 1st and 6st mL elution buffer with different imidazole concentration was run on SDS-gel separately.

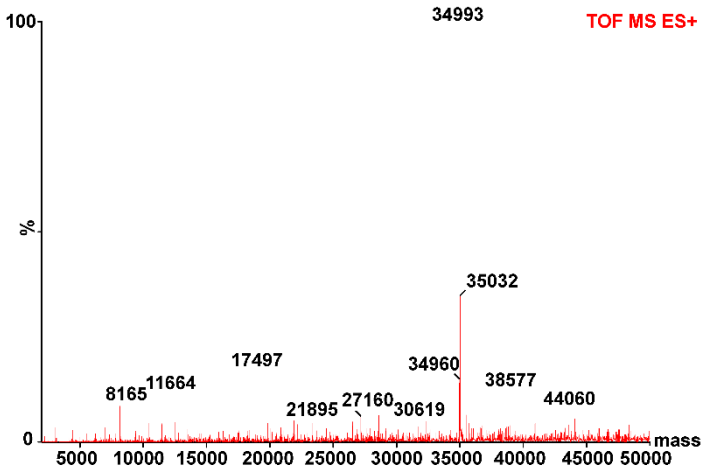

Figure S2. Deconvoluted mass spectrum of the purified WT αHL. LC-MS was conducted to confirm the molecule weight (MW) of αHL. The experimental molecule weight (MW) of αHL is 34993, compared to theoretical MW 34991 Da.

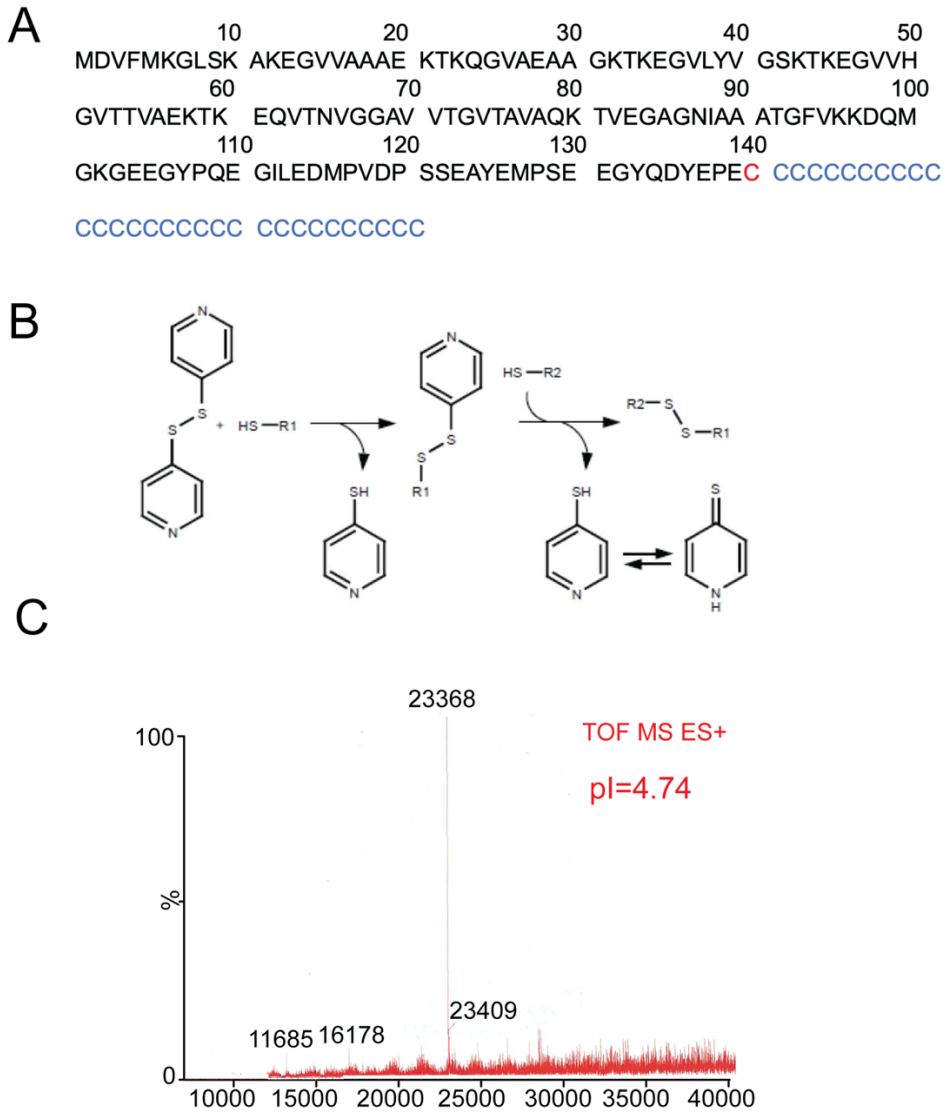

Figure S3. (A) The protein sequence of hybrid αSyn$_{(dC30)}$. The residue Ala^{140} of α-Syn was mutated to Cysteine (C) (Red). The linked oligo(dC30) is marked as blue. (B) Thiol–Disulfide interchange reaction was used to link αSyn(A140C) to C30 with 5′-thiol hexamethylene linker through 2,2′-dipyridyl disulphide. (C) Deconvoluted mass spectrum of the purified nucleotide oligo (dC30) conjucted α-Syn. LC-MS was conducted to confirm the molecular weight. The theoretical molecular weight is 23355 Da, which is made up of three parts: αSyn(A140C) 14547 Da, C30 8692 Da, and 5′-thiol hexamethylene linker 116 Da. The experimental molecular weight is 23368 Da and is slightly different from the theoretical one. It might be caused by the pronation. The isoelectric point (pI) of αSyn$_{(dC30)}$ is 4.74.

Chapter 7

7 Summary and perspective

The aggregation and accumulation of neurodegenerative-associated peptides to form the toxic amyloid oligomers and protofibrils inducing a progressive failure of the proteostasis network plays an important role in disease-relevant neurotoxicity. The transiency and structural heterogeneity of amyloid oligomeric aggregates hinders elucidating the exact mechanism of oligomer-induced neurotoxicity and impedes further bringing forward the diagnosis and subsequent therapy of neurodegenerative diseases. This thesis aimed to present a detailed understanding of the connection between amyloid assembly and toxicity through the characterization of amyloid oligomer formation and interferences, helping provide the perspectives on the future direction of diagnosis and subsequent therapy for curbing the progression of neurodegenerative diseases.

Based on my work, several following conclusions were proposed in my thesis. First, in the second chapter, single-molecule techniques (SMTs) provide complementary tools to the regularly used bulk techniques to characterize the biophysical properties of transient amyloid aggregates to correspond to the neurotoxicity in neurological disorders. Additionally, we present a series of evidence to show the indispensable role of SMTs in determining the oligomers binding to membranes, which manifest the permeabilization (membrane pore formation or membrane-thinning) of cellular membrane induced by amyloid oligomers as the main reason for disrupting cellular homeostasis. We summarized the detection of different size distributions of aggregates in different stages of neurodegenerative diseases like AD and PD via SMTs and proposed the feasibility and possibility assisted by SMTs to analyze their responses to toxicity (inflammation response, Ca^{2+} influx, or neuronal death) as complementary diagnostic criteria to enhance cerebrospinal fluid (CSF) biomarkers accuracy, besides the detection of the overall levels of CSF biomarker. However, the structural information of neurotoxic-associated oligomers obtained from these SMTs mentioned in the second chapter is limited, and the detailed knowledge of structure is known to be essential for further structure-based drug or antibody design and even potential therapies for neurodegenerative diseases. Thus, in the third chapter, we reconstructed a novel protein scaffold αHL for generating and

stabilizing a single Aβ42 oligomer for biochemical characterization and structural determination. The oligomerization of Aβ is determined by the sequence itself and the scaffold only determines its stoichiometry. Our hybrid Aβ42 oligomers retain the membrane-permeabilization ability with a similar channel conductance to the wild-type (WT) Aβ42 oligomers and share the structural similarities with WT Aβ42 oligomers on the β-barrel part. Single-particle Cryo-EM analysis presented a shorter length (35.5 Å) and a similar inner diameter (27.4 Å) of the largest circular cross-section of reconstituted Aβ42 oligomers, compared to the WT αHL barrel (47.8 Å high and 23.8 Å wide). The hybrid construct contributes to understanding membrane protein oligomerization in lipid membranes, especially with regard to the β-sheet-containing proteins that appear to form polymorphic ion channels.
We hope that the well-defined stoichiometric αHL-displayed oligomers can be used as a mimetic antigen to allow the development of novel, conformation-specific antibodies. However, one of the disadvantages of our scaffold is that the moiety of αHL only allows one aggregate species formation and no other oligomeric states. This limitation might influence the further understanding of the molecular mechanism of oligomer-induced neurotoxicity in cellular membranes. It is believed that membrane permeabilization induced by native amyloid oligomers is one of the main toxic mechanisms in progressive neurodegenerative disorders. Thus, in the fourth chapter, we employed the single-channel electrical recording technique to understand the membrane poration mechanism of truncated prion proteins in a lipid bilayer. We found that the primary N-terminal domain (residues 23-50) of prion fragment is essential for prion proteins permeabilizing lipid membranes, and the other N-terminal and C-terminal extended functional segments down-regulate the channel activity, thus might modulate the pathological effects of prion-medicated neurotoxicity. The observed pore formation of the primary N-terminus (residues 23-50) by cryo-EM images further supports the toxic oligomer hypothesis that the prion oligomers permeabilize cellular membranes to generate pores or channels and cause cell dysfunction. Our results provide insights into the new treatment or the drug screening that targets the toxic primary N-terminus and not other fragments. In summary, these three chapters provide information on understanding the amyloid oligomer formation by reviewing biophysical characterization, exploring structural determination, and membrane permeabilization verification.

Amyloid aggregation can be regulated by chaperones, non-chaperones, or other amyloidogenic proteins *in vitro* and *in vivo*. The fibrillation kinetic assays are typically carried out in *vitro*,

where these proteins themselves are prone to the formation of mesoscopic amorphous aggregates due to a lack of proteostasis. In our fifth chapter, we applied a series of biochemical and biophysical techniques to clarify the relationship between the amorphous aggregates and plaque deposits of the amyloid fibril, which are two typical forms observed in the AD brain. Our study demonstrates that as a byproduct, partially folded intermediate states of proteins from amorphous aggregates are more prone to co-aggregate with Aβ40, compared to the native states and their mature aggregates. The off-pathway hetero-aggregation significantly reduces the rate of primary nucleation and elongation in the Aβ40 fibrillation process and meanwhile modulates Aβ40 cytotoxicities presumably caused by the formation of oligomeric complexes, responsible for lipid membrane permeabilization and other oligomer toxicity pathways. The co-aggregation can be of high potential for AD therapeutics and importance for the understanding of molecular pathogenesis in AD. In addition to globular proteins, some environmental factors, such as metal ions and lipids, also modulate amyloid protein aggregation and misfolding. To understand how metal ions modulate amyloid protein interaction with a lipid membrane, in our sixth chapter, we linked α-Syn with a single-strand DNA oligonucleotide dC30 (oligo(dC30)) and employed the single-molecular nanopore technique. Oligo(dC30) was trapped in the nanopore, allowing us to understand one α-Syn protein binding and unbinding to lipid membranes at the single molecular level. We found that metal ions can regulate α-Syn conformational switch in lipid membranes. Cu^{2+} ions refold α-Syn in a more compacted structure and form a stable complex with α-Syn than Zn^{2+} ions in the lipid membrane. We also showed that single-nanopore trapping is suitable to characterize the effect small molecules exert on α-Syn conformational dynamics in the presence of lipid membranes and the potential of being used as a primary tool for screening and optimizing aggregation inhibitors.

In conclusion, this thesis talked about the characterization of biophysical properties of amyloid proteins, including a systematical review of the application of single-molecular techniques on amyloid oligomers and the diagnostic perspectives in chapter 2. Additionally, we explored the amyloid oligomeric formation and interferences from different scopes in chapters 3-6 to understand the connection between amyloid assembly and neurotoxicity. Our results provide the new design ideas to study the heterogeneous amyloid system such as the oligomer stabilization, the off-pathway co-aggregation, the membrane permeabilization, and lipid membrane interaction. These results certainly enhance the deep understanding of the toxic

pathogenic molecular mechanisms of protein misfolding diseases and present the perspectives on the future potential diagnosis or even subsequent therapy for these diseases.

Appendix

Acknowledgments

How time flies! Since I made my first step in Switzerland on the 1st of November, 2018, it has been four years at Paul Scherrer Institute (PSI), Villigen, Switzerland. First and foremost, I would like to appreciate and give my warmest thanks to my supervisor Dr. Luo Jinghui for his support during my Ph.D. study. Furthermore, I would like to acknowledge my committee members: Prof. Jan Pieter Abrahams (University of Basel) for accepting and registering me as a Ph.D. student at the University of Basel (Basel, Switzerland), Prof. Roland Riek (ETH, Zurich, Switzerland) and Prof. Henning Stahlberg (Previous address: University of Basel; Present address: EPFL, Laussane, Switzerland) for their insightful and thoughtful comments and suggestions for my research and dissertation.

My sincere gratitude also goes to all the members of LNB and LBR for their fruitless support and help throughout my whole Ph.D. time at PSI. Especially, I would like to thank my research group members Hongzhi Wang, Rebecca Sternke-Hoffmann, Chang Liu, Fangyuan Duan, and Xun Sun for their help, understanding, and encouragement. I also would like to say big thanks to my internal collaborator Thorsten Blum for his contribution to my project. I also appreciate a lot to my several external PSI collaborating groups, especially Prof. Astrid Gräslund's group from Stockholm University and Prof. Adriano Aguzzi's group from Zurich University, for their insightful advice and contributions to my research work.

Last but not the least, I would like to acknowledge my family in China with my full love. Their unreserved support, love, encouragement, and understanding keep me going throughout my Ph.D. life.